Lithium-Ion battery SOC estimation

by

Sepideh Afshar

A thesis
presented to the University of Waterloo
in fulfillment of the
thesis requirement for the degree of
Doctor of Philosophy
in
Applied Mathematics

Waterloo, Ontario, Canada, 2017

Examining Committee Membership

The following served on the Examining Committee for this thesis. The decision of the Examining Committee is by majority vote.

External Examiner	Chunming Wang Professor
Supervisor	Kirsten Morris Professor
Supervisor	Amir Khajepour Professor
Internal Member	Lilia Krivodonova Associate Professor
Internal Member	Francis Poulin Associate Professor
Internal-external Member	Michael Fowler Professor

I hereby declare that I am the sole author of this thesis. This is a true copy of the thesis, including any required final revisions, as accepted by my examiners.

I understand that my thesis may be made electronically available to the public.

Abstract

Lithium-ion batteries are frequently used in Hybrid electric vehicles (HEVs), which are taking the place of gas-engine vehicles. An important but not measurable quantity in HEVs is the amount of charge remaining in the battery in a drive cycle. The remaining charge is normally identified by a variable called state of charge (SOC). A potential way of estimating the SOC is relating this variable with the state of a dynamical system. Afterwards, the SOC can be estimated through an observer design. As a precise model, electrochemical equations are chosen in this research to estimate the SOC.

The first part of this thesis considers comparison studies of commonly-used finite-dimensional estimation methods for different distributed parameter systems (DPSs). In this part, the system is first approximated by a finite-dimensional representation; the observer dynamics is a copy of the finite-dimensional representation and a filtering gain obtained through observer design. The main outcome of these studies is comparing the performance of different observers in the state estimation of different types of DPSs after truncation. The studies are then expanded to investigate the effect of the truncated model by increasing the order of finite-dimensional approximation of the system numerically. The simulation results are also compared to the mathematical properties of the systems.

A modified sliding mode observer is improved next to take care of the system's nonlinearity and compensate for the estimation error due to disturbances coming from an external input. It is proved that the modified SMO provides an exponential convergence of the estimation error in the existence of an external input. In most cases, the simulations results of the comparison studies indicate the improved performance of the modified SMO observer.

Approximation and well-posedness of two general classes of nonlinear DPSs are studied next. The main concern of these studies is to produce a low-order model which converges to the original equation as the order of approximation increases. The available results in the literature are limited to specified classes of systems. These classes do not cover the lithium-ion cell model; however, the general forms presented here include the electrochemical equations as a specific version.

In order to facilitate the electrochemical model for observer design, simplification of the model is considered in the next step. The original electrochemical equations are composed of both dynamical and constraint equations. They are simplified such that a fully dynamical representation can be derived. The fully dynamical representation is beneficial for real-time application since it does not require solving the constraint equation at

every time iteration while solving the dynamical equations. Next, the electrochemical equations can be transformed into the general state space form studied in this thesis.

Finally, an adaptive EKF observer is designed via the low-order model for SOC estimation. The electrochemical model employed here is a variable solid-state diffusivity model. Compared to other models, the variable solid-state diffusivity model is more accurate for cells with Lithium ion phosphate positive electrode, which are considered here, than others. The adaptive observer is constructed based on considering an adaptive model for the open circuit potential term in the electrochemical equations. The parameters of this model are identified simultaneously with the state estimation. Compared to the experimental data, simulation results show the efficiency of the designed observer in the existence of modeling inaccuracy.

Acknowledgements

First, I would like to sincerely express my gratitude to my advisers Prof. Kirsten Morris and Prof. Amir Khajepour for their support in my PhD studies. This work would not be accomplished without their support, patience, motivation, and immense knowledge. Their continuous guidance helped me during my research and writing this thesis. Furthermore I appreciate the love, patience, and support of my family and my parents.

I would also like to thank the Laboratoire De Réactivité Et Chimie Des Solides (LRCS) in Amiens, France for the permission to use their experimental data to compare with simulations. The financial support of Automotive Partnership Canada (APC), Ontario Research Fund (ORF), and General Motors for this research is also gratefully acknowledged.

Table of Contents

List of Figures

List of Tables

List of Symbols

l_{cat}	thickness of the negative electrode, m
l_{sep}	thickness of the separator, m
R_s	radius of the spherical solid particles, m
ϵ_e	volume fraction of the electrolyte phase
k^{eff}	effective conductivity in the electrolyte phase, Sm^{-1}
σ^{eff}	cathode effective electronic conductivity, Sm^{-1}
a_k	active surface area of the k^{th} LFP particle per unit volume, m^2m^{-3}
c_{max}	maximum concentrationof Li-intercalated sites in LFP, $molm^{-3}$
c_1	electrolyte concentration, $molm^{-3}$
c_T	total concentration of the electrolytic solution, $molm^{-3}$
c_{ini}	initial electrolyte concentration, $molm^{-3}$
$\mathcal{D}$	solid-state binary diffusion coefficient, m^2s^{-1}
D_s	Fickian diffusion coefficient inside the LFP particle, m^2s^{-1}
$\mathcal{D}_{LiPF_6}$	diffusion coefficient of electrolyte , m^2s^{-1}
D_{LiPF_6}	diffusion coefficient of electrolyte, m^2s^{-1}
D_e^{eff}	effective diffusivity in the electrolyte phase, m^2s^{-1}
F	Faraday's constant, $Cmol^{-1}$
i_0	exchange current density for LFP lithiation/delithiation, Am^{-2}
i_f	exchange current density of lithium foil counter electrode, Am^{-2}
i_k	current density normal to the surface of the k^{th} LFP particle, Am^{-2}
I	total current density referred to the geometric area, Am^{-2}
k_c^0	reaction rate constant for LFP lithiation/delithiation, $molm^{-2}s^{-1}(molm^{-3})^{-1.5}$
R	universal gas constant, $Jmol^{-1}K^{-1}$
R_k	radius of the k^{th} LFP particle, m
T	temperature, K
t_+^0	Li^+ transference number

β	charge-transfer coefficient for LFP lithiation/delithiation
β_f	charge-transfer coefficient of lithium foil counter electrode
ϵ_k	volume of k^{th} LFP particle per unit volume of electrode
ϵ_t	total volume of the cathode active material per volume of the electrode
ϵ	component porosity
γ	Bruggeman exponent
k	ionic conductivity of electrolyte, Sm^{-1}

Chapter 1

Introduction

Batteries are the storage unit of electric vehicles and hybrid electric vehicles. They play an important role in providing an efficient source of energy for vehicles. Therefore, the proper choice of battery type and a management system are crucial. Among different chemistries, lithium-ion chemistry is the most promising option for the batteries used for mobile electrification including electric/hybrid electric vehicles. Compared to other cell chemistries, the lithium-ion chemistry is characterised by its delivering high power and energy density, lack of memory effect, low self discharge, and high life cycle [3, 4], and [5]. The memory effect is a well known issue to the users of nickel-cadmium and nickel-metal-hydride batteries. Frequently recharging these batteries after they are partially discharged leads to a loss of usable capacity. Lithium-ion batteries are known to have no memory effect.

Lithium ion phosphate, LiFePO4, (LFP) offers the advantage of better lithium insertion over other conventional materials. Its numerous features have drawn a considerable interest. Some of these features are listed in [6] as

- The LFP material is not only relatively inexpensive and available, but also less toxic compared to other materials like cobalt, nickel, or manganese.
- The operating voltage of the LFP electrode is about 3.4 V with respect to a lithium reference electrode; thus, it provides high energy while minimizing the electrolyte decomposition side reactions.
- This material has a high theoretical specific energy of about 580 Wh/kg elevating it as a proper choice for the cell's positive electrode.

Cells are elementary units of a battery pack. One or more battery packs with different cell configurations may be utilized in electric/hybrid electric vehicles. Therefore, an adequate management system is required to monitor, diagnose, and synchronize among the battery cells. This unit is called a battery management system [5]. On the importance of the battery management system, one can refer to its role in compensating for the costs that come with the lithium-ion batteries. Safety and aging are two important issues that must be overcome by the battery management system. For this reason, the battery management system is required to monitor the state of the battery and perform an organized charging and discharging strategy in the cells [3].

State of Charge (SOC) is the relative amount of the charge inside the cells to what is available when the battery is fully charged. Tracking the SOC of each cell in a battery pack is a key role of the battery management system. At every measurement step, the cells' SOC estimation is updated via measuring the terminal voltage, current, and temperature. In practice, the SOC can be defined as an indication of the amount of remaining charge inside the cell. A number between %0 to %100 is assigned to this indication. Precise estimation of the SOC is important since [7]:

- In contrast to the gasoline tank, the batteries can be overcharged or undercharged if there is no accurate SOC estimation.
- It lets the driver use the entire battery's capacity.
- It provides reliability on the overall energy storage in the sense that the SOC can be used to improve safety and consider aging effects.
- The battery pack can be used aggressively when an accurate SOC is given; thus, lighter battery packs can be used.
- The maximum available charge is given by the SOC estimation. In this case, fewer cycles of charging is required and the life cycle is improved.
- the SOCs of the cells in a battery pack are utilized by the battery management system to balance the state of cells. They become unbalanced over time due to the small differences in their dynamics. It may happen when one cell is at a high SOC limit while some other cells are in a low SOC limit. In a drive cycle, balancing the cells' state is done by boosting the cells with the low SOCs and bucking the cells with the high SOCs [7].

The importance of accurate SOC estimation is even more crucial in the hybrid electric vehicles compared to electric vehicles since their environment characteristics are more demanding. While the absolute value of the current rates in the electric vehicles are not more than 5C, the hybrid electric vehicles draw current rates up to ±20C. Moreover, the profile of the current rate shows more dynamics in the hybrid vehicles since they are designed to overcome sudden load transitions via a battery/motor couple [7] and [8]. This means that an efficient estimation method is required to accurately calculate the SOC from available measurements.

Although direct and precise measurement of the SOC of a cell is not achievable by existing sensors, other quantities like the battery's terminal voltage and current can be easily measured. The importance of accurate SOC evaluation in a safe operation necessitates an alternative method of estimation from the available measurements. The different estimation methods proposed in literature are categorized as direct measurements, indirect/book-keeping, and model based/adaptive methods [9].

An inaccurate but cheap method of SOC estimation is online measurement of current and/or terminal voltage to approximate the value of the SOC. Examples can be found in [4, 10], and [11]. This method highly depends on the temperature, charge/discharge rate, and aging [9]. Open circuit potential (OCP) measurement ([12]) and Impedance measurement ([13]) can be offered as alternative measurements whose assignment to the SOC depends on fewer factors; however, they are not proper for real-time application since they highly depends on environmental conditions.

The second category of SOC estimation methods relies on measuring and integrating the current. This technique is called coulomb counting. The coulomb counting in which the battery effects like discharge efficiency, self discharge, and capacity loss are compensated is called a book-keeping method [9]. The application of the coulomb counting in the SOC estimation can be found in [14, 15, 16, 17, 12, 18, 19, 20, 21], and [22]. Some important factors reducing the estimation accuracy of the coulomb counting are the temperature, charge and discharge efficiency, and cycle life [9]. More importantly, the cumulative effect introduced by an integration approximation makes the estimation sensitive to the measurement errors due to the noise, resolution, and rounding [14].

Model-based techniques are more accurate ways of SOC estimation. Among different models, equivalent circuit models are mostly reported in the literature in this matter. Simplicity and a relatively few number of parameters are the main characteristics of these models [23]. One of the first and important efforts on SOC estimation is the comparative analysis introduced in [24] via Kalman filter. A similar application of Kamlman and

extended Kalman filter to the equivalent circuit models for the SOC estimation can be found in [14, 25, 26], and [27]. Dealing with the model nonlinearity can be evaluated by using sigma-point Kalman filtering. Utilizing this filter in observing the SOC from the voltage measurement is improved in [28] and [29]. Some other examples of the equivalent circuit model-based estimation methods use a sliding mode observer in [30, 31], and [32], adaptive observer in [33], and Luenberger observer in [34, 35], and [5].

More accurate and physical models are electrochemical models since they closely represent the physical behavior inside the cell. Therefore, adding the effect of the temperature and modeling the aging phenomenon, the inherent features of Li-ion batteries, are more feasible. Unfortunately, the electrochemical models are not applicable for real-time observation because of their complexity. A review on most simplified electrochemical models is given in [36]. Averaging over the entire electrode region is also used in [37, 38], and [3] wherein the observation is evaluated by the extended Kalman filter (EKF) and output injection-based observer combined with the mass conservation law respectively.

Employing the Laplace transformation to produce a reduced order model is used in [39] and [40]. A more accurate observation method is given in [41, 42], and [43]. Employing a single particle model in observation is also suggested in some other works including via the Kalman filtering [39, 40], and [44], the sliding mode observer [45], the backstepping observation method [41, 42], and [43]. More recent studies using full electrochemical equations can be found in [46] and [47].

In all of the aforementioned work, a simple model is adequate to represent the cell behavior; however, the employed models will not provide a similar performance for cells with the LFP positive electrode. In these cells, modeling the time variation of the active material distribution in the solid phase is challenging. The battery cell works based on the principle of lithium insertion/deinsertion where the electrons are consumed or produced. This two-phase behavior plays an important role in the cell response and must be considered in the modeling process.

A few models are improved in literature to conduct the two-phase behavior in LFP cells. They consist of core-shell [6], phase field, resistive-reactant, and variable solid-state diffusivity models. The efficiency of different models depends on their way of treating the two-phase process of lithium insertion/deinsertion. More physical intuition brings around a more adequate approximation. Since the variable solid-state diffusivity is a trade off between simplicity and physical accuracy, it is used here as a reliable platform. Details on this model can be found in [48, 2], and [49].

The main objective of this thesis is to design an observer for an LFP cell represented

by a variable solid-state diffusivity model to predict the battery SOC during a drive cycle. Although the electrochemical model-based estimation provides a higher accuracy, an efficient approximation is required due to the model complexity. The simplified models, however, might lose their application for chemical compositions like LFP at high current rates and dynamics. More accurate approximation of the original equation that is simple enough to be solved in real-time SOC estimation is required.

In the first step, comparison studies of commonly-used finite-dimensional estimation methods for different distributed parameter systems (DPSs) is considered in Chapter 2. The system is first approximated by a finite-dimensional representation; the observer dynamics is then designed via the finite-dimensional representation. Comparing the performance of different observers in the state estimation of different types of DPSs after truncation is the main concern of these studies. In addition, the comparison is expanded to the investigation of the effect of the truncated model by increasing the order of the finite-dimensional approximation of the system numerically. The simulation results are also compared with the mathematical properties of the systems.

The comparison studies are performed in both the existence and absence of an external unknown input modeling disturbances to the system. A modified sliding mode observer is improved in the same chapter to take care of system's nonlinearity and compensate for the external input. It is proved that the modified sliding mode observer provides exponential convergence of the estimation error in the existence of an external input. Simulation results of the comparison studies indicate the improved performance of this observer in most cases.

In Chapter 3, the well-posedness of two general classes of nonlinear DPSs is studied. In addition, approximating the system with a finite-dimensional version is developed as a part of proving the existence of a solution. The main concern of these studies is to produce a low-order model which converges to the original equation in some sense as the order of approximation increases. The results provided in the literature are limited to specified classes of systems and are not applicable to a lithium-ion cell model; however, the electrochemical equations can be represented as a specific version of the considered general forms.

Before designing an observer for SOC estimation, the dynamical properties of the electrochemical equations are explored in Chapter 4. One of these properties is hysteretic behavior coming from the cell's dynamical equations. Path dependency is observed in the current-voltage response of the LFP cells. Two sources of hysteresis can be introduced; hysteresis coming from the OCP term and the one caused by the system's dynamics. In

this chapter, it is shown that the system's dynamics is in fact a source of hysteresis; this result suggests that not every simplified model is proper for observer design.

Simplification of the model is considered in the next step, in Chapter 5; the simplified model is constructed in a way that most of the system dynamics is preserved. The original electrochemical equations are composed of both dynamical and constraint equations. The equations are simplified to a fully dynamical representation. This fully dynamical representation is beneficial for real-time application since it does not require solving the constraint equation at every time iteration while solving the dynamical equations. The electrochemical equations can next be transformed into a general form for which a low order model is improved.

Finally, an EKF observer is designed via the low-order model for the SOC estimation in Chapter 5. The electrochemical model employed here is the variable solid-state diffusivity model. Compared to other models, this model provides more accuracy for cells with an LFP positive electrode. However, simulation results show that the variable solid-state diffusivity model with a few number of particle bins is not yet a precise match to experimental data. Therefore, the observer is improved based upon considering an adaptive model for the OCP term in the electrochemical equations. The parameters of this model are identified simultaneously with the state estimation. Compared to the experimental data, the simulation results show the efficiency of the designed observer in the existence of modeling inaccuracy.

Chapter 2

Comparing different observers for different dynamical systems

The full state cannot be observed for distributed parameter systems. Although many observation methods have been developed for lumped parameter systems, fewer results are available for DPSs. In practice, a DPS model is approximated by a lumped model and then a method designed for the estimation of lumped systems is used. The issue of the effect of the neglected modes needs to be considered. Problems are even more complex for nonlinear systems, for which almost no theoretical results are available.

In this chapter, a number of commonly used methods for the estimation of nonlinear systems are compared: unscented Kalman filter (UKF), extended Kalman filtering (EKF), as well as a modified version of the sliding mode observer (SMO). The proposed modified SMO combines the efficiency of a nonlinear observer with the robustness of the SMO; the resultant error convergence is proved here to converge to zero under natural assumptions. The three methods are compared for three different versions of the heat equation, a linear, a quasi-linear, and a nonlinear heat equation. The methods are also compared for two wave equations, one linear, and the other nonlinear. All the comparisons are done with and without an external disturbance.

2.1 Introduction and literature review

A major issue in observer design for partial differential equations is that, in general, a copy of the original partial differential equation cannot be kept in the observer dynamics. The usual way of dealing with this problem is to approximate the system by a system

of ODEs via some approximation method, such as finite elements. The key requirement for this approximation is the convergence of the finite-dimensional state estimate to the true one as a result of increasing the order of approximation. This criterion is not easy to prove for nonlinear partial differential equations.

Although observer design for linear ODEs is well studied (see [50] for a review), it can be challenging for nonlinear ODEs. Some nonlinear systems can be transformed into a linear form [51, 52, 53, 54, 55, 56], and [57]. Checking the necessary and sufficient conditions for the existence of such a transformation is not easy; This transformation might not exist in a general case.

A comparison of nonlinear observers for ODEs can be found in [58] and [59]. Among different nonlinear observers, the extended Kalman filter, unscented Kalman filter, and sliding mode observer are very popular estimation techniques. They require few conditions on the system and do not involve complicated nonlinear transformations. Kalman filtering is optimal for a linear system if there is Gaussian white noise in both the measurement and system model. The EKF and UKF are extensions of the Kalman filter for handling nonlinearities. An SMO is designed to handle arbitrary disturbances.

As described in [60, 61] and [62], a Luenberger observer is usually used with the SMO. For a nonlinear system, the Luenberger observer must overcome the nonlinearities and stabilize the error dynamics on the sliding surface. Generally, an linear matrix inequality (LMI) problem is solved to obtain the Luenberger observer [61] and [62]. Solving the LMI problem is not easy, however, and it might in fact have no solution.

In this chapter, a modified version of the SMO is first developed. This modified SMO combines an exponentially stabilizing nonlinear observer with the sliding mode observation to increase the estimation performance. The exponential convergence of the estimation error to zero is proved.

In a subsequent section, the performance of the EKF, the UKF, and the modified SMO is compared for a number of standard PDEs. Estimators are designed for three different versions of the diffusion equation, a linear, a quasi-linear, and a nonlinear model, as well as two versions of the wave equation, a linear and a nonlinear wave equation. Two sources of uncertainties are introduced in the observer design: the disturbances coming from the unknown input $\xi(t)$ and the modeling uncertainty due to the order reduction in the observer design. The sliding mode observer is designed to account for the former uncertainties but not the latter. The performance of the different observation techniques in existence of both sources is numerically examined for a variety of DPSs.

2.2 A review of the observer design for ODE

Consider the following ordinary differential equation (ODE) model consisting of n differential equations:

$$\begin{aligned} \frac{d\mathbf{z}_{orig}}{dt} &= \boldsymbol{f}(\mathbf{z}_{orig}) + \boldsymbol{B}u + \boldsymbol{g}(\mathbf{z}_{orig})\xi(t) \\ y(t) &= \boldsymbol{C}\mathbf{z}_{orig}(t) \end{aligned} \tag{2.1}$$

with the initial condition

$$\mathbf{z}_{orig}(0) = \boldsymbol{z}_{orig,0},$$

where $\mathbf{z}_{orig} \in \mathbb{R}^n$ is the state variable, $u \in \mathbb{R}$ is the control, $\xi \in \mathbb{R}$ is the disturbance input, and $y \in \mathbb{R}$ is the measured output. Here $\boldsymbol{B} \in \mathbb{R}^{n\times 1}$, $\boldsymbol{C} \in \mathbb{R}^{1\times n}$, $\boldsymbol{f}$ and $\boldsymbol{g}$ are smooth vector fields on $\mathbb{R}^n$. The vector field $\boldsymbol{g}(.)$ is called the distribution matrix and indicates the spatial distribution of the disturbance. The disturbance is assumed to be bounded, that is a positive number M exists such that $\|\xi\| \leq M$.

Assumption 2.2.1. *The functions $\boldsymbol{f}(\boldsymbol{z}_{orig})$ and $\boldsymbol{g}(\boldsymbol{z}_{orig})$ are smooth vector fields up to the nth order. In other words, they are continuously differentiable of the nth order with respect to their arguments.*

In this section, different popular observation techniques for nonlinear systems are reviewed, and an extension for the estimation of the nonlinear systems with disturbances is developed.

Extended Kalman filter

Kalman filtering is a technique for estimating the state vector of a linear system such that the variance of the estimation error (the difference between the true state and the observer state) is minimized. The main assumption is that the system and measurement noise are zero-mean and also mutually independent processes (one process does not affect the other one). With these assumptions, the Kalman filtering evaluates the conditional probability distribution function of the state vector conditioned by the measurements. The mean value of this distribution function is addressed as the state estimate [63] and[64].

The EKF is an extension of the Kalman filter to nonlinear systems. In the EKF, an approximation is obtained by linearizing the nonlinear system around the last state estimation. After linearizing the system, the usual Kalman filtering is used to estimate the state vector.

Table 2.1: Extended Kalman filtering algorithm

Initialize at $k = 0$:

$\hat{\boldsymbol{z}}_0 = E[\boldsymbol{z}_0]$,

$\boldsymbol{P}_{\boldsymbol{z}_0} = E[(\boldsymbol{z}_0 - \hat{\boldsymbol{z}}_0)(\boldsymbol{z}_0 - \hat{\boldsymbol{z}}_0)^T]$,

$\boldsymbol{P}_{\boldsymbol{\nu}} = E[(\boldsymbol{\nu} - \bar{\boldsymbol{\nu}})(\boldsymbol{\nu} - \bar{\boldsymbol{\nu}})^T]$,

$\boldsymbol{P}_{\omega} = E[(\omega - \bar{\omega})(\omega - \bar{\omega})^T]$.

For $k = 1, 2, \cdots, \infty$,

Prediction step:

$\boldsymbol{F}_{\boldsymbol{z}_k} = \frac{\partial \boldsymbol{f}_d}{\partial \boldsymbol{z}} \mid_{\boldsymbol{z}=\hat{\boldsymbol{z}}_{k-1}}$,

$\hat{\boldsymbol{z}}_k^- = \boldsymbol{f}_d(\hat{\boldsymbol{z}}_{k-1}) + \boldsymbol{B}_d u_k$,

$\boldsymbol{P}_{\boldsymbol{z}_k}^- = \boldsymbol{F}_{\boldsymbol{z}_k} \boldsymbol{P}_{\boldsymbol{z}_{k-1}} \boldsymbol{F}_{\boldsymbol{z}_k}^T + \boldsymbol{P}_{\boldsymbol{\nu}}$.

Correction step:

$\boldsymbol{H}_{\boldsymbol{z}_k} = \frac{\partial h}{\partial \boldsymbol{z}} \mid_{\boldsymbol{z}=\hat{\boldsymbol{z}}_k^-}$,

$\boldsymbol{K}_k = \boldsymbol{P}_{\boldsymbol{z}_k}^- \boldsymbol{H}_{\boldsymbol{z}_k}^T (\boldsymbol{H}_{\boldsymbol{z}_k} \boldsymbol{P}_{\boldsymbol{z}_k}^- \boldsymbol{H}_{\boldsymbol{z}_k}^T + \boldsymbol{P}_{\omega})^{-1}$,

$\hat{\boldsymbol{z}}_k = \hat{\boldsymbol{z}}_k^- + \boldsymbol{K}_k (y_k - h(\hat{\boldsymbol{z}}_k^-))$,

$\boldsymbol{P}_{\boldsymbol{z}_k} = (\boldsymbol{I} - \boldsymbol{K}_k \boldsymbol{H}_{\boldsymbol{z}_k}) \boldsymbol{P}_{z_k}^-$.

For simplicity of exposition, consider a discrete-time implementation

$$\begin{aligned} \boldsymbol{z}_{k+1} &= \boldsymbol{f}_d(\boldsymbol{z}_k) + \boldsymbol{B}_d u_k + \boldsymbol{\nu}_k \\ y_k &= h(\boldsymbol{z}_k) + \omega_k \end{aligned} \tag{2.2}$$

where $\boldsymbol{z}_k$, u_k, and y_k are respectively the state vector, input variable, and output at time step $t = t_k$, $\boldsymbol{\nu}_k$ is the system noise, and ω_k is the measurement noise.

The EKF algorithm is summarized in Table 2.1 where $\boldsymbol{z}_0$ is the state vector at time $t = t_0$ and $\bar{\boldsymbol{s}} = E(\boldsymbol{s})$ represents the mean value of the random vector $\boldsymbol{s}$. This algorithm is composed of two steps, a prediction and a correction step. In the first step, the system's model is used to predict both the state vector's mean value and the covariance matrix. Next, the output measurements are employed to correct the prediction results in the correction step. More details on this estimation technique can be found in [65]. Exponential convergence, provided that certain conditions are satisfied, of the EKF is shown to hold in [66] and [67]. These conditions are

1. There exists positive numbers $c_1, c_2, p_1, p_2 \in \mathbb{R}^+$ such that for every time step k,

$$\begin{aligned} \|\boldsymbol{F}_{\boldsymbol{z}_k}\| \leq c_1, \qquad & \|\boldsymbol{H}_{\boldsymbol{z}_k}\| \leq c_2 \\ p_1 \leq \|\boldsymbol{P}_{\boldsymbol{z}_k}^-\| \leq p_2, \qquad & p_1 \leq \|\boldsymbol{P}_{\boldsymbol{z}_k}\| \leq p_2. \end{aligned}$$

2. At all time steps, the linear operator F_{z_k} is nonsingular.

3. Let $\boldsymbol{\varphi}(\boldsymbol{z}_k, \hat{\boldsymbol{z}}_k) = \boldsymbol{f}_d(\boldsymbol{z}_k) - \boldsymbol{f}_d(\hat{\boldsymbol{z}}_k) - \boldsymbol{F}_{\boldsymbol{z}_k}(\boldsymbol{z} - \hat{\boldsymbol{z}})$ and $\psi(\boldsymbol{z}_k, \hat{\boldsymbol{z}}_k^-) = h(\boldsymbol{z}_k) - h(\hat{\boldsymbol{z}}_k^-) - \boldsymbol{H}_{\boldsymbol{z}_k}(\boldsymbol{z}_k - \hat{\boldsymbol{z}}_k^-)$. There exists positive real numbers $\epsilon_\phi, \epsilon_\psi, k_\phi, k_\psi \in \mathbb{R}^+$ such that for every $\boldsymbol{z}_k, \hat{\boldsymbol{z}}_k, \hat{\boldsymbol{z}}_k^- \in \mathbb{R}^n$ preserving $\|\boldsymbol{z}_k - \hat{\boldsymbol{z}}_k\| \leq \epsilon_\phi$ and $\|\boldsymbol{z}_k - \hat{\boldsymbol{z}}_k^-\| \leq \epsilon_\psi$,

$$\begin{aligned} \|\boldsymbol{\varphi}(\boldsymbol{z}_k, \hat{\boldsymbol{z}}_k)\| &\leq k_\phi \|\boldsymbol{z}_k - \hat{\boldsymbol{z}}_k\|^2 \\ \|\psi(\boldsymbol{z}_k, \hat{\boldsymbol{z}}_k^-)\| &\leq k_\psi \|\boldsymbol{z}_k - \hat{\boldsymbol{z}}_k^-\|^2. \end{aligned}$$

A modified EKF is used in this paper, [66] and [67], wherein the covariance prediction is improved by using the update at each step

$$\boldsymbol{P}_{\boldsymbol{z}_k}^- = a^2 \boldsymbol{F}_{\boldsymbol{z}_k} \boldsymbol{P}_{\boldsymbol{z}_{k-1}} \boldsymbol{F}_{\boldsymbol{z}_k}^T + \boldsymbol{P}_{\boldsymbol{\nu}} \tag{2.3}$$

where $a \in \mathbb{R}^+$ defines the rate of exponential convergence.

Unscented Kalman filter

The UKF is an alternative to the EKF intended to obtain a more precise estimation. In this approach, the probability distribution functions are specified by a minimal set of sample points. For a random vector of dimension N, $2N + 1$ sample points, which are also called sigma points, are used [68]. The sigma points completely capture the mean and covariance of Gaussian random variables. Furthermore, the posterior mean and covariance of the Gaussian random variables are captured up to the third order when they undergo a nonlinear transformation over time [68].

Details of the UKF estimation technique can be found in [68]. The UKF is a recursive estimation technique in which the mean value and covariance matrix of the state vector as well as the sample points are updated at every time step [68]. The sigma points and their corresponding weights are defined as

$$\begin{aligned} &\boldsymbol{z}_{s,0} = \bar{\boldsymbol{z}} \\ &\boldsymbol{z}_{s,i} = \bar{\boldsymbol{z}} + (\sqrt{(N+\lambda)\boldsymbol{P}_{\boldsymbol{z}}})_i \quad i = 1, \cdots, N \\ &\boldsymbol{z}_{s,i} = \bar{\boldsymbol{z}} - (\sqrt{(N+\lambda)\boldsymbol{P}_{\boldsymbol{z}}})_{i-N} \quad i = N+1, \cdots, 2N \\ &W_0^m = \frac{\lambda}{N+\lambda}, \quad W_0^c = \frac{\lambda}{N+\lambda} + (1 - \alpha_0^2 + \beta) \\ &W_i^m = W_i^c = \frac{1}{2(N+\lambda)} \end{aligned} \tag{2.4}$$

Table 2.2: Unscented Kalman filtering

Initialize at $k = 0$:

$\hat{\boldsymbol{z}}_0 = E[\boldsymbol{z}_0]$,
$\boldsymbol{P}_{\boldsymbol{z}_0} = E[(\boldsymbol{z}_0 - \hat{\boldsymbol{z}}_0)(\boldsymbol{z}_0 - \hat{\boldsymbol{z}}_0)^T]$.
$\boldsymbol{P}_{\boldsymbol{\nu}} = E[(\boldsymbol{\nu} - \bar{\boldsymbol{\nu}})(\boldsymbol{\nu} - \bar{\boldsymbol{\nu}})^T]$,
$\boldsymbol{P}_{\omega} = E[(\omega - \bar{\omega})(\omega - \bar{\omega})^T]$.

For $k = 1, \cdots, \infty$,

Calculate Sigma points via equation (2.4), $\boldsymbol{z}_{s,i}$

Prediction step:

$\boldsymbol{z}^-_{s,i} = \boldsymbol{f}_d(\boldsymbol{z}_{s,i}) + \boldsymbol{B}_d u$, $i = 0, \ldots 2N$,
$\hat{\boldsymbol{z}}^-_k = \sum_{i=0}^{2N} W_i^m(\boldsymbol{Z}_{s,i})$,
$\boldsymbol{P}^-_{\boldsymbol{z}_k} = \sum_{i=0}^{2N} W_i^c((\boldsymbol{z}_{s,i}) - \hat{\boldsymbol{z}}^-_k)((\boldsymbol{z}_{s,i}) - \hat{\boldsymbol{z}}^-_k)^T + \boldsymbol{P}_{\boldsymbol{\nu}}$,
$y_{s,i} = h(\boldsymbol{z}_{s,i})$, $i = 0, \ldots 2N$
$\hat{y}^-_k = \sum_{i=0}^{2N} W_i^m(y_{s,i})$.

Correction step:

$\boldsymbol{P}_{y_k} = \sum_{i=0}^{2N} W_i^c(y_{s,i} - \hat{y}^-_k)(y_{s,i} - \hat{y}^-_k)^T + \boldsymbol{P}_{\omega}$,
$\boldsymbol{P}_{\boldsymbol{z}_k y_k} = \sum_{i=0}^{2N} (\boldsymbol{z}_{s,i} - \hat{\boldsymbol{z}}^-_k)(y_{s,i} - \hat{y}^-_k)^T$,
$\boldsymbol{K}_k = \boldsymbol{P}_{\boldsymbol{z}_k y_k} \boldsymbol{P}^{-1}_{y_k}$,
$\hat{\boldsymbol{z}}_k = \hat{\boldsymbol{z}}^-_k + \boldsymbol{K}_k(y_k - \hat{y}^-_k)$,
$\boldsymbol{P}_{\boldsymbol{z}_k} = \boldsymbol{P}^-_{\boldsymbol{z}_k} - \boldsymbol{K}_k \boldsymbol{P}_{y_k} \boldsymbol{K}_k^T$.

where $\boldsymbol{z}_{s,i}$ for $i = 0, \cdots, 2N$ are sample points, W_i^m for $i = 0, \cdots, 2N$ are associated weights for calculation of the means, W_i^c for $i = 0, \cdots, 2N$ are associated weights for covariance calculation, $\lambda = \alpha_0^2(N + \kappa) - N$ is a scaling parameter, and α_0 and κ are tuning parameters. The algorithm is given in Table 2.2.

2.3 Sliding mode observer

The standard Kalman filter and the two variants discussed above depend on exactness of the system model. It is also assumed that other than noise as described above, there are no disturbances. However, disturbances are frequently present. Also, any type of Kalman filter will have errors when the system model is incorrect. Modeling errors are common for distributed parameters systems, which typically have complex dynamics. Furthermore, for computation, the partial differential equations need to be replaced by ordinary differential equations, that is called a lumped approximation. This approximation also introduce errors. Nonlinearities, modelling errors, and approximation errors can be viewed as additional disturbances to the nominal model.

A robust observer is intended to compensate for disturbances. A potential way of

including robustness in the observer design is to improve the Riccati equation solved for Kalman filtering. Examples can be found in [69, 70, 71], and [72]. However, this type of observer is efficient in compensating for multiplicative disturbances and zero mean bounded noises. A different approach is employing sliding mode techniques in which the disturbances are modeled by some unknown inputs. In this case, no restriction is tagged along the unknown input except for boundedness. They were first employed for observation in the 1980's [73], and incorporated in the design of a robust observation method.

A good review of sliding mode observation methods for both linear and nonlinear systems can be found in [60]. The basic idea is to use a discontinuous output feedback to drive the estimated state vector towards some reference manifold. The main advantages of the SMO are insensitivity to unknown inputs, robustness, and providing an equivalent output error injection that can also be used as a source of information [74]. An important challenge is the inclusion of the disturbances. In general, consideration of disturbances induces either structural conditions or matching assumptions to ensure finite time convergence [75]. Different designs handle disturbances and system nonlinearities in different ways [76], [77, 78, 79], and [61]. A standard version of the SMO is briefly described here; for more details see [79], and [80].

The first step in the SMO design is to transform the system representation (2.1) into a standard form. This form is not necessarily a linearized one; rather, it provides the proper distribution of an unknown input to the system dynamics. The transformation divides the system into two parts; the part affected directly by the unknown input and the part that is not.

Definition 2.3.1. *[81] Let $\boldsymbol{f}_1(\boldsymbol{z}_{orig})$ and $\boldsymbol{f}_2(\boldsymbol{z}_{orig})$ be smooth vector fields up to the first order. The Lie derivative $L_{\boldsymbol{f}_1(\boldsymbol{z}_{orig})}\boldsymbol{f}_2(\boldsymbol{z}_{orig})$ of $\boldsymbol{f}_2(\boldsymbol{z}_{orig})$ with respect to $\boldsymbol{f}_1(\boldsymbol{z}_{orig})$ is defined as*

$$L_{\boldsymbol{f}_1(\boldsymbol{z}_{orig})}\boldsymbol{f}_2(\boldsymbol{z}_{orig}) = \frac{\partial \boldsymbol{f}_2(\boldsymbol{z}_{orig})}{\partial \boldsymbol{z}_{orig}}\boldsymbol{f}_1(\boldsymbol{z}_{orig}).$$

A single-input single-output (SISO) system of order n given by equation (2.1) has a relative degree q at point $\boldsymbol{z}_p \in \mathcal{R}^n$ from the input ξ to the output y if for every $k < q-1$,

$$L_{\boldsymbol{g}(\boldsymbol{z}_{orig})}L^k_{\boldsymbol{f}(\boldsymbol{z}_{orig})}\boldsymbol{C}\boldsymbol{z}_{orig} = 0$$

and

$$L_{\boldsymbol{g}(\boldsymbol{z}_{orig})}L^{q-1}_{\boldsymbol{f}(\boldsymbol{z}_{orig})}\boldsymbol{C}\boldsymbol{z}_{orig} \neq 0$$

in a neighborhood of $\boldsymbol{z}_p$.

Definition 2.3.2. *[81] A distribution is called involutive if it is closed under the Lie bracket operator, $[.,.]$, defined as*

$$[\boldsymbol{f}_1(\boldsymbol{z}_{orig}), \boldsymbol{f}_2(\boldsymbol{z}_{orig})] = L_{\boldsymbol{f}_1(\boldsymbol{z}_{orig})}\boldsymbol{f}_2(\boldsymbol{z}_{orig}) - L_{\boldsymbol{f}_2(\boldsymbol{z}_{orig})}\boldsymbol{f}_1(\boldsymbol{z}_{orig})$$

for every $\boldsymbol{f}_1(\boldsymbol{z}_{orig}), \boldsymbol{f}_2(\boldsymbol{z}_{orig}) \in \mathcal{C}^n(\mathbb{R}^n)$.

The following assumption on the system is required.

Assumption 2.3.3. *The relative degree of the system (2.1) from the input ξ to the output y is independent of $\boldsymbol{z}_p \in \mathcal{R}^n$.*

For a system to have the relative degree of one that satisfies Assumption 2.3.3, it is required that $\boldsymbol{C}\boldsymbol{g}(\boldsymbol{z}_p) \neq 0$ for every $\boldsymbol{z}_p \in \mathcal{R}^n$. This is not a hard condition to check.

Let the relative degree be q. Given Assumption 2.3.3, it can be concluded that $q \leq n$ [81, Prop. 5.1.2] for every $\boldsymbol{z}_p \in \mathbb{R}^n$. Set

$$\begin{aligned}
\phi_1(\mathbf{z}_{orig}) &= \boldsymbol{C}\mathbf{z}_{orig} \\
\phi_2(\mathbf{z}_{orig}) &= L_{\boldsymbol{f}}\boldsymbol{C}\mathbf{z}_{orig} \\
&\vdots \\
\phi_q(\mathbf{z}_{orig}) &= L_{\boldsymbol{f}}^{q-1}\boldsymbol{C}\mathbf{z}_{orig}.
\end{aligned}$$

If $q < n$, $n - q$ functions, $\phi_{q+1}(\mathbf{z}_{orig}), \cdots, \phi_n(\mathbf{z}_{orig})$, can be found such that the Jacobian matrix of the mapping

$$\boldsymbol{z}_c = \boldsymbol{\phi}(\mathbf{z}_{\boldsymbol{orig}}) = \text{col}(\phi_1(\mathbf{z}_{orig}), \cdots, \phi_q(\mathbf{z}_{orig}), \phi_{q+1}(\mathbf{z}_{orig}), \cdots, \phi_n(\mathbf{z}_{orig})) \tag{2.5}$$

is nonsingular at every $\boldsymbol{z}_p \in \mathcal{R}^n$. Furthermore, since $\boldsymbol{g}(\mathbf{z}_{orig})$ is a base of an involutive distribution (that is true because g constructs a 1-D vector space which is involutive by Definition 2.3.2), the Frobenius Theorem implies that the functions $\phi_{q+1}(\mathbf{z}_{orig}), \cdots, \phi_n(\mathbf{z}_{orig})$ can be chosen so that

$$L_{\boldsymbol{g}}\phi_i(\mathbf{z}_{orig}) = 0$$

for $i = q+1, \cdots, n$ and all $\boldsymbol{z}_p \in \mathcal{R}^n$ [81].

Now, set the new state vector to be composed of

$$\boldsymbol{z}_d = \begin{bmatrix} z_{d,1} \\ z_{d,2} \\ \vdots \\ z_{d,q} \end{bmatrix} = \begin{bmatrix} \phi_1(\mathbf{z}_{orig}) \\ \phi_2(\mathbf{z}_{orig}) \\ \vdots \\ \phi_q(\mathbf{z}_{orig}) \end{bmatrix} \tag{2.6}$$

and

$$\boldsymbol{z}_r = \begin{bmatrix} z_{r,1} \\ z_{r,2} \\ \vdots \\ z_{r,n-q} \end{bmatrix} = \begin{bmatrix} \phi_{q+1}(\mathbf{z}_{orig}) \\ \phi_{q+2}(\mathbf{z}_{orig}) \\ \vdots \\ \phi_n(\mathbf{z}_{orig}) \end{bmatrix} . \tag{2.7}$$

The transformation given by equations (2.6) and (2.7) decomposes the system into two subsystems so that only $\boldsymbol{z}_d$ is directly affected by disturbances.

In the new coordinates, define the state vector as $\boldsymbol{z}_c^T = [\boldsymbol{z}_d^T, \boldsymbol{z}_r^T]$; the system representation is

$$\begin{aligned} \frac{d\boldsymbol{z}_c}{dt} &= \bar{\boldsymbol{f}}(\boldsymbol{z}_c) + \bar{\boldsymbol{g}}(\boldsymbol{z}_c, u) + \Gamma(\boldsymbol{z}_c)\xi \\ y &= z_{d,1} \end{aligned} \tag{2.8}$$

where

$$\bar{\boldsymbol{f}}(\boldsymbol{z}_c) = \begin{bmatrix} z_{d,2} \\ \vdots \\ z_{d,q} \\ a_d(z_d, z_r) \\ \boldsymbol{a}_r(z_d, z_r) \end{bmatrix}, \quad \bar{\boldsymbol{g}}(\boldsymbol{z}_c, u) = \begin{bmatrix} b_1(\boldsymbol{z}_d, \boldsymbol{z}_r, u) \\ \vdots \\ b_{q-1}(\boldsymbol{z}_d, \boldsymbol{z}_r, u) \\ b_q(\boldsymbol{z}_d, \boldsymbol{z}_r, u) \\ \boldsymbol{b}_r(\boldsymbol{z}_d, \boldsymbol{z}_r, u) \end{bmatrix}, \tag{2.9}$$

$$\boldsymbol{\Gamma}(\boldsymbol{z}_c) = \begin{bmatrix} 0 \\ \vdots \\ 0 \\ c(\boldsymbol{z}_d, \boldsymbol{z}_r) \\ \mathbf{0}_{(n-q)\times 1} \end{bmatrix} . \tag{2.10}$$

The functions a_d, c, and b_k produced by transformation (2.5) are defined as

$$\begin{aligned} a_d(\boldsymbol{z}_d, \boldsymbol{z}_r) &= L^q_{\boldsymbol{f}(\mathbf{z}_{orig})} \boldsymbol{C}\mathbf{z}_{orig} \mid_{\mathbf{z}_{orig}=\boldsymbol{\phi}^{-1}(\boldsymbol{z}_d, \boldsymbol{z}_r)} \\ c(\boldsymbol{z}_d, \boldsymbol{z}_r) &= L_{\boldsymbol{g}(\mathbf{z}_{orig})} L^{q-1}_{\boldsymbol{f}(\mathbf{z}_{orig})} \boldsymbol{C}\mathbf{z}_{orig} \mid_{\mathbf{z}_{orig}=\boldsymbol{\phi}^{-1}(\boldsymbol{z}_d, \boldsymbol{z}_r)} \\ b_k(\boldsymbol{z}_d, \boldsymbol{z}_r, u) &= L_{\boldsymbol{B}u} L^{k-1}_{\boldsymbol{f}(\mathbf{z}_{orig})} \boldsymbol{C}\mathbf{z}_{orig} \mid_{\mathbf{z}_{orig}=\boldsymbol{\phi}^{-1}(\boldsymbol{z}_d, \boldsymbol{z}_r)} . \end{aligned} \tag{2.11}$$

Assumption 2.3.4. *The input terms in the transformed equations can be put into the*

form

$$
\begin{aligned}
&b_1(\boldsymbol{z}_d, \boldsymbol{z}_r, u) = b_1(y, u)\\
&b_2(\boldsymbol{z}_d, \boldsymbol{z}_r, u) = b_2(z_{d,2}, y, u)\\
&\vdots\\
&b_{q-1}(\boldsymbol{z}_d, \boldsymbol{z}_r, u) = b_{q-1}(z_{d,2}, \cdots, z_{d,q-1}, y, u)\\
&b_q(\boldsymbol{z}_d, \boldsymbol{z}_r, u) = b_q(\boldsymbol{z}_d, \boldsymbol{z}_r, u).
\end{aligned}
$$

Definition 2.3.5. *[82] Let $\boldsymbol{\chi}(t-t_0, \boldsymbol{z}_0, u_{[t_0,t]}, \xi_{[t_0,t]})$ be a solution to the system (2.1) with a initial condition $\boldsymbol{z}_0$ at time t_0. The input vector $[u, \xi]^T$ is called universal for the system if for $\boldsymbol{z}_1 \neq \boldsymbol{z}_2$, there exists $t_f > t_0$ such that*

$$\boldsymbol{C}\boldsymbol{\chi}(t_f - t_0, \boldsymbol{z}_1, u_{[t_0,t_f]}, \xi_{[t_0,t_f]}) \neq \boldsymbol{C}\boldsymbol{\chi}(t_f - t_0, \boldsymbol{z}_2, u_{[t_0,t_f]}, \xi_{[t_0,t_f]}).$$

Definition 2.3.6. *[82] A system is uniformly observable if every input vector is universal.*

Definition 2.3.7. *[82] A system satisfies a property of detectability if for every two indistinguishable initial conditions $\boldsymbol{z}_1 \neq \boldsymbol{z}_2$ by the input vector $[u, \xi]^T$,*

$$\|\boldsymbol{\chi}(t_f - t_0, \boldsymbol{z}_1, u_{[t_0,t_f]}, \xi_{[t_0,t_f]}) - \boldsymbol{C}\boldsymbol{\chi}(t_f - t_0, \boldsymbol{z}_2, u_{[t_0,t_f]}, \xi_{[t_0,t_f]})\| \to 0$$

as $t_f \to \infty$.

Assumption 2.3.8. *Both the original system and its transformed form preserve a detectability property as defined in Definition 2.3.7.*

Definition 2.3.9. *[83] A system is bounded-input bounded-output (BIBO) stable if for every bounded input vector, the output or response of the system is also bounded.*

Assumption 2.3.10. *The system with representation (2.1) and its corresponding transformed form given by equations (2.6) and (2.7) are BIBO stable when the output operator is the identity operator.*

The SMO design involves forcing the states towards a surface followed by the convergence of the error vector on the sliding surface. Several more assumptions are required for the convergence proof. The Lipshitz continuity of the functions (2.11) is usually an assumption in the literature as seen in [75] and [79]. This continuity follows from the smoothness of the original system (2.1).

Lemma 2.3.11. *Let Assumption 2.2.1 be satisfied. There exist* $M_a, M_b, M_1, \cdots, M_q \in \mathbb{R}+$ *such that for every* $\boldsymbol{z}_c^T = [\boldsymbol{z}_d^T, \boldsymbol{z}_r^T]$ *and* $\hat{\boldsymbol{z}}_c^T = [\hat{\boldsymbol{z}}_d^T, \hat{\boldsymbol{z}}_r^T]$ *with* $\|\boldsymbol{z}_c - \hat{\boldsymbol{z}}_c\| \leq \epsilon_L$ *where* $\epsilon_L \in \mathbb{R}^+$,

$$\begin{aligned}
\|a_d(\boldsymbol{z}_d, \boldsymbol{z}_r) - a_d(\hat{\boldsymbol{z}}_d, \hat{\boldsymbol{z}}_r)\| &\leq M_a \|\boldsymbol{z}_c - \hat{\boldsymbol{z}}_c\|, \\
\|c(\boldsymbol{z}_d, \boldsymbol{z}_r) - c(\hat{\boldsymbol{z}}_d, \hat{\boldsymbol{z}}_r)\| &\leq M_c \|\boldsymbol{z}_c - \hat{\boldsymbol{z}}_c\|, \\
\|b_1(\boldsymbol{z}_d, \boldsymbol{z}_r, u) - b_1(\hat{\boldsymbol{z}}_d, \hat{\boldsymbol{z}}_r, u)\| &\leq M_1 \|\boldsymbol{z}_c - \hat{\boldsymbol{z}}_c\|, \\
&\vdots \\
\|b_q(\boldsymbol{z}_d, \boldsymbol{z}_r, u) - b_q(\hat{\boldsymbol{z}}_d, \hat{\boldsymbol{z}}_r, u)\| &\leq M_q \|\boldsymbol{z}_c - \hat{\boldsymbol{z}}_c\|.
\end{aligned} \tag{2.12}$$

Proof: The dynamics of the system in the two realizations (2.1) and (2.8), are related through the coordinate transformation given by equations (2.6) and (2.7) as

$$\begin{bmatrix}
\boldsymbol{z}_{d,2} + b_1(\boldsymbol{z}_d, \boldsymbol{z}_r, u) \\
\vdots \\
\boldsymbol{z}_{d,q} + b_{q-1}(\boldsymbol{z}_d, \boldsymbol{z}_r, u) \\
a_d(\boldsymbol{z}_d, \boldsymbol{z}_r) + b_q(\boldsymbol{z}_d, \boldsymbol{z}_r, u) + c(\boldsymbol{z}_d, \boldsymbol{z}_r)\xi \\
\boldsymbol{a}_r(\boldsymbol{z}_d, \boldsymbol{z}_r) + \boldsymbol{b}_r(\boldsymbol{z}_d, \boldsymbol{z}_r, u)
\end{bmatrix} = \frac{\partial \boldsymbol{\phi}(\mathbf{z}_{orig})}{\partial \mathbf{z}_{orig}} (\boldsymbol{f}(\mathbf{z}_{orig}) + \boldsymbol{B}u + \boldsymbol{g}(\mathbf{z}_{orig})\xi) \,.$$

Assumption 2.2.1 implies that every function defined in equation (2.11) is continuously differentiable with respect to the vector $\mathbf{z}_{orig}$. Since the transformation $\boldsymbol{z}_c = [\boldsymbol{z}_d^T, \boldsymbol{z}_r^T]^T = \boldsymbol{\phi}(\mathbf{z}_{orig})$ given by equations (2.6) and (2.7) is a diffeomorphism, the vector $\mathbf{z}_{orig}$ is also continuously differentiable with respect to the vectors $\boldsymbol{z}_d$ and $\boldsymbol{z}_r$. In conclusion, the functions (2.11) are continuously differentiable with respect to the vectors $\boldsymbol{z}_d$ and $\boldsymbol{z}_r$. Finally, the Mean Value Theorem implies that the coefficients a_d, c, and b_k for $k = 1, \cdots, q$ are locally Lipschitz continuous on every closed and bounded set. The conclusion (2.12) follows. □

For any signal v, calculate $(v)_{eq}$ by low pass filtering the signal v. This filtering was introduced in [80] to avoid a peaking phenomenon. Define $\bar{e}_1 = e_1$ and $\bar{e}_k =$

$(\lambda_{k-1}\,\mathrm{sign}(\bar{e}_{k-1}))_{eq}$ for $k = 2 \cdots q$ [79]. For some $\lambda_1, \cdots, \lambda_q \in \mathbb{R}^+$ define the SMO

$$\begin{aligned}
\frac{d\hat{z}_{d,1}}{dt} &= \hat{z}_{d,2} + b_1(y,u) + \lambda_1\,\mathrm{sign}(e_1) \\
&\vdots \\
\frac{d\hat{z}_{d,q-1}}{dt} &= \hat{z}_{d,q} + b_{q-1}(\hat{z}_{d,2}, \cdots, \hat{z}_{d,q-1}, y, u) + \lambda_{q-1}\,\mathrm{sign}(\bar{e}_{q-1}) \\
\frac{d\hat{z}_{d,q}}{dt} &= a_d(\hat{\boldsymbol{z}}_d, \hat{\boldsymbol{z}}_r) + b_q(\hat{\boldsymbol{z}}_d, \hat{\boldsymbol{z}}_r, u) + \lambda_q\,\mathrm{sign}(\bar{e}_q) \\
\frac{d\hat{\boldsymbol{z}}_r}{dt} &= \boldsymbol{a}_r(\hat{\boldsymbol{z}}_d, \hat{\boldsymbol{z}}_r) + \boldsymbol{b}_r(\hat{\boldsymbol{z}}_d, \hat{\boldsymbol{z}}_r, u).
\end{aligned} \tag{2.13}$$

In this strategy, the sliding surfaces are reached one by one in a recursive fashion.

Theorem 2.3.12. *[79] Given Assumptions 2.2.1-2.3.10, for sufficiently large $\lambda_1, \cdots, \lambda_q \in \mathbb{R}^+$ the state $\hat{\boldsymbol{z}}_d$ of the observer (2.13) converges to the disturbed state vector z_d in finite time.*

Modified SMO

Theorem 2.3.12 shows that the SMO (2.13) provides an estimate $\hat{\boldsymbol{z}}_d$ of the disturbed states $\boldsymbol{z}_d$. An estimate $\hat{\boldsymbol{z}}_r$ of the residual states $\hat{\boldsymbol{z}}_r$ needs to be obtained by some other method. Typically, a Luenberger observer is used with the SMO to estimate the full state; see [60, 61] and [62]. The Luenberger observer must overcome the nonlinearities and stabilize the error dynamics on the sliding surface. Normally, a linear matrix inequality (LMI) must be solved to obtain the proper gain for the Luenberger observer [61] and [62]. However, solving the LMI problem is computationally expensive and sometimes the inequality has no solution.

Another approach is to combine a method for estimating the undisturbed nonlinear system with the SMO for the disturbed system. Define the state vector $\tilde{\boldsymbol{z}}_c^T = [\tilde{\boldsymbol{z}}_d^T, \tilde{\boldsymbol{z}}_r^T]$; if $\xi \equiv 0$, the transformed system (2.8) can be written as

$$\begin{aligned}
\frac{d\tilde{\boldsymbol{z}}_c}{dt} &= \bar{\boldsymbol{f}}(\tilde{\boldsymbol{z}}_c) + \bar{\boldsymbol{g}}(\tilde{\boldsymbol{z}}_c, u) \\
y &= \tilde{z}_{d,1}
\end{aligned} \tag{2.14}$$

The system in equation (2.14) is observable (Assumption 2.3.8)) and an observer gain $\boldsymbol{K}$ can be designed for this system. Define $\tilde{\mathbf{e}} = \tilde{\boldsymbol{z}}_c - \hat{\boldsymbol{z}}_c = [\tilde{e}_1, \cdots, \tilde{e}_q, \tilde{e}_{q+1}, \cdots, \tilde{e}_n]^T$ and $\tilde{e}_1 = \tilde{z}_{d,1} - \hat{z}_{d,1}$; let the observer dynamics be denoted by

$$\frac{d\hat{\boldsymbol{z}}_c}{dt} = \bar{\boldsymbol{f}}(\hat{\boldsymbol{z}}_c) + \bar{\boldsymbol{g}}(\hat{\boldsymbol{z}}_c, u) + \boldsymbol{K}(\hat{\boldsymbol{z}}_c, \tilde{e}_1) \tag{2.15}$$

where $\boldsymbol{K}^T(\hat{\boldsymbol{z}}_c, \tilde{e}_1) = [K_1(\hat{\boldsymbol{z}}_c, \tilde{e}_1), \ldots, K_n(\hat{\boldsymbol{z}}_c, \tilde{e}_1)]$ is designed such that

$$\| \boldsymbol{K}(\hat{\boldsymbol{z}}_c, \tilde{e}_1) \| \leq k \| \tilde{e}_1 \| . \tag{2.16}$$

The dynamics of the error $\tilde{\boldsymbol{e}}$ are

$$\frac{d\tilde{\boldsymbol{e}}}{dt} = \bar{\boldsymbol{f}}(\tilde{\boldsymbol{z}}_c) - \bar{\boldsymbol{f}}(\hat{\boldsymbol{z}}_c) + \bar{\boldsymbol{g}}(\tilde{\boldsymbol{z}}_c, u) - \bar{\boldsymbol{g}}(\hat{\boldsymbol{z}}_c, u) - \boldsymbol{K}(\hat{\boldsymbol{z}}_c, \tilde{e}_1). \tag{2.17}$$

The following assumption is made for the error dynamics (2.17).

Assumption 2.3.13. *Let the observer dynamics and its corresponding error dynamics be given by equation (2.15) and (2.17) respectively. There exists a continuously differentiable Lyapunov function $V : \mathcal{D} \to \mathbb{R}$ such that*

$$\beta_1 \| \tilde{\boldsymbol{e}} \|^2 \leq V(\tilde{\boldsymbol{e}}) \leq \beta_2 \| \tilde{\mathbf{e}} \|^2 \tag{2.18}$$

$$\left\| \frac{\partial V(\tilde{\boldsymbol{e}})}{\partial \tilde{\boldsymbol{e}}} \right\| \leq \beta_4 \|\tilde{\boldsymbol{e}}\| \tag{2.19}$$

for some $\beta_1, \beta_2, \beta_3, \beta_4 \in \mathbb{R}^+$ and along trajectories

$$\dot{V}(\tilde{\boldsymbol{e}}) \leq -\beta_3 \| \tilde{\boldsymbol{e}} \|^2 . \tag{2.20}$$

It is evident that β_4 depends on the observer design and is determined by the rate of error convergence. To cope with a disturbance, that is $\xi \neq 0$, the observer is modified by adding sliding mode terms. Combining the exponential convergent observer dynamics satisfying Assumption 2.3.13 with the sliding mode term reduces the effect of chattering expected from the sliding mode observers. Furthermore, it also emerges employing smaller gains for sliding mode term and thus less chattering. Defining $e_1 = z_{d,1} - \hat{z}_{d,1}$ where $\hat{\boldsymbol{z}}_c^T = [\hat{\boldsymbol{z}}_d^T, \hat{\boldsymbol{z}}_r^T]$ is the observer state vector, $\bar{e}_1 = e_1$ and $\bar{e}_k = (\lambda_{k-1} \operatorname{sign}(\bar{e}_{k-1}))_{eq}$ for $k = 2 \cdots q$. Thus,

$$\begin{aligned}
\frac{d\hat{z}_{d,1}}{dt} &= \hat{z}_{d,2} + b_1(y, u) + K_1(\hat{\boldsymbol{z}}, e_1) + \lambda_1 \operatorname{sign}(e_1) \\
&\vdots \\
\frac{d\hat{z}_{d,q-1}}{dt} &= \hat{z}_{d,q} + b_{q-1}(\hat{z}_{d,2}, \cdots, \hat{z}_{d,q-1}, y, u) + K_2(\hat{\boldsymbol{z}}, e_1) + \lambda_{q-1} \operatorname{sign}(\bar{e}_{q-1}) \\
\frac{d\hat{z}_{d,q}}{dt} &= a_d(\hat{\boldsymbol{z}}_d, \hat{\boldsymbol{z}}_r) + b_q(\hat{\boldsymbol{z}}_d, \hat{\boldsymbol{z}}_r, u) + K_q(\hat{\boldsymbol{z}}, e_1) + \lambda_q \operatorname{sign}(\bar{e}_q) \\
\frac{d\hat{\boldsymbol{z}}_r}{dt} &= \boldsymbol{a}_r(\hat{\boldsymbol{z}}_d, \hat{\boldsymbol{z}}_r) + b_r(\hat{\boldsymbol{z}}_d, \hat{\boldsymbol{z}}_r, u) + K_{q+1:n}(\hat{\boldsymbol{z}}_c, e_1).
\end{aligned} \tag{2.21}$$

This observer can also be written

$$\frac{d\hat{\boldsymbol{z}}_c}{dt} = \bar{\boldsymbol{f}}(\hat{\boldsymbol{z}}_c) + \bar{\boldsymbol{g}}(\hat{\boldsymbol{z}}_c, u) + \boldsymbol{K}(\hat{\boldsymbol{z}}_c, e_1) + \boldsymbol{u}_r \tag{2.22}$$

where

$$\boldsymbol{u}_r = [\lambda_1 \operatorname{sign}(e_1), \ldots, \lambda_q \operatorname{sign}(\bar{e}_q), 0_{1\times(n-q)}]^T.$$

Lemma 2.3.14. *Let Assumptions 2.3.10 and 2.3.13 be satisfied. The estimation error provided by the observer (2.21) is bounded.*

Proof: Define the error vector $\boldsymbol{e} = \boldsymbol{z}_c - \hat{\boldsymbol{z}}_c$; the error dynamics can be obtained from equations (2.8) and (2.22) as

$$\frac{d\boldsymbol{e}}{dt} = \bar{\boldsymbol{f}}(\boldsymbol{z}_c) - \bar{\boldsymbol{f}}(\hat{\boldsymbol{z}}_c) + \bar{\boldsymbol{g}}(\boldsymbol{z}_c, u) - \bar{\boldsymbol{g}}(\hat{\boldsymbol{z}}_c, u) - \boldsymbol{K}(\hat{\boldsymbol{z}}_c, e_1) + \boldsymbol{\Gamma}(\boldsymbol{z_c})\xi - \boldsymbol{u}_r\,. \tag{2.23}$$

Consider a continuously differentiable Lyapunov function V that satisfies Assumption 2.3.13. Along trajectories,

$$\frac{dV(\boldsymbol{e})}{dt} = \frac{\partial V(\boldsymbol{e})}{\partial \boldsymbol{e}} \left(\bar{\boldsymbol{f}}(\boldsymbol{z}_c) - \bar{\boldsymbol{f}}(\hat{\boldsymbol{z}}_c) + \bar{\boldsymbol{g}}(\boldsymbol{z}_c, u) - \bar{\boldsymbol{g}}(\hat{\boldsymbol{z}}_c, u) - \boldsymbol{K}(\hat{\boldsymbol{z}}_c, e_1) + \boldsymbol{\Gamma}(\boldsymbol{z}_c)\xi - \boldsymbol{u}_r\right).$$

Substituting inequalities (2.20) and (2.19) leads to

$$\frac{dV(\boldsymbol{e})}{dt} \leq -\beta_3\|\boldsymbol{e}\|^2 + \beta_4\|\boldsymbol{\Gamma}(\boldsymbol{z}_c)\xi - \boldsymbol{u}_r\|\|\boldsymbol{e}\|. \tag{2.24}$$

From the definition of $\boldsymbol{\Gamma}(\boldsymbol{z}_c)$, equation (2.10), Lemma 2.3.11, Assumption 2.3.9, and the boundedness of the vector $\boldsymbol{u}_r$ and unknown input ξ, it can be concluded that for some $M_d \in \mathbb{R}^+$,

$$\|\boldsymbol{\Gamma}(\boldsymbol{z}_c)\xi - \boldsymbol{u}_r\| \leq M_d.$$

Therefore,

$$\frac{dV(\boldsymbol{e})}{dt} \leq -\beta_3\|\boldsymbol{e}\|^2 + \beta_4 M_d\|\boldsymbol{e}\|. \tag{2.25}$$

If

$$\|\boldsymbol{e}\| < \frac{\beta_4 M_d}{\beta_3}$$

the error vector is of course bounded and the proof is complete.

Now, suppose that

$$\|\boldsymbol{e}\| \geq \frac{\beta_4 M_d}{\beta_3}.$$

From inequalities (2.18) and (2.25), this implies that

$$\frac{dV(\boldsymbol{e})}{dt} \leq 0, \quad \text{and} \quad \|\boldsymbol{e}\| \leq \sqrt{\frac{V(\boldsymbol{e})}{\beta_1}} \leq \sqrt{\frac{V(\boldsymbol{e}(0))}{\beta_1}}.$$

Therefore, in this case, the error vector is bounded by

$$\max((\beta_4 M_d)/\beta_3, \sqrt{V(\boldsymbol{e}(0))/\beta_1}).$$

□

Theorem 2.3.15. *Suppose that Assumptions 2.2.1-2.3.10 hold and also that the error dynamics for the undisturbed system ($\xi \equiv 0$) defined in equation (2.17) satisfy Assumption 2.3.13 with*

$$\beta_3 > \beta_4(1 + M_a + M_q).$$

Then, there exists $\lambda_1, \cdots, \lambda_q \in \mathbb{R}^+$ such that the modified sliding mode observer (2.21) provides exponential convergence of the estimation vector $\hat{\boldsymbol{z}}_c$ to the state vector $\boldsymbol{z}_c = \boldsymbol{\phi}(x)$.

Proof: If the disturbance input ξ is zero, the result follows trivially from the assumptions. Consider then a non-zero disturbance term $\xi \neq 0$. The proof involves several steps.

Step one:

This step is along the lines of the proof of Theorem 2.3.12 in [79]. Let $\boldsymbol{e}^T = [\boldsymbol{e}_d^T, \boldsymbol{e}_r^T] = \boldsymbol{z}_c - \hat{\boldsymbol{z}}_c$ where $\boldsymbol{e}_d^T = [e_1, \ldots, e_q]$, and $\boldsymbol{e}_q^T = [e_{q-1}, \ldots, e_n]$. The error dynamics of the vector $\boldsymbol{e}_d$ is expanded as

$$\frac{de_1}{dt} = e_2 - K_1(\hat{\boldsymbol{z}}_c, e_1) - \lambda_1 \operatorname{sign}(e_1) \tag{2.26}$$

$$\frac{de_2}{dt} = e_3 + b_2(z_{d,2}, y, u) - b_{q-1}(\hat{z}_{d,2}, y, u) - K_2(\hat{\boldsymbol{z}}_c, e_1) - \lambda_2 \operatorname{sign}(e_2) \tag{2.27}$$

$$\vdots$$

$$\begin{aligned}\frac{de_{q-1}}{dt} &= e_q + b_{q-1}(z_{d,2}, \ldots, z_{d,q-1}, y, u) \\ &\quad - b_{q-1}(\hat{z}_{d,2}, \ldots, \hat{z}_{d,q-1}, y, u) - K_{q-1}(\hat{\boldsymbol{z}}_c, e_1) - \lambda_{q-1} \operatorname{sign}(\bar{e}_{q-1})\end{aligned} \tag{2.28}$$

$$\begin{aligned}\frac{de_q}{dt} &= a_d(\boldsymbol{z}_d, \boldsymbol{z}_r) - a_d(\hat{\boldsymbol{z}}_d, \hat{\boldsymbol{z}}_r) + b_q(\boldsymbol{z}_d, \boldsymbol{z}_r, u) - b_q(\hat{\boldsymbol{z}}_d, \hat{\boldsymbol{z}}_r, u) \\ &\quad - K_q(\hat{\boldsymbol{z}}_c, e_1) + c(\boldsymbol{z}_d, \boldsymbol{z}_r)\xi - \lambda_q \operatorname{sign}(\bar{e}_q).\end{aligned} \tag{2.29}$$

Consider the first dynamical equation of the error dynamics (2.26). Define a Lyapunov function as

$$V_1(e_1) = \frac{1}{2}|e_1|^2.$$

The time differentiation of $V_1(e_1)$ is

$$\frac{dV_1(e_1)}{dt} = e_1 e_2 - e_1 K_1(\hat{z}_c, e_1) - \lambda_1 |e_1| \tag{2.30}$$

From Lemma 2.3.14, the error vector e is bounded, so $(|e_2| + k|e_1|)$ has an upper bound, and it is possible to choose $\lambda_1 > \sup(|e_2| + k|e_1|)$. For such λ_1, since the observer gain satisfies inequality (2.16), for some $\beta_5 \in \mathbb{R}^+$, equation (2.30) leads to

$$\frac{dV_1(e_1)}{dt} \leq -\beta_5 |(e_1)|.$$

Therefore, the system reaches the switching surface $e_1 = 0$ after a finite time t_1. After this ideal sliding motion takes place, $e_1 = 0$ and $de_1/dt = 0$ for $t > t_1$. The second equation (2.27) becomes

$$\frac{de_2}{dt} = e_3 + b_2(z_{d,2}, y, u) - b_{q-1}(\hat{z}_{d,2}, y, u) - K_2(\hat{\boldsymbol{z}}_c, e_1) - \lambda_2 \operatorname{sign}(e_2).$$

Similarly, given inequalities (2.16) and (2.12) as well as the boundedness of e_2, for $\lambda_2 > \sup(|e_3| + M_2|e_2| + k|e_1|)$, the system reaches the switching surface $e_2 = 0$ after a finite time $t_2 > t_1$. Following the same reasoning implies that after finite time $T > t_q > \ldots > t_2 > t_1$, the system reaches the sliding surfaces $e_1 = 0, \ldots, e_q = 0$ one by one.

Step two:

Once the motion is along the intersection of the sliding surfaces, $e_1 = 0, \ldots, e_q = 0$, the discontinuous vector $\boldsymbol{u}_r$ in equation (2.22) can be replaced by its equivalent smooth counterpart [84]

$$\boldsymbol{u}_{eq} = (\boldsymbol{u}_r)_{eq} = \begin{bmatrix} e_2 \\ \vdots \\ e_q \\ a_d(\boldsymbol{z}_d, \boldsymbol{z}_r) - a_d(\boldsymbol{z}_d, \hat{\boldsymbol{z}}_r) + \\ b_q(\boldsymbol{z}_d, \boldsymbol{z}_r, u) - b_q(\boldsymbol{z}_d, \hat{\boldsymbol{z}}_r, u) + c(\boldsymbol{z}_d, \boldsymbol{z}_r)\xi \\ \mathbf{0}_{(n-q)\times 1} \end{bmatrix}, \tag{2.31}$$

where $\boldsymbol{u}_{eq}$ forces the system's motion stay along the intersection of some sliding surfaces; then, the error dynamics of the system takes the form

$$\frac{d\boldsymbol{e}}{dt} = \bar{\boldsymbol{f}}(\boldsymbol{z}_c) - \bar{\boldsymbol{f}}(\hat{\boldsymbol{z}}_c) + \bar{\boldsymbol{g}}(\boldsymbol{z}_c, u) - \bar{\boldsymbol{g}}(\hat{\boldsymbol{z}}_c, u) - \boldsymbol{K}(\hat{\boldsymbol{z}}_c, e_1) + \boldsymbol{\Gamma}(\boldsymbol{z}_c)\xi - \boldsymbol{u}_{eq}. \tag{2.32}$$

From equation (2.31) and the inequalities (2.12),

$$\|\boldsymbol{\Gamma}(\boldsymbol{z}_c)\xi - \boldsymbol{u}_{eq}\| \leq (1 + M_a + M_q)\|\boldsymbol{e}\|. \tag{2.33}$$

Step three:
The observer $\boldsymbol{K}(\hat{\boldsymbol{z}}_c, e_1)$ was proved in Lemma 2.3.14 to provide a bounded error even for a system with disturbances. In sliding mode, which occurs after a finite time, the error dynamics is given by equation (2.32). Differentiating the Lyapunov function V that satisfies Assumption 2.3.13 leads to

$$\frac{dV(\boldsymbol{e})}{dt} = V_0(\boldsymbol{e}) + \frac{\partial V(\boldsymbol{e})}{\partial \boldsymbol{e}}(\boldsymbol{\Gamma}(\boldsymbol{z}_c)\xi - \boldsymbol{u}_{eq}). \tag{2.34}$$

Inequalities (2.20), (2.19) and (2.33) imply that

$$\frac{dV(\boldsymbol{e})}{dt} \leq -\beta_3\|\boldsymbol{e}\|^2 + \beta_4(1 + M_a + M_q)\|\boldsymbol{e}\|^2 . \tag{2.35}$$

Since $\beta_3 > \beta_4(1 + M_a + M_q)$, for some $\beta_5 = \beta_3 - \beta_4(1 + M_a + M_q) \in \mathbb{R}^+$

$$\frac{dV(\boldsymbol{e})}{dt} \leq -\beta_5\|\boldsymbol{e}\|^2 \tag{2.36}$$

and the estimation error $\boldsymbol{e}$ goes to zero exponentially. □

Theorem 2.3.15 shows that an exponentially convergent observer of the undisturbed nonlinear system can be combined with a sliding mode observer. The result is an exponentially convergent observer of the system in the presence of disturbances coming from an unknown input.

There are two ways of considering the inverse transformation: finding the state space representation of the observer in the original coordinates, and transforming the state estimate back into the original coordinates. In this thesis, the second method is chosen since the simulations will be applied in a sample-data framework. The observer state in the original coordinates is obtained by

$$\hat{\boldsymbol{z}}_{orig} = \boldsymbol{\phi}^{-1}(\hat{\boldsymbol{z}}_c).$$

A potential nonlinear observer with an exponential convergence rate is the modified EKF introduced [66, 67]. This method is easier to apply than other nonlinear observers and suggests a sub-optimal state estimation. In this chapter, this filtering is used to replace the nonlinear observer of Theorem 2.3.15.

2.4 Observer design for DPS

The dynamical systems considered in this paper have PDE form. Let the state space be a separable Hilbert space $\mathcal{H}$. In general, the system can be represented by

$$\begin{aligned} \frac{\partial \boldsymbol{z}}{\partial t} &= \boldsymbol{\mathcal{F}}(\boldsymbol{z}) + \boldsymbol{\mathcal{B}}u(t) + \boldsymbol{\mathcal{G}}\xi(t) \\ y(t) &= \mathcal{C}\boldsymbol{z} \end{aligned} \tag{2.37}$$

where $\boldsymbol{z} \in \mathcal{H}$, $\boldsymbol{x} \in \mathbb{R}^m$ is the spatial variable, $\boldsymbol{\mathcal{F}} : \mathcal{D}(\boldsymbol{\mathcal{F}}) \subset \mathcal{H} \to \mathcal{H}$ is a nonlinear operator, $\boldsymbol{\mathcal{B}} : \mathbb{R} \to \mathcal{H}$ is a bounded input operator, $\boldsymbol{\mathcal{G}} : \mathbb{R} \to \mathcal{H}$ is a bounded disturbance operator, $u \in \mathbb{R}$ is the input signal, $\xi \in \mathbb{R}$ is the disturbance input, $y \in \mathbb{R}$ is the output, and $\mathcal{C} : \mathcal{H} \to \mathbb{R}$ is a bounded output operator. The initial condition is

$$\boldsymbol{z}(0, \boldsymbol{x}) = \boldsymbol{z}_0 \in \mathcal{H}. \tag{2.38}$$

In order to proceed the observer design, a finite-dimensional approximation is introduced. Since the Hilbert space is separable, a basis $\{\boldsymbol{v}_i\}_{i=1}^{\infty}$ can be chosen for the Hilbert space $\mathcal{H}$. Now, define the Hilbert space

$$\mathcal{H}_M = \text{span}\{\boldsymbol{v}_k, k = 1 \dots M\}.$$

The orthogonal projection of the Hilbert space $\mathcal{H}$ onto $\mathcal{H}_M$ is defined by

$$\boldsymbol{\mathcal{P}}_M \boldsymbol{z} = \sum_{i=1}^{M} z_i \boldsymbol{v}_i \tag{2.39}$$

for $\boldsymbol{z} \in \mathcal{H}$ and $z_i \in \mathbb{R}$. Let the state vector be decomposed into two parts:

$$\boldsymbol{z} = \boldsymbol{z}_M + \boldsymbol{z}_M^c \tag{2.40}$$

with

$$\boldsymbol{z}_M = \boldsymbol{\mathcal{P}}_M \boldsymbol{z}, \tag{2.41}$$

$$\boldsymbol{z}_M^c = (\boldsymbol{\mathcal{I}} - \boldsymbol{\mathcal{P}}_M)\boldsymbol{z} \tag{2.42}$$

where $\boldsymbol{\mathcal{I}}$ is an identity operator.

Define a finite-dimensional nonlinear operator

$$\boldsymbol{\mathcal{F}}_M(\boldsymbol{z}) = \sum_{i=1}^{M} f_i(\boldsymbol{z}) \boldsymbol{v}_i$$

where $f_i(.)$ are derived using Galerkin method and a weak form of 2.37,

$$\boldsymbol{\mathcal{F}}_M^c(\boldsymbol{z}) = \boldsymbol{\mathcal{F}}(\boldsymbol{z}) - \boldsymbol{\mathcal{F}}_M(\boldsymbol{z}),$$

and

$$\begin{aligned} \boldsymbol{\mathcal{G}}_M &= \boldsymbol{\mathcal{P}}_M \boldsymbol{\mathcal{G}}, \qquad & \boldsymbol{\mathcal{G}}_M^c &= (\boldsymbol{\mathcal{I}} - \boldsymbol{\mathcal{P}}_M)\boldsymbol{\mathcal{G}} \\ \boldsymbol{\mathcal{B}}_M &= \boldsymbol{\mathcal{P}}_M \boldsymbol{\mathcal{B}}, \qquad & \boldsymbol{\mathcal{B}}_M^c &= (\boldsymbol{\mathcal{I}} - \boldsymbol{\mathcal{P}}_M)\boldsymbol{\mathcal{B}}. \end{aligned}$$

The projection defined in equation (2.41) can be used to rewrite (2.37) as

$$\frac{\partial \boldsymbol{z}_M}{\partial t} = \boldsymbol{\mathcal{F}}_M(\boldsymbol{z}) + \boldsymbol{\mathcal{B}}_M u(t) + \boldsymbol{\mathcal{G}}_M \xi(t) \tag{2.43}$$

$$\frac{\partial \boldsymbol{z}_M^c}{\partial t} = \boldsymbol{\mathcal{F}}_M^c(\boldsymbol{z}) + \boldsymbol{\mathcal{B}}_M^c u(t) + \boldsymbol{\mathcal{G}}_M^c \xi(t) \tag{2.44}$$

$$y(t) = \mathcal{C}\boldsymbol{z}_M + \mathcal{C}\boldsymbol{z}_M^c.$$

Next, the system is approximated by the finite-dimensional version; The state vector $\boldsymbol{z}$ is approximated by

$$\bar{\boldsymbol{z}}_M = \sum_{i=1}^{M} \bar{z}_i \boldsymbol{v}_i,$$

The two state variables $\bar{\boldsymbol{z}}_M$ and $\boldsymbol{z}_M$ are different since they satisfy two different equations. The state $\boldsymbol{z}_M$ is the solution to (2.43) and (2.44) and $\bar{\boldsymbol{z}}_M$ satisfies the finite-dimensional system defined as

$$\begin{aligned} \frac{\partial \bar{\boldsymbol{z}}_M}{\partial t} &= \boldsymbol{\mathcal{F}}_M(\bar{\boldsymbol{z}}_M) + \boldsymbol{\mathcal{B}}_M u(t) + \boldsymbol{\mathcal{G}}_M \xi(t) \\ y(t) &= \boldsymbol{\mathcal{C}} \bar{\boldsymbol{z}}_M. \end{aligned} \tag{2.45}$$

An equivalent ODE representation to (2.45) can be obtained via multiplying both sides of (2.45) by $\boldsymbol{v}_i$ for $i = 1 \dots N$ in the sense of $\mathcal{H}$ inner product denoted by $(.,.)_{\mathcal{H}}$. Define

$$\mathbf{z}_{orig,N} = \begin{bmatrix} \bar{z}_1 \\ \bar{z}_2 \\ \vdots \\ \bar{z}_M \end{bmatrix}, \quad \boldsymbol{f}_M(\mathbf{z}_{orig,N}) = \begin{bmatrix} f_1(\mathbf{z}_{orig,N}) \\ f_2(\mathbf{z}_{orig,N}) \\ \vdots \\ f_M(\mathbf{z}_{orig,N}) \end{bmatrix}$$

$$\boldsymbol{B}_M = \begin{bmatrix} B_1 \\ B_2 \\ \vdots \\ B_M \end{bmatrix}, \quad \boldsymbol{g}_M(\mathbf{z}_{orig,N}) = \begin{bmatrix} g_1(\mathbf{z}_{orig,N}) \\ g_2(\mathbf{z}_{orig,N}) \\ \vdots \\ g_M(\mathbf{z}_{orig,N}) \end{bmatrix}$$

$$\boldsymbol{C}_M = [\mathcal{C}\boldsymbol{v}_1, \mathcal{C}\boldsymbol{v}_2, \dots, \mathcal{C}\boldsymbol{v}_M]$$

where

$$\boldsymbol{\mathcal{F}}_M(\bar{\boldsymbol{z}}_M) = \sum_{i=1}^{M} f_i(\mathbf{z}_{orig,N})\boldsymbol{v}_i, \quad \boldsymbol{\mathcal{B}}_M = \sum_{i=1}^{M} B_i(\mathbf{z}_{orig,N})\boldsymbol{v}_i, \quad \boldsymbol{\mathcal{G}}_M(\bar{\boldsymbol{z}}_M) = \sum_{i=1}^{M} g_i(\mathbf{z}_{orig,N})\boldsymbol{v}_i.$$

The equivalent ODE representation is

$$\begin{aligned} \frac{d\mathbf{z}_{orig,N}}{dt} &= \boldsymbol{f}_M(\mathbf{z}_{orig,N}) + \boldsymbol{B}_M u(t) + \boldsymbol{g}_M(\mathbf{z}_{orig,N})\xi(t) \\ y &= \boldsymbol{C}_M \mathbf{z}_{orig,N}. \end{aligned} \tag{2.46}$$

For every $N > 0$, (2.46) preserve the same properties as those of (2.1).

The observer dynamics is composed of a copy of the system's approximate dynamics (2.46) with $N \leq M$ and a filtering feedback operation. Note that when different base functions are used to construct $\mathcal{H}_N$ and $\mathcal{H}_M$ for $N < M$, the bases of the Hilbert space $\mathcal{H}_M$ must be transformable into a new bases via a linear transformation such that it includes the bases of $\mathcal{H}_N$. In this way, the first N component of the state vector of both observer and system are comparable. This condition is satisfied for linear shape functions used in finite element method. Define

$$\mathbf{z}_{orig,N_0} = [\bar{z}_1, \bar{z}_2, \ldots, \bar{z}_N]^T, \quad \mathbf{z}^c_{orig,N_0} = [\bar{z}_{N+1}, \bar{z}_{N+2}, \ldots, \bar{z}_N]^T$$

and

$$\boldsymbol{f}_N(.) = \begin{bmatrix} f_1(.) \\ f_2(.) \\ \vdots \\ f_N(.) \end{bmatrix}, \quad \boldsymbol{f}^c_N(.) = \begin{bmatrix} f_{N+1}(.) \\ f_{N+2}(.) \\ \vdots \\ f_N(.) \end{bmatrix}$$

$$\boldsymbol{g}_N(.) = \begin{bmatrix} g_1(.) \\ g_2(.) \\ \vdots \\ g_N(.) \end{bmatrix}, \quad \boldsymbol{g}^c_N(.) = \begin{bmatrix} g_{N+1}(.) \\ g_{N+2}(.) \\ \vdots \\ g_N(.) \end{bmatrix}$$

$$\boldsymbol{B}_N = \begin{bmatrix} B_1 \\ B_2 \\ \vdots \\ B_N \end{bmatrix}, \quad \boldsymbol{B}^c_N = \begin{bmatrix} B_{N+1} \\ B_{N+2} \\ \vdots \\ B_N \end{bmatrix}$$

$$\boldsymbol{C}_N = [\boldsymbol{\mathcal{C}}\boldsymbol{v}_1, \boldsymbol{\mathcal{C}}\boldsymbol{v}_2, \ldots, \boldsymbol{\mathcal{C}}\boldsymbol{v}_N]$$

$$\boldsymbol{C}^c_N = [\boldsymbol{\mathcal{C}}\boldsymbol{v}_{N+1}, \boldsymbol{\mathcal{C}}\boldsymbol{v}_{N+2}, \ldots, \boldsymbol{\mathcal{C}}\boldsymbol{v}_N].$$

The system (2.46) can be rewriten as

$$\begin{aligned}
\frac{d\mathbf{z}_{orig,N_0}}{dt} &= \boldsymbol{f}_N(\mathbf{z}_{orig,N_0}) + \boldsymbol{B}_N u(t) + \boldsymbol{g}_N(\mathbf{z}_{orig,N_0})\xi(t) + \boldsymbol{h}_N(\mathbf{z}_{orig,N_0}, \mathbf{z}_{orig,N}) \\
\frac{d\mathbf{z}^c_{orig,N_0}}{dt} &= \boldsymbol{f}^c_N(\mathbf{z}_{orig,N}) + \boldsymbol{B}^c_N u(t) + \boldsymbol{g}^c_N(\mathbf{z}_{orig,N})\xi(t) \\
y &= \boldsymbol{C}_M \mathbf{z}_{orig,N}
\end{aligned} \tag{2.47}$$

where

$$\boldsymbol{h}_N(\mathbf{z}_{orig,N_0}, \mathbf{z}_{orig,N}) = \boldsymbol{f}_N(\mathbf{z}_{orig,N}) - \boldsymbol{f}_N(\mathbf{z}_{orig,N_0}) + (\boldsymbol{g}_N(\mathbf{z}_{orig,N}) - \boldsymbol{g}_N(\mathbf{z}_{orig,N_0}))\xi(t).$$

Next the following change of coordinate

$$\boldsymbol{z}_{c,M} = \begin{bmatrix} \boldsymbol{z}_{c,N} \\ \boldsymbol{z}^c_{c,N} \end{bmatrix} = \boldsymbol{T}_M \boldsymbol{w} = \begin{bmatrix} \boldsymbol{\phi}_N(\mathbf{z}_{orig,N_0}) \\ \mathbf{z}^c_{orig,N_0} \end{bmatrix}$$

is applied wherein $\boldsymbol{\phi}_N(\mathbf{z}_{orig,N_0})$ is defined as in (2.5) with $\boldsymbol{f}$ and $\boldsymbol{g}$ respectively replaced by $\boldsymbol{f}_N$ and $\boldsymbol{g}_N$.

In new coordinates, the system takes the form

$$\begin{aligned}
\frac{d\boldsymbol{z}_{c,N}}{dt} &= \bar{\boldsymbol{f}}_N(\boldsymbol{z}_{c,N}) + \bar{\boldsymbol{g}}_N(\boldsymbol{z}_{c,N}, u(t)) + \boldsymbol{\Gamma}_N(\boldsymbol{z}_{c,N})\xi(t) + \bar{\boldsymbol{h}}_N(\boldsymbol{z}_{c,N}, \boldsymbol{z}_{c,M}) \\
\frac{d\mathbf{z}^c_{orig,N_0}}{dt} &= \boldsymbol{f}^c_N(\boldsymbol{z}_{c,M}) + \boldsymbol{B}^c_N u(t) + \boldsymbol{g}^c_N(\boldsymbol{z}_{c,M})\xi(t) \\
y &= \bar{\boldsymbol{C}}_M \boldsymbol{z}_{c,M}
\end{aligned} \tag{2.48}$$

where

$$\begin{aligned}
\bar{\boldsymbol{f}}_N(\boldsymbol{z}_{c,N}) &= \frac{\partial \boldsymbol{\phi}_N(\mathbf{z}_{orig,N_0})}{\partial \mathbf{z}_{orig,N_0}} \mid_{\mathbf{z}_{orig,N_0}=\boldsymbol{z}_{c,N}} \boldsymbol{f}_N(\boldsymbol{\phi}_N^{-1}(\boldsymbol{z}_{c,N})), \\
\bar{\boldsymbol{g}}_N(\boldsymbol{z}_{c,N}, u(t)) &= \frac{\partial \boldsymbol{\phi}_N(\mathbf{z}_{orig,N_0})}{\partial \mathbf{z}_{orig,N_0}} \mid_{\mathbf{z}_{orig,N_0}=\boldsymbol{z}_{c,N}} \boldsymbol{B}_N u(t), \\
\boldsymbol{\Gamma}_N(\boldsymbol{z}_{c,N}) &= \frac{\partial \boldsymbol{\phi}_N(\mathbf{z}_{orig,N_0})}{\partial \mathbf{z}_{orig,N_0}} \mid_{\mathbf{z}_{orig,N_0}=\boldsymbol{z}_{c,N}} \boldsymbol{g}_N(\boldsymbol{\phi}_N^{-1}(\boldsymbol{z}_{c,N})), \\
\bar{\boldsymbol{h}}_N(\boldsymbol{z}_{c,N}, \boldsymbol{z}_{c,M}) &= \frac{\partial \boldsymbol{\phi}_N(\mathbf{z}_{orig,N_0})}{\partial \mathbf{z}_{orig,N_0}} \mid_{\mathbf{z}_{orig,N_0}=\boldsymbol{z}_{c,N}} \boldsymbol{h}_N(\boldsymbol{\phi}_N^{-1}(\boldsymbol{z}_{c,N}), \boldsymbol{T}_M^{-1}(\boldsymbol{z}_{c,M})), \\
\bar{\boldsymbol{C}}_M &= [1, 0, \ldots, 0].
\end{aligned}$$

Note that $\bar{\boldsymbol{f}}_N$, $\bar{\boldsymbol{g}}_N$, and $\boldsymbol{\Gamma}_N$ have the same structures as but different dimensions from that of $\bar{\boldsymbol{f}}$, $\bar{\boldsymbol{g}}$, and $\boldsymbol{\Gamma}$ since the mappings $\boldsymbol{\phi}_N$ and $\boldsymbol{\phi}$ are constructed based on the same logic.

Define $\hat{\boldsymbol{z}}_{c,N} = [\hat{z}_{c,1}, \hat{z}_{c,2}, \ldots, \hat{z}_{c,N}]^T$. The general observer dynamics is

$$\frac{d\hat{\boldsymbol{z}}_{c,N}}{dt} = \bar{\boldsymbol{f}}_N(\hat{\boldsymbol{z}}_{c,N}) + \bar{\boldsymbol{g}}_N(\hat{\boldsymbol{z}}_{c,N}, u(t)) + \boldsymbol{K}_N(\hat{\boldsymbol{z}}_{c,N}, y - \hat{z}_{c,1}) + \boldsymbol{u}_{r,N} \tag{2.49}$$

where $\boldsymbol{K}_N$ and $\boldsymbol{u}_{r,N}$ are defined in the same way as $\boldsymbol{K}$ and $\boldsymbol{u}_r$ (2.22) for $n = N$. Define $\boldsymbol{e}_N = [e_{N,1}, e_{N,2}, \ldots, e_{N,N}]^T = \boldsymbol{z}_{c,N} - \hat{\boldsymbol{z}}_{c,N}$. The error dynamics is

$$\begin{aligned}\frac{d\boldsymbol{e}_N}{dt} &= \bar{\boldsymbol{f}}_N(\boldsymbol{z}_{c,N}) - \bar{\boldsymbol{f}}_N(\hat{\boldsymbol{z}}_{c,N}) + \bar{\boldsymbol{g}}_N(\boldsymbol{z}_{c,N}, u(t)) - \bar{\boldsymbol{g}}_N(\hat{\boldsymbol{z}}_{c,N}, u(t)) \\ &\quad - \boldsymbol{K}_N(\hat{\boldsymbol{z}}_{c,N}, e_{N,1}) + \boldsymbol{\Gamma}_N(\boldsymbol{z}_{c,N})\xi(t) - \boldsymbol{u}_{r,N} + \bar{\boldsymbol{h}}_N(\boldsymbol{z}_{c,N}, \boldsymbol{z}_{c,M}) \\ \frac{d\mathbf{z}^c_{orig,N_0}}{dt} &= \boldsymbol{f}^c_N(\boldsymbol{z}_{c,M}) + \boldsymbol{B}^c_N u(t) + \boldsymbol{g}^c_N(\boldsymbol{z}_{c,M})\xi(t).\end{aligned} \tag{2.50}$$

Lemma 2.4.1. *Let the system (2.47) satisfy Assumption 2.3.10. For $\mathbf{z}^c_{orig,N_0} \equiv 0$, $u_{r,N} \equiv 0$, and $\xi(t) \equiv 0$, let the error dynamics (2.50) satisfy Assumption 2.3.13 with $n = N$. Furthermore, suppose that $\bar{\boldsymbol{h}}_N(\boldsymbol{z}_{c,N}, \boldsymbol{z}_{c,M})$ is bounded for every N. In other words,*

$$\|\bar{\boldsymbol{h}}_N(\boldsymbol{z}_{c,N}, \boldsymbol{z}_{c,M})\| \leq M_h$$

for some $M_h \in \mathbb{R}^+$. The state estimation provided by the observer (2.49) is bounded.

Proof: Consider a continuously differentiable Lyapunov function V similar to what is chosen in Lemma 2.3.14 that satisfies Assumption 2.3.13. Followed by the same procedure as in Lemma 2.3.14, along the trajectories given by (2.50),

$$\frac{dV(\boldsymbol{e}_N)}{dt} \leq -\beta_3\|\boldsymbol{e}_N\|^2 + \beta_4\|\boldsymbol{\Gamma}_N(\boldsymbol{z}_{c,N})\xi - \boldsymbol{u}_{r,N} + \bar{\boldsymbol{h}}_N(\boldsymbol{z}_{c,N}, \boldsymbol{z}_{c,M})\|\|\boldsymbol{e}_N\|. \tag{2.51}$$

From the definition of $\boldsymbol{\Gamma}_N(\boldsymbol{z}_{c,N})$; equation (2.10); Lemma 2.3.11; Assumption 2.3.9; and the boundedness of the vector $\boldsymbol{u}_{r,N}$, unknown input ξ, and $\bar{\boldsymbol{h}}_N(\boldsymbol{z}_{c,N}, \boldsymbol{z}_{c,M})$, it can be concluded that for some $M_d \in \mathbb{R}^+$,

$$\|\boldsymbol{\Gamma}_N(\boldsymbol{z}_{c,N})\xi - \boldsymbol{u}_{r,N} + \bar{\boldsymbol{h}}_N(\boldsymbol{z}_{c,N}, \boldsymbol{z}_{c,M})\| \leq M_d + M_h.$$

Therefore,

$$\frac{dV(\boldsymbol{e}_N)}{dt} \leq -\beta_3\|\boldsymbol{e}_N\|^2 + \beta_4(M_d + M_h)\|\boldsymbol{e}_N\|,$$

and

$$\|\boldsymbol{e}_N\| \leq \frac{\beta_4(M_d + M_h)}{\beta_3}.$$

Since the error vector and the system state are bounded so does the observer state, and the proof is complete. □

The boundedness of the estimation error is given by the following theorem.

Theorem 2.4.2. *Suppose that Assumptions 2.2.1-2.3.8 hold for* $\boldsymbol{f} = \boldsymbol{f}_N$, $\boldsymbol{g} = \boldsymbol{g}_N$, $n = N$, *and* $q = 1$, *and the system (2.47) satisfies Assumption 2.3.10. For* $\boldsymbol{z}^{\mathcal{E}}_{orig,N_0} \equiv 0$, $u_{r,N} \equiv 0$, *and* $\xi(t) \equiv 0$, *let the error dynamics (2.50) satisfy Assumption 2.3.13 with* $n = N$ *and*

$$\beta_3 > \beta_4(1 + M_a + M_q).$$

Furthermore, suppose that $\bar{\boldsymbol{h}}_N(\boldsymbol{z}_{c,N}, \boldsymbol{z}_{c,M})$ *is bounded for every* N *as defined in Lemma 2.4.1. Then, there exists* $\lambda_1, \cdots, \lambda_q \in \mathbb{R}^+$ *such that the approximate observer (2.49) provides a bounded estimation error compared to the higher order approximated system (2.48).*

Proof: If the disturbance input ξ is zero, the result follows trivially from the assumptions. Consider a non-zero disturbance term $\xi \neq 0$. The proof is similar to that of Theorem 2.3.15. Followed by the same procedure as in the step one, for $q = 1$, there exists $\lambda_1 > 0$ such that the observer reaches the sliding surface in a finite time; the equivalent signal is

$$\boldsymbol{u}_{eq,N} = (\boldsymbol{u}_{r,N})_{eq} = \begin{bmatrix} \bar{\boldsymbol{C}}_N(\bar{\boldsymbol{f}}_N(\boldsymbol{z}_{c,N}) - \bar{\boldsymbol{f}}_N(\hat{\boldsymbol{z}}_{c,N}))+ \\ \bar{\boldsymbol{C}}_N(\bar{\boldsymbol{g}}_N(\boldsymbol{z}_{c,N}, u(t)) - \bar{\boldsymbol{g}}_N(\hat{\boldsymbol{z}}_{c,N}, u(t)))+ \\ \bar{\boldsymbol{C}}_N\boldsymbol{\Gamma}_N(\boldsymbol{z}_{c,N})\xi(t)+ \\ \bar{\boldsymbol{C}}_N\bar{\boldsymbol{h}}_N(\boldsymbol{z}_{c,N}, \boldsymbol{z}_{c,M}) \\ \boldsymbol{0}_{(n-1)\times 1} \end{bmatrix}, \tag{2.52}$$

where $\bar{\boldsymbol{C}}_N = [1, 0, \ldots, 0]$ is a row matrix of dimension N. From equation (2.52) and the inequalities (2.12),

$$\|\boldsymbol{\Gamma}_N(\boldsymbol{z}_{c,N})\xi - \boldsymbol{u}_{eq,N}\| \leq (1 + M_a + M_q)\|\boldsymbol{e}_N\| + M_h. \tag{2.53}$$

In the sliding mode, which occurs after a finite time, the differentiation of a Lyapunov function V that satisfies Assumption 2.3.13 leads to

$$\frac{dV(\boldsymbol{e}_N)}{dt} = V_0(\boldsymbol{e}_N) + \frac{\partial V(\boldsymbol{e}_N)}{\partial \boldsymbol{e}_N}(\boldsymbol{\Gamma}_N(\boldsymbol{z}_{c,N})\xi - \boldsymbol{u}_{eq,N} + \bar{\boldsymbol{h}}_N(\boldsymbol{z}_{c,N}, \boldsymbol{z}_{c,M})). \tag{2.54}$$

Inequalities (2.20), (2.19) and (2.53) imply that

$$\frac{dV(\boldsymbol{e}_N)}{dt} \leq -\beta_3\|\boldsymbol{e}_N\|^2 + \beta_4(1 + M_a + M_q)\|\boldsymbol{e}_N\|^2 + 2M_h\|\boldsymbol{e}_N\|. \tag{2.55}$$

Since $\beta_3 > \beta_4(1 + M_a + M_q)$, for some $\beta_5 = \beta_3 - \beta_4(1 + M_a + M_q) \in \mathbb{R}^+$

$$\frac{dV(\boldsymbol{e}_N)}{dt} \leq -\beta_5\|\boldsymbol{e}_N\|^2 + 2M_h\|\boldsymbol{e}_N\| \tag{2.56}$$

and the estimation error $\boldsymbol{e}$ is bounded by

$$\|\boldsymbol{e}\| \leq \|\boldsymbol{e}_N\| + \|\mathbf{z}^c_{orig,N_0}\| \leq \frac{2M_h}{\beta_5} + \|\mathbf{z}^c_{orig,N_0}\|. \tag{2.57}$$

□

The nonlinear observer can be substituted by the modified EKF which stability conditions are defined in Section 2. When the effect of the sliding mode is ignored, $u_{r,N}$ is set to zero, and the estimation error bound is given by Lemma 2.4.1.

Note that all the constants employed in Lemma 2.4.1 and Theorem 2.4.2 depend on the functions $\boldsymbol{f}_N$, $\boldsymbol{g}_N$, and $\boldsymbol{h}_N$ and thus on N. In addition, the observer dynamics (2.49) depends on the nonlinear filtering gain $\boldsymbol{K}_N$. In other words, proving that the solution to the approximate observer converges to the true state as the order of approximation increases requires adding conditions on the upper bounds of these constants as well as some conditions necessary to show the convergence of engaged functions. Finding these conditions and the convergence proof are not easily achieved in general nonlinear PDEs because of involved unbounded operators. The convergence result cannot be proved for the UKF even in the case of ODEs since it is purely based on stochastic analysis.

In this thesis, the order of approximation for the original system is chosen to be large enough such that the approximate solution is close to the exact solution of the system (2.37). With this setting, two sources of uncertainties are introduced in the observer design: the disturbances coming from the unknown input $\xi(t)$ and the modeling uncertainty due to the order reduction in the observer design. The sliding mode observer introduced in the previous section is designed to take care of former uncertainties but not the latter one. The performance of the different introduced observation techniques in the existence of both sources are examined for a variety of DPSs.

2.5 Simulations

In this section, different estimation methods are compared using variations of several standard equations, the heat and wave equations. Linear, quasi-linear, and fully nonlinear versions are considered, as well as versions with and without disturbances. Heat and wave equations are fundamentally different in that for the heat equation, the energy in each mode decreases rapidly to zero, while the energy in the wave equation is distributed over all modes. This has consequences for estimation. In the following simulations, the EKF and the modified SMO are designed for the transformed coordinates defined by equations (2.6) and (2.7). The UKF is designed with the original coordinates.

In the continuous-time EKF, a differential Riccati equation must be solved simultaneously with the system's dynamical equations. It is faster to use the discrete-time version of the EKF. In order to use the discrete-time EKF, the time span of interest is divided into small sub-intervals of the same sizes Δt. The time step should be chosen to be faster than the observer's dynamics such that the effect of time discretization can be neglected. The value $\Delta t = 0.01$ was found to be adequate for all the simulations.

On every sub-interval, the observer's dynamical equations given by (2.49) are solved with $\boldsymbol{K}_N$ set to zero. Next, the discrete-time EKF [66] is used to provide the state estimate at every time step; the observer term $\boldsymbol{K}_N$ acts as a correction to the state prediction. The systems equations are solved off line and its output is recalled at every time step. Note that MATLAB ODE15s is used to solve the ODEs on every time sub-intervals. The linearized dynamics of the system around the state prediction as described in the EKF algorithm must be defined. The solution at time step $k+1$ is

$$\boldsymbol{z}_{k+1} = \boldsymbol{\chi}(\Delta t, \boldsymbol{z}_k, u_{[t_k, t_{k+1}]}, \xi_{[t_k, t_{k+1}]}) \tag{2.58}$$

where $\boldsymbol{\chi}$ is an evolution operator describing the state at different time steps. The connection between the linearization in continuous-time and sampled-time systems around the estimation vector is demonstrated through Theorem A.0.1 (please see Appendix A). In the rest of this section, Theorem A.0.1 is employed to find the linearization of χ around the state estimate $\hat{\boldsymbol{z}}$ as the linear operator $\boldsymbol{B}_{\boldsymbol{z}_k}$ in Table 2.1.

The observer gains including the EKF, UKF, and modified SMO parameters are chosen by trial such that they achieve their best performance. The objective is that every observer achieves its best performance before being compared to others. In other words, for every order of approximation and each observer technique, different observer gains are tried and compared in order to reach an optimal point of performance. This tuning is done separately for every observer before being compared to others.

Comparing the results of the EKF and UKF in the following section shows that they both perform the same in the absence of disturbances. Note that the EKF employed here is a robust version of the EKF; it provides control over the rate of convergence via the parameter a. Selecting the right value for a is done through increasing this value such that the covarience matrix remains bounded and until no further improvement of the performance can be observed. The same approach is used to find the SMO gain. Finally, in the standard SMO, which added for the sake of comparison, the EKF is tuned using just the linear part of the system.

Heat equations

Now, different estimation methods are used for various versions of the heat equation, linear, quasi-linear, nonlinear heat equation, with and without unknown disturbances. Two sets of simulations are run; first, the disturbance ξ is zero and is not included in the system's dynamics. In the second set of simulations, the disturbance ξ is non-zero and unknown by the estimator. The parameters used are in Table 2.3. In both sets, as a non-persistent source of disturbances, a fraction of initial condition $\omega z(0,x)$ is added to the system state. This type of disturbance is added to keep the system modes excited in time. For linear and quasi-linear heat equations, $\omega = 0.1$, and for nonlinear equation, $\omega = 0.3$.

Finite element method (FEM) with piece-wise linear functions is used to approximate all three versions of the partial differential equation. The order of approximation is defined as the number of employed elements. The "true" system was simulated in COMSOL with seventeen linear elements to imitate true measurements and states. Increasing the number of the elements more than seventeen showed small changes in the system's solution.

The observer designs are shown for different orders of approximation. In the modified SMO, the EKF, was combined with a sliding mode observer. In all of the plots, the estimation error

$$e_{est} = \sqrt{\int_{x=0}^{L} e^2 dx}$$

where $e = z_M - \hat{z}_N$. The system's initial condition is

$$z(0,x) = 0.5\sin(\pi x)\,\mathrm{sech}(3(x-0.5))$$

and the observer's initial condition is $\hat{z}(0,x) = 0$. The shared observer's parameters are chosen as, for the EKF,

$$\boldsymbol{P}_{\boldsymbol{\nu}} = 0.1\boldsymbol{I}_{n\times n}, \quad \boldsymbol{P}_{\omega} = 0.1, \quad \boldsymbol{P}_{\boldsymbol{z}_0} = \boldsymbol{0}_{n\times n};$$

for the UKF,

$$\boldsymbol{P}_{\boldsymbol{\nu}} = 0.1\boldsymbol{I}_{n\times n}, \quad \boldsymbol{P}_{\omega} = 0.1, \quad \alpha = 0.05, \quad \kappa = 0, \quad \beta = 2, \quad \boldsymbol{P}_{\boldsymbol{z}_0} = 1e-6\boldsymbol{I}_{n\times n};$$

and for the modified SMO,

$$\boldsymbol{P}_{\boldsymbol{\nu}} = 0.1\boldsymbol{I}_{n\times n}, \quad \boldsymbol{P}_{\omega} = 0.1, \quad \boldsymbol{P}_{\boldsymbol{z}_0} = \boldsymbol{0}_{n\times n}.$$

Table 2.3: Heat and wave equation parameters.

parameters	L	α_1	α_2	η_1	η_2	θ_1	θ_2	ϵ	L_0	H	c_d
values	1	6	4	0.2	π^2	6	0.02	5	5	1	0.005

The linear heat equation was

$$\frac{\partial z}{\partial t} = \frac{\partial}{\partial x}(\alpha_1 \frac{\partial z}{\partial x}) + b(x)u(t) + g(x)\xi(t) \tag{2.59}$$

with boundary conditions

$$\frac{\partial z}{\partial x}(0,t) = 0, \quad z(L,t) = 0, \tag{2.60}$$

and localized observation

$$y = \frac{1}{\delta}\int_{\frac{L}{2}-\delta}^{\frac{L}{2}+\delta} z(x)dx. \tag{2.61}$$

where α_1 is the diffusivity coefficient, $z \in \mathcal{L}_2(0,L)$ is the state variable, $u(t)$ is the control input, $\xi(t)$ is an unknown input attributed to the disturbances, $g(x) \in \mathcal{C}([0,L])$ is the spatial distribution of the disturbance function, $b(x) \in \mathcal{C}([0,L])$ is the spatial distribution of the control. In the simulations,

$$g(x) = \sin(\pi x), \quad \xi(t) = 20\sin(t),$$

$$b(x) = \sin(2\pi x), \quad u(t) = 10\sin(t),$$

and $\delta = 1e-4$. Other observer parameters are

$$a = 20, \quad \lambda_1 = 50.$$

Results of the simulations are shown in Figures 2.1, 2.2, and 2.3. These figures show that for all methods, the estimation error not surprisingly decreases by increasing the order of approximation. In the absence of a disturbance, both EKF and UKF show the same performance. Furthermore, the modified SMO performs similarly to the EKF. When a disturbance is added, that is, $\xi \neq 0$, the EKF offers slightly better estimation error than the UKF.

In the presence of a disturbance, the modified SMO provides an even smaller estimation error; compared to other estimation methods, this method shows a considerable decrease in error for higher orders of approximation. The error for different observation techniques with a fixed approximation order is shown in Figure 2.4 and Table 2.4.

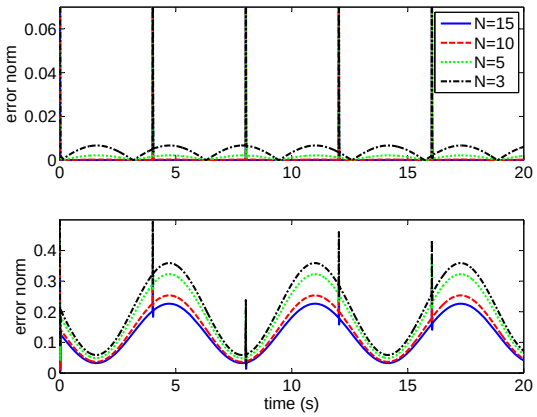

Figure 2.1: Estimation error of the EKF against time when applied to the linear heat equation with different orders of approximation N. The top plot shows the results in the absence of a disturbance and the bottom plot the results when there is an unknown disturbance. In the absence of disturbance, the error is very small even for $N = 5$. When a disturbance is present, the error is significant.

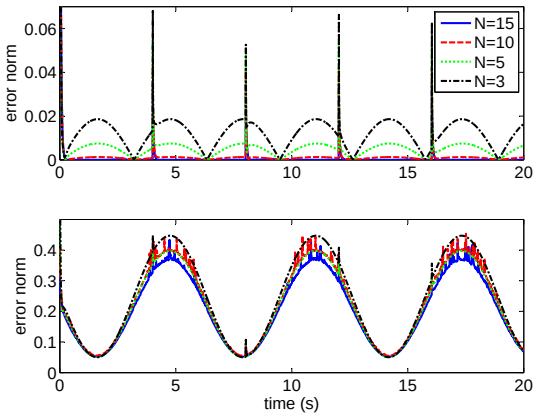

Figure 2.2: Estimation error of the UKF against time when applied to the linear heat equation with different orders of approximation N. The top plot shows the results in the absence of a disturbance and the bottom plot the results when there is an unknown disturbance. In the absence of disturbance, the error is very small even for $N = 5$. When a disturbance is present, the error is significant.

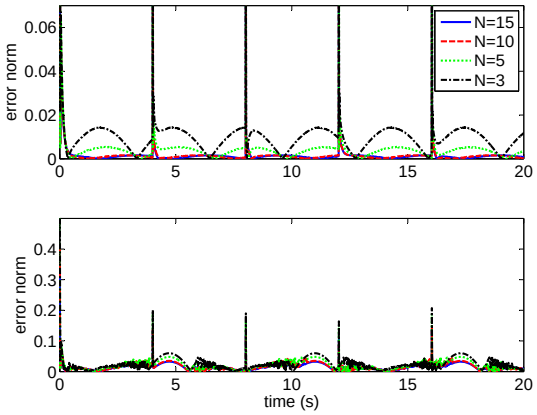

Figure 2.3: Estimation error of the modified SMO against time when applied to the linear heat equation with different orders of approximation N. The top plot shows the results in the absence of a disturbance and the bottom plot the results when there is an unknown disturbance. In the absence of disturbance, the error is very small even for $N = 5$. When a disturbance is present, the error is still small.

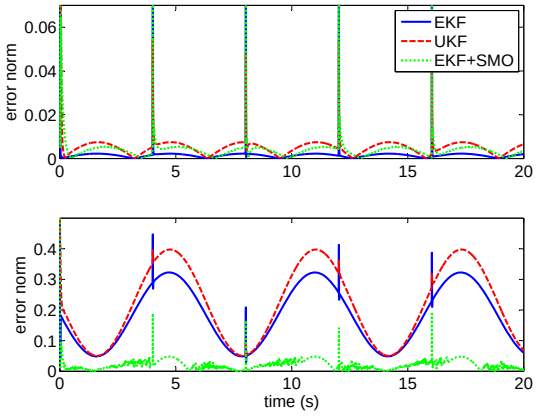

Figure 2.4: Comparison of the different estimation methods, the EKF, UKF, and modified SMO, in estimating the state vector of the linear heat equation for the order of approximation $N = 5$. The top plot shows the results in the absence of a disturbance and the bottom plot the results when there is an unknown disturbance.

The next model considered was a reaction-diffusion system, the quasi-linear heat equation

$$\frac{\partial z}{\partial t} = \frac{\partial}{\partial x}(\alpha_2 \frac{\partial z}{\partial x}) + R(z) + b(x)u(t) + g(x)\xi(t). \tag{2.62}$$

The values of α_2, η_1, and η_2 are given in Table 2.3 and

$$R(z) = \eta_1 z(\eta_2 - z).$$

The boundary conditions are again (2.60), and the observation is defined by equation (2.61). In the simulations,

$$g(x) = \sin(\pi x), \quad \xi(t) = -18(2 + 1.5\sin(t)),$$

$$b(x) = \sin(2\pi x), \quad u(t) = 10\sin(t).$$

Other observer parameters are

$$a = 2, \lambda_1 = 40$$

for the EKF and the modified SMO and $a = 2, \lambda_1 = 60$ for the standard SMO.

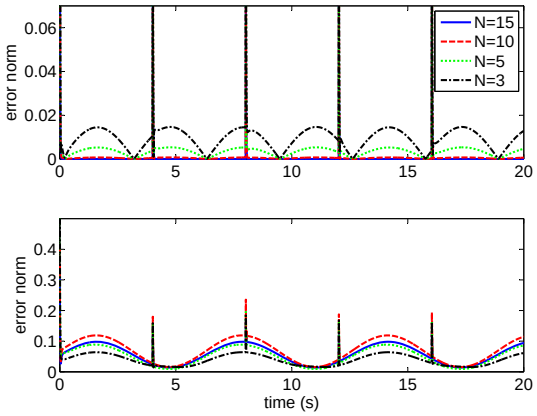

Figure 2.5: Estimation error of the EKF against time when applied to the quasi-linear heat equation with different orders of approximation N. The top plot shows the results in the absence of a disturbance and the bottom plot the results when there is an unknown disturbance. In the absence of disturbance, the error is very small even for $N = 5$. When a disturbance is present, the error grows larger.

Simulation results are shown in Figures 2.5, 2.6, and 2.7. Again, estimation error decreases as the order of approximation decreases in the absence of disturbances. Figures

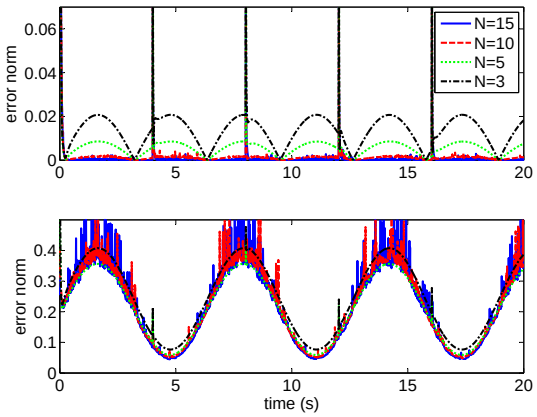

Figure 2.6: Estimation error of the UKF against time when applied to the quasi-linear heat equation with different orders of approximation N. The top plot shows the results in the absence of a disturbance and the bottom plot the results when there is an unknown disturbance. In the absence of disturbance, the error is very small even for $N = 5$. When a disturbance is present, the error is significant.

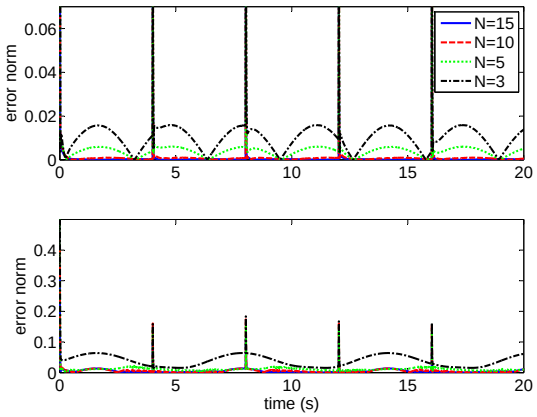

Figure 2.7: Estimation error of the modified SMO against time when applied to the quasi-linear heat equation with different orders of approximation N. The top plot shows the results in the absence of a disturbance and the bottom plot the results when there is an unknown disturbance. In the absence of disturbance, the error is very small even for $N = 5$. When a disturbance is present, the error is still small.

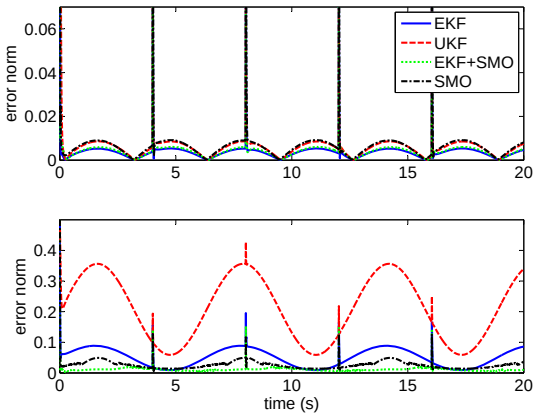

Figure 2.8: Comparison of the different estimation methods, the EKF, UKF, and modified SMO in estimating the state vector of the quasi-linear heat equation for the order of approximation $N = 5$. The top plot shows the results in the absence of a disturbance and the bottom plot the results when there is an unknown disturbance.

2.5 and 2.6 indicate that in the absence of disturbances, the estimation error provided by both EKF and UKF is nearly the same. Moreover, adding the sliding term to the EKF does not change its performance in the absence of disturbances.

However, estimation error of the UKF in the existence of the disturbances is more than two times larger than that of the EKF. According to Figure 2.7, the modified SMO reduces the estimation error by four times compared to the EKF. This improvement can be seen from Figure 2.8 and Table 2.4 where different observation techniques, all with approximation order $N = 5$, are compared. It is also observed that the modified SMO produces an error around three time less than the standard SMO.

The last heat equation considered was a nonlinear heat equation. The system is similar to the linear equation (2.59) except that the diffusivity is not constant but becomes a function of the state

$$\alpha_3(z) = \theta_1(1 + \theta_2 z^2),$$

where θ_1 and θ_2 are defined in Table 2.3. Thus, the governing equation is

$$\frac{\partial z}{\partial t} = \frac{\partial}{\partial x}(\alpha_3(z)\frac{\partial z}{\partial x}) + b(x)u(t) + g(x)\xi(t) \tag{2.63}$$

The same boundary conditions (2.60) hold, and the observation is again defined by (2.61). In the simulations,

$$g(x) = \sin(\pi x), \quad \xi(t) = 5.45(-2 + 1.5\sin(t)),$$

$$b(x) = \sin(2\pi x), \quad u(t) = 10\sin(t).$$

Other observer parameters are

$$a = 20, \lambda_1 = 10$$

for the EKF and the modified SMO and $a = 20, \lambda_1 = 30$ for the standard SMO.

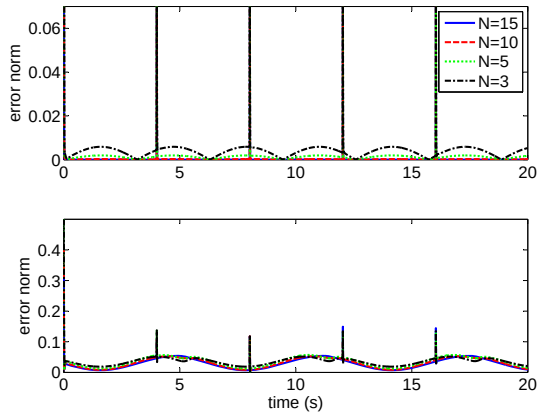

Figure 2.9: Estimation error of the EKF against time when applied to the nonlinear heat equation with different orders of approximation N. The top plot shows the results in the absence of a disturbance and the bottom plot the results when there is an unknown disturbance. In the absence of disturbance, the error is very small even for $N = 5$. When a disturbance is present, the error grows larger.

The simulation results are shown in Figures 2.9, 2.10, and 2.11. The same pattern of the error decreasing when the order of approximation increases can be seen in the absence of disturbances. The estimation errors of both EKF and UKF are almost the same in the absence of disturbances (Figures 2.9 and 2.10). However, the estimation error associated with the UKF is larger than EKF when disturbances are present. Like the previous two examples of the heat equation, the modified SMO performs similarly to the EKF when there is a disturbance. On the other hand, the error with the existence of disturbances is reduced by the modified SMO up to four times compared to the EKF (Figure 2.11). This is illustrated by Figure 2.12 and Table 2.4 where all the observation methods are compared with the order of approximation $N = 5$. It is also observed that the modified SMO produces an error around four time less than the standard SMO.

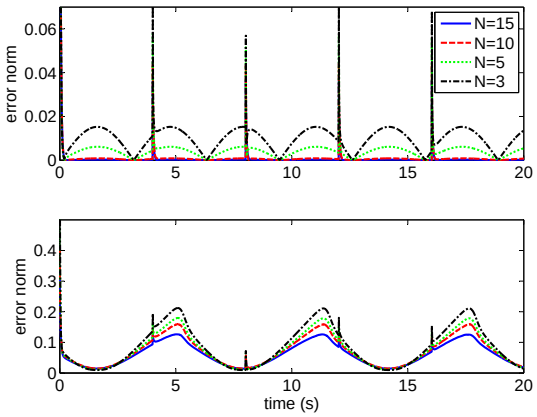

Figure 2.10: Estimation error of the UKF against time when applied to the nonlinear heat equation with different orders of approximation N. The top plot shows the results in the absence of a disturbance and the bottom plot the results when there is an unknown disturbance. In the absence of disturbance, the error is very small even for $N = 5$. When a disturbance is present, the error is significant.

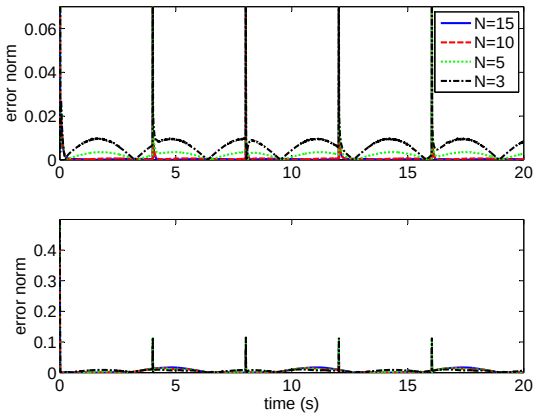

Figure 2.11: Estimation error of the modified SMO against time when applied to the nonlinear heat equation with different orders of approximation N. The top plot shows the results in the absence of a disturbance and the bottom plot the results when there is an unknown disturbance. In the absence of disturbance, the error is very small even for $N = 5$. When a disturbance is present, the error is still small.

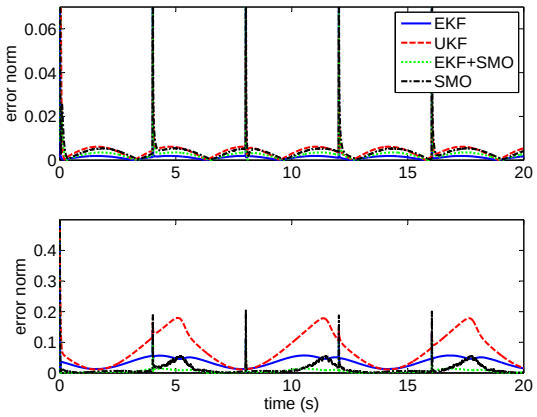

Figure 2.12: Comparison of the different estimation methods, the EKF, UKF, and modified SMO in estimating the state vector of the nonlinear heat equation for the order of approximation $N = 5$. The top plot shows the results in the absence of a disturbance and the bottom plot the results when there is an unknown disturbance.

Wave equations

The second category of infinite-dimensional systems considered is the wave equation. Unlike the linear heat equation, where the eigenvalues are all negative and real, the eigenvalues of even a damped wave equation lie in a vertical strip in the complex plane. The energy associated with different modes in the wave equation does decay to zero quickly similar to the case of the heat equation. Three different observation methods were applied to two different versions of a wave equation. Similar to the previous case, two sets of simulations, one with disturbance and one without disturbance, are run.

For the approximation of all the wave partial differential equations by a system of ODEs, and the resulting observer, a Galerkin method with trigonometric sin(.) base functions satisfying boundary conditions was used. The simulation results are exhibited for different orders of approximation. The "true" system was assumed to be obtained as the solution to the approximating ODEs with twenty five modes. This number of modes are enough to show the effect of model truncation in the observer design. Increasing the number of modes more than twenty five modes will only change the system solution. In all plots, the estimation error is

$$e_{est} = \sqrt{\int_{x=0}^{L} e^2 dx}$$

where $e = z_M - \hat{z}_N$.

The linear wave equation was

$$\frac{\partial^2 z}{\partial t^2} + \epsilon \langle \frac{\partial z}{\partial t}, d \rangle d(x) = \frac{\partial^2 z}{\partial x^2} + b(x)u(t) + g(x)\xi(t)$$

where ϵ is given in Table 2.3 [85]. Some damping is introduced so that the system is stable. However, with this damping, the eigenvalues asymptote to the imaginary axis and so the system is not exponentially detectable [86]. In the simulations,

$$d(x) = (x - 0.5)^2, \quad b(x) = 200x(x-1)\exp(-10(x-0.5)^2),$$

$$g(x) = \begin{cases} 100 & \text{if } 0 \leq x < 0.1 \\ 0 & \text{if } x \geq 0.1 \end{cases},$$

$$u(t) = \exp(-(t - [t/10])^2), \quad \xi(t) = \sin(t) + \cos(t),$$

with boundary conditions

$$\frac{\partial z}{\partial x}(0,t) = \frac{\partial z}{\partial x}(L,0) = 0,$$

and the localized observation

$$y = \frac{1}{\delta} \int_{x=L-\delta}^{L} z(x)\, dx$$

where $\delta = 1e-2$. The system's initial condition is

$$z(0,x) = 5(x-1)(x-1/3)\exp(-20(x-2/3)^2), \quad \frac{\partial z(0,x)}{\partial t} = 0$$

and the observer's initial condition is $\hat{z}(0,x) = 0$. Note that with these choices of initial condition and spatial distributions $b(x)$, $d(x)$, all the modes are affected by the external inputs and the initial condition.

Other observers' parameters are chosen as, for the EKF,

$$\boldsymbol{P_\nu} = 0.01\boldsymbol{I}_{n\times n}, \quad \boldsymbol{P}_\omega = 0.1, \quad a = 1, \quad \boldsymbol{P}_{\boldsymbol{z}_0} = \boldsymbol{0}_{n\times n};$$

for the UKF,

$$\boldsymbol{P_\nu} = 0.1\boldsymbol{I}_{n\times n}, \quad \boldsymbol{P}_\omega = 0.1, \quad \alpha = 0.05, \quad \kappa = 0, \quad \beta = 2, \quad \boldsymbol{P}_{\boldsymbol{z}_0} = 1e-6\boldsymbol{I}_{n\times n};$$

and for the modified SMO,

$$\boldsymbol{P_\nu} = 0.01\boldsymbol{I}_{n\times n}, \quad \boldsymbol{P}_\omega = 0.1, \quad a = 1, \quad \boldsymbol{P}_{\boldsymbol{z}_0} = \boldsymbol{0}_{n\times n}, \quad \lambda_1 = 30.$$

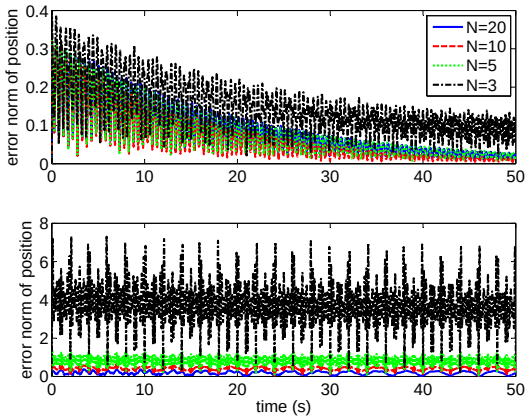

Figure 2.13: Estimation error of the EKF against time when applied to the linear wave equation with different orders of approximation N. The top plot shows the results in the absence of a disturbance and the bottom plot the results when there is an unknown disturbance. In the absence of disturbance, the error drops asymptotically to a small value even for $N = 5$. When a disturbance is present, the error is significant especially for the larger N.

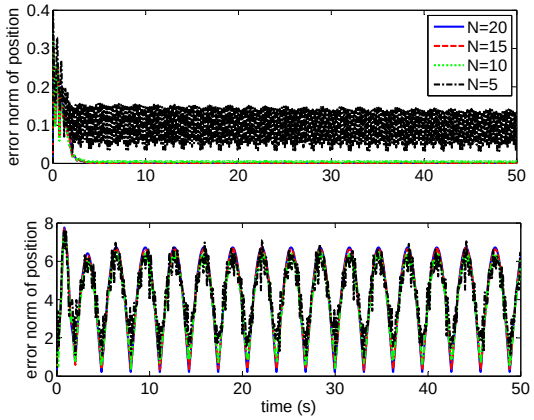

Figure 2.14: Estimation error of the UKF against time when applied to the linear wave equation with different orders of approximation N. The top plot shows the results in the absence of a disturbance and the bottom plot the results when there is an unknown disturbance. In the absence of disturbance, the error exponentially goes to a small value even for $N = 5$. When a disturbance is present, the error is significant.

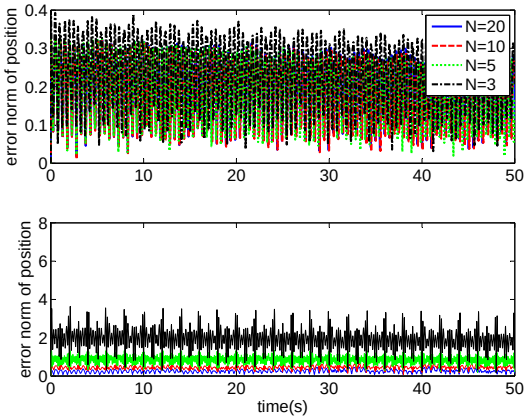

Figure 2.15: Estimation error of the modified SMO against time when applied to the linear wave equation with different orders of approximation N. The top plot shows the results in the absence of a disturbance and the bottom plot the results when there is an unknown disturbance. In the absence of disturbance, the error grows compared with the results of the EKF. When a disturbance is present, the error is large but less than what is provided by the EKF.

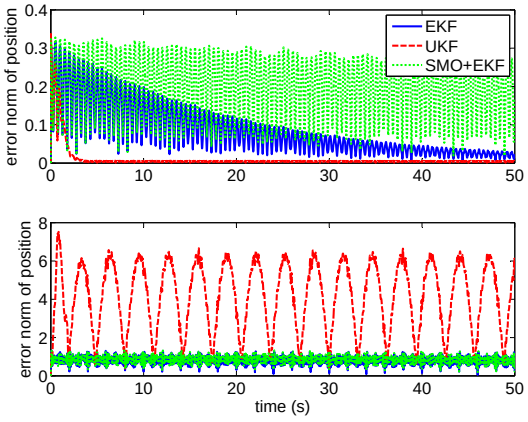

Figure 2.16: Comparison of the different estimation methods, the EKF, UKF, and modified SMO in estimating the state vector of the linear wave equation for the order of approximation $N = 5$. The top plot shows the results in the absence of a disturbance and the bottom plot the results when there is an unknown disturbance.

The simulation results are shown in Figures 2.13, 2.14, and 2.15. The pattern of increasing error by decreasing the order of approximation is observed. According to Figures 2.13 and 2.14, the UKF generally shows better performance over the EKF in the absence of a disturbance.

By adding disturbances, the EKF offers better performance over the UKF for higher modes, $N \geq 5$. Unlike the heat equations, the linear wave equation experiences a slight drop in the performance when the sliding mode is added to the EKF and the system is undisturbed. However, Figure 2.15 indicates that when a disturbance is present, the modified SMO has less estimation error than either the EKF or the UKF. This is also illustrated by Figure 2.16 and Table 2.4 where the errors with different observers is shown for the approximation order $N = 5$.

A nonlinear wave equation, which models the behavior of the one-layer shallow water waves in a channel of length L_0 is

$$\begin{aligned} \frac{\partial \eta}{\partial t} &= -H\frac{\partial v}{\partial x} - \eta\frac{\partial v}{\partial x} - v\frac{\partial \eta}{\partial x} \quad 0 < x < L_0, t \geq 0 \\ \frac{\partial v}{\partial t} &= -g\frac{\partial \eta}{\partial x} - v\frac{\partial v}{\partial x} - c_d v + g(x)\xi(t) \end{aligned} \tag{2.64}$$

where v is the velocity and η is the height of the water with respect to the steady level H [87]. Parameters H and L_0 are given in Table 2.3. The boundary conditions are

$$v(0,t) = v(L_0,t) = 0.$$

The linearization of the nonlinear wave equation about the zero equilibrium point is

$$\begin{aligned} \frac{\partial \eta}{\partial t} &= -H\frac{\partial v}{\partial x} \quad 0 < x < L_0, t \geq 0 \\ \frac{\partial v}{\partial t} &= -g\frac{\partial \eta}{\partial x} - c_d v + g(x)\xi(t). \end{aligned} \tag{2.65}$$

The eigenvalues of this linear system are

$$\gamma_k = -c_d \pm \frac{1}{2} i \sqrt{4\frac{4k^2\pi^2 g^2 H^2}{L_0^2} - c_d^2}.$$

The eigenvalues have a fixed negative real part, and since the spectrum determined growth assumption holds for this system, it is exponentially stable [86].

In the simulations, the initial condition is

$$v(x,0) = \operatorname{sech}(0.5L_0(x - 0.5L_0)), \quad \eta(x,0) = 0,$$

and the observer's initial conditions are both zero. The observations are

$$y_v = \int_{x=0}^{L_0} \operatorname{sech}(15(x - 0.4L_0))v(t,x)\,dx,$$

$$y_\eta = \int_{x=0}^{L_0} \operatorname{sech}(15(x - 0.4L_0))\eta(t,x)\,dx.$$

Furthermore, the disturbance term is chosen such that the physical constraints are satisfied as

$$g(x) = \operatorname{sech}(15(x - 0.4L_0)), \quad \xi(t) = \sin(10t).$$

Before approximating the PDEs by ODEs, the variables of equation (2.64) are scaled as

$$\bar{\eta} = \frac{\eta}{H}, \quad \bar{v} = \frac{v}{\sqrt{gH}}, \quad \bar{x} = \frac{x}{L_0}.$$

The new governing partial differential equations are then transformed into the ODEs using a Galerkin method with $\sin(k\pi x/L_0)$ basis functions for v and $\cos(k\pi x/L_0)$ for η. The observer initial condition is $\hat{z}(0,z) = 0$. Other observers' parameters are chosen as, for the EKF,

$$\boldsymbol{P_\nu} = 0.001\boldsymbol{I}_{n\times n}, \quad \boldsymbol{P}_\omega = 10,$$

$$a = 1.5, \quad \boldsymbol{P}_{\boldsymbol{z}_0} = \boldsymbol{0}_{n\times n},$$

for the UKF,

$$\boldsymbol{P_\nu} = 0.01\boldsymbol{I}_{n\times n}, \quad \boldsymbol{P}_\omega = 0.01,$$

$$\alpha = 0.001, \quad \kappa = 0, \quad \beta = 2, \quad \boldsymbol{P}_{\boldsymbol{z}_0} = 1e-6I_{n\times n}$$

and, for the modified SMO,

$$\boldsymbol{P_\nu} = 0.001\boldsymbol{I}_{n\times n}, \quad \boldsymbol{P}_\omega = 10,$$

$$a = 1.5, \quad \boldsymbol{P}_{\boldsymbol{z}_0} = \boldsymbol{0}_{n\times n}, \quad \lambda_1 = 1.$$

In the estimation of the nonlinear wave equation, the error dynamics were unstable with both versions of Kalman filtering. To overcome this problem, for the EKF, the modes whose amplitudes are greater than one were set to zero at every sampling time step. In addition, the covariance matrix was set to a value that makes the linear part of ODEs stable. For the UKF, first, the profile of the water's height and velocity is derived; if the maximum value of a profile is greater than one, it is scaled down by the maximum value; however, the estimation error is calculated based on the original estimation in both cases.

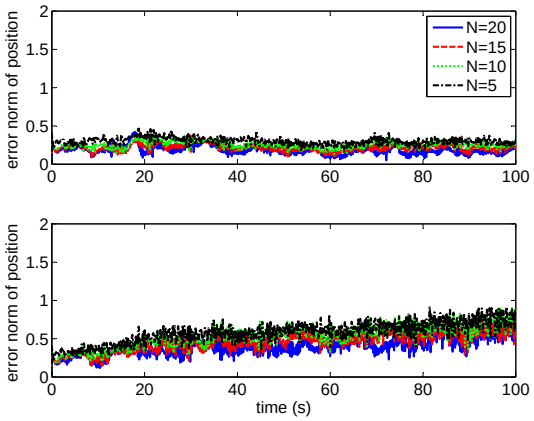

Figure 2.17: Estimation error of the EKF against time when applied to the nonlinear wave equation with different orders of approximation N. The top plot shows the results in the absence of a disturbance and the bottom plot the results when there is an unknown disturbance. In the absence of disturbance, the error is the same for all the N. When a disturbance is present, the error grows over time.

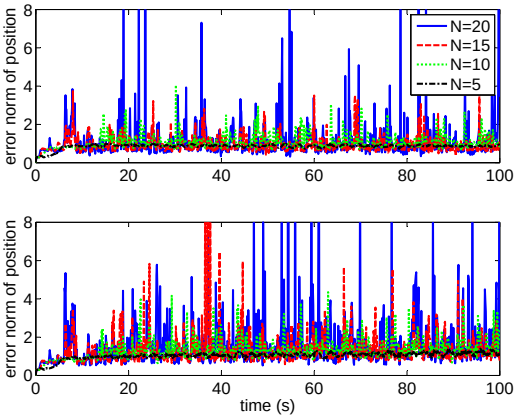

Figure 2.18: Estimation error of the UKF against time when applied to the nonlinear wave equation with different orders of approximation N. The top plot shows the results in the absence of a disturbance and the bottom plot the results when there is an unknown disturbance. In the absence of disturbance, the error is large and the same for all the N; however, more oscillation in the error profile is observed for smaller N. When a disturbance is present, the error grows in average over time and shows even more oscillation.

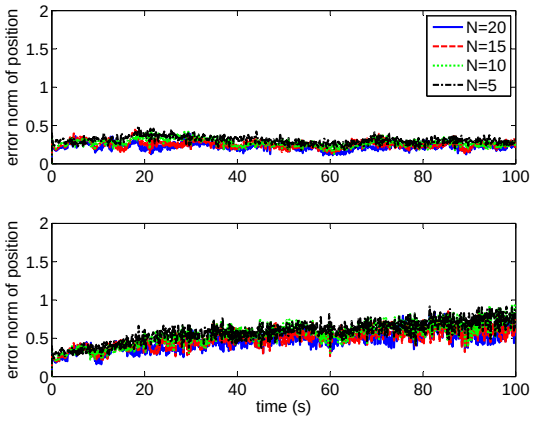

Figure 2.19: Estimation error of the modified SMO against time when applied to the nonlinear wave equation with different orders of approximation N. The top plot shows the results in the absence of a disturbance and the bottom plot the results when there is an unknown disturbance. In the absence of disturbance, the error is the same for all the N. When a disturbance is present, the error grows over time. The same performance as the EKF can be detected.

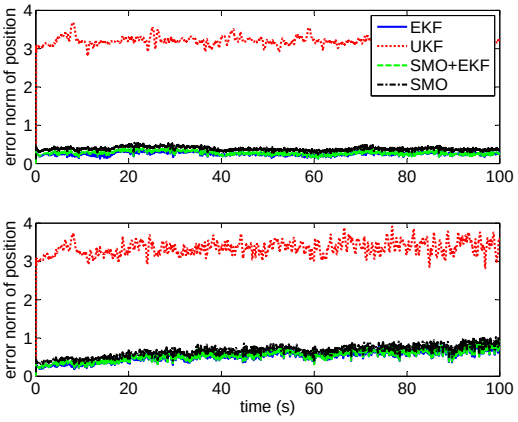

Figure 2.20: Comparison of the different estimation methods, the EKF, UKF, and modified SMO in estimating the state vector of the nonlinear wave equation for the order of approximation $N = 10$. The top plot shows the results in the absence of a disturbance and the bottom plot the results when there is an unknown disturbance.

Table 2.4: Estimation error for different observation methods after transient period.

		Undisturbed			Disturbed		
	Method	Run time	Error max	Error min	Run time	Error max	Error min
Linear heat	EKF	77.6289	0.0022	1.6570e-05	135.4456	0.3227	0.0295
	UKF	114.9613	0.0075	5.7367e-05	184.2440	0.3975	0.0505
	SMO	82.0645	0.0053	2.8478e-05	193.6996	0.0480	2.3187e-04
Quasi-linear heat	EKF	200.6813	0.0053	8.5963e-06	207.3505	0.0886	0.0093
	UKF	246.0649	0.0086	6.2819e-05	255.1652	0.3562	0.0590
	SMO-EKF	102.7612	0.0060	1.1006e-04	117.8632	0.0190	0.0019
	SMO	69.4914	0.0090	6.2597e-05	73.3460	0.0491	0.0031
Nonlinear heat	EKF	168.2633	0.0019	1.1318e-05	177.9907	0.0566	0.0025
	UKF	209.0683	0.0060	3.9765e-05	215.6899	0.1797	0.0111
	SMO-EKF	178.3828	0.0036	2.2721e-05	186.0943	0.0138	7.7844e-05
	SMO	167.7243	0.0053	6.2597e-05	177.4914	0.0532	9.1899e-04
Linear wave	EKF	255.9711	0.3171	0.0110	259.0665	1.2860	0.2801
	UKF	672.1987	0.2615	0.0054	649.3558	6.5160	0.7668
	SMO	809.1518	0.3257	0.0188	475.2380	0.3255	0.0187
Nonlinear wave	EKF	8340.0319	0.4111	0.1239	8558.0329	0.9015	0.1939
	UKF	11109.3265	3.6790	3.0270	11329.8198	3.9110	3.0270
	SMO-EKF	9229.8942	0.4339	0.1266	8391.4789	0.9309	0.2099
	SMO	8307.7356	0.5349	0.2260	7553.0863	1.0310	0.3354

The simulation results are shown in Figures 2.17, 2.18 and 2.19. A comparison of the different observation techniques applied to the nonlinear wave equation can be found in Figure 2.20 and Table 2.4 for the order of approximation $N = 10$. For the UKF, the error does not seem to be converging to zero as the approximation order decreases. For the EKF and modified SMO, the error decreases slightly as the order of approximation increases. Other simulations with a linearized version of of the shallow wave equations (2.64) showed the estimation error converging to zero with increasing approximation order. Therefore, the errors in each method are likely due to the effect of the nonlinearity on estimation. Finally, according to Figure 2.20, the modified SMO does not improve the estimation error over that of the EKF, even when disturbances are present.

2.6 Conclusions

The theoretical contribution of this chapter is a modified SMO. Unlike the standard versions of the SMO, the modified version can take care of both nonlinearities and disturbances coming from an unknown input. This modified SMO provided the possibility of combining an exponential stabilizing nonlinear observer with sliding mode observation to increase the estimation performance. The exponential convergence of the estimation error to zero is shown in Theorem 2.3.15. Simulation results indicated a better performance of this method over other filtering methods and, in particular, the standard SMO in the case of the heat equation.

The fluctuation observed in error profiles is partly coming from the fact that the designed observers are based on a prediction-correction algorithm; thus, discontinuity or even chattering is quite usual. In fact, the modified SMO provides the possibility of using smaller sliding gains, which leads to less chattering. On the other hand, as mentioned before, unlike sliding mode control, chattering is not an issue in observer design as long as it does not increase the computation time. Table 2.4 shows that this time does not increase significantly.

A major focus of this chapter was to compare different estimation methods for a variety of distributed parameter systems. The state estimation of three different diffusion equations and two wave equations was considered: a linear, a quasi-linear, and a nonlinear diffusion equation as well as a linear and a nonlinear wave equation. In all the examples, measurement was localized around a single point. Different methods, the EKF, UKF and a modified version of the SMO, were implemented to estimate the states. The simulations were run for each model and estimator without any external input and for situations with an unknown external disturbance. In the simulations, the order of approximation used to design the observer was smaller than the order used in the simulation of the "true" system in order to simulate the effect of the neglected modes. Therefore, the error was expected to be only bounded since a part of the system model was omitted in the observer dynamics. In the absence of any unknown input, the pattern of increasing error by decreasing the order of approximation is observed. The reason for this can be observed from the proof of Theorem 2.4.2. Increasing the order of approximation results in a closer approximation to the true system and thus less estimation error.

The estimation error tends to be less and converges to zero faster for the various versions of the heat equation than for the wave equation. This is a consequence of the qualitative difference between the two types of partial differential equations. The

eigenvalues of the linear heat equation are negative real, converging to minus infinity along the negative real axis. Also, most of the energy of the solution is concentrated in the first few modes. The influence of modes beyond the first few is negligible so the error induced by a lumped approximation is quite small. On the other hand, the real part of the eigenvalues of the wave equation do not converge to minus infinity and the energy is spread over all modes. Error due to neglecting the higher modes is much more significant for the wave equation.

For the undisturbed heat equation, the EKF and the UKF showed almost the same performance. In the case of the wave equation, the UKF provided a better performance over the other two methods for the linear case and worse for the nonlinear equation. When a disturbance is present, the EKF performed better than the UKF, and the modified SMO performed better than both UKF and EKF in the case of the heat equations. The modeling error can be regarded as a disturbance, and the success of the nonlinear SMO suggests that it will be preferable for handling errors due to modelling and truncation of higher order modes. Adding the sliding mode term did not change the observer's performance when there was a disturbance. Future work will consider this issue further.

The UKF was satisfactory for the heat and linear wave equations. However, the UKF did not converge for the undisturbed nonlinear wave equations. The UKF is based on searching for new sample points in a neighbourhood of the available estimate vector; the geometry of this neighbourhood is defined by the covariance matrix eigenvalues. The samples calculated by the UKF might fail to lie in the region of attraction when applied to the nonlinear wave equations.

Disturbances worsen the effect of neglecting higher modes (or equivalently, using a lumped model). Since the modeling error due to approximating the equation is very small for the heat equation, it is not surprising that the modified SMO performs as well for the heat equation examples as it does for lumped systems. The error improvement provided by SMO is less for the wave equation. There are several possible reasons for this. This may be because the nonlinear part of the nonlinear wave equation is unbounded so an assumption of Theorem 2.3.15 is not satisfied. Also, as noted above, the energy in the neglected modes may be significant.

A general observation can be made that for systems without disturbances, the EKF was generally better, and even for the examples where UKF was superior, EKF performance was adequate. For systems with disturbances, the modified SMO (with EKF) exhibited the smallest error in most of the cases. A useful conclusion of the comparison was that UKF cannot be applied to the nonlinear wave equation even for high orders

of approximation. Furthermore, it was shown that the importance of disturbance is greater in the case of the wave equation than heat equation; A more expensive observer is required which will be considered in future works.

As mentioned previously, the modeling error is an extra source of disturbance that can be compensated by an exponential convergent observer. Unlike the robust observers, the modified SMO provides exponential convergence which leads to reducing the error coming from model approximation error. In addition, the employed EKF is a modified version with the increased rate of convergence as required.

In the next chapter, the convergence result given by Lemma 2.4.1 and Theorem 2.4.2 is extended to a class of nonlinear DPSs for the EKF. It will be proved that under some conditions they are still satisfied when $M, N \to \infty$. In other words, the EKF observer's well-posedness along with its convergence results will be proved.

Chapter 3

Well-posedness of two classes of nonlinear systems

In the previous chapter, comparison studies between different estimation techniques were conducted. The EKF presented efficient results even in existence of external disturbances. Furthermore, it was shown that the estimation error decreases as the order of approximation increases. These results motivate the idea that the EKF can be designed for the DPSs. In this chapter, the well-posedness and finite-dimensional approximation of two general classes of infinite-dimensional systems are investigated. These forms will be used later to introduce a low-order model for electrochemical equations via which an adaptive EKF will be improved.

3.1 Introduction and literature review

Observer design for linear DPSs has been well studied; see for instance [88, 89, 90, 91, 92, 93, 94, 95], and [86]. However, it has not been well explored for nonlinear DPSs. Observer design for a general form of DPSs can be categorized into early lumping and late lumping techniques. In the early lumping observer design, the system is first approximated by some finite-dimensional representation; next, an observer is designed for the resultant finite-dimensional approximate system. Some examples are the robust fuzzy technique and robust adaptive observer proposed for quasi-linear DPSs respectively in [96] and [97]. Other examples can be found in [98] and [99].

Unlike early lumping, in the late lumping techniques, the finite-dimensional approximation is applied after the observer is designed. In some work, the output measurement

is assumed to be available or can be constructed as a spatially distributed function of the space variable. For instance, in [100], a second order sliding mode observer is employed to provide stability with the assumption that the measurement is available everywhere. In [101], the observer dynamic is corrected by a linear output error injection term via a constructed spatially distributed measurement. Distributed linear output injection is also proposed in [102] for a one-dimensional nonlinear Burgers equation. In fact, the measurement is not often available in sufficient detail. In most applications, not only is the system nonlinear, but also the measurements are only available as a vector of finite dimension.

As an abstract form of late lumping nonlinear observer design, in [103], augmenting a copy of the system's dynamics with a nonlinear feedback term is studied on a reflexive Banach space. Extending the maximum likelihood technique to a general class of nonlinear DPSs is used in [104]. This maximization is operated via dynamic programming and leads to a distributed-parameter Hamilton-Jacobi equation. Similarly, in [105], the distributed Hamilton-Jacobi equation is derived by minimizing a cost function and is approximated by some simpler form. Observer design based on optimization is also used in [106] to construct a PDE for filtering gain for a specific form of DPSs.

More examples include [107] and [108] wherein a backstepping observer is designed for the linearized system around some set points. Nonlinear observer design for a specific class of hyperbolic systems is considered in [109], where an operator-based linear matrix inequality problem must be solved. A similar approach is proposed in [110] for a class of quasi-linear parabolic systems. Another example not based on feedback design can be found in [111].

In this research, observer design via early lumping technique is considered. In other words, the system's representation needs to be approximated by a finite-dimensional version first. In this chapter, the well-posedness of two classes of nonlinear DPSs is studied. More importantly, the finite-dimensional approximation of these two forms of systems as well as the convergence of the approximate system are developed. The objective of these studies is to introduce a low-order model for observer design.

3.2 Quasi-linear systems

In this section, a class of nonlinear infinite-dimensional systems is introduced for which an EKF is to be designed. The system is assumed to be disturbed by some external unknown input. Under some conditions on the external input, the well-posedness of the

introduced system is investigated. Furthermore, the approximation of the system by an infinite-dimensional form is studied. To begin with, some basic definitions required to identify the system and its properties are introduced.

Definition 3.2.1. *(Locally Lipschitz Continuous Function)*
Let $\mathcal{B}_1$ and $\mathcal{B}_2$ be normed linear spaces. An operator $\boldsymbol{\mathcal{J}}(.) : \mathcal{B}_1 \to \mathcal{B}_2$ is called locally Lipschitz continuous if for every $\boldsymbol{w} \in \mathcal{B}_1$, there exists a neighborhood $\mathcal{N}$ and $L_{\boldsymbol{\mathcal{J}}} \in \mathbb{R}^+$ so that

$$\|\boldsymbol{\mathcal{J}}(\boldsymbol{w}_1) - \boldsymbol{\mathcal{J}}(\boldsymbol{w}_2)\|_{\mathcal{B}_2} \leq L_{\boldsymbol{\mathcal{J}}} \|\boldsymbol{w}_1 - \boldsymbol{w}_2\|_{\mathcal{B}_1}$$

for all $\boldsymbol{w}_1, \boldsymbol{w}_2 \in \mathcal{N}$.

Definition 3.2.2. *(Globally Lipschitz Continuous Function)*
Let $\mathcal{B}_1$ and $\mathcal{B}_2$ be normed spaces. An operator $\boldsymbol{\mathcal{J}}(.) : \mathcal{B}_1 \to \mathcal{B}_2$ is called globally Lipschitz continuous if there exists $L_{\boldsymbol{\mathcal{J}}} \in \mathbb{R}^+$ so that

$$\|\boldsymbol{\mathcal{J}}(\boldsymbol{w}_1) - \boldsymbol{\mathcal{J}}(\boldsymbol{w}_2)\|_{\mathcal{B}_2} \leq L_{\boldsymbol{\mathcal{J}}} \|\boldsymbol{w}_1 - \boldsymbol{w}_2\|_{\mathcal{B}_1}$$

for $\boldsymbol{w}_1, \boldsymbol{w}_2 \in \mathcal{B}_1$.

Definition 3.2.3. *(Fréchet Differentiability, [112, Defenition 9.4.1])*
Let $\mathcal{B}_1$ and $\mathcal{B}_2$ be normed linear spaces. An operator $\boldsymbol{\mathcal{J}} : \mathcal{D}(\boldsymbol{\mathcal{J}}) \subset \mathcal{B}_1 \to \mathcal{B}_2$ is Fréchet differentiable at $\boldsymbol{w} \in \mathcal{B}_1$ if there exists a bounded linear operator $\boldsymbol{D\mathcal{J}}(\boldsymbol{w}) : \mathcal{B}_1 \to \mathcal{B}_2$ such that

$$\lim_{\|\boldsymbol{h}\|_{\mathcal{B}_1} \to 0} \frac{\|\boldsymbol{\mathcal{J}}(\boldsymbol{w} + \boldsymbol{h}) - \boldsymbol{\mathcal{J}}(\boldsymbol{w}) - \boldsymbol{D\mathcal{J}}(\boldsymbol{w})\boldsymbol{h}\|_{\mathcal{B}_2}}{\|\boldsymbol{h}\|_{\mathcal{B}_1}} = 0$$

for every $\boldsymbol{h} \in \mathcal{B}_1$. It is Fréchet differentiable if it is Fréchet differentiable for every $\boldsymbol{w} \in \mathcal{D}(\boldsymbol{\mathcal{J}})$.

Definition 3.2.4. *[113] Let $\mathcal{B}_1$ and $\mathcal{B}_2$ be normed linear spaces. An operator $\boldsymbol{\mathcal{J}} : \mathcal{D}(\boldsymbol{\mathcal{J}}) \subset \mathcal{B}_1 \to \mathcal{B}_2$ is monotonic if for every $\boldsymbol{w}_1, \boldsymbol{w}_2 \in \mathcal{D}(\boldsymbol{\mathcal{J}})$ and $\alpha_0 \in \mathbb{R}^+$,*

$$\|\boldsymbol{w}_2 - \boldsymbol{w}_1 + \alpha_0 \boldsymbol{\mathcal{J}}(\boldsymbol{w}_2 - \boldsymbol{w}_1)\|_{\mathcal{H}} \geq \|\boldsymbol{w}_2 - \boldsymbol{w}_1\|_{\mathcal{H}}.$$

The operator is m-monotonic if $\mathcal{D}((\boldsymbol{\mathcal{I}} + \alpha_0 \boldsymbol{\mathcal{J}})^{-1}) = \mathcal{B}_1$.

The dynamical system considered in these studies is a semi-linear parabolic PDE. Let the state space be a separable Hilbert space $\mathcal{H}$. Suppose the state vector be denoted by $\boldsymbol{z} \in \mathcal{H}$. The system is

$$\begin{aligned} &\frac{\partial \boldsymbol{z}}{\partial t} + \boldsymbol{\mathcal{A}}\boldsymbol{z} = \boldsymbol{\mathcal{R}}(\boldsymbol{z}) + \boldsymbol{\mathcal{F}}\boldsymbol{u}(t) + \boldsymbol{\mathcal{G}}\xi(t) \\ &y(t) = \mathcal{C}\boldsymbol{z} = (\boldsymbol{c}, \boldsymbol{z})_{\mathcal{H}} \end{aligned} \tag{3.1}$$

where $\boldsymbol{x} \in \mathbb{R}^m$ is the spatial variable, $\boldsymbol{\mathcal{A}} : \mathcal{D}(\boldsymbol{\mathcal{A}}) \subset \mathcal{H} \to \mathcal{H}$ is a linear operator, $\boldsymbol{\mathcal{R}} : \mathcal{H} \to \mathcal{H}$ is a Fréchet differentiable nonlinear operator which satisfies $\boldsymbol{\mathcal{R}}(\mathbf{0}) = 0$, $\boldsymbol{\mathcal{F}} : \mathbb{R} \to \mathcal{H}$ is the input operator and linear bounded, $\boldsymbol{\mathcal{G}} : \mathbb{R} \to \mathcal{H}$ is the disturbance operator and linear bounded, $u \in \mathbb{R}$ is the input signal, $\xi \in \mathbb{R}$ is the disturbance input, $y \in \mathbb{R}$ is the output, $\boldsymbol{c} \in \mathcal{H}$, and $\mathcal{C} : \mathcal{H} \to \mathbb{R}$ is the output operator and linear bounded. The initial condition is

$$\boldsymbol{z}(0, \boldsymbol{x}) = \boldsymbol{z}_0 \in \mathcal{H}. \tag{3.2}$$

The following assumptions are made for the system (3.1).

Assumption 3.2.5. *The control input $\boldsymbol{u}(t)$ and the unknown input $\xi(t)$ are continuous in time and of bounded variation. In addition, there exist some $M_\xi \in \mathbb{R}^+$ and $M_u \in \mathbb{R}^+$ such that $|\xi(t)| \leq M_\xi$ and $|\boldsymbol{u}(t)| \leq M_u$.*

Assumption 3.2.6. *The operator $\boldsymbol{\mathcal{A}}$ is assumed to be a self-adjoint closed operator with a compact inverse $\boldsymbol{\mathcal{A}}^{-1}$. It has also dense domain in Hilbert space $\overline{\mathcal{D}(\boldsymbol{\mathcal{A}})} = \mathcal{H}$ and is assumed to be positive such that $(\boldsymbol{\mathcal{A}}\boldsymbol{w}, \boldsymbol{w})_{\mathcal{H}} \geq \kappa \|\boldsymbol{w}\|^2$ for every $\boldsymbol{w} \in \mathcal{D}(\boldsymbol{\mathcal{A}})$ and some $\kappa > 0$.*

Assumption 3.2.7. *The nonlinear operator $\boldsymbol{\mathcal{R}}(.)$ is Lipschitz continuous on the Hilbert space $\mathcal{H}$. In other words, for every $\boldsymbol{w}_1, \boldsymbol{w}_2 \in \mathcal{H}$, there exist a positive constant $L_R \in \mathbb{R}^+$ such that*

$$\|\boldsymbol{\mathcal{R}}(\boldsymbol{w}_1) - \boldsymbol{\mathcal{R}}(\boldsymbol{w}_2)\|_{\mathcal{H}} \leq L_R \|\boldsymbol{w}_1 - \boldsymbol{w}_2\|_{\mathcal{H}}.$$

The linear operator $\boldsymbol{\mathcal{A}}$ can also be used to define a new Hilbert space with more smoothness properties. Before the normed space of interest can be defined, the concept of evolution triple and duality pairing are introduced first. This definition will be used in next section to prove the well-posedness of the observer equations.

Definition 3.2.8. *(Duality Pairing, [114, Definition 3.4.3])*
Let $\mathcal{V} \subseteq \mathcal{H}$ be a linear space whose dual space is denoted by $\mathcal{V}'$. The triple $(\mathcal{V}, \mathcal{H}, \mathcal{V}')$ is called an evolution triple if it satisfies the following conditions:

- *the linear space $\mathcal{V}$ is a separable and reflexive Banach space.*
- *the linear space $\mathcal{H}$ is a separable Hilbert space.*
- *For $\mathcal{V} \subseteq \mathcal{H} \subseteq \mathcal{V}'$, $\mathcal{V}$ is dense and continuously embedded in $\mathcal{H}$.*

The duality pairing between $\mathcal{V}$ and $\mathcal{V}'$ is denoted by $\langle .,. \rangle_{\mathcal{V}',\mathcal{V}}$ and defined as a continuous extension of the inner product on the Hilbert space $\mathcal{H}$, denoted by $(.,.)_{\mathcal{H}}$.

From Assumption 3.2.6, it is evident that $\boldsymbol{\mathcal{A}}$ is positive definite. Moreover, since the operator $\boldsymbol{\mathcal{A}}$ is self-adjoint, also $\boldsymbol{\mathcal{A}}^{1/2}$ is well-defined positive definite operator; thus it is possible to define a Hilbert space $\mathcal{V} = \mathcal{D}(\boldsymbol{\mathcal{A}}^{1/2})$ with norm $\|\boldsymbol{\mathcal{A}}^{1/2}.\|_{\mathcal{H}}$. With this setting, $\mathcal{V}$ is dense in the Hilbert space $\mathcal{H}$ and $\boldsymbol{\mathcal{A}}^{1/2}$ defines an isomorphism between $\mathcal{V}$ and $\mathcal{H}$ since it is a bounded linear operator from $\mathcal{V}$ to $\mathcal{H}$ with bounded linear inverse from $\mathcal{H}$ to $\mathcal{V}$. Therefore, $(\mathcal{V}, \mathcal{H}, \mathcal{V}')$ is a evolution triple and a duality pairing can be defined as in Definition 3.2.8.

Furthermore, for every $w \in \mathcal{V}$,

$$(\boldsymbol{\mathcal{A}}^{1/2}., w)_{\mathcal{H}} : \mathcal{V} \to \mathbb{C}$$

is a linear functional with domain $\mathcal{V}$ dense in $\mathcal{H}$; thus, it can be extended uniquely to the Hilbert space $\mathcal{H}$ by Hahn-Banach theorem. This extension is the dual pairing between $\mathcal{V}$ and $\mathcal{V}'$. Respectively, from the definition of duality pairing, Definition 3.2.8, for $\boldsymbol{w}_1 \in \mathcal{H}$ and $\boldsymbol{w}_2, \boldsymbol{w}_3 \in \mathcal{V}$,

$$\begin{aligned} (\boldsymbol{w}_1, \boldsymbol{w}_2)_{\mathcal{H}} &= \langle \boldsymbol{w}_1, \boldsymbol{w}_2 \rangle_{\mathcal{V}',\mathcal{V}}, \\ (\boldsymbol{\mathcal{A}}^{1/2}\boldsymbol{w}_2, \boldsymbol{\mathcal{A}}^{1/2}\boldsymbol{w}_3)_{\mathcal{H}} &= \langle \boldsymbol{\mathcal{A}}\boldsymbol{w}_2, \boldsymbol{w}_3 \rangle_{\mathcal{V}',\mathcal{V}}. \end{aligned} \tag{3.3}$$

Next, the well-posedness of the system (3.1) is studied. The system (3.1) is a specific form of

$$\begin{aligned} &\frac{\partial \boldsymbol{z}}{\partial t} + \boldsymbol{\mathcal{A}}\boldsymbol{z} = \boldsymbol{\mathcal{E}}(t, \boldsymbol{z}), \\ &\boldsymbol{z}(0) = \boldsymbol{z}_0 \end{aligned} \tag{3.4}$$

where $\boldsymbol{\mathcal{E}} : [0, T] \times \mathcal{H} \to \mathcal{H}$ with $0 < T < \infty$ is a nonlinear operator that depends on both time t and the state vector $\boldsymbol{z}$.

Definition 3.2.9. *(Well-posedness)*
The system (3.4) is well-posed on a bounded time interval $[0, T]$ if for initial condition $\boldsymbol{z}_0 \in \mathcal{D}(\boldsymbol{\mathcal{A}})$, it has a unique solution $\boldsymbol{z} : [0, T] \to \mathcal{D}(\boldsymbol{\mathcal{A}})$ such that $\boldsymbol{z}$ is strongly continuous in t, $\boldsymbol{\mathcal{A}}\boldsymbol{z}$ is weakly continuous in t, and $\boldsymbol{z}$ satisfies (3.4) on $[0, T]$.

Theorem 3.2.10. *[115, Theorem 1]*
In (3.4), let $\boldsymbol{\mathcal{A}}$ be m-monotonic from its domain to the Hilbert space $\mathcal{H}$ (Definition 3.2.4). Given a bounded time interval $[0, T]$, suppose that for every $\boldsymbol{w}_1, \boldsymbol{w}_2 \in \mathcal{H}$ and $t_1, t_2 \in [0, T]$, $\boldsymbol{\mathcal{E}}(.)$ satisfies

$$\|\boldsymbol{\mathcal{E}}(t_1, \boldsymbol{w}_1) - \boldsymbol{\mathcal{E}}(t_2, \boldsymbol{w}_2)\|_{\mathcal{H}} \leq \|\boldsymbol{\mathcal{O}}(t_1) - \boldsymbol{\mathcal{O}}(t_2)\|_{\mathcal{H}} + L_0\|\boldsymbol{w}_1 - \boldsymbol{w}_2\|$$

where $\boldsymbol{\mathcal{O}}(.) : [0,T] \to \mathcal{H}$ is continuous and of bounded variation on $[0,T]$, and $L_0 \in \mathbb{R}^+$. Then, the system (3.4) is well-posed on the bounded time interval $[0,T]$ in the sense of Definition 3.2.9.

Corollary 3.2.11. *Let Assumption 3.2.5-3.2.7 be satisfied. For every initial condition $\boldsymbol{z}_0 \in \mathcal{H}$, the system (3.1) and (3.2) is well-posed on every bounded time interval $[0,T]$ in the sense of Definition 3.2.9.*

Proof. First, define

$$\boldsymbol{\mathcal{E}}(t,\boldsymbol{z}) = \boldsymbol{\mathcal{R}}(\boldsymbol{z}) + \boldsymbol{\mathcal{F}}\boldsymbol{u}(t) + \boldsymbol{\mathcal{G}}\xi(t).$$

From Assumptions 3.2.5 and 3.2.7 and the boundedness of $\boldsymbol{\mathcal{F}}$ and $\boldsymbol{\mathcal{G}}$, it can be concluded that $\boldsymbol{\mathcal{E}}(t,\boldsymbol{z})$ satisfies the conditions of Theorem 3.2.10. Since $\boldsymbol{\mathcal{A}}$ is positive definite by Assumption 3.2.6,

$$\begin{aligned}
&\|\boldsymbol{w}_2 - \boldsymbol{w}_1 + \alpha_0\boldsymbol{\mathcal{A}}(\boldsymbol{w}_2 - \boldsymbol{w}_1)\|_{\mathcal{H}} \\
&= (\|\boldsymbol{w}_2 - \boldsymbol{w}_1\|_{\mathcal{H}}^2 + 2(\boldsymbol{w}_2 - \boldsymbol{w}_1, \alpha_0\boldsymbol{\mathcal{A}}(\boldsymbol{w}_2 - \boldsymbol{w}_1))_{\mathcal{H}} + \|\alpha_0\boldsymbol{\mathcal{A}}(\boldsymbol{w}_2 - \boldsymbol{w}_1)\|_{\mathcal{H}}^2)^{1/2} \\
&\geq \|\boldsymbol{w}_2 - \boldsymbol{w}_1\|_{\mathcal{H}}.
\end{aligned}$$

Furthermore, from Assumption 3.2.6, $\mathcal{D}((\boldsymbol{\mathcal{I}}+\alpha_0\boldsymbol{\mathcal{A}})^{-1}) = \mathcal{H}$ for $\alpha_0 > 0$ as $\boldsymbol{\mathcal{A}}$ has compact inverse. This result along with Assumption 3.2.6 implies that $\boldsymbol{\mathcal{A}}$ and $\boldsymbol{\mathcal{E}}(t,\boldsymbol{z})$ satisfy the conditions of Theorem 3.2.10. Therefore, the system (3.1) with initial condition (3.2) admits a unique solution on a bounded time interval $[0,t_f]$ in the sense of Definition 3.2.9. □

Corollary 3.2.12. *Let Assumption 3.2.5-3.2.7 be satisfied. For every initial condition $\boldsymbol{z}_0 \in \mathcal{H}$, the solution to (3.1), $\boldsymbol{z}$, is bounded on every bounded time interval $[0,T]$. In other words, for every $\boldsymbol{z}_0 \in \mathcal{H}$ and bounded time interval, there exist $M_z \in \mathbb{R}^+$ such that $\|\boldsymbol{z}\|_{\mathcal{H}} \leq M_z$.*

Proof. The boundedness of the solution is the direct result of Corollary 3.2.11 according to which the solution $\boldsymbol{z}$ is continuous in time. As a result, it is bounded on any bounded and closed time interval $[0,T]$. □

Now, a new representation for the system (3.1) is introduced. It is of particular interest since it can be used to approximate the system with a finite-dimensional one. In this representation, the system dynamics is decomposed into two parts. Since the

Hilbert space is separable, a basis $\{\boldsymbol{v}_i\}_{i=1}^{\infty}$ can be chosen for the Hilbert space $\mathcal{H}$. Now, define the Hilbert space

$$\mathcal{H}_N = \text{span}\{\boldsymbol{v}_k, k = 1 \dots N\}.$$

For $\boldsymbol{z} \in \mathcal{H}$, the orthogonal projection of the Hilbert space $\mathcal{H}$ onto $\mathcal{H}_N$ is defined by

$$\boldsymbol{\mathcal{P}}_N \boldsymbol{z} = \sum_{i=1}^{N} z_i \boldsymbol{v}_i \tag{3.5}$$

where $z_i \in \mathbb{R}$. Let the state vector be decomposed into two parts:

$$\boldsymbol{z} = \boldsymbol{z}_N + \boldsymbol{z}_N^c \tag{3.6}$$

with

$$\boldsymbol{z}_N = \boldsymbol{\mathcal{P}}_N \boldsymbol{z}, \tag{3.7}$$
$$\boldsymbol{z}_N^c = (\boldsymbol{\mathcal{I}} - \boldsymbol{\mathcal{P}}_N)\boldsymbol{z}. \tag{3.8}$$

Define

$$\begin{aligned} \boldsymbol{\mathcal{A}}_N \boldsymbol{z} &= \boldsymbol{\mathcal{P}}_N \boldsymbol{\mathcal{A}} \boldsymbol{z}, & \boldsymbol{\mathcal{A}}_N^c \boldsymbol{z} &= (\boldsymbol{\mathcal{I}} - \boldsymbol{\mathcal{P}}_N)\boldsymbol{\mathcal{A}} \boldsymbol{z} \\ \boldsymbol{\mathcal{R}}_N(\boldsymbol{z}) &= \boldsymbol{\mathcal{P}}_N \boldsymbol{\mathcal{R}}(\boldsymbol{z}), & \boldsymbol{\mathcal{R}}_N^c(\boldsymbol{z}) &= (\boldsymbol{\mathcal{I}} - \boldsymbol{\mathcal{P}}_N)\boldsymbol{\mathcal{R}}(\boldsymbol{z}) \\ \boldsymbol{\mathcal{G}}_N &= \boldsymbol{\mathcal{P}}_N \boldsymbol{\mathcal{G}}, & \boldsymbol{\mathcal{G}}_N^c &= (\boldsymbol{\mathcal{I}} - \boldsymbol{\mathcal{P}}_N)\boldsymbol{\mathcal{G}} \\ \boldsymbol{\mathcal{F}}_N &= \boldsymbol{\mathcal{P}}_N \boldsymbol{\mathcal{F}}, & \boldsymbol{\mathcal{F}}_N^c &= (\boldsymbol{\mathcal{I}} - \boldsymbol{\mathcal{P}}_N)\boldsymbol{\mathcal{F}}. \end{aligned}$$

The projection defined in equation (3.5) can be used to decompose (3.1) as

$$\frac{\partial \boldsymbol{z}_N}{\partial t} + \boldsymbol{\mathcal{A}}_N \boldsymbol{z} = \boldsymbol{\mathcal{R}}_N(\boldsymbol{z}) + \boldsymbol{\mathcal{F}}_N \boldsymbol{u}(t) + \boldsymbol{\mathcal{G}}_N \xi(t) \tag{3.9}$$
$$\frac{\partial \boldsymbol{z}_N^c}{\partial t} + \boldsymbol{\mathcal{A}}_N^c \boldsymbol{z} = \boldsymbol{\mathcal{R}}_N^c(\boldsymbol{z}) + \boldsymbol{\mathcal{F}}_N^c \boldsymbol{u}(t) + \boldsymbol{\mathcal{G}}_N^c \xi(t) \tag{3.10}$$
$$y(t) = \mathcal{C}\boldsymbol{z}_N + \mathcal{C}\boldsymbol{z}_N^c.$$

Given assumption 3.2.6, the eigenfunctions of the linear operator $\boldsymbol{\mathcal{A}}$ provides an orthogonal basis for the Hilbert space $\mathcal{H}$ [116, theorem VIII.6]. Since the operator $-\boldsymbol{\mathcal{A}}$ is negative definite, its eigenvalues λ_k can be arranged as

$$\dots \leq \lambda_k \leq \dots \leq \lambda_2 \leq \lambda_1 < 0$$

where $\lambda_k \to -\infty$ as $k \to \infty$. Also

$$(-\boldsymbol{\mathcal{A}}\boldsymbol{w}, \boldsymbol{w})_{\mathcal{H}} \leq \lambda_1 (\boldsymbol{w}, \boldsymbol{w})_{\mathcal{H}} \tag{3.11}$$

for every $\boldsymbol{w} \in \mathcal{D}(\boldsymbol{\mathcal{A}})$.

In order to find a finite-dimensional approximation for the system, the basis $\boldsymbol{v}_k$ for $k = 1, \ldots, \infty$ are chosen to be the eigenfunctions of $\boldsymbol{\mathcal{A}}$. Employing these eigenfunctions implies that

$$\boldsymbol{\mathcal{A}}_N \boldsymbol{z} = \boldsymbol{\mathcal{A}}_N \boldsymbol{z}_N, \quad \boldsymbol{\mathcal{A}}_N^c \boldsymbol{z} = \boldsymbol{\mathcal{A}}_N^c \boldsymbol{z}_N^c.$$

Let the state vector $\boldsymbol{z}$ be approximated by $\bar{\boldsymbol{z}}_N$. While the $\boldsymbol{z}_N$ is the solution to (3.9), $\bar{\boldsymbol{z}}_N$ satisfies the finite-dimensional system defined as

$$\begin{aligned} &\frac{\partial \bar{\boldsymbol{z}}_N}{\partial t} + \boldsymbol{\mathcal{A}}_N \bar{\boldsymbol{z}}_N = \boldsymbol{\mathcal{R}}_N(\bar{\boldsymbol{z}}_N) + \boldsymbol{\mathcal{F}}_N \boldsymbol{u}(t) + \boldsymbol{\mathcal{G}}_N \xi(t) \\ &y(t) = \boldsymbol{\mathcal{C}} \bar{\boldsymbol{z}}_N. \end{aligned} \tag{3.12}$$

The convergence of the solution to the approximate system to the true one in $\mathcal{L}^2$-norm can be found in [117]; the uniform convergence of $\bar{\boldsymbol{z}}_N$ to $\boldsymbol{z}$ as $N \to \infty$ is shown in the following theorem.

Theorem 3.2.13. *Let Assumption 3.2.5-3.2.7 be satisfied. For any finite time interval $[0, T]$, the dynamical equation (3.12) admits a unique solution $\bar{\boldsymbol{z}}_N$ converging to the solution of (3.1), $\boldsymbol{z}$, in $\mathcal{L}^\infty([0, T], \mathcal{H})$ as $N \to \infty$.*

Proof. First, following the same reasoning as in the proof of Corollary 3.2.11 shows that the system (3.12) satisfies the conditions of Theorem 3.2.10; therefore, it is well-posed on every bounded time interval $[0, T]$. Moreover, the system (3.1) also admits a unique solution $\boldsymbol{z} \in \text{Ł}^\infty([0, T]; \mathcal{H})$ according to Corollary 3.2.11 and 3.2.12.

The error dynamics between the approximate systems (3.12) and the original system (3.9) and (3.10) is

$$\frac{\partial (\boldsymbol{z}_N - \bar{\boldsymbol{z}}_N)}{\partial t} + \boldsymbol{\mathcal{A}}_N (\boldsymbol{z}_N - \bar{\boldsymbol{z}}_N) = \boldsymbol{\mathcal{R}}_N (\boldsymbol{z}_N + \boldsymbol{z}_N^c) - \boldsymbol{\mathcal{R}}_N (\bar{\boldsymbol{z}}_N) \tag{3.13}$$

$$\frac{\partial \boldsymbol{z}_N^c}{\partial t} + \boldsymbol{\mathcal{A}}_N^c \boldsymbol{z}_N^c = \boldsymbol{\mathcal{R}}_N^c (\boldsymbol{z}_N + \boldsymbol{z}_N^c) + \boldsymbol{\mathcal{F}}_N^c \boldsymbol{u}(t) + \boldsymbol{\mathcal{G}}_N^c \xi(t) \tag{3.14}$$

Define $\bar{\boldsymbol{e}}_N = \boldsymbol{z}_N - \bar{\boldsymbol{z}}_N$. The error between the approximate state $\bar{\boldsymbol{z}}_N$ and the original state $\boldsymbol{z}$ is

$$\boldsymbol{z} - \bar{\boldsymbol{z}}_N = \bar{\boldsymbol{e}}_N + \boldsymbol{z}_N^c.$$

Next, both sides of the equation (3.13) are multiplied by $\bar{\boldsymbol{e}}_N$ in the sense of $\mathcal{H}$ inner product;

$$\begin{aligned}\left(\frac{\partial \bar{\boldsymbol{e}}_N}{\partial t}, \bar{\boldsymbol{e}}_N\right)_{\mathcal{H}} + (\boldsymbol{\mathcal{A}}_N \bar{\boldsymbol{e}}_N, \bar{\boldsymbol{e}}_N)_{\mathcal{H}} = \\ + (\boldsymbol{\mathcal{R}}_N(\boldsymbol{z}_N + \boldsymbol{z}_N^c) - \boldsymbol{\mathcal{R}}_N(\bar{\boldsymbol{z}}_N), \bar{\boldsymbol{e}}_N)_{\mathcal{H}}.\end{aligned} \tag{3.15}$$

Similarly,

$$\begin{aligned}(\bar{\boldsymbol{e}}_N, \frac{\partial \bar{\boldsymbol{e}}_N}{\partial t})_{\mathcal{H}} + (\bar{\boldsymbol{e}}_N, \boldsymbol{\mathcal{A}}_N \bar{\boldsymbol{e}}_N)_{\mathcal{H}} = \\ + (\bar{\boldsymbol{e}}_N, \boldsymbol{\mathcal{R}}_N(\boldsymbol{z}_N + \boldsymbol{z}_N^c) - \boldsymbol{\mathcal{R}}_N(\bar{\boldsymbol{z}}_N))_{\mathcal{H}}.\end{aligned} \tag{3.16}$$

Adding (3.15) and (3.16) results in

$$\begin{aligned}\frac{d(\bar{\boldsymbol{e}}_N, \bar{\boldsymbol{e}}_N)_{\mathcal{H}}}{dt} + 2(\bar{\boldsymbol{e}}_N, \boldsymbol{\mathcal{A}}_N \bar{\boldsymbol{e}}_N)_{\mathcal{H}} = \\ + 2\mathrm{Re}(\bar{\boldsymbol{e}}_N, \boldsymbol{\mathcal{R}}_N(\boldsymbol{z}_N + \boldsymbol{z}_N^c) - \boldsymbol{\mathcal{R}}_N(\bar{\boldsymbol{z}}_N)).\end{aligned} \tag{3.17}$$

From the fact that $\boldsymbol{\mathcal{A}}$ is positive definite, inequality (3.11), Lipschitz continuity of $\boldsymbol{\mathcal{R}}_N(.)$ (Assumption 3.2.7), and Young's inequality, equation (3.17) becomes

$$\frac{d\|\bar{\boldsymbol{e}}_N(t)\|_{\mathcal{H}}^2}{dt} \leq 2\rho_1 \|\bar{\boldsymbol{e}}_N(t)\|_{\mathcal{H}}^2 + \|\boldsymbol{z}_N^c(t)\|_{\mathcal{H}}^2 \tag{3.18}$$

where

$$\rho_1 = \lambda_1 + L_R + \frac{L_R}{2}.$$

Integrating (3.18) leads to

$$\|\bar{\boldsymbol{e}}_N(t)\|_{\mathcal{H}}^2 \leq \|\bar{\boldsymbol{e}}_N(0)\|_{\mathcal{H}}^2 \exp(2\rho_1 t) + L_R \exp(2\rho_1 t) \int_0^t \exp(-2\rho_1 \tau) \|\boldsymbol{z}_N^c(\tau)\|_{\mathcal{H}}^2 d\tau. \tag{3.19}$$

Furthermore,

$$\bar{\boldsymbol{z}}_N(0) = \boldsymbol{\mathcal{P}}_N \boldsymbol{z}(0), \text{ and } \bar{\boldsymbol{e}}_N(0) = 0;$$

thus, (3.19) turns into

$$\|\bar{\boldsymbol{e}}_N(t)\|_{\mathcal{H}}^2 \leq L_R \exp(2\rho_1 t) \max_{\tau \in [0, t_f]} \int_0^{t_f} \|\boldsymbol{z}_N^c(\tau)\|_{\mathcal{H}}^2 d\tau. \tag{3.20}$$

Since the vector $\boldsymbol{z}$ is bounded on $[0, T]$ by Corollary 3.2.12, and

$$\boldsymbol{\mathcal{P}}_N \to \boldsymbol{\mathcal{I}} \text{ strongly in } \mathcal{L}(\mathcal{H}) \tag{3.21}$$

as $N \to \infty$ due to choice of basis, by Dominant Convergence Theorem,

$$\boldsymbol{z}_N^c(t) \to 0 \text{ strongly in } \mathcal{L}^2([0, T]; \mathcal{H}); \tag{3.22}$$

it is obtained from inequality (3.20) and (3.22) that

$$\bar{\boldsymbol{e}}_N(t) \to 0 \,\text{strongly in}\, \mathcal{L}^\infty([0,T];\mathcal{H}) \tag{3.23}$$

as $N \to \infty$.

As a result of (3.23) and (3.22),

$$\bar{\boldsymbol{z}}_N(t) \to \boldsymbol{z}(t) \,\text{strongly in}\, \mathcal{L}^\infty([0,T];\mathcal{H})$$

as $N \to \infty$, and the proof is completed. □

3.3 A more general form

In general, the electrochemical equations cannot be transformed to the form introduced in the previous section. In this section a more general form of DPSs which covers the battery equations is studied. Consider

$$\frac{\partial \boldsymbol{z}}{\partial t} = \boldsymbol{\mathcal{A}}\boldsymbol{\mathcal{N}}(\boldsymbol{z}) + \boldsymbol{\mathcal{R}}(\boldsymbol{z},t) + \boldsymbol{\mathcal{F}}\boldsymbol{u}(t) \tag{3.24}$$

where $\boldsymbol{\mathcal{R}}(.) : \mathcal{H} \to \mathcal{H}$ is a Fréchet differentiable nonlinear operator with respect to $\boldsymbol{z}$ and strongly continuous with respect to t that satisfies $\boldsymbol{\mathcal{R}}(\boldsymbol{0},t) = 0$ and $\boldsymbol{\mathcal{N}} : \mathcal{H} \to \mathcal{H}$ is a Fréchet differentiable nonlinear operator that satisfies $\boldsymbol{\mathcal{N}}(\boldsymbol{0})$. The operator $\boldsymbol{\mathcal{F}}$ is defined as in the previous section.

Definition 3.3.1. *(Strong solution, [117])*
The strong solution $\boldsymbol{z}$ to (3.24) is called a strong solution if

- *it is strongly continuous and differentiable in time for almost every $t \in [0,t_f]$ with respect to $\mathcal{H}$-norm topology,*
- *it satisfies $\boldsymbol{z}(0) = \boldsymbol{z}_0$ for the initial condition $\boldsymbol{z}_0 \in \mathcal{H}$,*
- *and it satisfies equation (3.24) for almost every $t \in [0,t_f]$.*

Assumption 3.3.2. *The nonlinear operator $\boldsymbol{\mathcal{N}}(.)$ is Fréchet differentiable and satisfies*

$$\begin{aligned} \epsilon_1 \leq & \|D\boldsymbol{\mathcal{N}}(\boldsymbol{w}_2)\| \leq \epsilon_2 \\ \epsilon_1\|\boldsymbol{w}_1\|_{\mathcal{H}}^2 \leq & (\boldsymbol{w}_1, D\boldsymbol{\mathcal{N}}(\boldsymbol{w}_2)\boldsymbol{w}_1)_{\mathcal{H}} = (D\boldsymbol{\mathcal{N}}(\boldsymbol{w}_2)\boldsymbol{w}_1, \boldsymbol{w}_1)_{\mathcal{H}} \leq \epsilon_2\|\boldsymbol{w}_1\|_{\mathcal{H}}^2 \end{aligned}$$

for every $\boldsymbol{w}_1, \boldsymbol{w}_2 \in \mathcal{H}$ and some $\epsilon_1, \epsilon_2 > 0$.

Assumption 3.3.3. *The linear operator $\boldsymbol{\mathcal{A}}$ and the nonlinear operator $\boldsymbol{\mathcal{N}}(.)$ satisfy*

$$(\boldsymbol{w}, \boldsymbol{\mathcal{A}}\boldsymbol{\mathcal{N}}(\boldsymbol{w}))_{\mathcal{H}} = (\boldsymbol{\mathcal{A}}\boldsymbol{\mathcal{N}}(\boldsymbol{w}), \boldsymbol{w})_{\mathcal{H}} \geq \epsilon_3 \|\boldsymbol{w}\|^2$$

for every $\boldsymbol{w} \in \mathcal{D}(\boldsymbol{\mathcal{A}}^{1/2})$ such tat $\boldsymbol{\mathcal{N}}(\boldsymbol{w}) \in \mathcal{D}(\boldsymbol{\mathcal{A}})$ and some $\epsilon_3 > 0$.

As before, the eigenfunctions $\boldsymbol{v}_i$ of the linear operator $\boldsymbol{\mathcal{A}}$ and the Galerkin method are used to decompose the system representation (3.24) into two parts. The orthonormal projection onto $\mathcal{H}_N$ is

$$\boldsymbol{\mathcal{P}}_N \boldsymbol{z} = \sum_{i=1}^{N} z_i \boldsymbol{v}_i.$$

Let the system's state be approximated by $\boldsymbol{z}_N = \boldsymbol{\mathcal{P}}_N \boldsymbol{z}$. The reduced order system is defined as

$$\frac{\partial \boldsymbol{z}_N}{\partial t} = \boldsymbol{\mathcal{A}}\boldsymbol{\mathcal{N}}_N(\boldsymbol{z}_N) + \boldsymbol{\mathcal{R}}_N(\boldsymbol{z}_N, t) + \boldsymbol{\mathcal{F}}_N \boldsymbol{u}(t) \tag{3.25}$$

where

$$\begin{aligned}
\boldsymbol{\mathcal{N}}_N(.) &= \boldsymbol{\mathcal{P}}_N \boldsymbol{\mathcal{N}}(.) \\
\boldsymbol{\mathcal{A}}_N &= \boldsymbol{\mathcal{P}}_N \boldsymbol{\mathcal{A}} \\
\boldsymbol{\mathcal{R}}_N(.) &= \boldsymbol{\mathcal{P}}_N \boldsymbol{\mathcal{R}}(.) \\
\boldsymbol{\mathcal{F}}_N &= \boldsymbol{\mathcal{P}}_N \boldsymbol{\mathcal{F}}.
\end{aligned}$$

The following Lemma shows the boundedness of the solution to (3.25).

Lemma 3.3.4. *Let the system (3.24) satisfy Assumption 3.2.5-3.2.7, 3.3.2, and 3.3.3. Suppose that $\boldsymbol{\mathcal{N}}(\boldsymbol{z}(x,0)) \in \mathcal{V}$. The solutions to (3.25) on every bounded time interval $[0, t_f]$ are bounded;*

$$\|\boldsymbol{z}_N(t)\|_{\mathcal{H}} \leq M_{c,0} \tag{3.26}$$

$$\|\boldsymbol{\mathcal{A}}^{1/2}\boldsymbol{\mathcal{N}}_N(\boldsymbol{z}_N(t))\|_{\mathcal{H}} \leq M_{c,1} \tag{3.27}$$

$$\int_0^{t_f} \|\boldsymbol{\mathcal{A}}\boldsymbol{\mathcal{N}}_N(\boldsymbol{z}_N(t))\|_{\mathcal{H}}^2 dt \leq M_{c,2} \tag{3.28}$$

$$\tag{3.29}$$

for $M_{c,0}, M_{c,1}, M_{c,2} \in \mathbb{R}^+$ independent of N.

Proof: First, from Assumption 3.3.2 and Mean value theorem [118][Theorem 7.6-1], it is concluded that $\boldsymbol{\mathcal{N}}(.)$ is Lipschitz continuous. In other words, for every $\boldsymbol{w}_1, \boldsymbol{w}_2 \in \mathcal{H}$ and some $L_{\mathcal{N}} > 0$,

$$\|\boldsymbol{\mathcal{N}}(\boldsymbol{w}_2) - \boldsymbol{\mathcal{N}}(\boldsymbol{w}_1)\|_{\mathcal{H}} \leq L_{\mathcal{N}} \|\boldsymbol{w}_2 - \boldsymbol{w}_1\|_{\mathcal{H}} \tag{3.30}$$

Note that

$$\boldsymbol{\mathcal{R}}(\boldsymbol{0}, t) = \boldsymbol{0}, \quad \boldsymbol{\mathcal{N}}(\boldsymbol{0}) = \boldsymbol{0}. \tag{3.31}$$

Furthermore, by Assumption 3.3.3,

$$(\boldsymbol{z}_N, \boldsymbol{\mathcal{A}}\boldsymbol{\mathcal{N}}_N(\boldsymbol{z}_N))_{\mathcal{H}} = (\boldsymbol{z}_N, \boldsymbol{\mathcal{A}}\boldsymbol{\mathcal{N}}(\boldsymbol{z}_N))_{\mathcal{H}} \geq 0. \tag{3.32}$$

Let both sides of (3.25) be multiplied by $\boldsymbol{w} \in \mathcal{H}$;

$$(\boldsymbol{w}, \frac{\partial \boldsymbol{z}_N}{\partial t})_{\mathcal{H}} + (\boldsymbol{w}, \boldsymbol{\mathcal{A}}\boldsymbol{\mathcal{N}}_N(\boldsymbol{z}_N))_{\mathcal{H}} = (\boldsymbol{w}, \boldsymbol{\mathcal{R}}_N(\boldsymbol{z}_N, t) + \boldsymbol{\mathcal{F}}_N \boldsymbol{u}(t))_{\mathcal{H}}. \tag{3.33}$$

Similarly,

$$\left(\frac{\partial \boldsymbol{z}_N}{\partial t}, \boldsymbol{w}\right)_{\mathcal{H}} + (\boldsymbol{\mathcal{A}}\boldsymbol{\mathcal{N}}_N(\boldsymbol{z}_N), \boldsymbol{w})_{\mathcal{H}} = (\boldsymbol{\mathcal{R}}_N(\boldsymbol{z}_N, t) + \boldsymbol{\mathcal{F}}_N \boldsymbol{u}(t), \boldsymbol{w})_{\mathcal{H}}. \tag{3.34}$$

Next, replacing $\boldsymbol{w}$ by $\boldsymbol{z}_N$ in (3.33) and (3.34) and adding the resulting equations yield

$$\frac{d\|\boldsymbol{z}_N\|_{\mathcal{H}}^2}{dt} + 2(\boldsymbol{\mathcal{A}}\boldsymbol{\mathcal{N}}_N(\boldsymbol{z}_N), \boldsymbol{z}_N)_{\mathcal{H}} = 2\mathrm{Re}(\boldsymbol{\mathcal{R}}_N(\boldsymbol{z}_N, t) + \boldsymbol{\mathcal{F}}_N \boldsymbol{u}(t), \boldsymbol{z}_N)_{\mathcal{H}}. \tag{3.35}$$

Employing (3.32) and the Lipschitz continuity (3.30), and (3.31) as well as using Cauchy Schwarz and Young's inequality in (3.35) leads to

$$\frac{d\|\boldsymbol{z}_N(t)\|_{\mathcal{H}}^2}{dt} \leq L_1 \|\boldsymbol{z}_N(t)\|_{\mathcal{H}}^2 + L_2^2 \tag{3.36}$$

where

$$L_1 = 2L_R + 1, \quad L_2 = \|\boldsymbol{\mathcal{F}}\| M_u$$

and M_u is the upper bound of $\boldsymbol{u}(t)$. Integrating inequality (3.36) results in

$$\|\boldsymbol{z}_N(t)\|_{\mathcal{H}}^2 \leq \|\boldsymbol{z}_N(0)\|_{\mathcal{H}}^2 \exp(L_1 t) + \frac{L_2(\exp(L_1 t) - 1)}{L_1} \leq M_{c,0} \tag{3.37}$$

for some $M_{c,0} > 0$.

Now, let both sides of (3.25) be first operated by $D\boldsymbol{\mathcal{N}}_N(\boldsymbol{z}_N)$, the Fréchet derivative of $\boldsymbol{\mathcal{N}}_N(.)$, and then multiplied by $\boldsymbol{\mathcal{AN}}_N(\boldsymbol{z}_N)$ in the sense of the inner product; it is derived from following the same procedure as before that

$$\begin{aligned}(\boldsymbol{\mathcal{AN}}_N(\boldsymbol{z}_N), D\boldsymbol{\mathcal{N}}_N(\boldsymbol{z}_N)\frac{\partial \boldsymbol{z}_N}{\partial t})_{\mathcal{H}} + (D\boldsymbol{\mathcal{N}}_N(\boldsymbol{z}_N)\frac{\partial \boldsymbol{z}_N}{\partial t}, \boldsymbol{\mathcal{AN}}_N(\boldsymbol{z}_N))_{\mathcal{H}} = \\ -2(\boldsymbol{\mathcal{AN}}_N(\boldsymbol{z}_N), D\boldsymbol{\mathcal{N}}_N(\boldsymbol{z}_N)\boldsymbol{\mathcal{AN}}_N(\boldsymbol{z}_N))_{\mathcal{H}} + \\ 2\mathrm{Re}(\boldsymbol{\mathcal{AN}}_N(\boldsymbol{z}_N), D\boldsymbol{\mathcal{N}}_N(\boldsymbol{z}_N)(\boldsymbol{\mathcal{R}}_N(\boldsymbol{z}_N, t) + \boldsymbol{\mathcal{F}}_N\boldsymbol{u}(t)))_{\mathcal{H}}.\end{aligned} \tag{3.38}$$

Note that from Fréchet differentiability of $\boldsymbol{\mathcal{N}}(.)$, for $\boldsymbol{h} \in \mathcal{H}$,

$$\frac{\|\boldsymbol{\mathcal{P}}_N(\boldsymbol{\mathcal{N}}(\boldsymbol{z}_N + \boldsymbol{h}) - \boldsymbol{\mathcal{N}}(\boldsymbol{z}_N) - D\boldsymbol{\mathcal{N}}(\boldsymbol{z}_N)\boldsymbol{h})\|_{\mathcal{H}}}{\|\boldsymbol{h}\|_{\mathcal{H}}} \to 0$$

when $\|\boldsymbol{h}\|_{\mathcal{H}} \to 0$; therefore,

$$D\boldsymbol{\mathcal{N}}_N(\boldsymbol{z}_N) = \boldsymbol{\mathcal{P}}_N D\boldsymbol{\mathcal{N}}(\boldsymbol{z}_N). \tag{3.39}$$

From (3.39) and the fact that $\boldsymbol{\mathcal{AN}}_N(\boldsymbol{z}_N) \in \mathcal{H}_N$, it is concluded that

$$(\boldsymbol{\mathcal{AN}}_N(\boldsymbol{z}_N), D\boldsymbol{\mathcal{N}}_N(\boldsymbol{z}_N)\boldsymbol{\mathcal{AN}}_N(\boldsymbol{z}_N))_{\mathcal{H}} = (\boldsymbol{\mathcal{AN}}_N(\boldsymbol{z}_N), D\boldsymbol{\mathcal{N}}(\boldsymbol{z}_N)\boldsymbol{\mathcal{AN}}_N(\boldsymbol{z}_N))_{\mathcal{H}},$$

and, from Assumption 3.3.2

$$-(\boldsymbol{\mathcal{AN}}_N(\boldsymbol{z}_N), D\boldsymbol{\mathcal{N}}_N(\boldsymbol{z}_N)\boldsymbol{\mathcal{AN}}_N(\boldsymbol{z}_N))_{\mathcal{H}} \leq -\epsilon_1\|\boldsymbol{\mathcal{AN}}_N(\boldsymbol{z}_N)\|^2_{\mathcal{H}}. \tag{3.40}$$

Similarly,

$$-(D\boldsymbol{\mathcal{N}}_N(\boldsymbol{z}_N)\boldsymbol{\mathcal{AN}}_N(\boldsymbol{z}_N), \boldsymbol{\mathcal{AN}}_N(\boldsymbol{z}_N))_{\mathcal{H}} \leq -\epsilon_1\|\boldsymbol{\mathcal{AN}}_N(\boldsymbol{z}_N)\|^2_{\mathcal{H}}. \tag{3.41}$$

Substituting (3.40) and (3.41) into (3.38) and employing Cauchy Schwarz inequality; Young's inequality; and Assumption 3.2.5, 3.2.7, and 3.3.2 in (3.38) lead to

$$\frac{d\|\boldsymbol{\mathcal{A}}^{1/2}\boldsymbol{\mathcal{N}}_N(\boldsymbol{z}_N(t))\|^2_{\mathcal{H}}}{dt} \leq -L_3\|\boldsymbol{\mathcal{AN}}_N(\boldsymbol{z}_N(t))\|^2_{\mathcal{H}} + L_4 \tag{3.42}$$

where

$$L_3 = 2\epsilon_1 - \beta_5, \quad L_4 = \frac{1}{\beta_5}(\beta_3 L_R M_{c,0} + \|\boldsymbol{\mathcal{F}}\|M_u)^2$$

and β_5, which comes from Young's inequality, is set such that $L_3 > 0$. Since

$$-L_3\|\boldsymbol{\mathcal{AN}}_N(\boldsymbol{z}_N)\|^2_{\mathcal{H}} < 0,$$

by integrating (3.42) and employing (3.37) on the bounded time interval $[0, t_f]$ the second boundedness result is achieved as

$$\|\boldsymbol{\mathcal{A}}^{1/2}\boldsymbol{\mathcal{N}}_N(\boldsymbol{z}_N(t))\|^2_{\mathcal{H}} \leq \|\boldsymbol{\mathcal{A}}^{1/2}\boldsymbol{\mathcal{N}}_N(\boldsymbol{z}_N(0))\|^2_{\mathcal{H}} + L_4 t_f \leq M_{c,1} \tag{3.43}$$

for $M_{c,1} \in \mathbb{R}^+$.

Integrating (3.42) and considering the boundedness given by (3.43) leads to

$$\int_0^{t_f} L_3 \|\boldsymbol{\mathcal{A}}\boldsymbol{\mathcal{N}}_N(\boldsymbol{z}_N(t))\|^2_{\mathcal{H}} dt \leq L_4 t_f + (\|\boldsymbol{\mathcal{A}}^{1/2}\boldsymbol{\mathcal{N}}_N(\boldsymbol{z}_N(0))\|^2_{\mathcal{H}} - \|\boldsymbol{\mathcal{A}}^{1/2}\boldsymbol{\mathcal{N}}_N(\boldsymbol{z}_N(t_f))\|^2_{\mathcal{H}}) \leq M_{c,2} \tag{3.44}$$

for some $M_{c,2} \in \mathbb{R}^+$. □

Theorem 3.3.5. *Let the assumptions of Theorem 3.3.4 be satisfied. The system (3.24) has at least one strong solution $\boldsymbol{z} \in \mathcal{L}^2([0, t_f]; \mathcal{V}) \cap \mathcal{L}^\infty([0, t_f]; \mathcal{H})$. Furthermore, the approximation error $\boldsymbol{e}_N = \boldsymbol{z} - \boldsymbol{z}_N$ is bounded and it has a subsequence converging to zero in $\mathcal{L}^2([0, t_f]; \mathcal{H})$ as N goes to infinity.*

Proof: It can be concluded from Lemma 3.3.4 that the sequence $\boldsymbol{z}_N$ stays in bounded set in $\mathcal{L}^\infty([0, t_f]; \mathcal{V})$ and thus in $\mathcal{L}^2([0, t_f]; \mathcal{V}) \cap \mathcal{L}^\infty([0, t_f]; \mathcal{H})$. It is also concluded that $\boldsymbol{\mathcal{N}}_N(\boldsymbol{z}_N)$ stays in a bounded set in $\mathcal{L}^2([0, t_f]; \mathcal{V})$. By BanachAlaoglu theorem [119], there exists a subsequence $\boldsymbol{z}_M$ and $\boldsymbol{\mathcal{N}}_M(\boldsymbol{z}_M)$ such that

$$\begin{aligned} &\boldsymbol{z}_M(t) \to \boldsymbol{z}^*(t) \text{ weakly in } \mathcal{L}^2([0, t_f]; \mathcal{V}) \\ &\boldsymbol{z}_M(t) \to \boldsymbol{z}^*(t) \text{ in weak-star topology of } \mathcal{L}^\infty([0, t_f]; \mathcal{H}), \end{aligned} \tag{3.45}$$

and

$$\boldsymbol{\mathcal{N}}_M(\boldsymbol{z}_M(t)) \to \boldsymbol{w}^*(t) \text{ weakly in } \mathcal{L}^2([0, t_f]; \mathcal{V}) \tag{3.46}$$

for $\boldsymbol{z}^*(t) \in \mathcal{L}^2([0, t_f]; \mathcal{V}) \cap \mathcal{L}^\infty([0, t_f]; \mathcal{H})$ and $\boldsymbol{w}^*(t) \in \mathcal{L}^2([0, t_f]; \mathcal{V})$ since $\mathcal{L}^2([0, t_f]; \mathcal{V})$ and $\mathcal{L}^2([0, t_f]; \mathcal{H})$ are complete with respect to weak topology. From (3.25), Lipschitz continuity (3.30), boundedness of $\boldsymbol{u}(t)$, and Lemma 3.3.4, it is concluded that the sequence $d\boldsymbol{z}_M(t)/dt$ stays in a bounded set in $\mathcal{L}^2([0, t_f]; \mathcal{H})$. Therefore, by the compactness Theorem B.0.2,

$$\boldsymbol{z}_M(t) \to \boldsymbol{z}^*(t) \text{ strongly in } \mathcal{L}^2([0, t_f]; \mathcal{H}). \tag{3.47}$$

Note that from (3.46), it can be concluded that for $\boldsymbol{w}(t) \in \mathcal{L}^2([0, t_f]; \mathcal{D}(\boldsymbol{\mathcal{A}}))$,

$$\int_0^{t_f} (\boldsymbol{\mathcal{A}}^{\frac{1}{2}}\boldsymbol{\mathcal{N}}_M(\boldsymbol{z}_M(t)), \boldsymbol{\mathcal{A}}^{\frac{1}{2}}\boldsymbol{w}(t))_{\mathcal{H}} dt \to \int_0^{t_f} (\boldsymbol{\mathcal{A}}^{\frac{1}{2}}\boldsymbol{w}^*(t), \boldsymbol{\mathcal{A}}^{\frac{1}{2}}\boldsymbol{w}(t))_{\mathcal{H}} dt;$$

thus,

$$\int_0^{t_f} (\boldsymbol{\mathcal{N}}_M(\boldsymbol{z}_M(t)), \boldsymbol{\mathcal{A}}\boldsymbol{w}(t))_{\mathcal{H}} dt \to \int_0^{t_f} (\boldsymbol{w}^*(t), \boldsymbol{\mathcal{A}}\boldsymbol{w}(t))_{\mathcal{H}} dt. \tag{3.48}$$

In addition, by (3.47) and (3.21),

$$\int_0^{t_f} (\boldsymbol{\mathcal{N}}_M(\boldsymbol{z}_M(t)), \boldsymbol{\mathcal{A}}\boldsymbol{w}(t))_{\mathcal{H}} dt \to \int_0^{t_f} (\boldsymbol{\mathcal{N}}(\boldsymbol{z}^*(t)), \boldsymbol{\mathcal{A}}\boldsymbol{w}(t))_{\mathcal{H}} dt. \tag{3.49}$$

Since $\boldsymbol{\mathcal{A}}$ has a bounded linear inverse by Assumption 3.2.6, it is onto $\mathcal{H}$. Therefore, the convergence results (3.48) and (3.49) are satisfied for every $\bar{\boldsymbol{w}}(t) = \boldsymbol{\mathcal{A}}\boldsymbol{w}(t) \in \mathcal{L}^\infty([0, t_f]; \mathcal{H})$. Therefore, by uniqueness of the limit in weak topology, $\boldsymbol{w}^*(t) = \boldsymbol{\mathcal{N}}(\boldsymbol{z}^*(t))$, and

$$\boldsymbol{\mathcal{N}}_M(\boldsymbol{z}_M(t)) \to \boldsymbol{\mathcal{N}}(\boldsymbol{z}^*(t)) \text{ weakly in } \mathcal{L}^2([0, t_f]; \mathcal{V}). \tag{3.50}$$

Now, multiplying both sides of (3.34) by a smooth function $\phi(t)$ with $\phi(t_f) = 0$, employing (3.3), and integrating the resulting equation with respect to time yield

$$\begin{aligned} -\int_0^{t_f} ((\boldsymbol{z}_M(t), \boldsymbol{w})_{\mathcal{H}} \frac{d\phi(t)}{dt} + (\boldsymbol{\mathcal{A}}^{\frac{1}{2}} \boldsymbol{\mathcal{N}}_M(\boldsymbol{z}_M(t)), \boldsymbol{\mathcal{A}}^{\frac{1}{2}} \boldsymbol{w})_{\mathcal{H}} \phi(t)) dt \\ = \int_0^{t_f} (\boldsymbol{\mathcal{R}}_M(\boldsymbol{z}_M(t), t) + \boldsymbol{\mathcal{F}}_M \boldsymbol{u}(t), \boldsymbol{w})_{\mathcal{H}} \phi(t) dt + (\boldsymbol{z}_M(0), \boldsymbol{w})_{\mathcal{H}} \phi(0). \end{aligned} \tag{3.51}$$

For $\boldsymbol{w} \in \mathcal{D}(\boldsymbol{\mathcal{A}}^{1/2})$, passing the limits (3.21), (3.45), (3.47), (3.50), and the limit

$$\boldsymbol{z}_M(0) \to \boldsymbol{z}(0) \text{ strongly in } \mathcal{H}$$

to (3.51) and using Assumption 3.2.7 lead to

$$\begin{aligned} -\int_0^{t_f} ((\boldsymbol{z}^*(t), \boldsymbol{w})_{\mathcal{H}} \frac{d\phi(t)}{dt} + (\boldsymbol{\mathcal{A}}^{\frac{1}{2}} \boldsymbol{\mathcal{N}}(\boldsymbol{z}^*(t)), \boldsymbol{\mathcal{A}}^{\frac{1}{2}} \boldsymbol{w})_{\mathcal{H}} \phi(t)) dt \\ = \int_0^{t_f} (\boldsymbol{\mathcal{R}}(\boldsymbol{z}^*(t), t) + \boldsymbol{\mathcal{F}}\boldsymbol{u}(t), \boldsymbol{w})_{\mathcal{H}} \phi(t) dt + (\boldsymbol{z}(0), \boldsymbol{w})_{\mathcal{H}} \phi(0). \end{aligned} \tag{3.52}$$

Finally, integrating (3.52) by parts results in

$$\begin{aligned} \int_0^{t_f} \frac{d}{dt} (\boldsymbol{z}^*(t), \boldsymbol{w})_{\mathcal{H}} \phi(t) dt = &- \int_0^{t_f} (\boldsymbol{\mathcal{A}}^{\frac{1}{2}} \boldsymbol{\mathcal{N}}(\boldsymbol{z}^*(t)), \boldsymbol{\mathcal{A}}^{\frac{1}{2}} \boldsymbol{w})_{\mathcal{H}} \phi(t) dt \\ &+ \int_0^{t_f} (\boldsymbol{\mathcal{R}}(\boldsymbol{z}^*(t), t) + \boldsymbol{\mathcal{F}}\boldsymbol{u}(t), \boldsymbol{w})_{\mathcal{H}} \phi(t) dt. \end{aligned} \tag{3.53}$$

Using (3.3) in (3.53) yields to

$$\frac{d}{dt} \langle \boldsymbol{z}^*, \boldsymbol{w} \rangle_{\mathcal{V}', \mathcal{V}} = \langle -\boldsymbol{\mathcal{A}}\boldsymbol{\mathcal{N}}(\boldsymbol{z}^*) + \boldsymbol{\mathcal{R}}(\boldsymbol{z}^*, t) + \boldsymbol{\mathcal{F}}\boldsymbol{u}(t), \boldsymbol{w} \rangle_{\mathcal{V}', \mathcal{V}} \tag{3.54}$$

which is valid in distribution sense on $[0, t_f]$. Since

$$\begin{aligned} \boldsymbol{z}^*(t) &\in \mathcal{L}^2([0,t_f];\mathcal{H}), \\ -\boldsymbol{\mathcal{A}}\boldsymbol{\mathcal{N}}(\boldsymbol{z}^*(t)) + \boldsymbol{\mathcal{R}}(\boldsymbol{z}^*(t),t) + \boldsymbol{\mathcal{F}}\boldsymbol{u}(t) &\in \mathcal{L}^2([0,t_f];\mathcal{H}), \end{aligned}$$

by [117, Lemma II.3.1] and from (3.54)

$$\frac{\partial \boldsymbol{z}^*(t)}{\partial t} \in \mathcal{L}^2([0,t_f];\mathcal{H})$$

and $\boldsymbol{z}^*(t)$ satisfies (3.24) almost every where. Furthermore, by [117, Lemma II.3.1], $\boldsymbol{z}^*$ equals almost every where to a continuous function from $[0, t_f]$ to $\mathcal{H}$; thus, it is a strong solution to (3.24) by Definition 3.3.1. □

Chapter 4

Mathematical modeling of the lithium-ion cell

Among different estimation methods, model-based estimation is considered to evaluate the value of the SOC from voltage measurements; subsequently, an electrochemical model is offered to represent a battery cell's behavior. In this research, lithium-ion cells whose positive electrodes are made of LFP material are chosen as the chemistry of interest. Most of the theories in electrochemical modeling have been developed for battery chemistries like lead acid and nickel-metal hydride. The mathematical modeling of lithium-ion cells was first developed by Doyle et al. [1]. Their recent formulation presented in [120] constructs the majority of the equations used here.

4.1 Electrochemical model

A battery is composed of three major parts, the positive electrode, negative electrode and electrolyte. In a Li-ion cell, the negative electrode (n) is made of carbon and the positive electrode (p) is a metal oxide. The cell is sketched in Figure 4.1. In practice, the electrodes are composed of a slurry of active material, conductive filler, and binder coated onto a foil current collector. Therefore, a porous structure is provided where the electrochemical reactions are distributed over the surface of particles [121]. In order to derive the governing equations, two important theorems are used: porous electrode theory and concentration solution theory.

In porous electrode theory, considering the exact position and shape of the pores and particles in the electrode structure is substituted by utilizing average properties

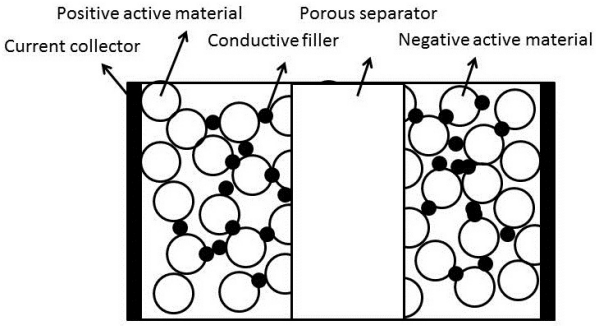

Figure 4.1: A Li-ion battery cell

over a small volume. The scale of the finite volume is small compared to the electrode width and large compared to particle size. Accordingly, the electrodes are treated as the superposition of the active material particles, filler, and electrolyte coexisting at the same point. Moreover, the particles of active material are assumed to have spherical shape. The coupling of the electrode phase to the electrolyte phase is made via mass balances and reaction rates [121].

Before setting the modeling process, some parameters should be defined. The superposition assumption of the electrode and electrolyte phase introduces two parameters: the interfacial area between two phases per unit volume, a, and the volume fraction of each phase, ϵ. These parameters can be defined by assuming an even distribution for the active material spherical particles along the electrodes. These parameters are respectively defined as follow:

$$a = N_P(4\pi R^2) \tag{4.1}$$

$$\epsilon_s = N_P(\frac{4}{3}\pi R^3) \tag{4.2}$$

where R is the radius of spherical particles, ϵ_s is the volume fraction of the electrode phase, and N_P is the number of particles per unit volume. By substituting equation 4.2 into equation 4.1, the specific interfacial area can be written in the form of

$$a = \frac{3\epsilon_s}{R}. \tag{4.3}$$

The volume fraction coefficient of each phase is also used to define some properties of the battery cell. The solid-phase conductivity, electrolyte diffusivity, and electrolyte conductivity are the properties affected by the electrode porosity. The porosity leading the definition of volume fraction causes a reduction in these parameters. This phenomenon

can be explained in the electrolyte phase by a longer path that the ions must take around the particles instead of a straight line. The Bruggeman relation is used to address the porosity effect. In this case, the effective conductivity in solid and electrolyte phases are defined as

$$\sigma^{eff} = \sigma \epsilon_s^P \tag{4.4}$$

$$\kappa^{eff} = \kappa \epsilon_e^P. \tag{4.5}$$

Similarly, the effective diffusivity in the electrolyte is defined as

$$D_e^{eff} = D_e \epsilon_e^P \tag{4.6}$$

where P is the Bruggeman exponent. This value is a function of the shape and distribution of the active material's particles, and this is usually set at 1.5 for Li-ion cells.

In this research, the representative variables are assumed to change only along the cell. Therefore, 1-D electrochemical modeling of the cell is considered in this chapter. Four variables are used to represent the cell behavior. These variables are concentration of the lithium in the solid phase $c_s(r, x, t)$, the lithium ions in the electrolyte phase $c_e(r, x, t)$, the electric potential of the solid phase $\varphi_s(x, t)$, and the potential of the electrolyte phase $\varphi_e(x, t)$. Next, the electrochemical equations are initiated for three regions, positive electrode, negative electrode, and separator. Although the positive and negative electrode regions are composed of both electrode and electrolyte, there exists only electrolyte in the separator which allows no electrochemical reactions.

Transport in solid phase

Modeling the time variation of active material distribution in solid phase is challenging in cells with LFP positive electrode. The battery cell works based on the principle of lithium insertion/deinsertion where electrons are consumed or produced. The insertion/deinsertion mechanism in the LFP electrode is a two phase process taking place between the lithium poor phase, $Li_\epsilon FePO_4$, and the lithium rich phase, $LI_{1-\epsilon} FePO_4$. This two-phase behavior plays an important role in the cell response and must be considered in the modeling process.

A few models in the literature improves the model of the two-phase behavior in LFP cells. They consist of core-shell [6], phase field, resistive-reactant, and variable solid-state diffusivity models. Since the variable solid-state diffusivity is simple and provides

a physical accuracy, it is used here as a reliable platform. The details on this model can be found in [48, 2], and [49].

Given the assumption that the composite electrodes are the superposition of spherical particles and electrolyte, the conservation law in every particle is used to find the time variation of lithium concentration. The modeling accuracy is elevated by solving for more than one particle at every position in the electrode. Furthermore, negligible volume change and high conductivity is assumed for the solid phase in the process of the lithium insertion/deinsertion. The solid phase's mass balance of the lithium in a single particle is described by the Fick's second law in the form of a diffusion equation as

$$\frac{\partial c_{s,k}(x, r_k, t)}{\partial t} = \frac{1}{r_k^2}\frac{\partial}{\partial r_k}(D_{s,k}(c_{s,k})\frac{1}{r_k^2}\frac{\partial}{\partial r_k}c_{s,k}(x, r_k, t)) \tag{4.7}$$

where the sub-index $k = 1 \cdot K$ corresponds to the index of the particle group (since there exists more than one particle size) and $D_{s,k}(.)$ is the diffusion coefficient of the kth spherical particle group. The diffusion coefficient is a function of lithium concentration and is defined by

$$D_{s,k}(.) = \alpha_k(.)\mathcal{D}_s$$

where $\mathcal{D}_s$ is the solid state binary diffusion coefficient and

$$\alpha_k(y_k) = -\frac{F}{RT}y_k(1 - y_k)\frac{\partial U_k(y_k)}{\partial y_k}, \quad y_k = \frac{c_{s,k}}{c_{max}}.$$

In this expression, $U_k(.)$ is the OCP of the kth particle and c_{max} is the maximum solid state concentration.

The OCP is normally defined for every particle group of each electrode as a function of the solid concentration on the particle surface $c_{s,k} \mid_{r_k=R_k}$ and with respect to a hypothetical lithium reference electrode. It indicates the potential of the electrode material at different solid concentration levels. The reference electrode is assumed to be immersed in the electrolyte in a neighborhood of solid/electrolyte interface. The formulations for the OCP is identified through a set of experimental data obtained by a half cell experiment.

In the experiment level of OCP identification, both solid concentration at the particle surface and the half cell open circuit voltage must be measured. Open circuit voltage can be easily measured after a long rest time since the current is turned off; however, measuring the solid concentration is not directly achievable. Given the assumption that the solid concentration reaches a uniform distribution after a long rest time, it is suggested that this be determined by the coulomb counting method. The number of electrons that

leave or enter into the electrode divided by the solid phase volume specifies the change in the solid concentration.

In order to collect the required data, the half cell is discharged (charged) from a fully charged (discharged) state in successive charging (discharging) periods. In every period, the cell is charged (discharged) by a fixed value with a constant current rate; thus, error augmentation would not be an issue in the integral calculation of the current. The experimental results display different values for the OCP in the charging and discharging cycles at a specific SOC. In fact, the value of OCP depends on the history of the system's state. In other words, the SOC-OCP graph includes hysteresis [122, 123], and [124]. However, in electrochemical equations this term is approximated by two single-valued functions for the charging and discharging process.

Finally, the diffusion equation is completed via the initial and boundary conditions given by

$$\begin{aligned}
&\frac{\partial c_{s,k}}{\partial r_k} \mid_{r_k=0} = 0 \\
&D_{s,k} \frac{\partial c_{s,k}}{\partial r_k} \mid_{r_k=R_k} = \frac{i_{n,k}}{F} \\
&c_{s,k} \mid_{t=0} = c^0_{s,k}
\end{aligned}$$

where R_k is the radius of the kth particle group, $i_{n,k}$ is the reaction current at the surface of the kth particle group, and F is the Faraday's constant. The total number of K diffusion equations of the form 4.7 must be solved in both electrode regions but not in the separator.

Transport in electrolyte phase

The next variable to be modeled is lithium ion concentration in the electrolyte phase. The lithium ions are the positive ions of a typical Li-ion cell. In the charging process, they are produced at the positive electrode solid/electrolyte interface, travel through the electrolyte, and are consumed at the negative electrode. Therefore, the concentration distribution of these ions over the cell plays an important role in the electrochemical reactions. The gradient in the concentration distribution drives the diffusion process. The diffusion process and electrochemical reactions then initiate the time variation of this distribution.

The main assumptions in this step are ignoring convection in the electrolyte, side reactions in the electrolyte, the volume change of the solid phase due to the lithium

insertion/deinsertion process and the binary electrolyte assumption (a binary electrolyte includes only two groups of ions). The lithium ion concentration in the electrolyte is defined by

$$\epsilon_e \frac{\partial c_e(x,t)}{\partial t} = \frac{\partial}{\partial x}(D_e^{eff} \frac{\partial c_e(x,t)}{\partial x}) + \frac{1-t_+^0}{F} \sum a_k i_{n,k} \tag{4.8}$$

where D_e^{eff} is the electrolyte effective diffusion coefficient and t_+^0 is the transference number of the lithium ion with respect to the solvent velocity.

Since electrolyte exists in every spot of the cell, equation 4.8 must be solved in all three regions, the negative electrode, positive electrode, and separator. On the right hand side of equation 4.8, the first term corresponds to the diffusion process of the lithium ions in the electrolyte and the second term adds the effect of the electrochemical reactions. The term representing the effect of the reactions vanishes in the separator region due to the absence of the solid phase. The boundary conditions are defined by zero flux at the current collectors as

$$\frac{\partial c_e}{\partial x} \mid_{x=0} = \frac{\partial c_e}{\partial x} \mid_{x=L} = 0$$

where L is the length of the cell. A more general form of equation 4.9 can be found in [121].

Potential in electrolyte phase

As discussed before, the electrolyte is assumed to be a binary electrolyte which is a standard choice for most of the lithium-ion batteries. The potential in the binary electrolyte is measured by a reference electrode having a reversible half-cell reaction. The gradient of the potential is measured as the potential of such a reference electrode with respect to the same kind of reference electrode at a fixed position. When employing the lithium metal as the reference electrode and 1:1 binary electrolyte, this gradient is defined by [121]

$$\frac{\partial \varphi_e(x,t)}{\partial x} = \frac{-i_e}{k^{eff}} + \frac{2RT(1-t_+^0)}{F}(1 + \frac{d \ln f_\pm}{d \ln c_e}) \frac{\partial \ln c_e(x,t)}{\partial x} \tag{4.9}$$

where R is the gas constant, i_e is the current assigned to the electrolyte phase, and $f_\pm$ is the mean molar activity coefficient in the electrolyte. The first and second term on the right hand side of this equation respectively accounts for a potential drop in the electrolyte and concentration overpotential arising from concentration variation of the lithium ions.

Using the electroneutrality of the electrolyte phase, a current balance gives the relation between the current divergence and the net pore-wall reaction flux as

$$\frac{\partial i_e(x,t)}{\partial x} = \sum a_k i_{n,k}. \tag{4.10}$$

Now, by substituting equation 4.10 into equation 4.9, the potential satisfies the expression

$$\frac{\partial}{\partial x}(k^{eff}\frac{\partial \varphi_e(x,t)}{\partial x} + k_D^{eff}\frac{\partial \ln c_e(x,t)}{\partial x}) = \sum a_k i_{n,k} \tag{4.11}$$

where $k_D^{eff} = k^{eff}\frac{2RT(1-t_+^0)}{F}(1 + \frac{d\ln f_\pm}{d\ln c_e})$. The boundary conditions are defined by

$$\frac{\partial \varphi_e}{\partial x} \mid_{x=0} = \frac{\partial \varphi_e}{\partial x} \mid_{x=L} = 0$$

These boundary conditions do not completely define the problem, and extra conditions are required, which are defined in the next section.

Potential in solid phase

The potential in the solid phase of the porous electrode is derived from Ohm's Law as

$$\sigma^{eff}\frac{\varphi_s(x,t)}{\partial x} = i_e(x,t) - I(t) \tag{4.12}$$

where $I(t)$ is the current, and $i_s(x,t) = I(t) - i_e(x,t)$ is the current in the solid phase. By substituting equation 4.10 into equation 4.12, the solid potential must satisfy the following equation.

$$\frac{\partial}{\partial x}(\sigma^{eff}\frac{\varphi_s(x,t)}{\partial x}) = \sum a_k i_{n,k} \tag{4.13}$$

The boundary conditions are given by the fact that the electrolyte current density is zero at the current collectors/electrodes interface and equals the total current, $I(t)$ at the electrodes/separator interface. Moreover, the solid potential is set to zero at one of the current collectors as the reference value. In general, the boundary conditions are

$$\begin{aligned}
&\frac{\partial \varphi_s}{\partial x} \mid_{x=\delta_n} = 0 \\
&\varphi_s \mid_{x=0} = 0 \\
&\sigma^{eff}\frac{\partial \varphi_s}{\partial x} \mid_{x=L} = I(t)
\end{aligned}$$

where δ_n is the length of the negative electrode.

Solving the electrochemical governing equations with the defined boundary conditions gives the potential in the solid phase such that the total amount of reaction along the electrode equals the applied current [121]. The output of the system is set as the terminal voltage. The open circuit voltage is obtained from the difference between the solid potential at two current collectors. By including the effect of the external load, the terminal voltage has the form of

$$V(t) = \varphi_s(L,t) - \varphi_s(0,t) - R_l I(t)$$

where R_l is the load resistance.

In the evaluated mathematical equations, the local electrochemical reaction rate, $i_{n,k}$, is an essential term. It can be determined as a function of the concentration and potential. The Butler-Volmer rate equation is usually used for this purpose, and for every particle group, is defined by

$$i_{n,k} = i_{0,k}\{\exp(\frac{\alpha_a F \eta_k}{RT}) - \exp(-\frac{\alpha_c F \eta_k}{RT})\}$$

where $i_{0,k}$ is the exchange current density, α_a and α_c are anodic and cathodic transfer coefficients,

$$\eta_k = \varphi_s - \varphi_e - U_k(y_{k,s})$$

wherein

$$y_{k,s} = \frac{c_{s,k} \mid_{r_k = R_k}}{c_{max}}$$

is the surface overpotential, and c_{max} is the maximum solid concentration. Furthermore,

$$i_{0,k} = \kappa(c_e)^{\alpha_a}(c_{max} - c_{s,k} \mid_{r_k=R_k})^{\alpha_c}(c_{s,k} \mid_{r_k=R_k})^{\alpha_a}$$

where κ is a kinetic rate constant. The surface overpotenial expresses the deviation from the difference between the thermodynamic potential of the solid and solution phases at the current surface concentrations.

As mentioned before, another important term in the electrochemical model is the OCP term. The OCP profile has an important effect on the simulation result and must be identified carefully. This effect is even more critical when comparing the simulation results for a full cell sandwich with the experimental data. Therefore, accurate data on the measurement of this quantity with respect to a lithium reference electrode must be collected. Moreover, an adequate physical or empirical model must be chosen to determine the shape of OCP profile.

Table 4.1: Lithium-ion cell parameters [1].

parameter	definition	value (negative electrode, separator, and positive electrode)
l_{cat}	thickness of the negative electrode, m	$160e-6$
l_{sep}	thickness of the separator, m	$52e-6$
L	thickness of the cell, m	$386e6$
R_s	radius of the spherical solid particle, m	$12.50e-6$, $-$, $8.50e-6$
R	gas constant, $Jmol^{-1}K^{-1}$	8.3145
F	Faraday's constant, $Cmol^{-1}$	96485
t_+^0	transference number	0.363, 0.363, 0.363
ϵ_e	volume fraction of the electrolyte phase	0.357, 0.724, 0.444
k^{eff}	effective conductivity in the electrolyte phase, Sm^{-1}	0.028, 0.027, 0.056
k_D^{eff}	$\frac{k^{eff}2RT(1-t_+^0)}{F}$	
σ^{eff}	effective conductivity in the solid phase, Sm^{-1}	35.038, $-$, 0.855
D_e^{eff}	effective diffusivity in the electrolyte phase, m^2s^{-1}	$7.768e-12$, $7.500e-11$, $1.633e-11$
D_s	Diffusion coefficient of the spherical particle, m^2s^{-1}	$3.9e-14$, $-$, $1e-13$
$c_{s,max}$	maximum solid state concentration, $molm^{-3}$	$26.390e3$, $-$, $22.860e3$
i_0	exchange current density, Am^{-2}	$1.140e-5$, 0, $8.29e-6$

4.2 Hysteresis from the cell dynamics

An important difficulty in estimating lithium-ion cell's state of charge is that the voltage of the cell's terminal depends on the charging and discharging history. This existence of hysteresis in the OCP graph is described in [122, 123], and [124] in great detail. To identify the OCP profile, a half cell is discharged (or charged) from the fully charged (or discharged) state in successive charging (or discharging) periods. Experimental results display different values for OCP in charging and discharging cycles at a specific SOC [122, 123], and [124]. In other words, the variation of OCP with respect to the solid surface concentration is hysteretic. Furthermore, this hysteresis has also been observed to be rate dependent. In many studies, the effect of the hysteresis associated with the OCP is added to the model [125, 33, 126, 10, 15, 12], and [16].

However, the OCP might not be the only source, or the most fundamental source of hysteresis; intrinsic dynamics can also induce hysteretic behavior. The system dynamics might lead to the hysteretic behavior; see for instance [127] for an example of this in the Landau-Lifshitz equations which is used to model magnetization. Therefore, the battery governing equations should be studied for the hysteresis in the system variables. A way of investigating this possibility is to study the dynamical equations with no hysteresis in the OCP. Here, the existence of hysteresis from the second source is studied by setting the OCP term as a single value continuous function.

In this section, a version of the lithium-ion cell whose positive electrode is made of the LFP material and has only one particle bin is considered. Furthermore, the solid-state diffusion is assumed to be constant. Define

$$\begin{aligned}
&\mathcal{X}_1 = \{z \in \mathcal{L}^2([L_1, L] \times [0, R_s]) : r^2 z \in \mathcal{L}^2([L_1, L] \times [0, R_s])\} \\
&\mathcal{X} = \mathcal{L}^2(0, L) \times \mathcal{X}_1 \\
&\mathcal{Y} = \mathcal{L}^2(0, L) \times \mathcal{L}^2(L_1, L)
\end{aligned}$$

where $L_1 = l_{sep}$, $L = l_{sep} + l_{cat}$. Let $\boldsymbol{c} = [c_1, c_2]^T = [c_e, c_s]^T \subseteq \mathcal{X}$ and $\boldsymbol{\varphi} = [\varphi_1, \varphi_2]^T = [\varphi_e, \varphi_s]^T \subseteq \mathcal{Y}$. Furthermore, i_n, the Butler-Volmer reaction current at the surface of solid particles, is defined by

$$i_n(\boldsymbol{c}, \boldsymbol{\varphi}) = i_0\{\exp(\frac{F\eta}{2RT}) - \exp(-\frac{F\eta}{2RT})\} \tag{4.14}$$

where

$$\eta = \varphi_2 - \varphi_1 - U(y_s) \tag{4.15}$$

where

$$y_s = \frac{c_2 \mid r = R_s}{c_{max}}$$

is the overpotential term where R_0 is the particle radius, and $U(.)$ indicates the OCP defined by

$$U(y_s) = -0.16 + 1.32\exp(-3y_s) + 10\exp(-2000y_s) \tag{4.16}$$

at negative electrode, and

$$\begin{aligned}
U(y_s) = 4.20 + 0.06\tanh(-14.55y_s + 8.61) - \frac{0.03}{(1 - y_s)^{0.49} - 1.90} \\
- 0.16\exp(-0.05y_s^8) + 0.81\exp(-40(y_s - 0.13))
\end{aligned} \tag{4.17}$$

at positive electrode.

As explained before, the OCP is derived based on static performance and cannot be measured during battery operation. Instead, empirically derived relations are used. The experimental results of the OCP vs. the SOC at the particle surface are used to find an empirical model via some curve fitting. The process of finding these experimental results is done before employing the battery in a drive cycle. For the example considered in this section, the results and empirical model are given in [1]. In general, these relations are multi-valued. However, in order to investigate the role of dynamics in hysteresis, a

single-valued function is used here. The OCP profile is obtained through curve fitting. The cell governing equations can be represented as

$$0 = \begin{bmatrix} \frac{\partial}{\partial x}(k^{eff}\frac{\partial}{\partial x}(\varphi_1) + k_D^{eff}\frac{\partial}{\partial x}(\ln c_1)) - i_n(\boldsymbol{c},\boldsymbol{\varphi}) \\ \frac{\partial}{\partial x}(\sigma^{eff}\frac{\partial}{\partial x}(\varphi_2)) - i_n(\boldsymbol{c},\boldsymbol{\varphi}) \end{bmatrix}, \tag{4.18}$$

$$\frac{\partial}{\partial t}\begin{bmatrix} c_1 \\ c_2 \end{bmatrix} = \begin{bmatrix} \frac{1}{\epsilon_e}\frac{\partial}{\partial x}(D_e^{eff}\frac{\partial c_1}{\partial x}) + \frac{1-t_+^0}{\epsilon_e F} i_n(\boldsymbol{c},\boldsymbol{\varphi}) \\ \frac{1}{r^2}\frac{\partial}{\partial r}(D_s r^2 \frac{\partial c_2}{\partial r}) \end{bmatrix}. \tag{4.19}$$

The boundary conditions are

$$\frac{\partial \varphi_1}{\partial x}\mid_{x=0} = \frac{\partial \varphi_1}{\partial x}\mid_{x=L} = 0, \tag{4.20}$$

$$\varphi_2 \mid_{x=0} = 0, \tag{4.21}$$

$$\frac{\partial \varphi_2}{\partial x}\mid_{x=\delta_n} = \frac{\partial \varphi_2}{\partial x}\mid_{x=\delta_{sp}} = 0, \tag{4.22}$$

$$\frac{\partial c_1}{\partial x}\mid_{x=0} = \frac{\partial c_1}{\partial x}\mid_{x=L} = 0, \tag{4.23}$$

$$\frac{\partial c_2}{\partial r}\mid_{r=0} = 0. \tag{4.24}$$

Also,

$$D_s \frac{\partial c_2}{\partial r}\mid_{r=R_s} = \frac{i_n(\boldsymbol{c},\boldsymbol{\varphi})}{F} \tag{4.25}$$

and the control occurs through the current $I(t)$ applied on the boundary,

$$\sigma^{eff}\frac{\partial \varphi_2}{\partial x}\mid_{x=L} = I(t)\,. \tag{4.26}$$

Let R_l indicate the load resistance; the voltage measurement can be represented by

$$V(t) = \varphi_2(L,t) - \varphi_2(0,t) - R_l I(t). \tag{4.27}$$

Substituting equation (4.15) into (4.27) results in

$$\begin{aligned} V(t) = {} & U(L,t) - U(0,t) + \\ & \eta(L,t) - \eta(0,t) + \varphi_1(L,t) - \varphi_1(0,t) - R_l I(t). \end{aligned} \tag{4.28}$$

From (4.28), it can be seen that the terminal voltage involves not only the OCP but also the overpotential $\eta(L,t) - \eta(0,t)$ and electrolyte potential $\varphi_1(L,t) - \varphi_1(0,t)$. Thus, even if the OCP is a single-valued function, the system dynamics can cause hysteretic behavior in the current-voltage relationship.

Roughly speaking, the response of a system is said to exhibit hysteresis if the input-output graph has a looping behavior; see for example [128]. There are a verity of definitions in the literature [128]. A common property that is shared among systems exhibiting hysteresis is multiple stable equilibrium points. This property along with other conditions can be used to construct a general definition.

Definition 4.2.1. *[128]*
A system is said to include hysteresis if it has

1. *multiple stable equilibrium points,*

2. *faster dynamics than the time scale at which the input is changing.*

In Definition 4.2.1, the second condition implies that the transient response of the system when moving towards equilibrium points is not visible

The equilibrium points of the lithium-ion cell can be found by setting the time derivatives to zero. From equation (4.19) and $\frac{\partial c_2}{\partial t} = 0$, $D_s r^2 \frac{\partial c_2}{\partial r}$ depends only on x, and so

$$r^2 \frac{\partial c_2}{\partial r} = E_{n,1}$$

where $E_{n,1}$ does not depend on r. This is consistent with the boundary condition (4.24) at $r = 0$ and furthermore, implies that $E_{n,1} \equiv 0$. Thus,

$$D_s \frac{\partial c_2}{\partial_r} \mid_{r=R} = -\frac{i_n}{F} = 0.$$

Therefore, $i_n = 0$ and also $\partial c_2 / \partial r \equiv 0$. Thus, the equilibrium solid concentration is

$$c_2 = E_{n,2}(x) \tag{4.29}$$

where $E_{n,2}$ does not depend on r. A similar calcuation can be followed for the positive electrode.

Now consider $\frac{\partial c_1}{\partial t} = 0$ in equation (4.19). Since $i_n = 0$, (4.19) leads to

$$D_e^{eff} \partial c_1 / \partial x = C_{n,1}$$

where $C_{n,1}$ is constant. The boundary condition at $x = 0$ (4.23) implies that $C_{n,1} = 0$ and so $\partial c_1 / \partial x \equiv 0$. Thus, equilibrium electrolyte concentration is

$$c_1 = C_{n,2} \tag{4.30}$$

where $C_{n,2}$ is some constant. Similarly, it is constant at the positive electrode and in the separator. Continuity yields that these values are equal.

Now consider the constraint equations (4.18). Since $i_n = 0$, equation (4.18) yields

$$\sigma_n^{eff} \frac{\partial \varphi_2}{\partial x} = B_{n,1}$$

where $B_{n,1}$ is a constant. The boundary condition (4.22) at $x = \delta_n$ implies that $B_{n,1} = 0$ and so $\partial \varphi_2 / \partial x \equiv 0$. The boundary condition at $x = 0$ (4.21) then implies that for the negative electrode,

$$\varphi_2 = 0. \tag{4.31}$$

From (4.26), and the other boundary conditions for ϕ_2, it follows that there is an equilibrium solution when $I(t)$ is not only constant but also equals 0. In this case, the equilibrium is $\phi_2 = 0$ at the negative electrode and a constant at the positive electrode.

In a similar manner, (4.18), and the equilibrium value of c_1 being a constant, implies that

$$k^{eff} \partial \varphi_1 / \partial x = A_{n,1}$$

where A_1 is a constant. The boundary conditions (4.20) imply that $A_{n,1} = 0$ and so $\partial \varphi_1 / \partial x \equiv 0$. Therefore, for the negative electrode

$$\varphi_1 = A_{n,2} \tag{4.32}$$

where $A_{n,2}$ is a constant. Similarly, it is constant at the positive electrode and in the separator. Continuity yields that these values are equal.

The equilibrium value $i_n = 0$ leads to a further characterization of the equililbrium points. Since for the negative electrode, $i_0 \neq 0$,

$$\eta = \varphi_2 - \varphi_1 - U(y_s) = 0. \tag{4.33}$$

where

$$y_s = \frac{E_{n,2}(x)}{c_{s,max}}.$$

Since φ_1 and φ_2 are constant at the equilibrium point from equations (4.31) and (4.32), taking the partial differentiation with respect to x from both sides of equation (4.33) shows that

$$0 - 0 - \frac{\partial E_{n,2}(x)}{\partial x} \frac{\partial U(y_s)}{\partial y_s} = 0. \tag{4.34}$$

It can be shown from the equations given for U in 4.16 and 4.17 that

$$\frac{\partial U(y_s)}{\partial y_s} \neq 0;$$

thus,

$$\frac{\partial E_{n,2}(x)}{\partial x} = 0,$$

and $E_{n,2}$ is constant. A similar result is obtained for the positive electrode. For the negative electrode, substituting (4.31) into (4.33) leads to

$$\varphi_1 = U(y_s) \tag{4.35}$$

and so

$$A_{n,2} = U(y_s).$$

For the positive electrode, equation (4.33) introduces a constraint.

Thus, the electrochemical model (4.18) and (4.19) has more than one equilibrium point. The equilbrium solutions can be arbitrarily many constant ones. It is difficult to determine the stability of this set of coupled nonlinear partial differential and algebraic equations, and the time constant is even more challenging to determine. The presence of multiple equilbria does suggest that, as for the Landau-Lifshitz equation [127], the dynamics are hysteretic.

An empirical definition of hysteresis can be used to further investigate the existence of hysteresis via simulations.

Definition 4.2.2. *[129] A system exhibits hysteresis if a nontrivial closed curve in the input-output map persists for a periodic input as the frequency component of the input signal approaches zero.*

Proving the existence of a persistent closed loop is not generally possible. However, simulations can be used to show whether the system response shows a closed loop that persists at low frequencies. The idea is to excite the system with different periodic inputs with decreasing frequencies and constant amplitude. Next, the second definition of hysteresis, Definition 4.2.2, is employed to check the existence of a persistent closed loop as the frequency goes to zero.

Now, simulation results are used to show the existence of a persistent non-trivial closed loop in the current-voltage graph. The battery equations (4.18) and (4.19) were solved using the parameters in Table 4.1. The inputs are chosen to be sinusoidal functions

with constant amplitude and different frequencies. COMSOL software with linear basis functions was used to approximately solve the governing equations.

The input to the equations is the current $I(t)$ and the output is given by equation (4.28). The inputs were first chosen to be (in A/m^2)

$$I(t) = 0.875 \sin(\omega\, t),$$

where $\omega = 1,\ 0.001,\ 0.00001$. The results are shown in Figures 4.2, 4.3 and 4.4. From these simulation results, it can be seen that a closed loop occurs that becomes wider as the input frequency ω decreases. A closed loop appears when the input frequency goes to zero. Other modeling parameters are given in Table 4.1.

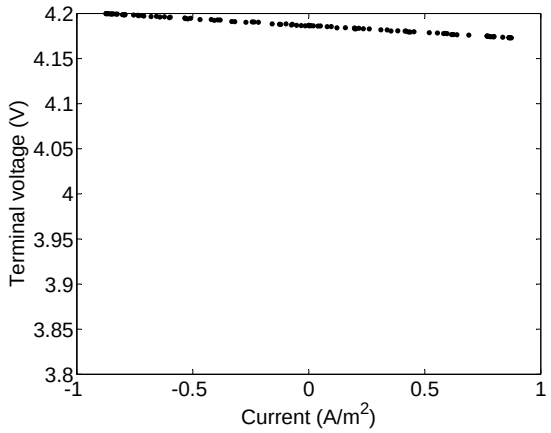

Figure 4.2: Current-voltage mapping for $I(t) = 0.875sin(t)(A/m^2)$. At this input frequency, no closed curve is observed. The frequency is too fast at this amplitude for the system to reach equilbrium during the cycle.

In the second set of simulations, the amplitude of the input current is increased to push the battery further away from its equilibrium state. Since the amount of active material must always be larger than zero, the frequency of the periodic input cannot be chosen to be too small; otherwise, the cell will finally reach the point where no active material will remain in battery cell. The input magnitude was increased so the input signals were (in A/m^2)

$$I(t) = 87.5 \sin(\omega\, t),$$

where $\omega = 10,\ 1,\ 10$. The results are shown in Figures 4.5, 4.6 and 4.7. According to these figures, the closed loop starts at lower frequencies than previously. The area enclosed by the curve again increases as the frequency is decreased.

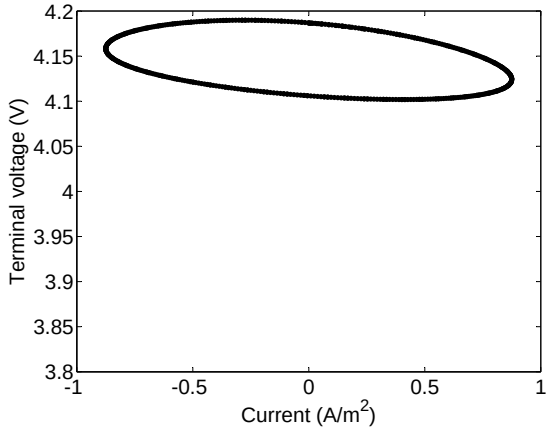

Figure 4.3: Current-voltage mapping for $I(t) = 0.875sin(1e-3t)(A/m^2)$. The closed curve appears at this frequency.

The purpose of this section was to investigate the role of system dynamics in the hysteresis observed in the current-voltage relationship for lithium-ion batteries. Two possible sources of hysteretic behavior were introduced: the OCP term, U, and the dynamics of the system. It is known that the OCP term may contain hysteresis. It was also proved that the battery governing equations have more than one equilibrium solution; the equilibria concentrations are a continuum of constant functions. The presence of multiple equilibria indicates that hysteresis can arise from the internal dynamics (Definiton 4.2.1).

Two sets of simulations were then used to investigate hysteresis further using Definition 4.2.2. In both sets of simulation results, the system's current-voltage response included a persistent nontrivial closed curve at low frequencies. Increasing the input amplitude led to the appearance of a closed loop at lower frequencies. That is, the system has more of a tendency to exhibit hysteresis specially with high current amplitudes. These results indicate that not every dynamical model is appropriate for SOC estimation. Even simplified lithium-ion models should be qualitiatively similar to the electrochemical equations so that this internal hysteresis is reproduced.

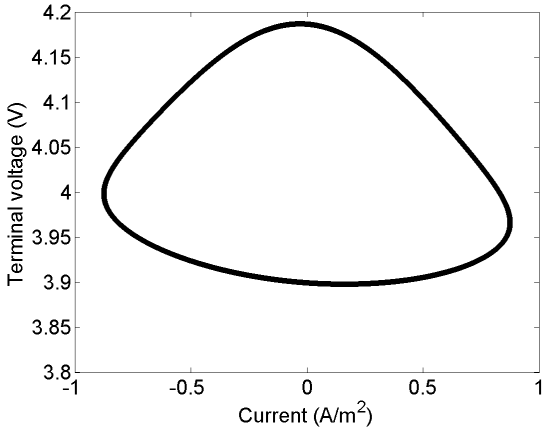

Figure 4.4: Current-voltage mapping for $I(t) = 0.875sin(1e-5t)(A/m^2)$. A closed curve occurs. Decreasing the input frequency increases the area enclosed by the curve.

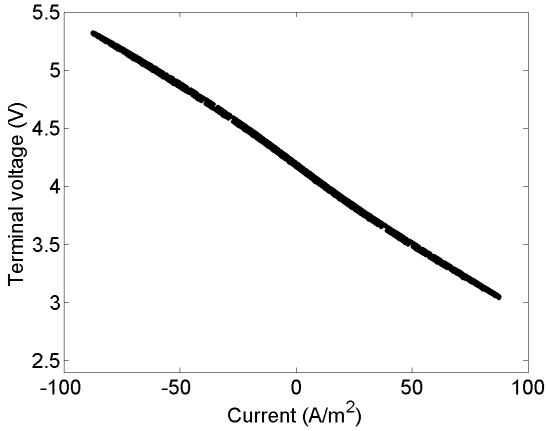

Figure 4.5: Current-voltage mapping for $I(t) = 87.5sin(10t)(A/m^2)$. At this frequency, no closed curve is observed.

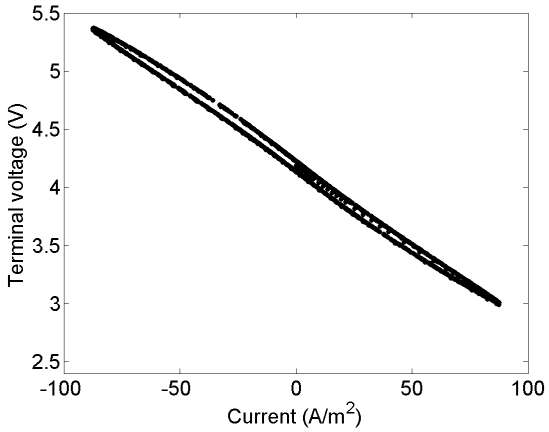

Figure 4.6: Current-voltage mapping for $I(t) = 87.5sin(1t)(A/m^2)$. At his amplitude of input, a closed curve appears. No loop was seen with an input at the same frequency and lower frequency (Figure 4.2

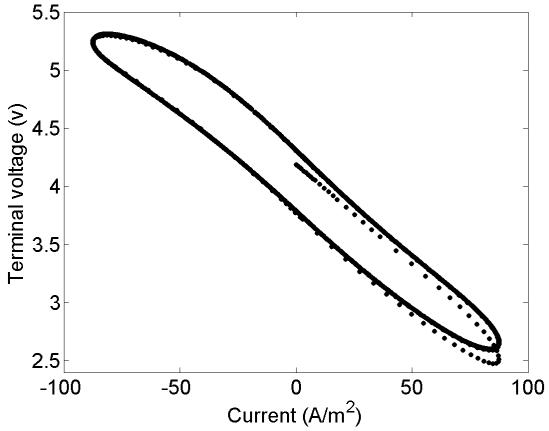

Figure 4.7: Current-voltage mapping for $I(t) = 87.5sin(1e-2t)(A/m^2)$. The closed curve persists and the enclosed area increases as the input frequency decreases.

Chapter 5

Electrochemical model based state of charge estimation of an LFP cell

In this chapter, the SOC estimation of an LFP cell is considered. As a precise model, electrochemical equations are chosen to estimate the SOC. For this purpose, first, these equations are approximated by reduced order ones keeping the accuracy of the original equations. Next, an adaptive observer is designed to estimate the SOC while capturing the system's dynamics.

The experimental data used in this chapter was generated in Laboratoire De Réactivité Et Chimie Des Solides (LRCS) in Amiens, France. In this experiment, the LFP electrode was recovered from a commercial graphite/LFP cell, LiFeBatt X2E (15 Ah, 40166, cell A) which is employed for hybrid electric applications [49]. The cell underwent discharge to 2 V at C/10 followed by a decrease of the current below C/50 while the potential was held to 2 V. Next, it was disassembled. Finally, the electrode whose area is 1.202 cm^2 was punched with a lithium metal foil for the counter electrode and a Whattman GF/D borosilicate glass fiber sheet for the separator to assemble a coin cell. For more details, please refer to [49].

The simulations were run in MATLAB R2015b on a PC with Intel(R) Xeon(R) CPU E31270 @ 3.40GHz processor and 32.0 GB RAM. The simulation time was 124 minutes, considerably less than the experimental time of over 1100 minutes.

5.1 Introduction and literature review

Cells are elementary units of a battery pack; tracking the SOC, the amount of deliverable energy, of each cell in a battery pack is a key role of every battery management system. At every measurement step, the cells' SOC estimate must be updated via measuring the terminal voltage, current, and temperatures. In practice, the SOC can be defined as an indication of the amount of remaining charge inside the cell. A number between 0% to 100% is assigned to this indication.

Among different chemical compositions, lithium-ion chemistry is one of the most promising options for the batteries used in hybrid electric vehicles. Compared to other cell chemistries, the Lithium-Ion chemistry boasts high power and energy density, a lack of memory effect, low self discharge, and a high life cycle. [3, 4, 5]. Lithium ion phosphate offers the advantage of better lithium insertion over other alternatives. Its numerous features have drawn considerable interest. Some of these features are listed in [6].

An inaccurate but numerically fast method of SOC estimation is voltage measurement wherein every voltage measurement is assigned with an approximate value of SOC. This method highly depends on temperature, charge/discharge rate, and aging [9]. In practice, the voltage measurement can not be trusted as the only estimation method and needs to be complemented with a more precise technique. Measurement of the OCP, introduced in Chapter 4, can be offered as an alternative measurement which assignment to SOC depends on fewer factors. In this case, a long resting time must be passed before measuring the value of the OCP. Once the OCP reaches a steady condition, the SOC can be calculated as the inverse image of the SOC-OCP map.

However, the OCP measurement is not applicable for real-time application due to the required long relaxation time. In other words, the OCP is unavailable while the battery is in use. This value also highly depends on environmental conditions especially, the current rate and hysteresis effect [12]. In addition, in most of the cases, finding the inverse SOC-OCP mapping is not feasible. The difficulty arises when further charge or discharge produces a two-phase behavior which constitutes the major part of the SOC-OCP plot. In the range of two-phase behavior, the SOC is assigned with almost invariant OCP values, and this phenomenon invalidates the inverse mapping [6].

Impedance measurement is a method of SOC estimation. It is defined as the ratio of voltage and current signals. This ratio is a complex quantity as the transfer function from current to voltage. The impedance carries information about dynamics of the battery cell

and can be obtained over a wide range of AC frequencies. In particular, a proper rational transfer function is set for impedance representation and the modeling parameters are found via least square optimization. The identified parameters of the transfer function differs from the SOC; therefore, impedance can be used to infer the SOC. A good review on SOC estimation by EIS can be found in [13]. This method is not useful for real-time applications [12] and [130].

Employing the battery impulse response as the measurement and a look-up table as the empirical model is suggested in [4]. On mapping a voltage measurement to the SOC, a utility-based technique and an impedance-based cell monitoring introduced respectively in [10] and [131] can be remarked. A neural network [11] or fuzzy logic [132] can also be used to map a measurement to the SOC prediction.

The second category of SOC estimation methods relies on measuring and integrating the current. Integrating the current over a drive cycle is mostly a part of real-time applications. This technique is called coulomb counting. Coulomb counting can be used in an open loop system to predict the SOC. When being compensated for the battery effects like discharge efficiency, self discharge, and capacity loss, the coulomb counting is referred to as a book-keeping system [9]. This method might be efficient for electric vehicles but not for hybrid electric vehicles in which no full charge/discharge state is achieved in a driving cycle [14]. Estimation using coulomb counting can also be done in a closed loop. The feedback might be calculated either empirically [15], [16], and [17] or by a mathematically optimized method [12] and [18]. Some examples of the coulomb counting method can be found in [19], [20], [21], and [22].

Some important factors reducing the estimation accuracy of coulomb counting are temperature, charge and discharge efficiencies, and cycle life [9]. Furthermore, the cumulative effect introduced by integration approximation makes the estimation sensitive to measurement errors due to noise, resolution, and rounding [14].

The model-based SOC estimation is the third class of SOC estimation techniques. The estimation via equivalent circuit models are mostly reported in literature. Simplicity and a relatively low number of parameters are the main characteristics of these models [23]. An equivalent circuit model is composed of basic elements, resistors, capacitors, and voltage source, in the form of a circuit network. Normally, the circuit includes a large capacitor or a voltage source to represent the OCP effect, and the rest of the circuit defines the cell's internal resistance and the effect of cell's dynamics [27]. Different groups of equivalent circuit models are introduced in [12] and [23].

Kalman filtering is the most cited technique; compensating for measurement noise

is the main property of this filter. One of the first and important efforts on the SOC estimation by the Kalman filter is the comparative studies introduced in [24] and applied in [133]. The descriptive model might be simplified before the filtering process is applied at the cost of lowered accuracy. Such a simplification is employed in [14] to predict the value of the OCP. Having the same elements but different configuration, the model introduced in [25] is observed with the EKF without any simplification assumption. Similarly, the EKF coupled with error least square optimization is established in [26] to estimate the OCP and update the modeling parameters. Robust extended Kalman filtering is the suggested method in [27] to cover the modeling uncertainty and reduce the strong dependency on the model accuracy.

Dealing with the model's nonlinearity can be evaluated by using sigma-point Kalman filtering. This type of filtering extends the idea of Kalman filter by using a set of points and weights to approximate the mean and covariance of the state vector at every time step. The application of the sigma-point Kalman filtering in observing the SOC from the voltage measurement is used in [28] and [29]. In this work, the modeling parameters are also allowed to have small variation in time; then, two variations of an adaptive approach, called joint and dual sigma-point filtering are improved to update the parameters at every time step. No proof of the convergence of the parameters and SOC is provided.

Some other examples of equivalent circuit model-based estimation methods are briefly listed here. A sliding mode observer is offered in [30], [31], and [32]; it is robust to uncertainties and simple at the same time. An adaptive observer is suggested based on a linear model in [126] and a nonlinear model in [33] to account for the parameters variation in time. A Luenberger observer which is an error rejection observation method is designed to predict the OCP via a nonlinear model in [34] and to predict the SOC via a linear parameter varying model in [35] and [5].

Electrochemical models are also employed for model-based SOC estimation since they closely represent the physical behavior inside the cell. Therefore, adding the effect of temperature and modeling the aging phenomenon, the inherent features of Li-ion batteries, to the model are more feasible. Unfortunately, electrochemical models are not applicable for real-time observation because of their complexity.

The cell's representative equations are a set of partial differential algebraic equations and are often transformed to a set of differential algebraic or ordinary differential equations. Two ways of transformation are addressed in the literature on electrochemical model-based SOC observation. The first way of constructing differential algebraic or ordinary differential equations from the original equations requires the discretization of the

system or their integration over space combined with simplifying assumptions. Another method of finite-dimensional approximation of the model is modifying the equations and taking Laplace transform of them with respect to time; then, the resulting equations are solved for an impedance transfer function. Finally, the ordinary differential equations of interest are derived from this transfer function [134].

Simplified versions of electrochemical models tackle the problem of complexity while keeping accuracy. A review on most simplified electrochemical models can be found in [36]. Single particle models are common models introduced to handle the unwanted complexities. These models are made under the assumptions that the electrodes are made of a single spherical particle, there is no change in the concentration and potential of the electrolyte, and the parameters are constant. Coupled with averaging the concentration of the active material, they are used in [135] to construct a finite-dimensional representation and estimate the SOC by the EKF. Averaging over the entire electrode region is also used in [37], [38], and [3] wherein the observation is evaluated by respectively the EKF and output injection-based observer combined with the mass conservation law.

Implementing Laplace transform with respect to time is used in [39] and [40] to transform a single particle model to a set of ordinary differential equations. Afterwards, the Kalman filter is used to estimate the SOC. A more accurate observation method is employed in [41, 42, 43]. In this work, the system is transformed to ordinary differential equations via the Laplace transform as a way of identifying the system's parameters using the impedance technique. An output injection observer is applied in both system dynamics and boundary conditions in a single particle model, and the backstepping approach is employed to design the gains.

Employing a single particle model in the observation is also suggested in some other works including via the Kalman filtering in [44], the sliding mode observer in [45], the backstepping observation method in [41, 42, 43]. More recent studies using full electrochemical equations can be found in [46, 47].

As mentioned in Chapter 1, In all of the aforementioned work, a simple model is adequate to represent the cell behavior; however, these simple models will not provide a similar performance for cells with LFP positive electrode because of a two-phase behavior. A few models have been improved in literature to conduct the two-phase behavior in LFP cells. The efficiency of the different models depends on their performance in treating the two-phase behavior of the lithium insertion/deinsertion. A more physical intuition brings around a more adequate approximation. Variable solid-state diffusivity model is used here as a reliable platform since it is a trade of between simplicity and physical accuracy.

Details on this model can be found in [48], [2], and [49].

In general, these electrochemical equations are nonlinear coupled partial differential equations. They consist of two parts: dynamical equations representing the variation of the active material concentration and constraint equations mapping the concentrations to the potential variables. An important part of an approximation is solving the constraint equations. In most simplified models, the constraint equations are simplified by ignoring the dependence of the exchange current density on the modeling variables [136, 137, 138, 139, 140], and [140]. Linearizing the exchange current density term around some operating points is another way of solving the constraint equations without numerical complications ([141] and [142]). However, in many applications of LFP cells, these approximations are not accurate.

The simplified electrochemical equations can be further reduced by approximation of the partial differential equations by ordinary differential equations. Laplace transforms and Padé approximation are potential ways of constructing a low-order model [143, 144, 140], and [142]. Low-order models can also be achieved via projection based techniques including proper orthogonal decomposition [145] and employing eigenfunctions of the solid diffusion equation [146] and [147]. These low-order models are introduced for a class of simplified models where the solid diffusion coefficient is often assumed to be constant.

The main objective of this chapter is to design an observer for an LFP cell represented by a variable solid-state diffusivity model to predict the battery SOC during a drive cycle. Although electrochemical model-based estimations provide higher accuracy, an efficient approximation is required due to their complexity. So far employed simplified models loose their utility for chemical compositions like LFP at high current rates and dynamics. A more accurate approximation of the original equation which is simple enough to be solved in the real-time SOC estimation is required.

As the first step of observer design, a numerically more efficient model is introduced in this chapter; for this purpose, physical continuity of modeling variables is used. Next, a reduced order model is developed via some base functions derived from the system dynamics. It is shown that as the dimension of the reduced order model increases a subsequence of the solutions converging to the solution of the cell original equations can be found.

In addition, due to the simplifying assumptions, the model has some uncertainties. In order to compensate for the uncertainties, an adaptive observer providing enough accuracy and robustness to the modeling uncertainties is developed. This observer is an

Table 5.1: Lithium-ion cell parameters [2].

parameter	definition	value (separator, and LFP electrode)
l_{cat}	thickness of the negative electrode	$72e-6$
l_{sep}	thickness of the separator	$675e-6$
R_s	radius of the spherical solid particles	$-,($ $1.44e-7, 2.70e-7, 5.42e-7)$
R	gas constant	8.3145
F	Faraday's constant	96485
t_+^0	transference number	0.363, 0.363
ϵ_e	volume fraction of the electrolyte phase	0.6, 0.5
k^{eff}	effective conductivity in the electrolyte phase	0.6042, 0.4596
k_D^{eff}	$\frac{k^{eff}2RT(1-t_+^0)}{F}$	
σ^{eff}	effective conductivity in the solid phase	$-$, 0.855
D_e^{eff}	effective diffusivity in the electrolyte phase	$7.500e-11$, $1.633e-11$
D_s	Diffusion coefficient of the spherical particle	$-$, $1e-13$
$c_{s,max}$	maximum solid state concentration	$-$, $22.860e3$
i_0	exchange current density	0, $3.25e-2$

adaptive EKF wherein the parameters of the OCP term, which is an important part of modeling, is allowed to change over time. In this way, the effect of hysteresis can be included even when the OCP has a single-value empirical representation. Compared to the experimental data, the simulation results confirm the performance of the proposed observer.

5.2 Mathematical model

As mentioned previously, in this section, a lithium-ion cell whose positive electrode is made of LFP material is considered. In LFP electrodes, the lithium insertion/deinsertion mechanism is a two phase process taking place between the lithium poor phase, $Li_\epsilon FePO_4$, and the lithium rich phase, $LI_{1-\epsilon}FePO_4$. The negative electrode is assumed to be a lithium foil. The details of the electrochemical model can be found in Chapter 4. Here, the number of particle sizes are set $K = 3$ and the solid-state diffusion coefficient is state dependent. This model is different from what is used to investigate the hysteresis coming from the system's dynamics; it has different parameters and number of particle sizes.

The battery cell's equations considered in this section are denoted in a state space

representation as follows. Define

$$\begin{aligned}
\mathcal{X}_1 &= \{z \in \mathcal{L}^2([L_1, L] \times [0, R_1]) : r_1^2 z \in \mathcal{L}^2([L_1, L] \times [0, R_1])\} \\
\mathcal{X}_2 &= \{z \in \mathcal{L}^2([L_1, L] \times [0, R_2]) : r_2^2 z \in \mathcal{L}^2([L_1, L] \times [0, R_1])\} \\
\mathcal{X}_3 &= \{z \in \mathcal{L}^2([L_1, L] \times [0, R_3]) : r_3^2 z \in \mathcal{L}^2([L_1, L] \times [0, R_1])\} \\
\mathcal{X} &= \mathcal{L}^2(0, L) \times \mathcal{X}_1 \times \mathcal{X}_2 \times \mathcal{X}_3 \\
\mathcal{Y} &= \mathcal{L}^2(0, L) \times \mathcal{L}^2(L_1, L)
\end{aligned}$$

where $L_1 = l_{sep}$, $L = l_{sep} + l_{cat}$. Let $\boldsymbol{c} = [c_1, c_2, c_3, c_4]^T = [c_e, c_{s,1}, c_{s,2}, c_{s,3}]^T \subseteq \mathcal{X}$ be the state vector and $\boldsymbol{\varphi} = [\varphi_1, \varphi_2]^T = [\varphi_e, \varphi_s]^T \subseteq \mathcal{Y}$ be the constraint vector; from a physical point of view, c_e represents the electrolyte concentration, $c_{s,k}$ are the solid concentration in every particle bin $k = 1, \ldots, 3$, and φ_e and φ_s represent respectively the electrolyte and solid potential.

Define

$$y_k = \mathrm{sat_y}(\frac{\mathrm{c_{k+1}}\ |_{\mathrm{r_k=R_k}}}{\mathrm{c_{max}}}) \tag{5.1}$$

where

$$sat_y(s) = \frac{1}{1 + \exp(-a_0 s)}$$

for $a_0, a_1 \in \mathbb{R}^+$ (see Table 5.2), and $\alpha_k(.)$, the Fréchet differentiable functions,

$$\alpha_k(c_{k+1}) = 6\exp(-25y_k) + 15\exp(-35(1 - y_k)) + 0.3/(1 + (y_k - 0.5)^2).$$

Note that

$$\delta_1 \leq |\alpha_k(c_{k+1})| \leq \delta_2 \tag{5.2}$$

for $k = 1, \ldots, 3$ and $\delta_1, \delta_2 \in \mathbb{R}^+$. The electrochemical reaction rate is defined as

$$i_k(\boldsymbol{c}, \boldsymbol{\varphi}) = \begin{cases} 2i_0 \sinh(\frac{F\eta_k}{2RT}) & \text{if } x \in [0, L_1] \\ 0 & \text{if } x \in [L_1, L] \end{cases} \tag{5.3}$$

where

$$\eta_k = \varphi_2 - \varphi_1 - U(y_k)$$

and $U(.)$ is the OCP term;

$$\begin{aligned}
U(y_k) = {} & 3.4510 - 0.009y_k \\
& + 0.6687\exp(-30y_k) - 0.5\exp(-200(1 - x))
\end{aligned}$$

for the charging cycle, and

$$U(y_k) = 3.4077 - 0.020269y_k + 0.5\exp(-200y_k) - 0.9\exp(-30(1-x))$$

for the discharging cycle. The OCP profile has an important effect on the simulations and must be identified carefully. The OCP identification is based on the static performance and cannot be measured during the battery operation. Instead, empirically derived relations are used. It is obtained through a curve fitting.

The cell governing equations are

$$\frac{\partial}{\partial t}\begin{bmatrix} c_1 \\ c_2 \\ c_3 \\ c_4 \end{bmatrix} = \begin{bmatrix} \frac{\partial}{\partial x}(D_e\frac{\partial c_1}{\partial x}) + \frac{1-t_+^0}{F\epsilon}\sum a_k i_k(\boldsymbol{c},\boldsymbol{\varphi}) \\ \frac{1}{r_1^2}\frac{\partial}{\partial r_1}(r_1^2\alpha_1(c_2)\mathcal{D}\frac{\partial c_2}{\partial r_1}) \\ \frac{1}{r_2^2}\frac{\partial}{\partial r_2}(r_2^2\alpha_2(c_3)\mathcal{D}\frac{\partial c_3}{\partial r_2}) \\ \frac{1}{r_3^2}\frac{\partial}{\partial r_3}(r_3^2\alpha_3(c_4)\mathcal{D}\frac{\partial c_4}{\partial r_3}) \end{bmatrix} \tag{5.4}$$

$$0 = \begin{bmatrix} \frac{\partial}{\partial x}(k_{eff}\frac{\partial \varphi_1}{\partial x}) + k_{eff}\frac{\partial}{\partial x}(\frac{2RT(1-t_+^0)}{Fc_1}\frac{\partial c_1}{\partial x}) + \sum a_k i_k(\boldsymbol{c},\boldsymbol{\varphi}) \\ \frac{\partial}{\partial x}(\sigma^{eff}\frac{\partial \varphi_2}{\partial x}) - \sum a_k i_k(\boldsymbol{c},\boldsymbol{\varphi}) \end{bmatrix} \tag{5.5}$$

The boundary conditions are

$$\frac{\partial c_1}{\partial x}\mid_{x=L} = 0 \tag{5.6}$$

$$\frac{\partial c_{k+1}}{\partial r_k}\mid_{r_k=0} = 0, \quad k = 1\ldots 3 \tag{5.7}$$

$$\varphi_1\mid_{x=0} = 0 \tag{5.8}$$

$$\frac{\partial \varphi_1}{\partial x}\mid_{x=L} = 0 \tag{5.9}$$

$$\frac{\partial \varphi_2}{\partial x}\mid_{x=L_1} = 0. \tag{5.10}$$

$$\tag{5.11}$$

The controlled input is current $I(t)$,

$$\epsilon_{sep}D_{eff,sep}\frac{\partial c_1}{\partial x}\mid_{x=0} = -\frac{(1-t_+^0)I(t)}{F} \tag{5.12}$$

$$-\sigma^{eff}\frac{\partial \varphi_2}{\partial x}\mid_{x=L} = I(t). \tag{5.13}$$

$$\tag{5.14}$$

Also

$$\alpha_k(c_{k+1})\mathcal{D}\frac{\partial c_{k+1}}{\partial r_k}\mid_{r_k=R_k} = \frac{i_k}{F}(\boldsymbol{c},\boldsymbol{\varphi}), \quad k = 1\ldots 3. \tag{5.15}$$

5.3 State space representation

The battery governing equations include both differential and algebraic equations respectively represented by (5.4) and (5.5). For infinite-dimensional systems, these types of equations are called partial differential algebraic equations. Finding the solution to these equations requires solving a set of algebraic equations simultaneously with the differential equations. The governing equations will be replaced by fully differential equations, which are numerically easier to handle.

Some approximations are now introduced to the model to facilitate computation. First, the reaction rate is approximated. For this purpose, the variable $y_{k,s}$ defined in (5.1) is substituted by an average value. Define

$$\bar{c}_{k+1} = \int_0^{R_k} \delta(x - R_k) c_{k+1} dr_k$$

and

$$\bar{y}_k = \mathrm{sat_y}(\frac{\bar{\mathrm{c}}_{\mathrm{k+1}}}{\mathrm{c_{max}}})$$

where

$$\delta(x - x0) = \begin{cases} \frac{1}{\epsilon_0} & \text{if } x \in [x0 - \epsilon_0, x0] \\ 0 & \text{if } x \in [0, x0 - \epsilon_0] \end{cases} \tag{5.16}$$

for some small $\epsilon_0 > 0$ (see Table 5.2). For parameters b_0, a_0 (see Table 5.2), define

$$\mathrm{sat(s)} = \frac{2\mathrm{b_0}}{1 + \exp(-\mathrm{a_0 s})} - \mathrm{b_0}$$

and also define

$$\bar{\eta}_k = \varphi_2 - \varphi_1 - U(\bar{y}_k).$$

The exchange current density is approximated by

$$\bar{i}_k(\boldsymbol{c}, \boldsymbol{\varphi}) = \begin{cases} 2i_0 \sinh(\mathrm{sat}(\frac{\mathrm{F}\bar{\eta}_\mathrm{k}}{2\mathrm{RT}})) & \text{if } x \in [0, L_1] \\ 0 & \text{if } x \in [L_1, L] \end{cases} \tag{5.17}$$

The argument of sinh(.) is saturated in (5.17) to keep the electrochemical solution bounded. This constraint aligns with the physics of the system.

A second approximation is used to ensure that the constraint equation (5.5) has a unique solution $\boldsymbol{\varphi}$ for every given state vector $\boldsymbol{c}$ and to facilitate its computation. The

constraint equations are approximated by replacing c_1 with its initial value c_{ini} in the denominator. This yields

$$0 = \begin{bmatrix} \frac{\partial}{\partial x}(k_{eff}\frac{\partial \varphi_1}{\partial x}) + k_{eff}\frac{\partial}{\partial x}(\frac{2RT(1-t_+^0)}{Fc_{ini}}\frac{\partial c_1}{\partial x}) + \sum a_k \bar{i}_k(\boldsymbol{c},\boldsymbol{\varphi}) \\ \frac{\partial}{\partial x}(\sigma^{eff}\frac{\partial \varphi_2}{\partial x}) - \sum a_k \bar{i}_k(\boldsymbol{c},\boldsymbol{\varphi}) \end{bmatrix} \tag{5.18}$$

The potential vector $\boldsymbol{\varphi}$ is a function of the state vector $\boldsymbol{c}$ as given by the following theorem.

Theorem 5.3.1. *Let the constraint equations (5.5) be approximated by (5.18). Define the operator $D\boldsymbol{\mathcal{O}}(.) : \mathcal{X} \times \mathcal{Y} \times \mathbb{R}^3 \to \mathcal{Y}^{3\times 3}$ as*

$$D\boldsymbol{\mathcal{O}}(\boldsymbol{c},\boldsymbol{\varphi},I(t),c_1(0),\varphi_2(L_1)) = \begin{bmatrix} k^{eff} + \sum_{k=1}^3 a_k \int_0^x \int_0^y \frac{\partial \bar{i}_k(\boldsymbol{c},\boldsymbol{\varphi})}{\partial \varphi_1} & \sum_{k=1}^3 a_k \int_0^x \int_0^y \frac{\partial \bar{i}_k(\boldsymbol{c},\boldsymbol{\varphi})}{\partial \varphi_2} & 0 \\ -x\int_0^L \sum_{k=1}^3 a_k \frac{\partial \bar{i}_k(\boldsymbol{c},\boldsymbol{\varphi})}{\partial \varphi_1} & -x\int_0^L \sum_{k=1}^3 a_k \frac{\partial \bar{i}_k(\boldsymbol{c},\boldsymbol{\varphi})}{\partial \varphi_2} & \\ -\sum_{k=1}^3 a_k \int_0^x \int_0^y \frac{\partial \bar{i}_k(\boldsymbol{c},\boldsymbol{\varphi})}{\partial \varphi_1} & \sigma^{eff} - \sum_{k=1}^3 a_k \int_0^x \int_0^y \frac{\partial \bar{i}_k(\boldsymbol{c},\boldsymbol{\varphi})}{\partial \varphi_2} & \sigma^{eff} \\ \int_0^L \sum_{k=1}^3 a_k \frac{\partial \bar{i}_k(\boldsymbol{c},\boldsymbol{\varphi})}{\partial \varphi_1} & \int_0^L \sum_{k=1}^3 a_k \frac{\partial \bar{i}_k(\boldsymbol{c},\boldsymbol{\varphi})}{\partial \varphi_2} & 0. \end{bmatrix} \tag{5.19}$$

If $D\boldsymbol{\mathcal{O}}(.)$ is nonsingular at $[\boldsymbol{c}^*,\boldsymbol{\varphi}^*,I^*,c_0^*,\varphi_0^*]^T \in \mathcal{X}\times\mathcal{Y}\times\mathbb{R}^3$, the potential vector $\boldsymbol{\varphi}$ can be written as a Fréchet differentiable function of the state vector $\boldsymbol{c}$ and the input $I(t)$ in a neighborhood of this point. In other words, in some neighborhood of $[\boldsymbol{c}^*,\boldsymbol{\varphi}^*,I^*,c_0^*,\varphi_0^*]$,

$$\boldsymbol{\varphi} = \boldsymbol{\mathcal{R}}_{\boldsymbol{\varphi}}(\boldsymbol{c},c_1(0),I(t)) \tag{5.20}$$

where $\boldsymbol{\mathcal{R}}_{\boldsymbol{\varphi}}(.) : \mathcal{X}\times\mathbb{R}^2 \to \mathcal{Y}$ is some Fréchet differentiable function.

Proof: In this proof, it is shown that $\boldsymbol{\varphi}$ is defined implicitly through the solution to a function $\boldsymbol{\mathcal{O}}(.)$ It is proved that this function is Fréchet differentiable with derivative (5.19). The result is a consequence of the Implicit Function Theorem [148, Theorem 1.1.23].

In the first step, define

$$\mathcal{O}_1(.),\mathcal{O}_2(.),\mathcal{O}_3(.) : \mathcal{X}\times\mathcal{Y}\times\mathbb{R}^3 \to \mathcal{Y}$$

as

$$
\begin{aligned}
&\mathcal{O}_1(\boldsymbol{c}, \boldsymbol{\varphi}, I(t), c_1(0), \varphi_2(L_1)) \\
&= \frac{x}{k^{eff}} \int_0^L \sum_{k=1}^{3} a_k \bar{i}_k(\boldsymbol{c}, \boldsymbol{\varphi}) - \frac{2RT(1-t_+^0)}{Fc_{ini}}(c_1 - c_1(0)) \\
&- \frac{1}{k^{eff}} \int_0^x \int_0^y \sum_{k=1}^{3} a_k \bar{i}_k(\boldsymbol{c}, \boldsymbol{\varphi}), \\
&\mathcal{O}_2(\boldsymbol{c}, \boldsymbol{\varphi}, I(t), c_1(0), \varphi_2(L_1)) \\
&= \varphi_2(L_1) + \frac{1}{\sigma^{eff}} \int_0^x \int_0^y \sum_{k=1}^{3} a_k \bar{i}_k(\boldsymbol{c}, \boldsymbol{\varphi}), \\
&\mathcal{O}_3(\boldsymbol{c}, \boldsymbol{\varphi}, I(t), c_1(0), \varphi_2(L_1)) \\
&= I(t) + \int_0^L \sum_{k=1}^{3} a_k \bar{i}_k(\boldsymbol{c}, \boldsymbol{\varphi}).
\end{aligned}
$$

combined with boundary conditions in (5.6), (5.8), (5.9), (5.10), (5.12), and (5.13), the algebraic equation (5.5) can be rewritten as

$$
\begin{aligned}
\varphi_1 &= \mathcal{O}_1(\boldsymbol{c}, \boldsymbol{\varphi}, I(t), c_1(0), \varphi_2(L_1)) \\
\varphi_2 &= \mathcal{O}_2(\boldsymbol{c}, \boldsymbol{\varphi}, I(t), c_1(0), \varphi_2(L_1)) \\
0 &= \mathcal{O}_3(\boldsymbol{c}, \boldsymbol{\varphi}, I(t), c_1(0), \varphi_2(L_1))
\end{aligned}
\tag{5.21}
$$

Note that the functions $\bar{i}_k(.)$ for $k = 1, \ldots, 3$ are Fréchet differentiable with respect to their arguments. This is due to the fact that sat(.), $\text{sat}_{\text{y}}(.)$, and the empirical function chosen for OCP $U(.)$, as well as the function sinh(.) are Fréchet differentiable with respect to their arguments. Therefore, from the definition of $\bar{i}_k(.)$ given by (5.3) and the chain rule, it can be concluded that $\bar{i}_k(.)$ are Fréchet differentiable functions.

Since integration is a linear operation, the fact that the functions $\bar{i}_k(.)$ are Fréchet differentiable leads to the Fréchet differentiability of the functions $\mathcal{O}_1(.)$, $\mathcal{O}_2(.)$, and $\mathcal{O}_3(.)$ with respect to $[c_2, \ldots, c_4]^T$ and $\boldsymbol{\varphi}$; these functions are linear and thus differentiable with respect to $(c_1 - c_1(0))$, $\varphi_2(L_1)$, and $I(t)$. Define

$$
\begin{aligned}
&\boldsymbol{\mathcal{O}}(\boldsymbol{c}, \boldsymbol{\varphi}, I(t), c_1(0), \varphi_2(L_1)) = \\
&\qquad \begin{bmatrix} k^{eff}(\varphi_1 - \mathcal{O}_1(\boldsymbol{c}, \boldsymbol{\varphi}, I(t), c_1(0), \varphi_2(L_1))) \\ \sigma^{eff}(\varphi_2 - \mathcal{O}_2(\boldsymbol{c}, \boldsymbol{\varphi}, I(t), c_1(0), \varphi_2(L_1))) \\ \mathcal{O}_3(\boldsymbol{c}, \boldsymbol{\varphi}, I(t), c_1(0), \varphi_2(L_1)) \end{bmatrix}.
\end{aligned}
\tag{5.22}
$$

The Fréchet derivative of the nonlinear operator $\boldsymbol{\mathcal{O}}(.)$ (5.22) with respect to the vector $[\boldsymbol{\varphi}, \varphi_2(L_1)]^T$ is (5.19). In addition, (5.21) can be written as

$$\boldsymbol{\mathcal{O}}(\boldsymbol{c}, \boldsymbol{\varphi}, I(t), c_1(0), \varphi_2(L_1)) = \mathbf{0}.$$

Now, by the Implicit Function Theorem and the assumption of $D\boldsymbol{\mathcal{O}}(.)$ being nonsingular in some neighborhood of $[\boldsymbol{c}^*, \boldsymbol{\varphi}^*, I^*, c_0^*, \varphi_0^*]^T$, (5.20) follows. □

At this point, for the sake of simplicity and future use, $\boldsymbol{\mathcal{R}}_{\boldsymbol{\varphi}}(.)$ in (5.20) is approximated by

$$\boldsymbol{\varphi} = \bar{\boldsymbol{\mathcal{R}}}_{\boldsymbol{\varphi}}(\boldsymbol{c}, I(t)) = \boldsymbol{\mathcal{R}}_{\boldsymbol{\varphi}}(\boldsymbol{c}, \int_0^L \delta(x) c_1, I(t)) \tag{5.23}$$

where

$$\delta(x) = \begin{cases} \frac{1}{\epsilon_0} & \text{if } x \in [0, \epsilon_0] \\ 0 & \text{if } x \in [\epsilon_0, L] \end{cases} \tag{5.24}$$

for some small $\epsilon_0 \in \mathbb{R}^+$ given in Table 5.2. This approximation is feasible due to the continuity of the electrolyte concentration.

Next, a new form of the constraint equations is achieved by taking the time differentiation of both sides of (5.23). Along with (5.4), differentiating (5.23) results in

$$\frac{\partial \boldsymbol{\varphi}}{\partial t} = D\bar{\boldsymbol{\mathcal{R}}}_{\boldsymbol{\varphi}}(\boldsymbol{c}, I(t))(\frac{\partial \boldsymbol{c}}{\partial t}) + \frac{\partial \bar{\boldsymbol{\mathcal{R}}}_{\boldsymbol{\varphi}}(\boldsymbol{c}, I(t))}{\partial I} \frac{dI(t)}{dt}. \tag{5.25}$$

The battery equations are solved by replacing the constraint equation (5.5) with its equivalent differential equations (5.25). With this setting, any standard technique of solving differential equations can be used without dealing with algebraic equations directly.

A difficulty involved in solving (5.4) and (5.25) is finding the time derivative of the input $I(t)$. This problem can be resolved by employing the saturated high-speed observer introduced in [81],

$$\frac{d\hat{x}}{dt} = \boldsymbol{M}\hat{x} + \boldsymbol{L}I(t) \tag{5.26}$$

where $\hat{x}^T = [\hat{I}, \hat{dI/dt}]$, and

$$\boldsymbol{M} = \begin{bmatrix} -ga_1 & 1 \\ -g^2 a_0 & 0 \end{bmatrix}, \quad \boldsymbol{L} = \begin{bmatrix} -ga_1 \\ -g^2 a_0 \end{bmatrix}$$

in which $g, a_0, a_1 \in \mathbb{R}^+$ are tuning parameters.

A third approximation of the cell's equations is made. Let both sides of (5.4) followed by approximation (5.17) be multiplied by $\boldsymbol{w} = [w_1, \ldots, w_4]^T \in \mathcal{X}$ in the sense of the $\mathcal{X}$-inner product as follows:

$$\begin{aligned}\int_0^L w_1 \frac{\partial c_1}{\partial t} dx &= \int_0^L w_1 (\frac{\partial}{\partial x}(D_{eff}\frac{\partial c_1}{\partial x}) \\ &\quad + \frac{1-t_+^0}{F\epsilon}\sum a_k \bar{i}_k(\boldsymbol{c}, \boldsymbol{\varphi}))dx \\ \int_{L_1}^L \int_0^{R_k} r_k^2 w_{k+1}\frac{\partial c_{k+1}}{\partial t} dr_k dx &= \int_{L_1}^L \int_0^{R_k} r_k^2 w_{k+1}\frac{1}{r_k^2}\frac{\partial}{\partial r_k}(r_k^2 \alpha_k(c_{k+1})\mathcal{D}\frac{\partial c_{k+1}}{\partial r_k})dr_k dx\end{aligned} \tag{5.27}$$

for $k = 1, \ldots, 3$. Now, applying integration by parts to (5.27) and employing boundary conditions (5.6), (5.7), (5.12), and (5.15) followed by approximation (5.17) lead to

$$\begin{aligned}\int_0^L w_1 \frac{\partial c_1}{\partial t} dx &= \int_0^L (-\frac{\partial w_1}{\partial x}(D_{eff}\frac{\partial c_1}{\partial x}) + w_1 \frac{1-t_+^0}{F\epsilon}\sum a_k \bar{i}_k(\boldsymbol{c}, \boldsymbol{\varphi}))dx \\ &\quad + \frac{1-t_+^0}{\epsilon F} w_1(0) I(t) \\ \int_{L_1}^L \int_0^{R_k} r_k^2 w_{k+1}\frac{\partial c_{k+1}}{\partial t} dr_k dx &= -\int_{L_1}^L \int_0^{R_k} \frac{\partial w_{k+1}}{\partial r_k}(r_k^2 \alpha_k(c_{k+1})\mathcal{D}\frac{\partial c_{k+1}}{\partial r_k})dr_k dx \\ &\quad + \frac{R_k^2}{F}\int_0^L w_{k+1}(R_k)\bar{i}_k(\boldsymbol{c}, \boldsymbol{\varphi}))dx.\end{aligned} \tag{5.28}$$

Next, (5.28) is approximated by

$$\begin{aligned}\int_0^L w_1 \frac{\partial c_1}{\partial t} dx &= \int_0^L (-\frac{\partial w_1}{\partial x}(D_{eff}\frac{\partial c_1}{\partial x}) + w_1 \frac{1-t_+^0}{F\epsilon}\sum a_k \bar{i}_k(\bar{\boldsymbol{c}}, \boldsymbol{\varphi}))dx + \\ &\quad \frac{1-t_+^0}{\epsilon F}\int_0^L \delta(x-L) w_1 I(t) dx \\ \int_{L_1}^L \int_0^{R_k} r_k^2 w_{k+1}\frac{\partial c_{k+1}}{\partial t} dr_k dx &= -\int_{L_1}^L \int_0^{R_k} \frac{\partial w_{k+1}}{\partial r_k}(r_k^2 \alpha_k(c_{k+1})\mathcal{D}\frac{\partial c_{k+1}}{\partial r_k})dr_k dx \\ &\quad + \frac{R_k^2}{F}\int_0^L \int_0^{R_k} r_k^2 \frac{\delta(r_k - R_k)}{r_k^2} w_{k+1}\bar{i}_k(\bar{\boldsymbol{c}}, \boldsymbol{\varphi}))dr_k dx.\end{aligned} \tag{5.29}$$

Using integration by parts in (5.29), the battery equations can be transformed into

$$\frac{\partial \boldsymbol{c}}{\partial t} + \boldsymbol{\mathcal{A}}\boldsymbol{\mathcal{N}}(\boldsymbol{c}) = \boldsymbol{\mathcal{R}}(\boldsymbol{c}, t) + \boldsymbol{\mathcal{F}}\boldsymbol{u}(t) \tag{5.30}$$

where $\boldsymbol{\mathcal{A}} : \mathcal{X} \to \mathcal{X}$ is a linear operator, $\boldsymbol{\mathcal{R}}(.), \boldsymbol{\mathcal{N}}(.) : \mathcal{X} \to \mathcal{X}$ are nonlinear Fréchet differentiable functions, $\boldsymbol{\mathcal{F}} : \mathbb{R}^q \to \mathcal{X}$ is a bounded linear input operator, and $\boldsymbol{u}(t)$ is the

input vector defined as

$$\boldsymbol{\mathcal{A}} = +\lambda \boldsymbol{\mathcal{I}} \tag{5.31}$$

$$- \begin{bmatrix} \frac{\partial}{\partial x}(D_e \frac{\partial}{\partial x}) & 0 & 0 & 0 \\ 0 & \frac{\mathcal{D}}{r_1^2}\frac{\partial}{\partial r_1}(r_1^2 \frac{\partial}{\partial r_1}) & 0 & 0 \\ 0 & 0 & \frac{\mathcal{D}}{r_2^2}\frac{\partial}{\partial r_2}(r_2^2 \frac{\partial}{\partial r_2}) & 0 \\ 0 & 0 & 0 & \frac{\mathcal{D}}{r_3^2}\frac{\partial}{\partial r_3}(r_3^2 \frac{\partial}{\partial r_3}) \end{bmatrix} \tag{5.32}$$

where $\lambda > 0$ is set such that $\boldsymbol{\mathcal{A}}$ is positive definite as in Assumption 3.2.6, and

$$\begin{aligned} \mathcal{D}(\boldsymbol{\mathcal{A}}) = \{ & \boldsymbol{c} \in \mathcal{X}, [\frac{\partial c_1}{\partial x}, \frac{\partial c_2}{\partial r}, \ldots, \frac{\partial c_4}{\partial r}]^T \in \mathcal{X}, \\ & [\frac{\partial^2 c_1}{\partial x^2}, \frac{\partial^2 c_2}{\partial r^2}, \ldots, \frac{\partial^2 c_4}{\partial r^2}]^T \in \mathcal{X} \\ & \frac{\partial c_1}{\partial x}(0) = \frac{\partial c_1}{\partial x}(L) = 0, \text{ and} \\ & \frac{\partial c_k}{\partial r}(0) = \frac{\partial c_k}{\partial r}(0)(R_k) = 0 \text{ for } \ k = 2 \ldots 4\}. \end{aligned} \tag{5.33}$$

$$\boldsymbol{\mathcal{N}}(\boldsymbol{c}) = \begin{bmatrix} c_1 \\ \int_0^{r_1} \alpha_1(c_2(s,t)) \frac{\partial c_2}{\partial r_1}(s,t) ds \\ \int_0^{r_2} \alpha_2(c_3(s,t)) \frac{\partial c_3}{\partial r_2}(s,t) ds \\ \int_0^{r_3} \alpha_3(c_4(s,t)) \frac{\partial c_4}{\partial r_3}(s,t) ds \end{bmatrix} \tag{5.34}$$

$$\boldsymbol{\mathcal{E}}(\boldsymbol{c}, \boldsymbol{\varphi}) = \begin{bmatrix} \frac{1-t_+^0}{F\epsilon} \sum a_k \bar{i}_k(\boldsymbol{c}, \boldsymbol{\varphi}) \\ \frac{R_1^2}{F} \frac{\delta(r_1 - R_1)}{r_1^2} \bar{i}_1(\boldsymbol{c}, \boldsymbol{\varphi}) \\ \frac{R_2^2}{F} \frac{\delta(r_2 - R_2)}{r_2^2} \bar{i}_2(\boldsymbol{c}, \boldsymbol{\varphi}) \\ \frac{R_3^2}{F} \frac{\delta(r_3 - R_3)}{r_3^2} \bar{i}_3(\boldsymbol{c}, \boldsymbol{\varphi}) \end{bmatrix} + \lambda \boldsymbol{\mathcal{N}}(\boldsymbol{c}) \tag{5.35}$$

$$\boldsymbol{\mathcal{B}} = \begin{bmatrix} \frac{1-t_+^0}{\epsilon F} \delta(x - L) \\ 0 \\ 0 \\ 0 \end{bmatrix} \tag{5.36}$$

$$\boldsymbol{\mathcal{R}}_{\boldsymbol{c}}(\boldsymbol{c}, \boldsymbol{\varphi}) = \boldsymbol{\mathcal{E}}(\boldsymbol{c}, \boldsymbol{\varphi}) - \boldsymbol{\mathcal{E}}(\boldsymbol{0}, \boldsymbol{\varphi}) \tag{5.37}$$

$$\boldsymbol{\mathcal{R}}(\boldsymbol{c}, t) = \boldsymbol{\mathcal{R}}_{\boldsymbol{c}}(\boldsymbol{c}, \bar{\boldsymbol{\mathcal{R}}}_{\boldsymbol{\varphi}}(\boldsymbol{c}, I(t))), \tag{5.38}$$

$$\boldsymbol{\mathcal{F}} = [\boldsymbol{\mathcal{B}}, \boldsymbol{\mathcal{I}}], \quad \boldsymbol{u}(t) = [I(t), \boldsymbol{\mathcal{E}}(\boldsymbol{0}, t)^T]^T. \tag{5.39}$$

Finally, a fully dynamical representation equivalent to (5.30) has been introduced as

$$\begin{aligned}\frac{\partial \boldsymbol{c}}{\partial t} + \boldsymbol{\mathcal{A}}\boldsymbol{c} &= \boldsymbol{\mathcal{R}}_{\boldsymbol{c}}(\boldsymbol{c}, \boldsymbol{\varphi}) + \boldsymbol{\mathcal{F}}\boldsymbol{u}(t) \\ \frac{\partial \boldsymbol{\varphi}}{\partial t} &= D_{\boldsymbol{c}}\bar{\boldsymbol{\mathcal{R}}}_{\boldsymbol{\varphi}}(\boldsymbol{c}, I(t))\frac{\partial \boldsymbol{c}}{\partial t} + \frac{\partial \bar{\boldsymbol{\mathcal{R}}}_{\boldsymbol{\varphi}}(\boldsymbol{c}, I(t))}{\partial I}\frac{dI(t)}{dt}\end{aligned} \tag{5.40}$$

where $D_{\boldsymbol{c}}$ represents the Fréchet derivative with respect to $\boldsymbol{c}$.

It can be shown that the state space representation (5.30) satisfies the conditions of Theorem 3.3.5. First, it is shown that the linear operator $\boldsymbol{\mathcal{A}}$ is self-adjoint.

Lemma 5.3.2. *The linear operator $\boldsymbol{\mathcal{A}} : \mathcal{D}(\boldsymbol{\mathcal{A}}) \in \mathcal{X} \to \mathcal{X}$ is self-adjoint.*

Proof: For $\boldsymbol{w} \in \mathcal{D}(\boldsymbol{\mathcal{A}})$ and $\boldsymbol{v} \in \mathcal{X}$, employing integration by parts and substituting the boundary conditions given by (5.33) result in

$$\begin{aligned}(\boldsymbol{\mathcal{A}}\boldsymbol{w}, \boldsymbol{v})_{\mathcal{X}} = &-D_{eff}(w_1(L)\frac{\partial w_1}{\partial x}(L) - w_1(0)\frac{\partial w_1}{\partial x}(0)) \\ &- \sum \int_0^L R_k^2 w_{k+1}(R_k)\frac{\partial v_{k+1}}{\partial r_k}(R_k)dx + (\boldsymbol{w}, \boldsymbol{\mathcal{A}}\boldsymbol{v})_{\mathcal{X}}.\end{aligned} \tag{5.41}$$

Now, by setting $\boldsymbol{v} \in \mathcal{D}(\boldsymbol{\mathcal{A}})$, one can conclude that

$$\mathcal{D}(\boldsymbol{\mathcal{A}}) = \mathcal{D}(\boldsymbol{\mathcal{A}}^*), \quad \boldsymbol{\mathcal{A}} = \boldsymbol{\mathcal{A}}^*$$

and the operator $\boldsymbol{\mathcal{A}}$ is self-adjoint. □

Corollary 5.3.3. *Let the input signal $\boldsymbol{u}$ and the initial condition respectively satisfy Assumption 3.2.5 and $\boldsymbol{\mathcal{N}}(\boldsymbol{c}(0)) \in \mathcal{D}(\boldsymbol{\mathcal{A}}^{1/2})$. The system (5.30) has a unique solution $\boldsymbol{c}$. Furthermore, for the state vector $\boldsymbol{z} = \boldsymbol{c}$, the system can be approximated by finite-dimensional equations (3.25) with solutions $\boldsymbol{c}_N$ admitting a convergent subsequence in $\mathcal{L}^2([0, t_f]; \mathcal{X})$ where $[0, t_f]$ is a finite time interval.*

Proof: First, by Lemma 5.3.2, $\boldsymbol{\mathcal{A}}$ is self-adjoint. Furthermore, it can be easily checked that the inverse of the linear operator $\boldsymbol{\mathcal{A}}$ can be represented as a Hilbert Schmidt integral; thus, it is a compact operator [149]. This property along with the self-adjointness leads to the fact that the linear operator $\boldsymbol{\mathcal{A}}$ satisfies Assumption 3.2.6 and has eigenfunctions which are an orthogonal basis for the Hilbert space $\mathcal{X}$ [116, theorem VIII.6].

Next, it is proved that the nonlinear operators $\boldsymbol{\mathcal{N}}(.)$ and $\boldsymbol{\mathcal{R}}(.)$ satisfy Assumptions 3.3.2, 3.3.3, and 3.2.7. First, it can be concluded from the definition of $\boldsymbol{\mathcal{N}}(.)$ and chain

rule theorem [150][Theorem 3.2.1] that

$$D\boldsymbol{\mathcal{N}}(\boldsymbol{c}) = \begin{bmatrix} \mathcal{I} & 0 & 0 & 0 \\ 0 & \alpha_1(c_2) & 0 & 0 \\ 0 & 0 & \alpha_2(c_3) & 0 \\ 0 & 0 & 0 & \alpha_3(c_4) \end{bmatrix}. \tag{5.42}$$

Define

$$\delta_3 = \min(1, \delta_1), \quad \delta_4 = \max(1, \delta_2).$$

From (5.42) and the boundedness given by (5.2), it is observed that

$$\begin{aligned} \delta_3 \leq & \|D\boldsymbol{\mathcal{N}}(\boldsymbol{w}_2)\| \leq \delta_4 \\ \delta_3\|\boldsymbol{w}_1\|_{\mathcal{X}}^2 \leq & (\boldsymbol{w}_1, D\boldsymbol{\mathcal{N}}(\boldsymbol{w}_2)\boldsymbol{w}_1)_{\mathcal{X}} \leq \delta_4\|\boldsymbol{w}_1\|_{\mathcal{X}}^2 \end{aligned} \tag{5.43}$$

for every $\boldsymbol{w}_1, \boldsymbol{w}_2 \in \mathcal{X}$, and thus Assumption 3.3.2 is satisfied. Furthermore, from definition of $\boldsymbol{\mathcal{A}}$ and $\boldsymbol{\mathcal{N}}(.)$,

$$(\boldsymbol{w}, \boldsymbol{\mathcal{A}}\boldsymbol{\mathcal{N}}(\boldsymbol{w}))_{\mathcal{X}} \geq \lambda\|\boldsymbol{w}\|_{\mathcal{X}}^2 \tag{5.44}$$

for $\boldsymbol{w} \in \mathcal{D}(\boldsymbol{\mathcal{A}}^{1/2})$ such that $\boldsymbol{\mathcal{N}}(\boldsymbol{w}) \in \mathcal{D}(\boldsymbol{\mathcal{A}})$; thus, Assumption 3.3.3 is satisfied.

Finally, the nonlinear operator $\boldsymbol{\mathcal{R}}(., t)$ is a composition of smooth functions of the potential vector $\boldsymbol{\varphi}$ and the vector $[\mathrm{sat_y(c_2)}, \ldots, \mathrm{sat_y(c_4)}]^{\mathrm{T}}$. Furthermore, $\boldsymbol{\varphi}$ is a Fréchet differentible function of $[c_1, c_2, \ldots, c_4]^T$. It is also observed that $\boldsymbol{\varphi}$ and $\boldsymbol{c}$ stay bounded due to the implication of the saturation functions sat(.) and $\mathrm{sat_y}(.)$ in (5.30); thus, $\boldsymbol{\mathcal{R}}(., t)$ is Lipschitz continuous with respect to $\boldsymbol{c}$; in other words, the nonlinearity of the system satisfies Assumption 3.2.7. Finally, the input vector $\boldsymbol{u}(t)$ is assumed to satisfy Assumption 3.2.5. The proof is then completed by Theorem 3.3.5. □

5.4 Finite-dimensional approximation

Before an observer can be designed, a low-order finite-dimensional model must be introduced. A potential way of approximating the system with a finite-dimensional low-order one is to employ FEM approximation with a few number of elements; however, this type of low-order model might not be an efficient choice.

The low-order model can be produced by starting from a high-order finite-dimensional approximation obtained possibly by FEM and employing an order reduction method. The order reduction techniques truncate the state vector with minimum effect on the system response; they are built upon different aspects of the system. Balanced order

reduction and proper orthogonal decomposition (POD) are frequently used in literature [151]; however, for a general nonlinear system, implementing these techniques is challenging.

Employing eigenfunctions of the linear operator $\boldsymbol{\mathcal{A}}$ is another way of producing the low-order model. Unlike balanced and POD order reduction, using eigenfunctions can be complemented by the possibility of proving the existence of an error bound due to the dynamics truncation. This technique was introduced in Chapter 3 for two general classes of systems. In this section, two forms of electrochemical equations are studied, with constant diffusion and variable diffusion; Both forms are included in the categories introduced in Chapter 3.

From Corollary 5.3.3, eigenfunctions of $\boldsymbol{\mathcal{A}}$ can be used to approximate the state vector such that a subsequence of the approximate solutions converges to a solution of (5.30). For the sake of simplicity, since the electrolyte concentration does not experience much change along the cell in time, it is set to be constant as in [49] to find the eigenfunctions. For the solid concentration, c_2-c_4, the eigenfunctions are derived from the following eigenvalue problems: for $k = 1, \ldots, 3$,

$$\frac{1}{r_k^2}\frac{\partial}{\partial r_k}(r_k^2\frac{\partial \boldsymbol{z}_{k+1}}{\partial r_k}) = \lambda_k \boldsymbol{v}_{k+1} \tag{5.45}$$

in which the linear operator's domain is defined in (5.33). Solving (5.45) leads to finding the eigenfunctions as

$$\boldsymbol{v}_{k+1} = \begin{cases} 1 & \text{if } j = 0 \\ \frac{\sin(\frac{\alpha_j}{R_k} r_k)}{r_k} & \text{otherwise} \end{cases} \tag{5.46}$$

where α_j satisfies

$$\alpha_j = \tan(\alpha_j).$$

Note that, in the original electrochemical equations the derivatives of the solid concentrations (c_2, c_3, c_4) with respect to the spatial variable x are not involved in the equations. For this reason and in order to add more accuracy to the system solution, in this research, the profile of the electrolyte concentration, c_1, is approximated by a piece-wise linear function instead of a constant.

The constraint equation (5.5) is approximated by a finite-dimensional one. Linear spline functions are appropriate choices for approximating the potential vector $\boldsymbol{\varphi}$ since (5.5) includes second order differentiation. The Galerkin method is then used to find finite-dimensional nonlinear approximate of both equations of 5.40.

In general, for the finite-dimensional approximation of the solid and electrolyte concentration dynamical equations, the first part of (5.40), the base functions are respectively chosen to be the eigenfunctions (5.46) and linear shape functions. The finite-dimensional approximation of the constraint equations is achieved using finite element method (FEM) with linear shape functions; this approximation leads to a set of finite-dimensional algebraic equations. The finite-dimensional approximate equations are next transformed into a dynamical form by applying time differentiation to the both sides of them. In this way, the finite-dimensional approximation of the operator (5.3.1) is also automatically achieved as a part of the finite-dimensional dynamical form.

Now, let the state vector be approximated by $\boldsymbol{c}_N$ and the potential vector by $\boldsymbol{\varphi}_M$. The fully dynamical form (5.40) is then approximated by

$$\begin{aligned} &\frac{d\boldsymbol{c}_N}{dt} + \boldsymbol{A}_N \boldsymbol{c}_N = \boldsymbol{R}_{\boldsymbol{c},N}(\boldsymbol{c}_N, \boldsymbol{\varphi}_M) + \boldsymbol{F}_N \boldsymbol{u}(t), \\ &\frac{d\boldsymbol{\varphi}_M}{dt} = \frac{\partial \bar{\boldsymbol{R}}_{\boldsymbol{\varphi},M}(\boldsymbol{c}_N, I(t))}{\partial \boldsymbol{c}_N} \frac{d\boldsymbol{c}_N}{dt} + \frac{\partial \bar{\boldsymbol{R}}_{\boldsymbol{\varphi},M}(\boldsymbol{c}_N, I(t))}{\partial I} \frac{dI(t)}{dt} \end{aligned} \tag{5.47}$$

where the linear matrix $\boldsymbol{A}_N$, the nonlinear functions $\boldsymbol{N}_N(.)$, $\boldsymbol{R}_{\boldsymbol{c},N}(.)$, $\bar{\boldsymbol{R}}_{\boldsymbol{\varphi},M}(.)$, and the linear operator $\boldsymbol{F}_N$ are found through the Galerkin method with the chosen bases for every variable as explained before.

In the rest of this chapter, the number of elements for the separator region is denoted by N_1 and for the electrode region by N_2. Depending on the method of approximation, N_3 represents the number of elements along or the number of eigenfunctions chosen for every particle. The distribution $\delta(x-x0)$ is set to the delta distribution. The parameters of the saturation functions sat(.) and sat_y(.) are defined in Table 5.2. Other modeling parameters are given in Table 5.1. These equations are solved in time using MATLAB ODE15s function.

Simulations via the FEM and linear base functions are compared to experimental data in Figure 5.1 and 5.2 for charging and discharging cycles with different current rates. Linear elements are used; the number of elements are chosen to be $N_1 = 5$ in the separator domain, $N_2 = 5$ along the positive electrode, and $N_3 = 9$ along every particle. The parameters of the saturation functions sat(.) and sat_y(.) are defined in Table 5.2. The simulation results show an adequate but not exact match to experimental data for charging and discharging cycles with different rates of discharge up to $1c$; the mismatch between experimental data and model will be improved in the observer design.

Simulation results of solving the system equations (5.30) and (5.25) using eigenfunctions for different charging and discharging current rates are respectively shown in Figure

Table 5.2: Filtering and Saturation functions parameters

g	c_0	c_1	a_0	b_0	ϵ
1	2	3	1	2.0251	.0001

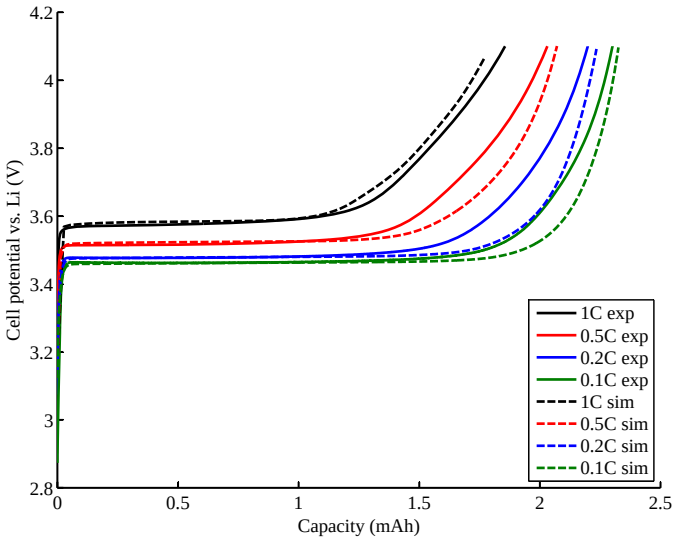

Figure 5.1: Comparison of the simulation results of the fully dynamical representation with the experimental data for different charging rates; The simulation is exercised by the FEM method with $N_1 = 5$ in the separator domain, $N_2 = 5$ along the positive electrode, and $N_3 = 9$ along every particle. A agreement with the experimental data is observed. In these plots, "sim" and "exp" respectively represent the simulation result and experimental data.

5.3 and 5.4 for $N_1 = 4$, $N_2 = 4$, and $N_3 = 5$, the number of the eigenfunctions for every particle size. Similarly, it is obvious from these figures that finding a set of parameters which matches all the current rates is not an easy task. In the next step, this problem is overcome by an adaptive filtering.

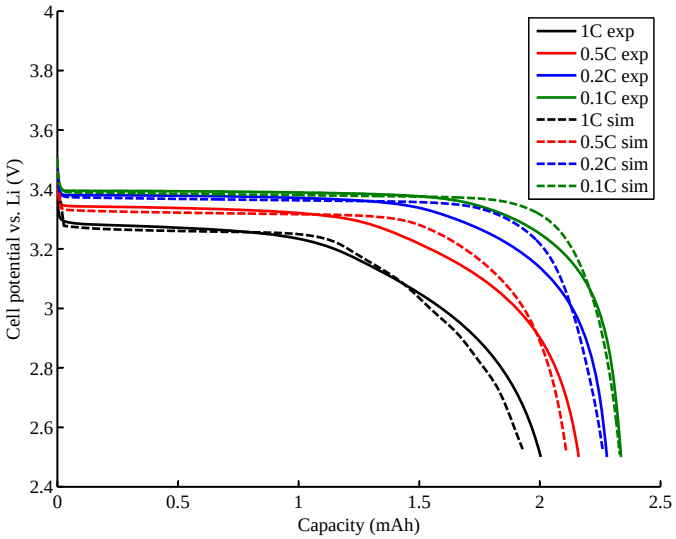

Figure 5.2: Comparison of the simulation results of the fully dynamical representation with the experimental data for different discharging rates; The simulation uses linear finite elements with $N_1 = 5$ in the separator domain, $N_2 = 5$ along the positive electrode, and $N_3 = 9$ along every particle. A agreement with the experimental data is observed. In these plots, "sim" and "exp" respectively represent the simulation result and experimental data.

5.5 Observer design with constant diffusion

First, the lithium-ion SOC estimation is considered for a constant diffusion coefficient $\boldsymbol{\mathcal{N}}(.) = \boldsymbol{\mathcal{I}}$. The fully dynamical form (5.40) can be rewritten as

$$\begin{aligned} &\frac{\partial \boldsymbol{c}}{\partial t} + \boldsymbol{\mathcal{A}}\boldsymbol{c} = \boldsymbol{\mathcal{R}}_{\boldsymbol{c}}(\boldsymbol{c}, \boldsymbol{\varphi}) + \boldsymbol{\mathcal{F}}\boldsymbol{u}(t) \\ &\frac{\partial \boldsymbol{\varphi}}{\partial t} = D_{\boldsymbol{c}}\bar{\boldsymbol{\mathcal{R}}}_{\boldsymbol{\varphi}}(\boldsymbol{c}, I(t))\frac{\partial \boldsymbol{c}}{\partial t} + \frac{\partial \bar{\boldsymbol{\mathcal{R}}}_{\boldsymbol{\varphi}}(\boldsymbol{c}, I(t))}{\partial I}\frac{dI(t)}{dt} \\ &\qquad - \boldsymbol{\Gamma}(\boldsymbol{\varphi} - \bar{\boldsymbol{\mathcal{R}}}_{\boldsymbol{\varphi}}(\boldsymbol{c}, \boldsymbol{\theta}, I(t))) \end{aligned} \tag{5.48}$$

where $D_{\boldsymbol{c}}$ represents the Fréchet derivative with respect to $\boldsymbol{c}$ and Γ is a matrix gain added to compensate for the numerical error of solving the constraint equations

$$\boldsymbol{\varphi} - \bar{\boldsymbol{\mathcal{R}}}_{\boldsymbol{\varphi}}(\boldsymbol{c}, I(t)) = 0$$

via transformation into dynamical form. Note that (5.48) is equivalent to (5.30) for $\boldsymbol{\mathcal{N}}(.) = \boldsymbol{\mathcal{I}}$ and is proved to satisfy Assumption 3.2.5-3.2.7.

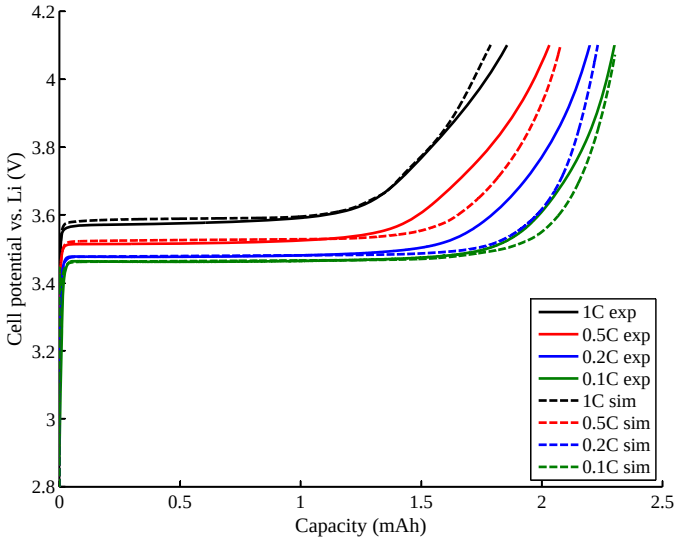

Figure 5.3: Comparison of the simulation results of the fully dynamical representation with the experimental data for different charging rates; The simulation is exercised by eigenfunctions (5.46) with $N_1 = 4$ in the separator domain, $N_2 = 4$ along the positive electrode, and $N_3 = 5$ for every particle. A good agreement with the experimental data is observed. In these plots, "sim" and "exp" respectively represent the simulation result and experimental data.

The actual operator is nonlinear. It represents the cell terminal voltage. In order to define this voltage, both positive and negative electrodes' solid potentials are required. The positive electrode's potential is achieved by solving the electrochemical equations on this electrode. The solid potential in the negative electrode φ_f satisfies

$$I(t) = i_f(\frac{c_e}{c_{ini}})(\exp(\frac{(1-\beta_f)F\varphi_f}{RT}) - \exp(\frac{\beta_f F\varphi_f}{RT}))$$

where c_{ini} is the initial value of the state variable c_1. The voltage measurement is defined by the output operator

$$\boldsymbol{\mathcal{C}}_0(\boldsymbol{\varphi}, I(t)) = \int_{L_1}^{L} \delta(x-L)\varphi_1 dx - \varphi_f - R_f I(t)$$

where R_f is the load resistance. In the measurement model, φ_1 and φ_2 are nonlinear functions of the state vector $\boldsymbol{c}$.

Also, in order to improve the observer's performance, the information from the current integration in time is used as an extra measurement. An improved output operator is

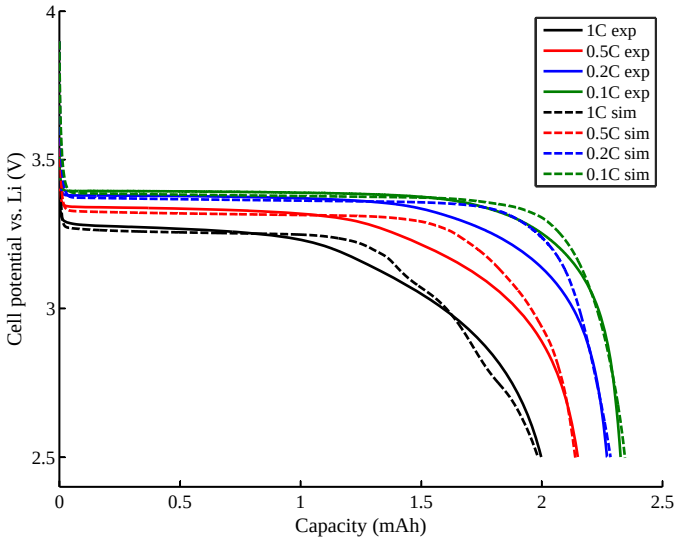

Figure 5.4: Comparison of the simulation results of the fully dynamical representation with the experimental data for different discharging rates; The simulation is exercised by eigenfunctions (5.46) with $N_1 = 4$ in the separator domain, $N_2 = 4$ along the positive electrode, and $N_3 = 5$ for every particle. A good agreement with the experimental data is observed. In these plots, "sim" and "exp" respectively represent the simulation result and experimental data.

built upon the fact that by conservation of charge, [37]

$$3\sum_{k=1}^{3}\frac{\epsilon_k}{R_k^3}\int_0^{R_k} r_k^2\frac{c_{k+1}}{C_{max}}dr_k = \frac{1}{F(L-L_1)C_{max}}\int_0^t I(t)dt.$$

The output is defined as

$$\boldsymbol{y} = \boldsymbol{\mathcal{C}}(\boldsymbol{c},\boldsymbol{\varphi},I(t)) = \begin{bmatrix} \boldsymbol{\mathcal{C}}_0(\boldsymbol{\varphi},I(t)) \\ 3\sum_{k=1}^{3}\frac{\epsilon_k}{R_k^3}\int_0^{R_k} r_k^2\frac{c_{k+1}}{c_{max}}dr_k. \end{bmatrix} \tag{5.49}$$

The second component is only used in estimation when the voltage estimation error is larger than a threshold.

In the simulations, the system is approximated via both the finite element method and using eigenfunctions (5.46) as explained in Section 5.4. Let the estimate potential vector and observer state be denoted by $\hat{\boldsymbol{\varphi}}_M$ and $\hat{\boldsymbol{c}}_N$ respectively. The observer dynamics

is approximated by

$$\begin{aligned}
&\frac{d\hat{\boldsymbol{c}}_N}{dt} + \boldsymbol{A}_N\hat{\boldsymbol{c}}_N = \boldsymbol{R}_{\boldsymbol{c},N}(\hat{\boldsymbol{c}}_N, \hat{\boldsymbol{\varphi}}_M) + \boldsymbol{F}_N\boldsymbol{u}(t) + \boldsymbol{K}_N(t)(\boldsymbol{y} - \boldsymbol{C}_N(\hat{\boldsymbol{\varphi}_M}, I(t))),\\
&\frac{d\hat{\boldsymbol{\varphi}}_M}{dt} = \frac{\partial\bar{\boldsymbol{R}}_{\boldsymbol{\varphi},M}(\hat{\boldsymbol{c}}_N, I(t))}{\partial\hat{\boldsymbol{c}}_N}\frac{d\hat{\boldsymbol{c}}_N}{dt} + \frac{\partial\bar{\boldsymbol{R}}_{\boldsymbol{\varphi},M}(\hat{\boldsymbol{c}}_N, I(t))}{\partial I}\frac{dI(t)}{dt}\\
&\qquad - \boldsymbol{\Gamma_N}(\hat{\boldsymbol{\varphi}}_M - \bar{\boldsymbol{R}}_{\boldsymbol{\varphi},M}(\hat{\boldsymbol{c}}_N, I(t)))
\end{aligned} \tag{5.50}$$

where the linear matrix $\boldsymbol{A}_N$, the nonlinear functions $\boldsymbol{R}_{\boldsymbol{c},N}(.)$, $\bar{\boldsymbol{R}}_{\boldsymbol{\varphi},M}(.)$, and the linear operator $\boldsymbol{F}_N$ are found through the Galerkin approximation of the system, $\boldsymbol{K}_N(t)$ is the filtering gain, and $\boldsymbol{C}_N(.)$ is the finite-dimensional approximation of the output operator.

Define

$$\begin{aligned}
&D\boldsymbol{R}_{\boldsymbol{c},N}(\hat{\boldsymbol{c}}_N) =\\
&(\frac{\partial\boldsymbol{R}_{\boldsymbol{c},N}(\boldsymbol{c}_N, \boldsymbol{\varphi}_M)}{\partial\boldsymbol{c}_N} + \frac{\partial\boldsymbol{R}_{\boldsymbol{c},N}(\boldsymbol{c}_N, \boldsymbol{\varphi}_M)}{\partial\boldsymbol{\varphi}_M}\frac{\partial\boldsymbol{\varphi}_M(\boldsymbol{c}_N, I(t))}{\partial\boldsymbol{c}_N}) \mid_{\hat{\boldsymbol{c}}_N},
\end{aligned}$$

and

$$D\boldsymbol{C}_N(\hat{\boldsymbol{c}}_N) = \frac{\partial\boldsymbol{C}_N(\boldsymbol{\varphi}_N, I(t))}{\partial\boldsymbol{\varphi}_N}\frac{\partial\boldsymbol{\varphi}_N(\boldsymbol{c}_N, I(t))}{\partial\boldsymbol{c}_N} \mid_{\hat{\boldsymbol{c}}_N}.$$

The Riccati equation is defined as

$$\begin{aligned}
\frac{d\boldsymbol{P}_N}{dt} &= (-\boldsymbol{A}_N + D\boldsymbol{R}_{\boldsymbol{c},N}(\hat{\boldsymbol{c}}_N))\boldsymbol{P}_N + \boldsymbol{P}_N(-\boldsymbol{A}_N + D\boldsymbol{R}_{\boldsymbol{c},N}(\hat{\boldsymbol{c}}_N))^*\\
&\quad - \beta(t)\boldsymbol{P}_N D\boldsymbol{C}_N^*(\hat{\boldsymbol{c}}_N)\boldsymbol{R}^{-1}D\boldsymbol{C}_N(\hat{\boldsymbol{c}}_N)\boldsymbol{P}_N + \boldsymbol{W}_N(t)
\end{aligned} \tag{5.51}$$

where $\beta(t) : \mathbb{R} \to \mathbb{R}^+$ is a continuous function and $\boldsymbol{W}_N(t)$ is a positive matrix. The observer gain is

$$\boldsymbol{K}_N(t) = \beta(t)\boldsymbol{P}_N D\boldsymbol{C}_N^*(\hat{\boldsymbol{c}}_N)\boldsymbol{R}^{-1}. \tag{5.52}$$

The number of elements are chosen to be $N_1 = 4$ in the separator domain and $N_2 = 4$ along the positive electrode. In the case where the FEM is used to approximate the system, the solid concentration in every particle bin is approximated by linear splines. The number of elements are $N_3 = 5$ along every particle. The same number of eigenfunctions are used when the eigenfunctions are used to approximate the equations. The parameters of the saturation functions sat(.) and sat_y(.) are defined in Table 5.2. The simulation parameters are

$$\begin{aligned}
\boldsymbol{P}_N(0) = \boldsymbol{0}, \quad \boldsymbol{W}_N(t) = 0.2 * \boldsymbol{I},\\
\beta(t) = 1, \quad \boldsymbol{R}^{-1} = \text{diag}(20, 0.5).
\end{aligned}$$

Other model parameters are given in Table 5.1. Note that the augmented output (5.49) is only active when the voltage estimation error is larger than $0.05(V)$.

An approximate steady state SOC is used to initialize the observer. This initial SOC approximation is obtained using conservation of charge:

$$\int_{l_{sep}}^{l_{sep}+l_{cat}} \sum a_k i_k(\boldsymbol{c}, \boldsymbol{\varphi}) = I(t). \tag{5.53}$$

In order to find the approximate SOC, $\varphi_2 = 0$ as well as φ_1 and y_k are considered to be constant over the particle bins and along the electrode. In order to initialize the observer, for a short period after the charging/discharging cycle starts, the measurement value of the second component of the output (5.49) is calculated from the algebraic equation (5.53). In the simulation results of this section, this period is set to be $50(s)$.

The SOC estimation is compared to the exact measurement. The exact measurement is obtained by precisely integrating the current in time as an indication of the consumed charge also called the coulomb counting measurement. Two types of SOC are considered in the simulations. The bulk SOC is defined as

$$SOC = \frac{\theta_b - \theta_0}{\theta_{100} - \theta_0}$$

where

$$\theta_b = \frac{3 \sum_k \epsilon_k \int_0^{R_k} r_k^2 c_{k+1}(r_k, x, t) dr_k}{c_{s,max} \sum_k \epsilon_s R_k^3}$$

and θ_0 and θ_{100} respectively represent the value of θ_b corresponding to the minimum and maximum capacity of the cell. The surface SOC is defined as

$$SOC = \frac{\theta_s - \theta_0}{\theta_{100} - \theta_0}$$

where

$$\theta_s = \frac{2 \sum_k \epsilon_k \int_0^{R_k} r_k c_{k+1}(r_k, x, t) dr_k}{c_{s,max} \sum_k \epsilon_s R_k^2}.$$

The bulk SOC indicates the amount of total charge remained in the cell and is comparable with the coulomb counting; the surface SOC represents the available charge on the the surface of the particle bins, which are involved in the electrochemical reactions.

The simulation results for a time-varying current for the system being approximated by the FEM (Figure 5.5) are shown in Figure 5.6 and 5.7 for the output estimation and in Figure 5.8 and 5.9 for the SOC estimation. These figures represents the charging process of the cell followed by discharging process. According to these figures, the observer

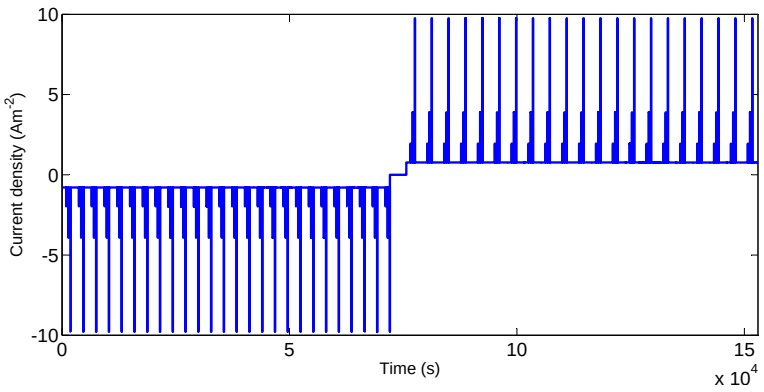

Figure 5.5: Input current to the cell in a charge/discharge course

output follows the measurements with good precision. It is observed that the observer recovers the initial SOC, and the bulk SOC estimation error is less than 6%.

Given the same observer parameters, the simulation results when the solid concentration is approximated using eigenfunctions (5.46) for a course of charging/discharging (Figure 5.5) are shown in Figures 5.10-5.13. These figures represents the charging process of the cell followed by discharging process. These figures indicate the same performance as before; the observer output follows the measurements with good precision. It is observed that the observer recovers the initial SOC, and the bulk SOC estimation error is less than 6%.

The simulation results show that the system approximation via both FEM and eigenfunction based approaches lead to similar results. However, in Theorem 3.2.13, employing eigenfunctions is proved to lead to a convergent sequence of the approximate solutions. The well-posedness of the electrochemical equations (5.30) for a constant diffusion $\boldsymbol{\mathcal{N}}(.) = \boldsymbol{\mathcal{I}}$ is given by Corollary 3.2.11. Similarly, the existence of a solution to (5.30) and a convergence subsequence of the approximate solutions for a nonlinear diffusion are shown by Corollary 5.3.3. Therefore, in the next section, the eigenfunctions are used to approximate the system.

5.6 Observer design for non-constant diffusion

In this section, the observer design for the approximation of (5.30) with a non-constant diffusion coefficient is considered. The observer dynamics has the same structure as the

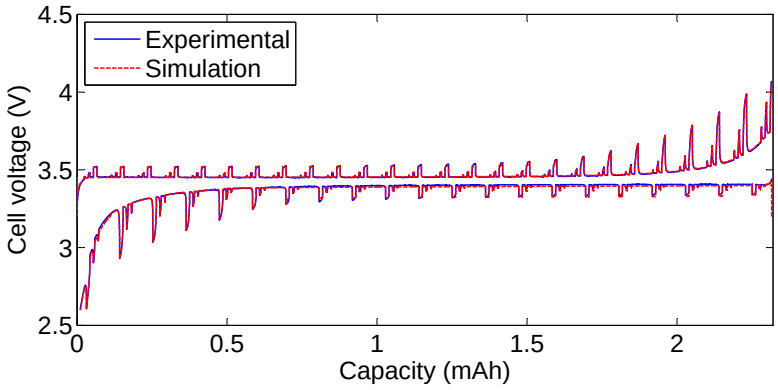

Figure 5.6: Comparison between the observation output and the measurements in a charging/discharging cycle for a constant diffusion model. The system is approximated via the FEM with $N_1 = 4$, $N_2 = 4$, and $N_3 = 5$. It is observed that the output estimate tracks the measurements.

previous section;

$$\begin{aligned}
&\frac{d\hat{\boldsymbol{c}}_N}{dt} + \boldsymbol{A}_N \boldsymbol{N}_N(\hat{\boldsymbol{c}}_N) = \boldsymbol{R}_{\boldsymbol{c},N}(\hat{\boldsymbol{c}}_N, \hat{\boldsymbol{\varphi}}_M) + \boldsymbol{F}_N \boldsymbol{u}(t) + \boldsymbol{K}_N(t)(\boldsymbol{y} - \boldsymbol{C}_N(\hat{\boldsymbol{\varphi}_M}, I(t))),\\
&\frac{d\hat{\boldsymbol{\varphi}}_M}{dt} = \frac{\partial \bar{\boldsymbol{R}}_{\boldsymbol{\varphi},M}(\hat{\boldsymbol{c}}_N, I(t))}{\partial \hat{\boldsymbol{c}}_N}\frac{d\hat{\boldsymbol{c}}_N}{dt} + \frac{\partial \bar{\boldsymbol{R}}_{\boldsymbol{\varphi},M}(\hat{\boldsymbol{c}}_N, I(t))}{\partial I}\frac{dI(t)}{dt}\\
&\qquad - \boldsymbol{\Gamma}_{\boldsymbol{N}}(\hat{\boldsymbol{\varphi}}_M - \bar{\boldsymbol{R}}_{\boldsymbol{\varphi},M}(\hat{\boldsymbol{c}}_N, I(t)))
\end{aligned} \tag{5.54}$$

where $\boldsymbol{N}_N(.)$ is the approximation of $\boldsymbol{\mathcal{N}}(.)$ through the Galerkin method when eigenfunctions (5.46) are used for approximating solid concentration. Define

$$D\boldsymbol{N}_N(\hat{\boldsymbol{c}}_N) = \frac{\partial \boldsymbol{N}_N(\check{\boldsymbol{c}}_N)}{\partial \check{\boldsymbol{c}}_N} \mid_{(\hat{\boldsymbol{c}}_N)} . \tag{5.55}$$

The Riccati equation takes the form

$$\begin{aligned}
\frac{d\boldsymbol{P}_N}{dt} &= (-\boldsymbol{A}_N D\boldsymbol{N}_N(\hat{\boldsymbol{c}}_N) + D\boldsymbol{R}_{\boldsymbol{c},N}(\hat{\boldsymbol{c}}_N))\boldsymbol{P}_N + \boldsymbol{P}_N(-\boldsymbol{A}_N D\boldsymbol{N}_N(\hat{\boldsymbol{c}}_N) + D\boldsymbol{R}_{\boldsymbol{c},N}(\hat{\boldsymbol{c}}_N))^*\\
&\quad - \beta(t)\boldsymbol{P}_N D\boldsymbol{C}_N^*(\hat{\boldsymbol{c}}_N)\boldsymbol{R}^{-1} D\boldsymbol{C}_N(\hat{\boldsymbol{c}}_N)\boldsymbol{P}_N + \boldsymbol{W}_N(t),
\end{aligned} \tag{5.56}$$

and the filtering gain is defined by (5.52).

The observer parameters are chosen to be the same as those used for the constant diffusion model. The simulation results of the observer (5.54) are shown in Figures 5.14-5.17. These figures represents the charging process of the cell followed by discharging process. It is observed that the SOC estimation error is less than 6%. Moreover, the

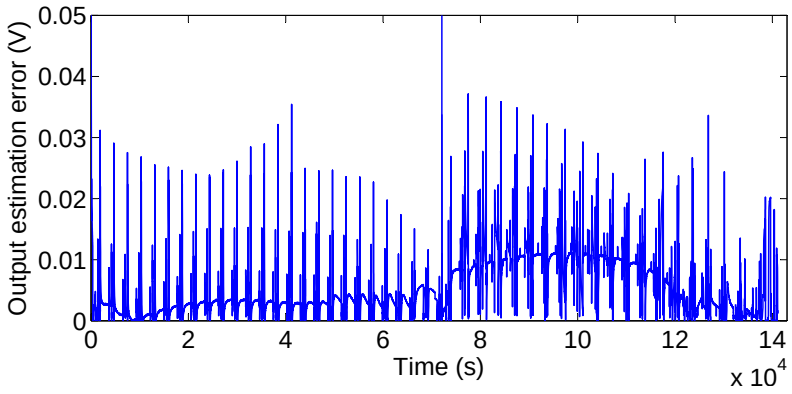

Figure 5.7: Cell voltage estimation error in a charging/discharging cycle for a constant diffusion model. The system is approximated via the FEM with $N_1 = 4$, $N_2 = 4$, and $N_3 = 5$. It is observed that the estimation error is small.

output estimation error is small, but the output does not exactly match the experimental data. Although the diffusion coefficient is now nonlinear, the observer has the same performance as the one with constant diffusion.

The mismatch between model output and experimental data is partly due to the dependency of the system output on the OCP term and this term being hysteretic and rate dependent. The hysteresis of the OCP term can not be efficiently identified by a mathematical equation since it depends on many enviornmental conditions including current rate.

A potential way of dealing with the model uncertainties is to include them in the output voltage model as disturbances coming from an unknown input. Next, the modified SMO as introduced in Chapter 2 is suggested for the observer's dynamics. However, the system does not satisfy the required conditions, Assumption 2.3.8 and 2.3.13, and the simulation results were not satisfactory.

An alternative way of including the effect of the hysteresis in the OCP term is to use a parametric representation for the OCP as a function of the solid concentration. For every set of parameters, a different curve emerges passing through a point assigned to the current state of the system. At every time step, these parameters need to be identified such that the electrochemical model's output matches the experimental data.

An adaptive extended Kalman filter is designed to both identify the OCP parameters and estimate the state vector. The observer dynamics allows the OCP term's representation to vary in a range to produce a proper fit to the measurements. Let the OCP

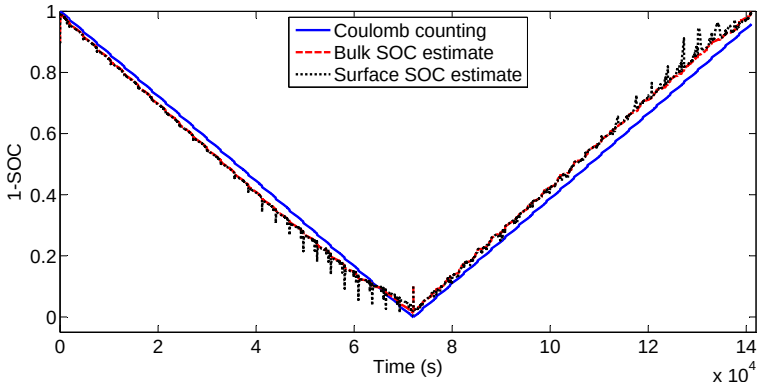

Figure 5.8: Comparison between the coulomb counting as the measurement and the SOC estimated values in a charging/discharging cycle for a constant diffusion model. The system is approximated via the FEM with $N_1 = 4$, $N_2 = 4$, and $N_3 = 5$. The estimation error is observed to be less than 6%. The initial SOC is 0.1 for charging process and 0.9 for discharging process.

term take the parametric form $U(\boldsymbol{c}, \boldsymbol{\theta})$, and (5.23) be written as

$$\boldsymbol{\varphi} = \bar{\boldsymbol{\mathcal{R}}}_{\boldsymbol{\varphi}}(\boldsymbol{c}, \boldsymbol{\theta}, I(t)) \tag{5.57}$$

where $\boldsymbol{\theta}$ is the parameter vector involved in the OCP representation.

The fully dynamical form (5.30) can be rewritten as

$$\begin{aligned}
&\frac{\partial \boldsymbol{c}}{\partial t} + \boldsymbol{\mathcal{A}}\boldsymbol{\mathcal{N}}(\boldsymbol{c}) = \boldsymbol{\mathcal{R}}_{\boldsymbol{c}}(\boldsymbol{c}, \boldsymbol{\varphi}, \boldsymbol{\theta}) + \boldsymbol{\mathcal{F}}\boldsymbol{u}(t) \\
&\frac{\partial \boldsymbol{\varphi}}{\partial t} = D_{\boldsymbol{c}}\bar{\boldsymbol{\mathcal{R}}}_{\boldsymbol{\varphi}}(\boldsymbol{c}, \boldsymbol{\theta}, I(t))\frac{\partial \boldsymbol{c}}{\partial t} + \frac{\partial \bar{\boldsymbol{\mathcal{R}}}_{\boldsymbol{\varphi}}(\boldsymbol{c}, \boldsymbol{\theta}, I(t))}{\partial I}\frac{dI(t)}{dt} \\
&\qquad - \boldsymbol{\Gamma}(\boldsymbol{\varphi} - \bar{\boldsymbol{\mathcal{R}}}_{\boldsymbol{\varphi}}(\boldsymbol{c}, \boldsymbol{\theta}, I(t))) + \frac{\partial \bar{\boldsymbol{\mathcal{R}}}_{\boldsymbol{\varphi}}(\boldsymbol{c}, \boldsymbol{\theta}, I(t))}{\partial \boldsymbol{\theta}}\boldsymbol{\omega}(t) \\
&\frac{d\boldsymbol{\theta}}{dt} = \boldsymbol{\omega}(t)
\end{aligned} \tag{5.58}$$

where $\boldsymbol{\omega}(t)$ is a zero-mean noise. The last equation of (5.58) represents the fact that the dynamics of the parameter variation is much smaller than the system's dynamics but not zero. This setting is frequently used when adaptation is involved [24].

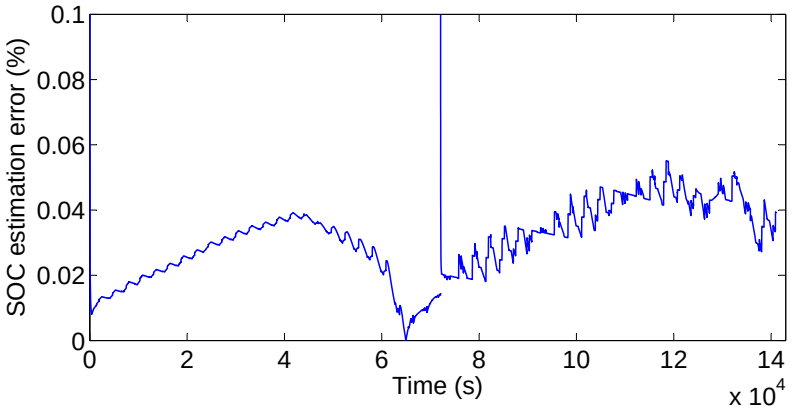

Figure 5.9: Error between the coulomb counting as the measurement and the SOC estimated values in a charging/discharging cycle for a constant diffusion model. The system is approximated via the FEM with $N_1 = 4$, $N_2 = 4$, and $N_3 = 5$. The estimation error is observed to be less than 6%. The estimation error is observed to be less than 6%. The initial SOC is 0.1 for charging process and 0.9 for discharging process.

The finite-dimensional approximation of the system is

$$\frac{d\boldsymbol{c}_N}{dt} + \boldsymbol{A}_N \boldsymbol{N}_N(\boldsymbol{c}_N) = \boldsymbol{R}_{\boldsymbol{c},N}(\boldsymbol{c}_N, \boldsymbol{\varphi}_M, \boldsymbol{\theta}) + \boldsymbol{F}_N \boldsymbol{u}(t) \tag{5.59}$$

$$\begin{aligned}\frac{d\boldsymbol{\varphi}_M}{dt} &= \frac{\partial \bar{\boldsymbol{R}}_{\boldsymbol{\varphi},M}(\boldsymbol{c}_N, \boldsymbol{\theta}, I(t))}{\partial \boldsymbol{c}_N}\frac{d\boldsymbol{c}_N}{dt} + \frac{\partial \bar{\boldsymbol{R}}_{\boldsymbol{\varphi},M}(\boldsymbol{c}_N, \boldsymbol{\theta}, I(t))}{\partial I}\frac{dI(t)}{dt} \\ &\quad - \boldsymbol{\Gamma}_{\boldsymbol{N}}(\boldsymbol{\varphi}_M - \bar{\boldsymbol{R}}_{\boldsymbol{\varphi},M}(\boldsymbol{c}_N, \boldsymbol{\theta}, I(t))) + \frac{\partial \bar{\boldsymbol{R}}_{\boldsymbol{\varphi},M}(\boldsymbol{c}_N, \boldsymbol{\theta}, I(t))}{\partial \boldsymbol{\theta}}\boldsymbol{\omega}(t)\end{aligned} \tag{5.60}$$

$$\frac{d\boldsymbol{\theta}}{dt} = \boldsymbol{\omega}(t) \tag{5.61}$$

where the nonlinear functions $\boldsymbol{N}_N(.)$, $\boldsymbol{R}_{\boldsymbol{c},N}(.)$ and $\bar{\boldsymbol{R}}_{\boldsymbol{\varphi},M}(.)$ are found through the Galerkin approximation of (5.58).

In the next step, the representation (5.59)-(5.61) are employed to design an adaptive observer. The observer dynamics is given as

$$\frac{d\hat{\boldsymbol{c}}_N}{dt} + \boldsymbol{A}_N \boldsymbol{N}_N(\hat{\boldsymbol{c}}_N) = \boldsymbol{R}_{\boldsymbol{c},N}(\hat{\boldsymbol{c}}_N, \hat{\boldsymbol{\varphi}}_M, \hat{\boldsymbol{\theta}}) + \boldsymbol{F}_N I(t) + \boldsymbol{K}_c(y - \boldsymbol{C}_N(\hat{\boldsymbol{c}}_N)) \tag{5.62}$$

$$\begin{aligned}\frac{d\hat{\boldsymbol{\varphi}}_M}{dt} &= D_{\boldsymbol{c}}\bar{\boldsymbol{R}}_{\boldsymbol{\varphi},M}(\hat{\boldsymbol{c}}_N, \hat{\boldsymbol{\theta}}, I(t))\frac{\partial \hat{\boldsymbol{c}}_N}{dt} + \frac{\partial \bar{\boldsymbol{R}}_{\boldsymbol{\varphi},M}(\hat{\boldsymbol{c}}_N, \hat{\boldsymbol{\theta}}, I(t))}{\partial I}\frac{dI(t)}{dt} \\ &\quad - \boldsymbol{\Gamma}_{\boldsymbol{N}}(\hat{\boldsymbol{\varphi}}_M - \bar{\boldsymbol{R}}_{\boldsymbol{\varphi},M}(\hat{\boldsymbol{c}}_N, \hat{\boldsymbol{\theta}}, I(t)))\end{aligned} \tag{5.63}$$

$$\frac{d\hat{\theta}}{dt} = \boldsymbol{K}_\theta(y - \boldsymbol{C}_N(\hat{\boldsymbol{c}}_N)). \tag{5.64}$$

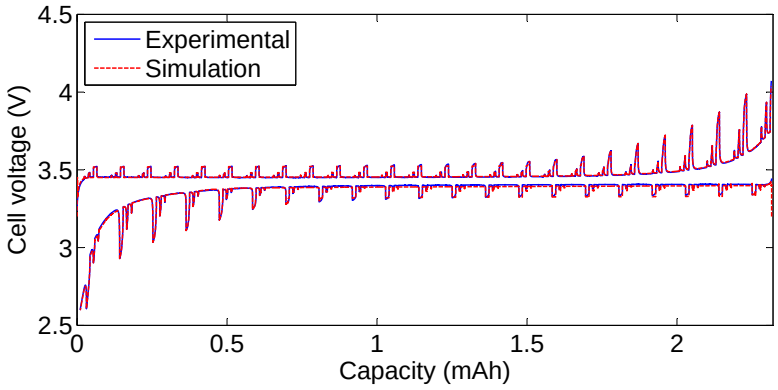

Figure 5.10: Comparison between the observation output and the measurements in a charging/discharging cycle for a constant diffusion model. The system is approximated using eigenfunctions with $N_1 = 4$, $N_2 = 4$, and $N_3 = 5$. It is observed that the output estimate tracks the measurements.

Define

$$D\boldsymbol{R}_N(\hat{\boldsymbol{c}}_N, \hat{\boldsymbol{\theta}}) = \left(\frac{\partial \boldsymbol{R}_{\boldsymbol{c},N}(\tilde{\boldsymbol{c}}_N, \tilde{\boldsymbol{\varphi}}_M, \boldsymbol{\theta})}{\partial(\tilde{\boldsymbol{c}}_N, \boldsymbol{\theta})} + \frac{\partial \boldsymbol{R}_{\boldsymbol{c},N}(\tilde{\boldsymbol{c}}_N, \tilde{\boldsymbol{\varphi}}_M, \boldsymbol{\theta})}{\partial \tilde{\boldsymbol{\varphi}}_M} \frac{\partial \bar{\boldsymbol{R}}_{\boldsymbol{\varphi},M}(\tilde{\boldsymbol{c}}_N, \boldsymbol{\theta}, I(t))}{\partial(\tilde{\boldsymbol{c}}_N, \boldsymbol{\theta})}\right) |_{(\hat{\boldsymbol{c}}_N, \hat{\boldsymbol{\theta}})}, \tag{5.65}$$

and

$$D\boldsymbol{C}_N(\hat{\boldsymbol{c}}_N, \hat{\boldsymbol{\theta}})) = \frac{\partial \boldsymbol{C}_N(\tilde{\boldsymbol{\varphi}}_N, I(t))}{\partial \tilde{\boldsymbol{\varphi}}_N} \frac{\partial \bar{\boldsymbol{R}}_{\boldsymbol{\varphi},M}(\tilde{\boldsymbol{c}}_N, \boldsymbol{\theta}, I(t))}{\partial(\tilde{\boldsymbol{c}}_N, \boldsymbol{\theta})} |_{(\hat{\boldsymbol{c}}_N, \hat{\boldsymbol{\theta}})}. \tag{5.66}$$

Define $\beta(t) > \mu_1 > 0$ a continuous function, $\boldsymbol{Q}_0$ a positive definite matrix and $\boldsymbol{W}_N$ a positive matrix. Let $\boldsymbol{P}_N$ satisfy the Riccati equation

$$\begin{aligned}\frac{d\boldsymbol{P}_N}{dt} &= (-\boldsymbol{\mathcal{A}}_N D\boldsymbol{N}_N(\hat{\boldsymbol{c}}_N) + D\boldsymbol{R}_N(\hat{\boldsymbol{c}}_N))\boldsymbol{P}_N + \boldsymbol{P}_N(-\boldsymbol{\mathcal{A}}_N D\boldsymbol{N}_N(\hat{\boldsymbol{c}}_N) + D\boldsymbol{R}_N(\hat{\boldsymbol{c}}_N))^* \\ &\quad - \beta(t)\boldsymbol{P}_N D\boldsymbol{C}_N^*(\hat{\boldsymbol{c}}_N)\boldsymbol{Q}_0 D\boldsymbol{C}_N(\hat{\boldsymbol{c}}_N)\boldsymbol{P}_N + \boldsymbol{W}_N.\end{aligned} \tag{5.67}$$

The observer gain is defined by

$$\boldsymbol{K} = [\boldsymbol{K}_c^T, \boldsymbol{K}_\theta]^T = \beta(t)\boldsymbol{P}_N \boldsymbol{C}_N^*(\hat{\boldsymbol{c}}_N)\boldsymbol{Q}_0. \tag{5.68}$$

For the observer design, the OCP term is set to be time-dependent. In other words, the OCP term is assumed to have the parametric form

$$U(y_{k,s}) = \theta_1 + \theta_2 y_{k,s} + \theta_3 \exp(-30y_{k,s}) + \theta \exp(-200(1 - y_{k,s}))$$

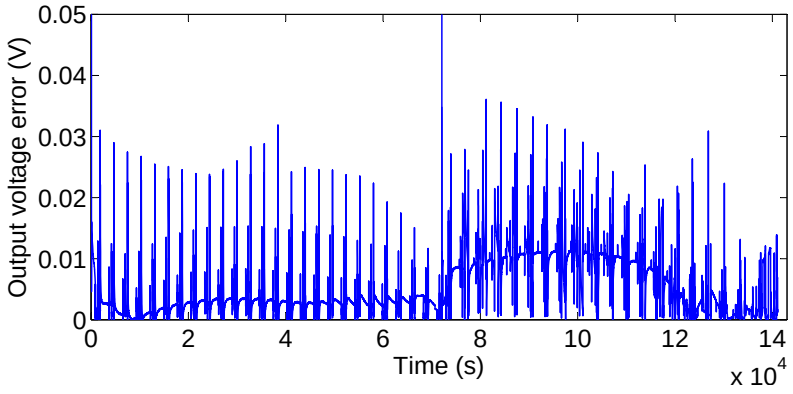

Figure 5.11: Cell voltage estimation error in a charging/discharging cycle for a constant diffusion model. The system is approximated using eigenfunctions with $N_1 = 4$, $N_2 = 4$, and $N_3 = 5$. It is observed that the estimation error is small.

for charging cycle, and

$$U(y_{k,s}) = \theta_1 + \theta_2 y_{k,s} + \theta_3 \exp(-210 y_{k,s}) + \theta_4 \exp(-35(1 - y_{k,s}))$$

for discharging cycle, where $\boldsymbol{\theta} = [\theta_1, \theta_2, \theta_3, \theta_4]^T$ is the parameter vector. The filtering matrices are set to

$$\beta(t) = 1,\ \boldsymbol{Q}_0 = \text{diag}(50, 0.5),\ \boldsymbol{W}_N = \text{diag}(0.2\boldsymbol{I}_{6\times 6}, 0.1\boldsymbol{I}_{45\times 45}, 2\boldsymbol{I}_{4\times 4})$$

with the initial conditions

$$\boldsymbol{P}_N(0) = \boldsymbol{0},$$

and

$$\boldsymbol{\theta}(0) = \begin{cases} [3.4510, -9e-3, 0.6678, -0.5]^T & \text{in charge} \\ [3.4077, -2.0269e-2, 0.5, -0.9]^T & \text{in discharge} \end{cases}.$$

Other observation parameters are given in Table 5.2. Note that the augmented output (5.49) is only active when the voltage estimation error is larger than $0.05(V)$.

Initialization of the observer is similar to what was introduced in the previous section. The simulation results for the charging/discharging course are shown in Figure 5.18-5.21. These figures represents the charging process of the cell followed by discharging process. According to these figures, the observer output follows the measurements precisely. Furthermore, It is observed that the observer recovers the initial SOC, and

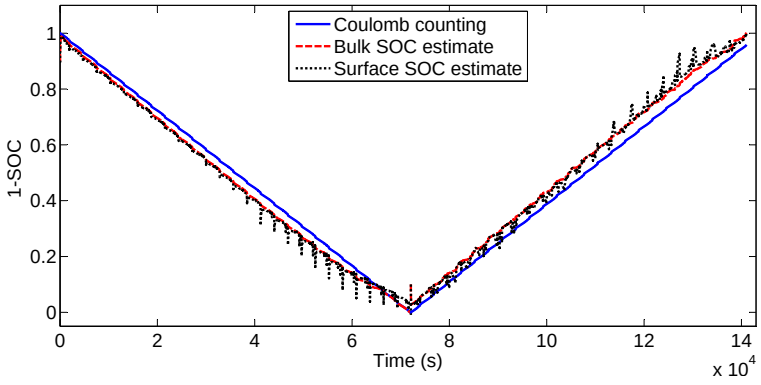

Figure 5.12: Comparison between the coulomb counting as the measurement and the SOC estimated values in a charging/discharging cycle for a constant diffusion model. The system is approximated using eigenfunctions with $N_1 = 4$, $N_2 = 4$, and $N_3 = 5$. The estimation error is observed to be less than 6%. The estimation error is observed to be less than 6%. The initial SOC is 0.1 for charging process and 0.9 for discharging process.

the bulk SOC estimation error is less than 4%. Compared to the results of the observer (5.54), Figures 5.14-5.17, both SOC estimation error and specially the output estimation error are decreased.

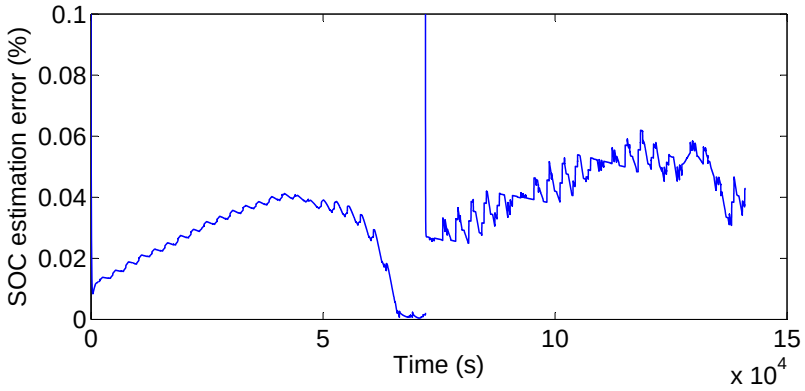

Figure 5.13: Error between coulomb counting as the measurement and the SOC estimated values in a charging/discharging cycle for a constant diffusion model. The system is approximated using eigenfunctions with $N_1 = 4$, $N_2 = 4$, and $N_3 = 5$. The estimation error is observed to be less than 6%. The estimation error is observed to be less than 6%. The initial SOC is 0.1 for charging process and 0.9 for discharging process.

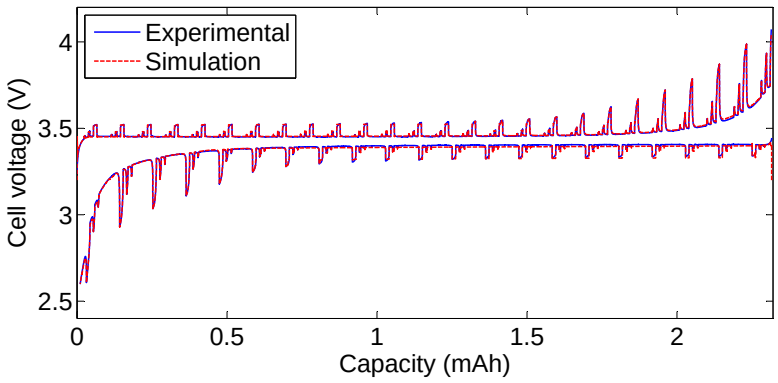

Figure 5.14: Comparison between the observation output and the measurements in a charging/discharging cycle for a nonlinear diffusion model. The system is approximated using eigenfunctions with $N_1 = 4$, $N_2 = 4$, and $N_3 = 5$. It is observed that the output estimate tracks the measurements.

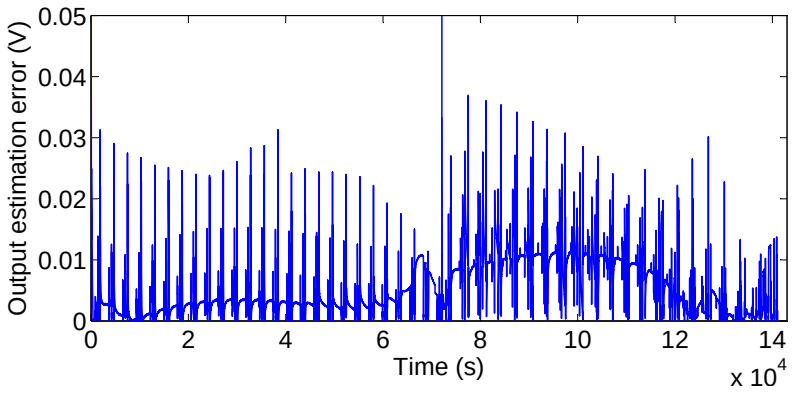

Figure 5.15: Cell voltage estimation error in a charging/discharging cycle for a nonlinear diffusion model. The system is approximated using eigenfunctions with $N_1 = 4$, $N_2 = 4$, and $N_3 = 5$. It is observed that the estimation error is small.

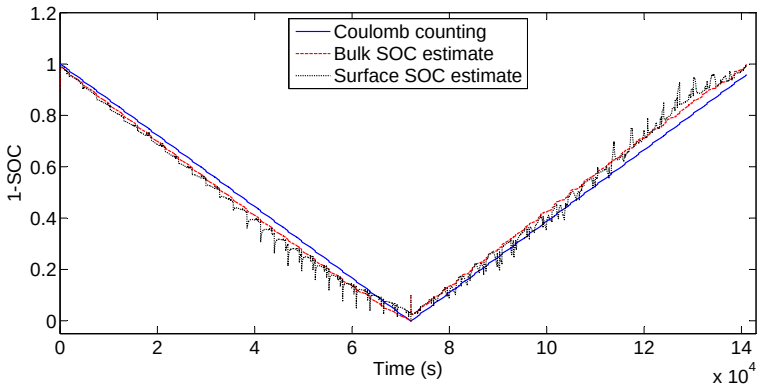

Figure 5.16: Comparison between the coulomb counting as the measurement and the SOC estimated values in a charging/discharging cycle for a nonlinear diffusion model. The system is approximated using eigenfunctions with $N_1 = 4$, $N_2 = 4$, and $N_3 = 5$. The estimation error is observed to be less than 6%. The initial SOC is 0.1 for charging process and 0.9 for discharging process.

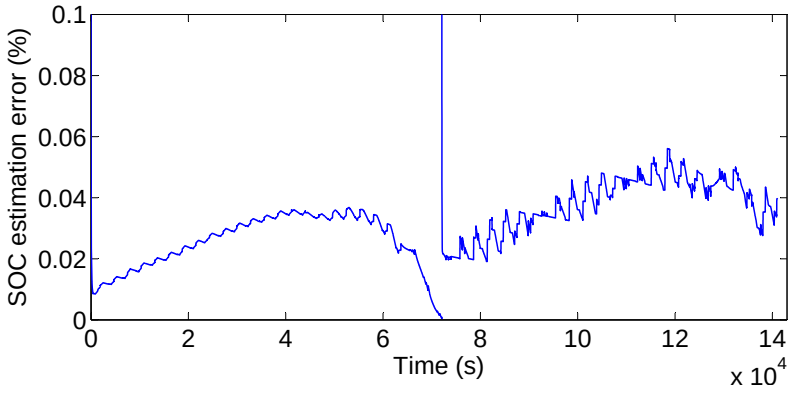

Figure 5.17: Error between the coulomb counting as the measurement and the SOC estimated values in a charging/discharging cycle for a nonlinear diffusion model. The system is approximated using eigenfunctions with $N_1 = 4$, $N_2 = 4$, and $N_3 = 5$. The estimation error is observed to be less than 6%. The initial SOC is 0.1 for charging process and 0.9 for discharging process.

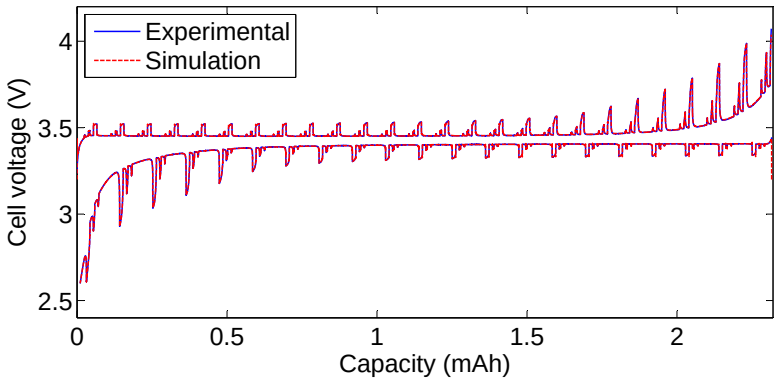

Figure 5.18: Comparison between the adaptive observation output and the measurements in a charging/discharging cycle for a nonlinear diffusion model. The system is approximated using eigenfunctions with $N1 = 4$, $N2 = 4$, and $N3 = 5$. It is observed that the output estimate precisely tracks the measurements.

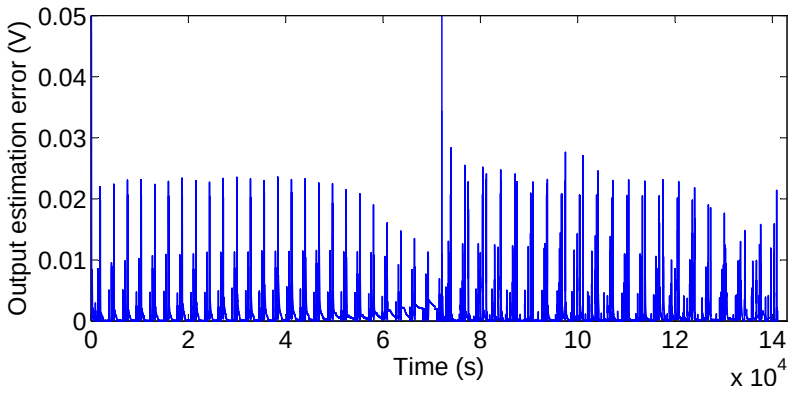

Figure 5.19: Cell voltage estimation error from the adaptive observer in a charging/discharging cycle for a nonlinear diffusion model. The system is approximated using eigenfunctions with $N1 = 4$, $N2 = 4$, and $N3 = 5$. It is observed that the estimation error is very small.

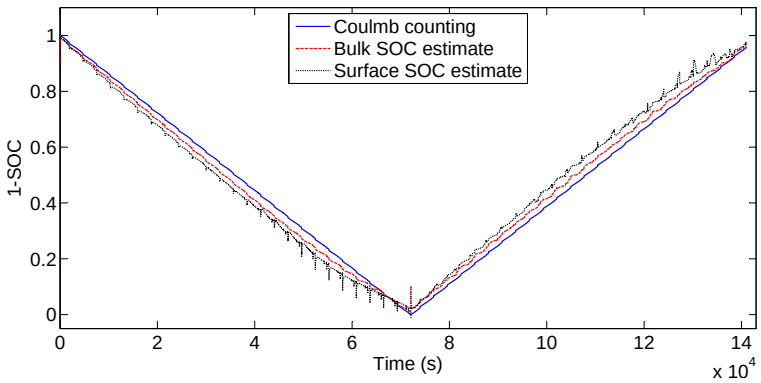

Figure 5.20: Comparison between the coulomb counting as the measurement and the SOC estimated values via the adaptive observer in a charging/discharging cycle for a nonlinear diffusion model. The system is approximated using eigenfunctions with $N1 = 4$, $N2 = 4$, and $N3 = 5$. The estimation error is observed to be less than 4%. The initial SOC is 0.1 for charging process and 0.9 for discharging process.

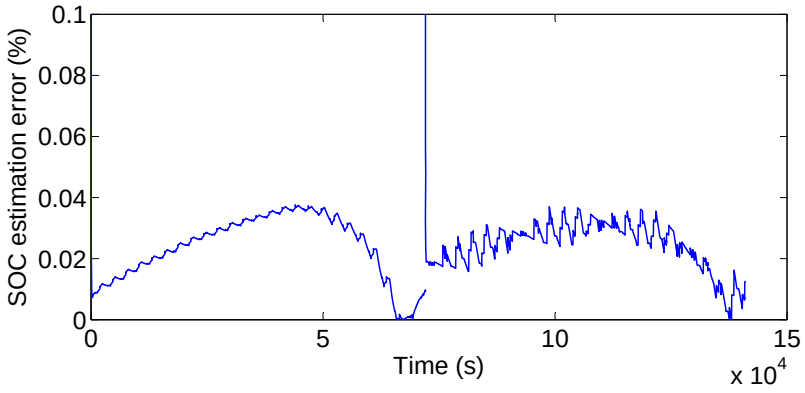

Figure 5.21: Error between coulomb counting as the measurement and the SOC estimated values via the adaptive observer in a charging/discharging cycle for a nonlinear diffusion model. The system is approximated using eigenfunctions with $N1 = 4$, $N2 = 4$, and $N3 = 5$. The estimation error is observed to be less than 4%. The initial SOC is 0.1 for charging process and 0.9 for discharging process.

Chapter 6

Conclusion and future work

The main objective of this thesis was to design a robust observer for SOC estimation of a lithium-ion cell via electrochemical equations. The thesis was divided into four major parts.

Comparing different finite-dimensional observation techniques for different types of distributed parameter systems was conducted first. According to the comparison studies, the EKF presents efficient results even in the existence of external disturbances. It was observed from simulation results that the estimation error decreases as the order of approximation increases for diffusion equations. These results motivated the next part of this research.

It was shown in Chapter 3 that for the system approximation with a finite-dimensional version, the convergence of the approximate equations can be proved. Two general classes of the systems were considered. It was proved that employing the eigenfunctions of a linear operator involved in the system's representation leads to convergent approximate solutions. The linear operator was assumed to satisfy Assumption 3.2.6.

As future work, the result of Chapter 3 could be extended to wider classes of systems. One extension is to the systems of the form

$$\begin{aligned} \frac{\partial^2 \boldsymbol{z}}{\partial t^2} + \boldsymbol{\mathcal{A}}\boldsymbol{z} + \boldsymbol{\mathcal{R}}_d(\frac{\partial \boldsymbol{z}}{\partial t}, t) = \\ \boldsymbol{\mathcal{R}}(t, \boldsymbol{z}) + \boldsymbol{\mathcal{F}}\boldsymbol{u}(t) \end{aligned} \tag{6.1}$$

where $\boldsymbol{z} \in \mathcal{H}$; the linear operator $\boldsymbol{\mathcal{A}} : \mathcal{D}(\boldsymbol{\mathcal{A}}) \in \mathcal{H} \to \mathcal{H}$, $\boldsymbol{\mathcal{F}} : \mathbb{R}^q \to \mathcal{H}$, the nonlinear operator $\boldsymbol{\mathcal{R}}(., t) : \mathcal{H} \to \mathcal{H}$, and the input signal $\boldsymbol{u} \in \mathbb{R}^q$ are defined as in Chapter 3. The nonlinear operator $\boldsymbol{\mathcal{R}}_d(., t) : \mathcal{V} \to \mathcal{H}$ represents damping.

Similar to Chapter 3, the eigenfunctions $\boldsymbol{v}_i$ of $\boldsymbol{\mathcal{A}}$ can be used to approximate the

system. Let the state $\boldsymbol{z}$ be approximated by $\boldsymbol{z}_N$. The orthonormal projection is defined by

$$\boldsymbol{z}_N = \boldsymbol{\mathcal{P}}_N \boldsymbol{z} = \sum_{i=1}^{N} z_i \boldsymbol{v}_i.$$

The system is approximated by

$$\frac{\partial^2 \boldsymbol{z}_N}{\partial t^2} + \boldsymbol{\mathcal{A}}_N \boldsymbol{z}_N + \boldsymbol{\mathcal{R}}_{d,N}(\frac{\partial \boldsymbol{z}_N}{\partial t}, t) = \boldsymbol{\mathcal{R}}_N(t, \boldsymbol{z}_N) + \boldsymbol{\mathcal{F}}_N \boldsymbol{u}(t)$$

where

$$\begin{aligned} \boldsymbol{\mathcal{A}}_N &= \boldsymbol{\mathcal{P}}_N \boldsymbol{\mathcal{A}}, \\ \boldsymbol{\mathcal{R}}_N(.) &= \boldsymbol{\mathcal{P}}_N \boldsymbol{\mathcal{R}}(.), \\ \boldsymbol{\mathcal{F}}_N &= \boldsymbol{\mathcal{P}}_N \boldsymbol{\mathcal{F}}, \\ \boldsymbol{\mathcal{R}}_{d,N}(\frac{\partial \boldsymbol{z}_N}{\partial t}, t) &= \boldsymbol{\mathcal{P}}_N \boldsymbol{\mathcal{R}}_d(\frac{\partial \boldsymbol{z}}{\partial t}, t). \end{aligned}$$

Defining the required assumptions on the system's dynamics such that the approximate solutions satisfy a convergence in some sense is a part of future work.

The observer dynamics considered in this thesis was a copy of a finite-dimensional approximation of the system and a filtering gain. It was proved that the finite-dimensional approximation of the system converges to the original system. An important question that needs to be answered is whether the approximate observer dynamics converges.

A more accurate way of observer design for infinite-dimensional systems is to allow the observer dynamics be a copy of the system's original representation and a filtering gain. Let the observer state be denoted by $\hat{\boldsymbol{z}}$. The observer dynamics for the form (3.1) is introduced by

$$\frac{\partial \hat{\boldsymbol{z}}}{\partial t} + \boldsymbol{\mathcal{A}} \hat{\boldsymbol{z}} = \boldsymbol{\mathcal{R}}(\hat{\boldsymbol{z}}) + \boldsymbol{\mathcal{F}} \boldsymbol{u}(t) + \boldsymbol{\mathcal{K}}(t) \mathcal{C}(\boldsymbol{z} - \hat{\boldsymbol{z}}) \tag{6.2}$$

where $\boldsymbol{\mathcal{K}}(t)$ is a filtering gain. The initial condition is

$$\hat{\boldsymbol{z}}(0) = \hat{\boldsymbol{z}}_0.$$

A potential way of defining an observer gain $\boldsymbol{\mathcal{K}}(t)$ is employing optimal filtering design. For a finite-dimensional system, EKF is suggested as a suboptimal way of constructing the filtering gain. The idea is extended here to a class of infinite-dimensional systems. Define $\boldsymbol{D\mathcal{R}}(.) : \mathcal{H} \to \mathcal{L}(\mathcal{H})$ by

$$\boldsymbol{D\mathcal{R}}(\hat{\boldsymbol{z}}) = \frac{\partial \boldsymbol{\mathcal{R}}(\boldsymbol{z})}{\partial \boldsymbol{z}} \mid_{\boldsymbol{z}=\hat{\boldsymbol{z}}} . \tag{6.3}$$

Let $\boldsymbol{T}(t)$ be the C_0-semigroup generated by $-\boldsymbol{\mathcal{A}} + \alpha\boldsymbol{\mathcal{I}}$. The parameter $\alpha > 0$ is added to provide a prescribed estimation error convergence rate.

Given a positive bounded linear operator $\boldsymbol{P}_0$, a nonnegative uniformly bounded linear operator $\boldsymbol{W}(t)$, a positive uniformly bounded linear operator $\boldsymbol{R}(t)$ such that

$$(\boldsymbol{R}(t)\boldsymbol{w}, \boldsymbol{w})_{\mathcal{H}} \geq \mu_0 \|\boldsymbol{w}\|^2_{\mathcal{X}}$$

for $\mu_0 > 0$, and a continuous function $\beta(t) \geq \mu_1 > 0$, $\boldsymbol{P}(t) : \mathcal{H} \to \mathcal{X}$ is the solution to the following coupled equations

$$\begin{aligned} \boldsymbol{P}(t)\boldsymbol{w} = &\boldsymbol{\mathcal{U}}_p(t,0)\boldsymbol{P}_0\boldsymbol{\mathcal{U}}_p^*(t,0)\boldsymbol{w} + \int_0^t \boldsymbol{\mathcal{U}}_p(t,s)(\boldsymbol{W}(s) \\ &+ \beta(s)\boldsymbol{P}(s)\mathcal{C}^*\boldsymbol{R}(t)^{-1}\mathcal{C}\boldsymbol{P}(s))\boldsymbol{\mathcal{U}}_p^*(t,s)\boldsymbol{w}ds, \end{aligned} \tag{6.4}$$

$$\begin{aligned} \boldsymbol{\mathcal{U}}_p(t,s) = &\boldsymbol{\mathcal{U}}(t,s) \\ &- \int_s^t \boldsymbol{\mathcal{U}}(t,r)\beta(r)\boldsymbol{P}(r)\mathcal{C}^*\boldsymbol{R}(t)^{-1}\mathcal{C}\boldsymbol{\mathcal{U}}_p(r,s)dr, \end{aligned} \tag{6.5}$$

$$\boldsymbol{\mathcal{U}}(t,s) = \boldsymbol{T}(t-s) + \int_s^t \boldsymbol{T}(t-r)\boldsymbol{D}\boldsymbol{\mathcal{R}}(\hat{\boldsymbol{z}}(r))\boldsymbol{\mathcal{U}}(r,s)dr. \tag{6.6}$$

The observer gain is defined as

$$\boldsymbol{\mathcal{K}}(t) = \beta(t)\boldsymbol{P}(t)\mathcal{C}^*\boldsymbol{R}(t)^{-1}. \tag{6.7}$$

The equation (6.4) is a generalized Riccati equation as the linear operator $\boldsymbol{D}\mathcal{R}(\hat{\boldsymbol{z}})$ is a possibly nonlinear function of the observer state $\hat{\boldsymbol{z}}$.

For general linear systems, the well-posedness of the Riccati equation is studied in literature [152]; however, the results are not valid for nonlinear systems. Proving the well-posedness and local exponential convergence of the developed Riccati equation (6.4) interconnected with the observer dynamics (6.2) are some open problems. Furthermore, developing the same observer for a system of the form (6.1) is also be considered as the future plan.

A future project is to prove that the observer dynamics (6.2) coupled with the Riccati equation (6.4) and the linear integral equations (6.6) and (6.5) are well-posed for a specific range of $\beta(t) \geq \mu_1 > 0$. Similarly, the well-posednesss and convergence of the observer for the system of the form (6.1) needs to be shown.

In the third part, the electrochemical equations governing the cell dynamics were introduced. It was shown that the system's dynamics contribute in an important phe-

nomenon in the output voltage called hysteresis. The existence of hysteresis, path dependency of the system's response, indicates that not every simplified model is appropriate for the observer design.

Finally, after simplifications, the battery equations were transformed into a state space representation studied in Chapter 3; next, an adaptive EKF observer was constructed for a low-order model. At the first step, the system's representation was replaced by a fully dynamic representation; then, a reduced order model was developed via the eigenfunctions of a linear operator involved in the system's representation. It was proved that as the dimension of the reduced order model increases, a subsequence of the approximate solutions converges to the solution of the cell's original equations.

The simulation time of solving the low-order fully dynamical model for different charging and discharging rates was much smaller than the real experiment duration. However, the numerical algorithm used to solve the equations needs to be improved such that it can be used by the battery management system in a real-time application.

The adaptive observer was developed to provide enough accuracy and robustness to the modeling uncertainties. In the observer's dynamics, the parameters of the OCP term, which is an important part of the model, was allowed to change in time. In this way, the effect of the hysteresis can be included even when the OCP has a single-value empirical representation. Compared to experimental data, the simulation results confirmed the performance of the proposed observer. The simulation results also show that the adaptive EKF developed in this research works better than the standard one.

The designed observer offers some advantages over the methods introduced in the literature. First, it is designed via electrochemical equations involving a minimum approximation; thus more accuracy can be provided. Furthermore, the observer can tune the parameters of the OCP such that the model output matches the experimental data. In other words, the observer is robust to the uncertainties involved in the OCP modeling including the effect of hysteresis. Finally, including environmental effects in the employed physic-based electrochemical equations can be achieved easily.

Last but not least, adding the environmental effects including the temperature and aging will be facilitated by the fact that the electrochemical model is physical-based in contrast to equivalent circuit models. Furthermore, the observer was designed for a half-cell; the observer design for a full cell will be studied in future.

Bibliography

[1] Marc Doyle, Thomas F Fuller, and John Newman. Modeling of galvanostatic charge and discharge of the lithium/polymer/insertion cell. *Journal of the Electrochemical Society*, 140(6):1526–1533, 1993.

[2] M Farkhondeh, M Safari, M Pritzker, M Fowler, Taeyoung Han, Jasmine Wang, and C Delacourt. Full-range simulation of a commercial lifepo4 electrode accounting for bulk and surface effects: A comparative analysis. *Journal of The Electrochemical Society*, 161(3):A201–A212, 2014.

[3] Reinhardt Klein, Nalin A Chaturvedi, Jake Christensen, Jasim Ahmed, Rolf Findeisen, and Aleksandar Kojic. Electrochemical model based observer design for a lithium-ion battery. 2012.

[4] Amir Hossein Ranjbar, Anahita Banaei, Amir Khoobroo, and Babak Fahimi. Online estimation of state of charge in li-ion batteries using impulse response concept. *Smart Grid, IEEE Transactions on*, 3(1):360–367, 2012.

[5] Meng-Feng Li, Wen Chen, Hai Wu, and David Gorski. Robust state of charge estimation of lithium-ion batteries via an iterative learning observer. *Training*, 2011:11–04, 2012.

[6] Venkat Srinivasan and John Newman. Discharge model for the lithium iron-phosphate electrode. *Journal of the Electrochemical Society*, 151(10):A1517–A1529, 2004.

[7] Gregory L Plett. Extended kalman filtering for battery management systems of lipb-based hev battery packs: Part 1. background. *Journal of Power sources*, 134(2):252–261, 2004.

[8] Shuo Pang, Jay Farrell, Jie Du, and Matthew Barth. Battery state-of-charge estimation. In *American Control Conference, 2001. Proceedings of the 2001*, volume 2, pages 1644–1649. IEEE, 2001.

[9] V Prajapati, H Hess, EJ William, V Gupta, M Huff, M Manic, F Rufus, A Thakker, and J Govar. A literature review of state of-charge estimation techniques applicable to lithium poly-carbon monoflouride (li/cfx) battery. In *Power Electronics (IICPE), 2010 India International Conference on*, pages 1–8. IEEE, 2011.

[10] Peng Rong and Massoud Pedram. An analytical model for predicting the remaining battery capacity of lithium-ion batteries. *Very Large Scale Integration (VLSI) Systems, IEEE Transactions on*, 14(5):441–451, 2006.

[11] Bi Jun, Shao Sai, Guan Wei, and Wang Lu. State of charge estimation of li-ion batteries in an electric vehicle based on a radial-basis-function neural network. *Chinese Physics B*, 21(11):118801, 2012.

[12] Gregory L Plett. Extended kalman filtering for battery management systems of lipb-based hev battery packs: Part 2. modeling and identification. *Journal of power sources*, 134(2):262–276, 2004.

[13] Shalini Rodrigues, N Munichandraiah, and AK Shukla. A review of state-of-charge indication of batteries by means of ac impedance measurements. *Journal of Power Sources*, 87(1):12–20, 2000.

[14] BS Bhangu, P Bentley, DA Stone, and CM Bingham. Observer techniques for estimating the state-of-charge and state-of-health of vrlabs for hybrid electric vehicles. In *Vehicle Power and Propulsion, 2005 IEEE Conference*, pages 10–pp. IEEE, 2005.

[15] Mark Verbrugge and Edward Tate. Adaptive state of charge algorithm for nickel metal hydride batteries including hysteresis phenomena. *Journal of Power Sources*, 126(1):236–249, 2004.

[16] Valer Pop, Henk Jan Bergveld, JHG Op het Veld, PPL Regtien, D Danilov, and PHL Notten. Modeling battery behavior for accurate state-of-charge indication. *Journal of the Electrochemical Society*, 153(11):A2013–A2022, 2006.

[17] Fabio Codecà, Sergio M Savaresi, and Giorgio Rizzoni. On battery state of charge estimation: A new mixed algorithm. In *Control Applications, 2008. CCA 2008. IEEE International Conference on*, pages 102–107. IEEE, 2008.

[18] Jean Alzieu, Hassan Smimite, and Christian Glaize. Improvement of intelligent battery controller: state-of-charge indicator and associated functions. *Journal of power sources*, 67(1):157–161, 1997.

[19] V Pop, HJ Bergveld, and PPL Regtien. Smart and accurate state-of-charge indication in portable applications. In *Power Electronics and Drives Systems, 2005. PEDS 2005. International Conference on*, volume 1, pages 262–267. IEEE, 2005.

[20] Koray Kutluay, Yigit Cadirci, Yakup S Ozkazanc, and Isik Cadirci. A new online state-of-charge estimation and monitoring system for sealed lead-acid batteries in telecommunication power supplies. *Industrial Electronics, IEEE Transactions on*, 52(5):1315–1327, 2005.

[21] O Caumont, P Le Moigne, C Rombaut, X Muneret, and P Lenain. Energy gauge for lead-acid batteries in electric vehicles. *Energy Conversion, IEEE Transactions on*, 15(3):354–360, 2000.

[22] Der-Tsai Lee, Shaw-Ji Shiah, Chien-Ming Lee, and Ying-Chung Wang. State-of-charge estimation for electric scooters by using learning mechanisms. *Vehicular Technology, IEEE Transactions on*, 56(2):544–556, 2007.

[23] Xiaosong Hu, Shengbo Li, and Huei Peng. A comparative study of equivalent circuit models for li-ion batteries. *Journal of Power Sources*, 198:359–367, 2012.

[24] Gregory L Plett. Extended kalman filtering for battery management systems of lipb-based hev battery packs: Part 3. state and parameter estimation. *Journal of Power sources*, 134(2):277–292, 2004.

[25] A Vasebi, SMT Bathaee, and M Partovibakhsh. Predicting state of charge of lead-acid batteries for hybrid electric vehicles by extended kalman filter. *Energy Conversion and Management*, 49(1):75–82, 2008.

[26] Dinh Vinh Do, Christophe Forgez, Khadija El Kadri Benkara, and Guy Friedrich. Impedance observer for a li-ion battery using kalman filter. *Vehicular Technology, IEEE Transactions on*, 58(8):3930–3937, 2009.

[27] Hongwen He, Rui Xiong, and Jinxin Fan. Evaluation of lithium-ion battery equivalent circuit models for state of charge estimation by an experimental approach. *energies*, 4(4):582–598, 2011.

[28] Gregory L Plett. Sigma-point kalman filtering for battery management systems of lipb-based hev battery packs: Part 2: Simultaneous state and parameter estimation. *Journal of Power Sources*, 161(2):1369–1384, 2006.

[29] Shriram Santhanagopalan and Ralph E White. State of charge estimation using an unscented filter for high power lithium ion cells. *International Journal of Energy Research*, 34(2):152–163, 2010.

[30] Il-Song Kim. The novel state of charge estimation method for lithium battery using sliding mode observer. *Journal of Power Sources*, 163(1):584–590, 2006.

[31] Il-Song Kim. Nonlinear state of charge estimator for hybrid electric vehicle battery. *Power Electronics, IEEE Transactions on*, 23(4):2027–2034, 2008.

[32] Nacer K MSirdi, Ahmed Belhani, and Aziz Naamane. Battery models for estimation of state of charge by sliding mode observer. In *Sustainability in Energy and Buildings*, pages 133–149. Springer, 2012.

[33] Michael A Roscher and Dirk Uwe Sauer. Dynamic electric behavior and open-circuit-voltage modeling of LiFePO4-based lithium ion secondary batteries. *Journal of Power Sources*, 196(1):331–336, 2011.

[34] Yonghua Li, R Dyche Anderson, Jing Song, Anthony M Phillips, and Xu Wang. A nonlinear adaptive observer approach for state of charge estimation of lithium-ion batteries. In *American Control Conference (ACC), 2011*, pages 370–375. IEEE, 2011.

[35] Yiran Hu and Stephen Yurkovich. Battery state of charge estimation in automotive applications using lpv techniques. In *American Control Conference (ACC), 2010*, pages 5043–5049. IEEE, 2010.

[36] Shriram Santhanagopalan, Qingzhi Guo, Premanand Ramadass, and Ralph E White. Review of models for predicting the cycling performance of lithium ion batteries. *Journal of Power Sources*, 156(2):620–628, 2006.

[37] Domenico Di Domenico, Anna Stefanopoulou, and Giovanni Fiengo. Lithium-ion battery state of charge and critical surface charge estimation using an electrochemical model-based extended Kalman filter. *Journal of Dynamic Systems, Measurement, and Control*, 132(6):061302, 2010.

[38] Reinhardt Klein, Nalin A Chaturvedi, Jake Christensen, Jasim Ahmed, Rolf Findeisen, and Aleksandar Kojic. State estimation of a reduced electrochemical model of a lithium-ion battery. In *American Control Conference (ACC), 2010*, pages 6618–6623. IEEE, 2010.

[39] Kandler A Smith, Christopher D Rahn, and Chao-Yang Wang. Model-based electrochemical estimation of lithium-ion batteries. In *Control Applications, 2008. CCA 2008. IEEE International Conference on*, pages 714–719. IEEE, 2008.

[40] Kandler A Smith, Christopher D Rahn, and Chao-Yang Wang. Model-based electrochemical estimation and constraint management for pulse operation of lithium ion batteries. *Control Systems Technology, IEEE Transactions on*, 18(3):654–663, 2010.

[41] SJ Moura, NA Chaturvedi, and M Krstic. Pde estimation techniques for advanced battery management systemspart i: Soc estimation. In *American Control Conference (ACC), 2012*, pages 559–565. IEEE, 2012.

[42] Scott J Moura, Miroslav Krstic, and Nalin A Chaturvedi. Adaptive PDE observer for battery SOC/SOH estimation. In *ASME 2012 5th Annual Dynamic Systems and Control Conference joint with the JSME 2012 11th Motion and Vibration Conference*, pages 101–110. American Society of Mechanical Engineers, 2012.

[43] Scott J Moura, Nalin A Chaturvedi, and Miroslav Krstić. Adaptive partial differential equation observer for battery state-of-charge/state-of-health estimation via an electrochemical model. *Journal of Dynamic Systems, Measurement, and Control*, 136(1):011015, 2014.

[44] Alexander Bartlett, James Marcicki, Simona Onori, Giorgio Rizzoni, Xiao Guang Yang, and Ted Miller. Electrochemical model-based state of charge and capacity estimation for a composite electrode lithium-ion battery. *IEEE Transactions on Control Systems Technology*, 24(2):384–399, 2016.

[45] Satadru Dey, Beshah Ayalew, and Pierluigi Pisu. Nonlinear robust observers for state-of-charge estimation of lithium-ion cells based on a reduced electrochemical model. *IEEE Transactions on Control Systems Technology*, 23(5):1935–1942, 2015.

[46] Matteo Corno, Nimitt Bhatt, Sergio M Savaresi, and Michel Verhaegen. Electrochemical model-based state of charge estimation for li-ion cells. *IEEE Transactions on Control Systems Technology*, 23(1):117–127, 2015.

[47] AM Bizeray, S Zhao, SR Duncan, and DA Howey. Lithium-ion battery thermal-electrochemical model-based state estimation using orthogonal collocation and a modified extended Kalman filter. *Journal of Power Sources*, 296:400–412, 2015.

[48] Indrajeet V Thorat. *Understanding Performance-limiting Mechanisms in Lithium-ion Batteries for High-rate Applications*. ProQuest, 2009.

[49] M Farkhondeh and C Delacourt. Mathematical modeling of commercial lifepo4 electrodes based on variable solid-state diffusivity. *Journal of The Electrochemical Society*, 159(2):A177–A192, 2011.

[50] EA Misawa and JK Hedrick. Nonlinear observers—a state-of-the-art survey. *Journal of dynamic systems, measurement, and control*, 111(3):344–352, 1989.

[51] Nikolaos Kazantzis and Costas Kravaris. Nonlinear observer design using lyapunov's auxiliary theorem. *Systems & Control Letters*, 34(5):241–247, 1998.

[52] Xiao Hua Xia and Wei Bin Gao. Nonlinear observer design by observer error linearization. *SIAM Journal on Control and Optimization*, 27(1):199–216, 1989.

[53] Daejong Noh, Nam H Jo, and Jin H Seo. Nonlinear observer design by dynamic observer error linearization. *Automatic Control, IEEE Transactions on*, 49(10):1746–1753, 2004.

[54] Xianchun Ding, Paul M Frank, and Limin Guo. Nonlinear observer design via an extended observer canonical form. *Systems & control letters*, 15(4):313–322, 1990.

[55] Gerasimos G Rigatos. Derivative-free nonlinear kalman filtering for mimo dynamical systems: application to multi-dof robotic manipulators. *International Journal of Advanced Robotic Systems*, 8(6):47–61, 2011.

[56] Gerasimos G Rigatos. Control of heat diffusion in arc welding using differential flatness theory and nonlinear kalman filtering. *IFAC-PapersOnLine*, 48(3):1368–1374, 2015.

[57] Gerasimos G Rigatos. *Nonlinear control and filtering using differential flatness approaches: applications to electromechanical systems*, volume 25. Springer, 2015.

[58] BL Walcott, MJ Corless, and SH Żak. Comparative study of non-linear state-observation techniques. *International Journal of Control*, 45(6):2109–2132, 1987.

[59] F Chen and MW Dunnigan. Comparative study of a sliding-mode observer and Kalman filters for full state estimation in an induction machine. *IEE Proceedings-Electric Power Applications*, 149(1):53–64, 2002.

[60] Sarah K Spurgeon. Sliding mode observers: a survey. *International Journal of Systems Science*, 39(8):751–764, 2008.

[61] Ali J Koshkouei and Alan SI Zinober. Sliding mode state observation for non-linear systems. *International Journal of Control*, 77(2):118–127, 2004.

[62] KC Veluvolu, YC Soh, and W Cao. Robust observer with sliding mode estimation for nonlinear uncertain systems. *Control Theory & Applications, IET*, 1(5):1533–1540, 2007.

[63] Simon J. Julier and Jeffrey K. Uhlmann. A new extension of the Kalman filter to nonlinear systems. In *Proceeding, SPIE*, volume 3068, pages 182–193, 1997.

[64] Maria Isabel Ribeiro. Kalman and extended Kalman filters: Concept, derivation and properties. Technical report, Institute for Systems and Robotics, Lisboa, 2004.

[65] Mohinder S Grewal and Angus P Andrews. *Kalman filtering: theory and practice using MATLAB*. John Wiley & Sons, 2011.

[66] Konrad Reif and Rolf Unbehauen. The extended kalman filter as an exponential observer for nonlinear systems. *IEEE Transactions on Signal Processing*, 47(8):2324–2328, 1999.

[67] Konrad Reif, Frank Sonnemann, and Rolf Unbehauen. An EKF-based nonlinear observer with a prescribed degree of stability. *Automatica*, 34(9):1119–1123, 1998.

[68] Eric A Wan and Rudolph Van Der Merwe. The unscented Kalman filter for nonlinear estimation. In *Adaptive Systems for Signal Processing, Communications, and Control Symposium 2000. AS-SPCC.*, pages 153–158. IEEE, 2000.

[69] Xiong Kai, Chunling Wei, and Liangdong Liu. Robust extended kalman filtering for nonlinear systems with stochastic uncertainties. *Systems, Man and Cybernetics, Part A: Systems and Humans, IEEE Transactions on*, 40(2):399–405, 2010.

[70] Xiong Kai, Liu Liangdong, and Liu Yiwu. Robust extended kalman filtering for nonlinear systems with multiplicative noises. *Optimal Control Applications and Methods*, 32(1):47–63, 2011.

[71] Garry A Einicke and Langford B White. Robust extended kalman filtering. *IEEE Transactions on Signal Processing*, 47(9):2596–2599, 1999.

[72] Konrad Reif, Frank Sonnemann, and Rolf Unbehauen. Nonlinear state observation using h/sub/spl infin//-filtering riccati design. *Automatic Control, IEEE Transactions on*, 44(1):203–208, 1999.

[73] B Walcott and SH Zak. State observation of nonlinear uncertain dynamical systems. *IEEE Transactions on Automatic Control*, 32(2):166–170, 1987.

[74] Leonid Fridman, Yuri Shtessel, Christopher Edwards, and Xing Gang Yan. Higher-order sliding-mode observer for state estimation and input reconstruction in nonlinear systems. *International Journal of Robust and Nonlinear Control*, 18(4-5):399–412, 2008.

[75] KC Veluvolu, YC Soh, and W Cao. Robust observer with sliding mode estimation for nonlinear uncertain systems. *Control Theory & Applications, IET*, 1(5):1533–1540, 2007.

[76] Sergey Drakunov and Vadim Utkin. Sliding mode observers. tutorial. In *Decision and Control, 1995., Proceedings of the 34th IEEE Conference on*, volume 4, pages 3376–3378. IEEE, 1995.

[77] Vadim Utkin. *Sliding mode estimation and optimization methods in nonlinear control problems*. PhD thesis, The Ohio State University, 1999.

[78] Sergey V Drakunov and Mahmut Reyhanoglu. Hierarchical sliding mode observers for distributed parameter systems. *Journal of Vibration and Control*, 17(10):1441–1453, 2011.

[79] Yi Xiong and Mehrdad Saif. Sliding mode observer for nonlinear uncertain systems. *IEEE Transactions on Automatic Control*, 46(12):2012–2017, 2001.

[80] Sergey V Drakunov. Sliding-mode observers based on equivalent control method. In *Proceedings of the 31st IEEE Conference on Decision and Control*, pages 2368–2369. IEEE, 1992.

[81] Alberto Isidori. *Nonlinear control systems*, volume 1. Springer, 1995.

[82] Gildas Besançon. *Nonlinear observers and applications*, volume 363. Springer, 2007.

[83] Katalin M Hangos, József Bokor, and Gábor Szederkényi. *Analysis and control of nonlinear process systems*. Springer Science & Business Media, 2004.

[84] C Edwards and S Spurgeon. *Sliding Mode Control: Theory And Applications*. CRC Press, 1998.

[85] Ruth Curtain and Kirsten Morris. Transfer functions of distributed parameter systems: A tutorial. *Automatica*, 45(5):1101–1116, 2009.

[86] Ruth F. Curtain and Hans Zwart. *An introduction to infinite-dimensional linear systems theory*. Springer New York, 1995.

[87] PK Kundu and IM Cohen. *Fluid mechanics*. Elsevier Academic Press, 4 edition, 2008.

[88] Andrey Smyshlyaev and Miroslav Krstic. Backstepping observers for a class of parabolic PDE's. *Systems & Control Letters*, 54(7):613–625, 2005.

[89] Zulkifli Hidayat, Robert Babuska, Bart De Schutter, and Alfredo Nunez. Observers for linear distributed-parameter systems: A survey. In *Robotic and Sensors Environments (ROSE), 2011 IEEE International Symposium on*, pages 166–171. IEEE, 2011.

[90] Y. A. Liu and L. Lapldus. Observer theory for distributed-parameter systems. *International Journal of Systems Science*, 7(7):731–742, 1976.

[91] Ramón Miranda, Isaac Chairez, and Jaime Moreno. Observer design for a class of parabolic PDE via sliding modes and backstepping. In *2010 11th International Workshop on Variable Structure Systems (VSS)*, pages 215–220. IEEE, 2010.

[92] Yury V Orlov. *Discontinuous systems: Lyapunov analysis and robust synthesis under uncertainty conditions*. Springer Science & Business Media, 2008.

[93] Ruth F Curtain. Finite-dimensional compensator design for parabolic distributed systems with point sensors and boundary input. *IEEE Transactions on Automatic Control*, 27(1):98–104, 1982.

[94] Michael A Demetriou. Natural second-order observers for second-order distributed parameter systems. *Systems & control letters*, 51(3):225–234, 2004.

[95] L Meirovitch and H Baruh. On the problem of observation spillover in self-adjoint distributed-parameter systems. *Journal of Optimization Theory and Applications*, 39(2):269–291, 1983.

[96] Huai-Ning Wu and Han-Xiong Li. H_∞ fuzzy observer-based control for a class of nonlinear distributed parameter systems with control constraints. *IEEE Transactions on Fuzzy Systems*, 16(2):502–516, 2008.

[97] Huai Ning Wu and Han Xiong Li. Robust adaptive neural observer design for a class of nonlinear parabolic PDE systems. *Journal of Process Control*, 21(8):1172–1182, 2011.

[98] Souvik Chandra, Sangeeta Nundy, and Siddhartha Mukhopadhyay. State-space modeling and estimation of coupled PDE system: A case study in sintering process. In *India Conference (INDICON), 2011 Annual IEEE*, pages 1–6. IEEE, 2011.

[99] S. Afshar, K. A. Morris, and A. Khajepour. Comparision of different observers for nonlinear distributed parameter systems. submitted.

[100] R Miranda, JA Moreno, J Chairez, and L Fridman. Observer design for a class of hyperbolic PDE equation based on a distributed super twisting algorithm. In *12th International Workshop on Variable Structure Systems (VSS)*, pages 367–372. IEEE, 2012.

[101] M Bitzer and M Zeitz. Design of a nonlinear distributed parameter observer for a pressure swing adsorption plant. *Journal of process control*, 12(4):533–543, 2002.

[102] MÖ Efe*, H Özbay, and M Samimy. Infinite dimensional and reduced order observers for burgers equation. *International Journal of Control*, 78(11):864–874, 2005.

[103] Jean-François Couchouron and P Ligarius. Nonlinear observers in reflexive banach spaces. *ESAIM: Control, Optimisation and Calculus of Variations*, 9:67–103, 2003.

[104] SG Tzafestas and JM Nightingale. Maximum-likelihood approach to the optimal filtering of distributed-parameter systems. In *Proceedings of the Institution of Electrical Engineers*, volume 116, pages 1085–1093. IET, 1969.

[105] JH Seinfeld. Nonlinear estimation for partial differential equations. *Chemical Engineering Science*, 24(1):75–83, 1969.

[106] JH Seinfeld, GR Gavalas, and M Hwang. Nonlinear filtering in distributed parameter systems. *Journal of Dynamic Systems, Measurement, and Control*, 93(3):157–163, 1971.

[107] Rafael Vazquez, Eugenio Schuster, and Miroslav Krstic. Magnetohydrodynamic state estimation with boundary sensors. *Automatica*, 44(10):2517–2527, 2008.

[108] Tim Meurer. On the extended luenberger-type observer for semilinear distributed-parameter systems. *Automatic Control, IEEE Transactions on*, 58(7):1732–1743, 2013.

[109] Felipe Castillo, Emmanuel Witrant, Christophe Prieur, and Luc Dugard. Boundary observers for linear and quasi-linear hyperbolic systems with application to flow control. *Automatica*, 49(11):3180–3188, 2013.

[110] Alexander Schaum, Jaime A Moreno, Emilia Fridman, and Jesus Alvarez. Matrix inequality-based observer design for a class of distributed transport-reaction systems. *International Journal of Robust and Nonlinear Control*, 24(16):2213–2230, 2014.

[111] N Carmichael, Alan Joseph Pritchard, and MD Quinn. State and parameter estimation for nonlinear systems. *Applied Mathematics and Optimization*, 9(1):133–161, 1982.

[112] Fabio Botelho. *Functional Analysis and Applied Optimization in Banach Spaces*. Springer, 2014.

[113] Tosio Kato. Nonlinear semigroups and evolution equations. *Journal of the Mathematical Society of Japan*, 19(4):508–520, 1967.

[114] Zdzislaw Denkowski, Stanislaw Migórski, and Nikolaos S Papageorgiou. *An introduction to nonlinear analysis: theory*. Springer Science & Business Media, 2013.

[115] AG Kartsatos and WR Zigler. Rothe's method and weak solutions of perturbed evolution equations in reflexive banach spaces. *Mathematische Annalen*, 219(2):159–166, 1976.

[116] Robert Dautray and Jacques-Louis Lions. *Mathematical Analysis and Numerical Methods for Science and Technology: Volume 1 Physical Origins and Classical Methods*, volume 3. Springer Science & Business Media, 1998.

[117] Roger Temam. *Infinite-dimensional dynamical systems in mechanics and physics*, volume 68. Springer Science & Business Media, 2012.

[118] Philippe G Ciarlet. *Linear and nonlinear functional analysis with applications*, volume 130. Siam, 2013.

[119] George R Sell and Yuncheng You. *Dynamics of evolutionary equations*, volume 143. Springer Science & Business Media, 2013.

[120] Walter van Schalkwijk and Bruno Scrosati. *Advances in lithium-ion batteries*. Springer, 2002.

[121] Karen Thomas, John Newman, and Robert Darling. Mathematical modeling of lithium batteries. *Advances in lithium-ion batteries*, pages 345–392, 2002.

[122] Peng Bai and Guangyu Tian. Statistical kinetics of phase-transforming nanoparticles in LiFePO4 porous electrodes. *Electrochimica Acta*, 89:644–651, 2013.

[123] Venkat Srinivasan and John Newman. Existence of path-dependence in the LiFePO4 electrode. *Electrochemical and solid-state letters*, 9(3):A110–A114, 2006.

[124] Wolfgang Dreyer, Janko Jamnik, Clemens Guhlke, Robert Huth, Jože Moškon, and Miran Gaberšček. The thermodynamic origin of hysteresis in insertion batteries. *Nature materials*, 9(5):448–453, 2010.

[125] Xiaosong Hu, Shengbo Li, and Huei Peng. A comparative study of equivalent circuit models for Li-ion batteries. *Journal of Power Sources*, 198:359–367, 2012.

[126] Mark Verbrugge. Adaptive, multi-parameter battery state estimator with optimized time-weighting factors. *Journal of applied electrochemistry*, 37(5):605–616, 2007.

[127] A Chow and K. A Morris. Hysteresis in the linearized Landau-Lifshitz equation. In *American Control Conference (ACC), 2014*, pages 4747–4752. IEEE, 2014.

[128] KA Morris. What is hysteresis? *Applied Mechanics Reviews*, 64(5):050801, 2011.

[129] J. Oh and D.S. Bernstein. Semilinear Duhem model for rate-independent and rate-dependent hysteresis. *IEEE Trans. Autom. Control (USA)*, 50(5):631 – 45, 2005.

[130] F Huet. A review of impedance measurements for determination of the state-of-charge or state-of-health of secondary batteries. *Journal of power sources*, 70(1):59–69, 1998.

[131] B Hariprakash, SK Martha, Arthi Jaikumar, and AK Shukla. On-line monitoring of lead–acid batteries by galvanostatic non-destructive technique. *Journal of Power Sources*, 137(1):128–133, 2004.

[132] Alvin J Salkind, Craig Fennie, Pritpal Singh, Terrill Atwater, and David E Reisner. Determination of state-of-charge and state-of-health of batteries by fuzzy logic methodology. *Journal of Power Sources*, 80(1):293–300, 1999.

[133] M Mastali, J Vazquez-Arenas, R Fraser, M Fowler, S Afshar, and M Stevens. Battery state of the charge estimation using kalman filtering. *Journal of Power Sources*, 239:294–307, 2013.

[134] Bala S Haran, Branko N Popov, and Ralph E White. Determination of the hydrogen diffusion coefficient in metal hydrides by impedance spectroscopy. *Journal of power sources*, 75(1):56–63, 1998.

[135] Shriram Santhanagopalan and Ralph E White. Online estimation of the state of charge of a lithium ion cell. *Journal of Power Sources*, 161(2):1346–1355, 2006.

[136] Xuebing Han, Minggao Ouyang, Languang Lu, and Jianqiu Li. Simplification of physics-based electrochemical model for lithium ion battery on electric vehicle. part i: Diffusion simplification and single particle model. *Journal of Power Sources*, 278:802–813, 2015.

[137] Yebin Wang, Huazhen Fang, Zafer Sahinoglu, Toshihiro Wada, and Satoshi Hara. Adaptive estimation of the state of charge for lithium-ion batteries: nonlinear geometric observer approach. *IEEE Transactions on Control Systems Technology*, 23(3):948–962, 2015.

[138] Linfeng Zheng, Lei Zhang, Jianguo Zhu, Guoxiu Wang, and Jiuchun Jiang. Co-estimation of state-of-charge, capacity and resistance for lithium-ion batteries based on a high-fidelity electrochemical model. *Applied Energy*, 180:424–434, 2016.

[139] Paulo Kemper, Shengbo Eben Li, and Dongsuk Kum. Simplification of pseudo two dimensional battery model using dynamic profile of lithium concentration. *Journal of Power Sources*, 286:510–525, 2015.

[140] Yinyin Zhao and Song-Yul Choe. A highly efficient reduced order electrochemical model for a large format limn 2 o 4/carbon polymer battery for real time applications. *Electrochimica Acta*, 164:97–107, 2015.

[141] Xiaoyu Li, Guodong Fan, Giorgio Rizzoni, Marcello Canova, Chunbo Zhu, and Guo Wei. A simplified multi-particle model for lithium ion batteries via a predictor-corrector strategy and quasi-linearization. *Energy*, 116:154–169, 2016.

[142] Joel C Forman, Saeid Bashash, Jeffrey L Stein, and Hosam K Fathy. Reduction of an electrochemistry-based li-ion battery model via quasi-linearization and pade approximation. *Journal of the Electrochemical Society*, 158(2):A93–A101, 2011.

[143] Kandler A Smith, Christopher D Rahn, and Chao-Yang Wang. Control oriented 1D electrochemical model of lithium ion battery. *Energy Conversion and Management*, 48(9):2565–2578, 2007.

[144] Tanvir R Tanim, Christopher D Rahn, and Chao-Yang Wang. A temperature dependent, single particle, lithium ion cell model including electrolyte diffusion. *Journal of Dynamic Systems, Measurement, and Control*, 137(1):011005, 2015.

[145] Long Cai and Ralph E White. Model reduction via proper orthogonal decomposition for the lithium ion battery. *ECS Transactions*, 13(19):13–26, 2008.

[146] Shengyi Liu. An analytical solution to li/li+ insertion into a porous electrode. *Solid State Ionics*, 177(1):53–58, 2006.

[147] Venkatasailanathan Ramadesigan, Vijayasekaran Boovaragavan, J Carl Pirkle, and Venkat R Subramanian. Efficient reformulation of solid-phase diffusion in physics-based lithium-ion battery models. *Journal of The Electrochemical Society*, 157(7):A854–A860, 2010.

[148] Nikolaos S Papageorgiou and Sophia Th Kyritsi-Yiallourou. *Handbook of applied analysis*, volume 19. Springer Science & Business Media, 2009.

[149] Arch W Naylor and George R Sell. *Linear operator theory in engineering and science*. Springer Science & Business Media, 2000.

[150] Ward Cheney. *Analysis for applied mathematics*, volume 208. Springer Science & Business Media, 2013.

[151] Athanasios C Antoulas. *Approximation of large-scale dynamical systems*, volume 6. Siam, 2005.

[152] Ruth Curtain and AJ Pritchard. The infinite-dimensional riccati equation for systems defined by evolution operators. *SIAM Journal on Control and Optimization*, 14(5):951–983, 1976.

[153] Roger Temam. *Navier-Stokes equations: theory and numerical analysis*, volume 343. American Mathematical Soc., 2001.

APPENDICES

Appendix A

Additional theorem

Theorem A.0.1. *Assume that the nonlinear function $\boldsymbol{f}(\boldsymbol{z})$ given in equation (2.1) is second-order differentiable and generates the evolution operator (2.58) which is also second-order differentiable with respect to the vector $\boldsymbol{z}_k$. Let the linearization of $\boldsymbol{f}(\boldsymbol{z})$ be defined by*

$$\boldsymbol{A}_{\bar{\boldsymbol{z}}} = \frac{\partial \boldsymbol{f}}{\partial \boldsymbol{z}} \mid_{\bar{\boldsymbol{z}}}$$

for some $\bar{\boldsymbol{z}} \in \mathbb{R}^n$. Furthermore, let the linearization of sampled-time model be defined as

$$\boldsymbol{F}_{\bar{\boldsymbol{z}}}(\Delta t, \bar{\boldsymbol{z}}, u_{[t_k,t_{k+1}]}) = \frac{\partial \boldsymbol{\chi}}{\partial \boldsymbol{z}} \mid_{(\Delta t, \bar{\boldsymbol{z}}, u_{[t_k,t_{k+1}]}, 0)} .$$

The operator $\boldsymbol{F}_{\bar{\boldsymbol{z}}_k}$ is the evolution operator assigned to the linear operator $\boldsymbol{A}_{\bar{\boldsymbol{z}}}$ when the disturbance term is set to zero. In addition,

$$\frac{\partial \boldsymbol{F}_{\bar{\boldsymbol{z}}}}{\partial u_{[t_k,t_{k+1}]}} = 0.$$

Proof: Let $\boldsymbol{z}(t)$ be a solution to the system dynamical equation (2.1); the time differentiation of this signal at time t can be defined as

$$\frac{d\boldsymbol{z}}{dt} = \lim_{\Delta t \to 0} \frac{\boldsymbol{z}(t+\Delta t) - \boldsymbol{z}(t)}{\Delta t}. \tag{A.1}$$

Now, by substituting equation (2.58) and (2.1) into (A.1) and setting $\xi(t) = 0$, it is obtained that

$$\boldsymbol{f}(\boldsymbol{z}(t)) + \boldsymbol{B}u = \lim_{\Delta t \to 0} \frac{\boldsymbol{\chi}(\Delta t, \boldsymbol{z}(t), u_{[t,t+\Delta t]}, 0) - \mathbf{z(t)}}{\Delta t}. \tag{A.2}$$

The expansion of the nonlinear function $\boldsymbol{f}(\boldsymbol{z})$ around the arbitrary vector $\bar{\boldsymbol{z}}$ reads as

$$\begin{aligned} \boldsymbol{f}(\boldsymbol{z}(t)) =& \boldsymbol{f}(\bar{\boldsymbol{z}}(t)) + \boldsymbol{A}_{\bar{\boldsymbol{z}}}(\boldsymbol{z}(t) - \bar{\boldsymbol{z}}(t)) + \\ & \sum_{i,j} \frac{\partial}{\partial z_i} \frac{\partial \boldsymbol{f}}{\partial z_j} \mid_{\check{\boldsymbol{z}}_1} (z_i(t) - \bar{z}_i(t))(z_j(t) - \bar{z}_j(t)) \end{aligned} \tag{A.3}$$

$\check{\boldsymbol{z}}_1(t) \in [\bar{\boldsymbol{z}}(t), \boldsymbol{z}(t)]$ for every t. Furthermore, the evolution operator can also be expanded around the arbitrary vector $\bar{z}$ as

$$\begin{aligned}
&\boldsymbol{\chi}(\Delta t, \boldsymbol{z}(t), u_{[t,t+\Delta t]}, 0) = \\
&\quad \boldsymbol{\chi}(\Delta t, \bar{\boldsymbol{z}}(t), u_{[t,t+\Delta t]}, 0) + \\
&\quad \boldsymbol{F}_{\bar{\boldsymbol{z}}(t)}(\Delta t, \bar{\boldsymbol{z}}(t), u_{[t,t+\Delta t]})(\boldsymbol{z}(t) - \bar{\boldsymbol{z}}(t)) + \\
&\quad \sum_{i,j} \frac{\partial}{\partial z_i} \frac{\partial \boldsymbol{\chi}}{\partial z_j} \mid_{(\Delta t, \check{\boldsymbol{z}}_2, u_{[t,t+\Delta t]}, 0)} (z_i(t) - \bar{z}_i(t))(z_j(t) - \bar{z}_j(t))
\end{aligned} \tag{A.4}$$

where $\check{\boldsymbol{z}}_2(t) \in [\bar{\boldsymbol{z}}(t), \boldsymbol{z}(t)]$ for every t.

Substituting equations (A.3) and (A.4) into (A.2) and employing equation (A.2) for $\boldsymbol{z} = \bar{\boldsymbol{z}}$ result in

$$\begin{aligned}
&\boldsymbol{A}_{\bar{\boldsymbol{z}}}(\boldsymbol{z}(t) - \bar{\boldsymbol{z}}(t)) + \\
&\sum_{i,j} \frac{\partial}{\partial z_i} \frac{\partial \boldsymbol{f}}{\partial z_j} \mid_{\check{\boldsymbol{z}}_1} (z_i(t) - \bar{z}_i(t))(z_j(t) - \bar{z}_j(t)) = \\
&\lim_{\Delta t \to 0} \frac{\boldsymbol{F}_{\bar{\boldsymbol{z}}(t)}(\Delta t, \bar{\boldsymbol{z}}(t), u_{[t,t+\Delta t]})(\boldsymbol{z}(t) - \bar{\boldsymbol{z}}(t)) - (\boldsymbol{z}(t) - \bar{\boldsymbol{z}}(t))}{\Delta t} + \\
&\lim_{\Delta t \to 0} \frac{\sum_{i,j} \frac{\partial}{\partial z_i} \frac{\partial \boldsymbol{\chi}}{\partial z_j} \mid_{(\Delta t, \check{\boldsymbol{z}}_2, u_{[t,t+\Delta t]}, 0)} (z_i(t) - \bar{z}_i(t))(z_j(t) - \bar{z}_j(t))}{\Delta t}.
\end{aligned} \tag{A.5}$$

Since equation (A.5) is satisfied for all $\boldsymbol{z}, \bar{\boldsymbol{z}} \in C^1([0, T], \mathbb{R}^n)$, it can be concluded that

$$\begin{aligned}
&\boldsymbol{A}_{\bar{\boldsymbol{z}}}(\boldsymbol{z}(t) - \bar{\boldsymbol{z}}(t)) = \\
&\quad \lim_{\Delta t \to 0} \frac{\boldsymbol{F}_{\bar{\boldsymbol{z}}(t)}(\Delta t, \bar{\boldsymbol{z}}(t))(\boldsymbol{z}(t) - \bar{\boldsymbol{z}}(t)) - (\boldsymbol{z}(t) - \bar{\boldsymbol{z}}(t))}{\Delta t}
\end{aligned}$$

which simply indicate that $\boldsymbol{A}_{\bar{\boldsymbol{z}}}(\boldsymbol{z}(t) - \bar{\boldsymbol{z}}(t))$ generates $\boldsymbol{F}_{\bar{\boldsymbol{z}}(t)}(\Delta t, \bar{\boldsymbol{z}}(t))(\boldsymbol{z}(t) - \bar{\boldsymbol{z}}(t))$ and is independent of the input vector $u(t)$. □

Appendix B

Compactness theorem

Theorem B.0.2. *[153, Theorem III.2.1]*
Let $\mathcal{H}_1$ and $\mathcal{H}_2$ be two Banach spaces such that

$$\mathcal{H}_2 \subset \mathcal{H}_1, \text{ the injection being compact.}$$

Let $\boldsymbol{\mathcal{J}}$ be a set of functions in $\mathcal{L}^1(\mathbb{R}, \mathcal{H}_2) \cap \mathcal{L}^p(\mathbb{R}, \mathcal{H}_1)$ for $p > 1$ satisfying

$$\mathcal{J} \text{ is bounded in } \mathcal{L}^1(\mathbb{R}, \mathcal{H}_2) \text{ and } \mathcal{L}^p(\mathbb{R}, \mathcal{H}_1)$$
$$\int_{-\infty}^{\infty} \|\boldsymbol{J}(s+t) - \boldsymbol{J}(s) ds\|_{\mathcal{H}_1}^2 \to 0 \, as \, t \to 0$$

uniformly for $\boldsymbol{J} \in \boldsymbol{\mathcal{J}}$. Furthermore, suppose that the support of functions $\boldsymbol{J} \in \boldsymbol{\mathcal{J}}$ is in a fixed compact set of $\mathbb{R}$. Then, the set $\boldsymbol{\mathcal{J}}$ is relatively compact in $\mathcal{L}^p(\mathbb{R}; \mathcal{H}_1)$.